Geological Survey of Finland 2019

Origin of the concealed continental crust of Vestfjella, western Dronning Maud Land, Antarctica – Evidence from xenoliths hosted by Jurassic lamproites

K. R. Ilona Romu

Bulletin 409 • Monograph: Academic Dissertation

GTK

GEOLOGICAL SURVEY OF FINLAND

Bulletin 409

Origin of the concealed continental crust of Vestfjella, western Dronning Maud Land, Antarctica – Evidence from xenoliths hosted by Jurassic lamproites

by

K. R. Ilona Romu

ACADEMIC DISSERTATION

Department of Geosciences and Geography, University of Helsinki

To be presented, with the permission of the Faculty of Science of the University of Helsinki, for public examination in auditorium D101, Physicum, Kumpula campus, on September 12th, 2019, at 12 o'clock noon.

Unless otherwise indicated, the figures have been prepared by the author of the publication.

https://doi.org/10.30440/bt409

Layout: Elvi Turtiainen Oy
Printing house: Edita Prima Oy

Espoo 2019

Supervisor Dr Arto V. Luttinen
Luomus Finnish Museum of Natural History
University of Helsinki
Helsinki, Finland

Pre-examiners Associate Professor Wilfried Bauer
Department of Applied Geosciences
German University of Technology in Oman
Muscat, Sultanate of Oman

Professor Olav Eklund
Åbo Akademi University
Turku, Finland

Opponent Professor Joachim Jacobs
University of Bergen
Bergen, Norway

Romu, K. R. I. 2019. Origin of the concealed continental crust of Vestfjella, western Dronning Maud Land, Antarctica – Evidence from xenoliths hosted by Jurassic lamproites. *Geological Survey of Finland, Bulletin 409,* 106 pages, 25 figures, 10 tables and 2 appendices.

This work considers with the origin, age and geological environment of the concealed continental crust of Vestfjella, western Dronning Maud Land, Antarctica (WDML). In the Jurassic, the bedrock of Vestfjella experienced the latest major period of extension and rifting. The WDML Jurassic crust has been correlated with the Karoo Large Igneous Province of Africa, and with the Archean and Proterozoic domains, where exposed, of the Archean Kaapvaal Craton and Mesoproterozoic Natal Belt of Africa. The lamproite-hosted xenoliths investigated in this study show metamorphic (including metasomatic) modification from their primary geochemical composition. In the classification of the examined samples, the mineral mode proved to be superior to geochemical classification in protolith identification.

The zircon populations of arc affinity metatonalite, quartz metadiorite and metagranite xenoliths record multiple thermal events at 1150–590 Ma. However, the evolution of the WDML Proterozoic crust began earlier, in the Mesoproterozoic, with arc magmatism at ca. 1450–1300 Ma. The accretion of arc terrains and development of the continental Namaqua–Natal–Maud belt by the Grenvillian-Kibaran orogeny was followed by the break-up of the Rodinia Supercontinent. Granite crystallization at ca. 1100–1090 Ma and at 1050–990 Ma records crustal anatexis, cooling and Neoproterozoic mylonitic deformation. The Proterozoic zircon ages are similar to the crustal domains in the Natal Belt of southern Africa, the Maud Belt of central Dronning Maud Land and remote Mesoproterozoic basement exposed in the West Falkland Islands and Haag nunataks, West Antarctica.

The initial εNd (1450) of +7.1 for a pargasite-rich garnet-free metagabbro and the initial εNd (180) of -8.5 for a garnet-bearing metagabbro resemble the isotopic signature of enriched lithospheric mantle and old enriched crust. The present-day Nd isotope composition of these xenoliths conforms to the array of the Triassic Karoo igneous province gabbroic rocks and granulite xenoliths (Proterozoic or undefined), similar to the Lesotho lower crustal xenoliths. The youngest xenolith zircon age, 165 Ma, records crustal heating and granite magmatism post-dating the Karoo magmatism in WDML. The Vestfjella crust cooled below 300 °C at ca. 100 Ma ago (Rb-Sr).

This work provides new direct information on the concealed Precambrian of East Antarctica, the regional geology of East Antarctica and southern Africa, and geological processes in the Vestfjella bedrock. The results may be used to resolve the palaeogeography of the supercontinents Rodinia and Gondwana and to interpret existing and forthcoming chronological, geochemical and geophysical data.

Keywords: bedrock, continental crust, supercontinents, xenoliths, metagranitoids, metagabbroids, quartz metadioritoids, lamproite, absolute age, zircon, Jurassic, Neoproterozoic, Mesoproterozoic, East Antarctica, Vestfjella, Kjakebeinet

K. R. Ilona Romu
Geological Survey of Finland
P.O. Box 1237
FI-70211 Kuopio
Finland

E-mail: ilona.romu@gtk.fi

ISBN 978-952-217-401-7 (pdf)
ISBN 978-952-217-402-4 (paperback)
ISSN 0367-522X (print)
ISSN 2489-639X (online)

CONTENTS

1 INTRODUCTION 9

2 PROTEROZOIC CRUSTAL EVOLUTION 10
2.1 Proterozoic continental crust and processes therein 10
2.2 Supercontinent Rodinia 11

3 GEOLOGICAL SETTING 12
3.1 Regional crustal domain of western Dronning Maud Land 12
3.2 The Kalahari-Grunehogna craton 14
3.3 The Precambrian of the Natal-Maud mobile belt 14
3.3.1 Heimefrontfjella Mountains and Mannefallknausane nunataks 14
3.3.2 Umkondo and Ritscherflya supracrustal sequences 15
3.3.3 Mzumbe, Margate and Tugela accretionary terrains 15
3.4 Falkland and Ellsworth-Haag microplates 16
3.4.1 Falkland microplate 16
3.4.2 Ellsworth-Haag microplate 16

4 XENOLITHS 17
4.1 Challenges in xenolith research 17
4.2 Relevance of xenolith studies 18

5 MATERIALS 18
5.1 Samples 18
5.2 Representativeness of the samples 22

6 ANALYTICAL METHODS 22
6.1 Petrography 22
6.2 Mineral chemistry 22
6.3 Whole-rock geochemistry 23
6.4 U-Pb geochronology 23
6.5 Sm-Nd and Rb-Sr isotope geochemistry 24

7 PETROGRAPHY AND MINERALOGY 25
7.1 Metagabbroids and quartz metadiorites. 36
7.1.1 Metagabbros 36
7.1.2 Metagabbronorites 36
7.1.3 Quartz metadiorites 37
7.2 Metagranitoids 37
7.2.1 Metatonalites 37
7.2.2 Equigranular metagranite 38
7.2.3 Gneissic metagranites 38
7.2.3. Mylonitic metagranites 38
7.3 Metasedimentary rock types 38
7.3.1 Metapelites 38
7.3.2 Other metasedimentary xenoliths 39
7.4 Rutile in quartz metadiorite and equigranular granite xenoliths 39

7.5 Petrographic peculiarities and indications of melting of the studied xenoliths 42
7.6 Data evaluation and interpretation 42
7.6.1 QAPF classification 42
7.6.2 Mineral microanalyses 43

8 GEOCHEMISTRY 44
8.1 The studied Kjakebeinet xenoliths and their hosts 44
8.2 Geochemical classification of the studied metaigneous xenoliths 50
8.3 Metagabbros and metadiorites 54
8.3.1 Metagabbros 54
8.3.2 Quartz metadiorites 54
8.4 Metagranitoids 55
8.4.1 Metatonalites 55
8.4.2 Mylonitic and gneissic metagranites 55
8.4.3 Equigranular metagranite 55
8.5 Geochemical classification of the metasedimentary xenoliths 56
8.5.1 Metapelite 56
8.5.2 Metagreywacke 56
8.6 Data evaluation and interpretation 57
8.6.1 Geochemical modification of the studied xenoliths 57
8.6.2 The geochemical rock type classifications 58
8.6.3 The use of tectonic discrimination diagrams based on incompatible trace elements 58
8.6.4 REE geochemistry of the studied xenoliths 59

9 U-PB, RB-SR AND SM-ND ISOTOPE GEOLOGY 60
9.1 Metagranitoids 68
9.1.1 Metatonalites Xe1 and Xe4 68
9.1.2 Mylonitic metagranite Xe2 68
9.1.3 Gneissic metagranite Xe6 68
9.1.4 Equigranular metagranite ALKBM6 69
9.2 Metagabbroids and metadiorites 69
9.2.1 Quartz metadiorite ALKBM1 69
9.2.2 Garnet-free metagabbro Xe11 69
9.2.3 Garnet-bearing metagabbro Xe16 73
9.3 Isotopic data evaluation 75
9.3.1 Secondary ion mass spectrometry in zircon U-Th-Pb studies 75
9.3.2 Rb-Sr and Sm-Nd results 76

10 CRUSTAL PROVENANCE OF THE VESTFJELLA XENOLITHS 76
10.1 Zr-in-rutile and Zr-in-whole-rock saturation temperatures 77
10.2 Thermobarometry and metamorphism 80
10.2.1 Metagabbros 80
10.2.2 Metatonalites and quartz metadiorites 80
10.3 Incompatible element geochemical constraints 81
10.3.1 The continental crust reference values used 81
10.3.2 Metagabbros 83
10.3.3 Metatonalites and quartz metadiorites 83
10.3.4 Metagranites 84
10.3.5 Metasedimentary rock types 84
10.4 Control points from geochronology and isotopic tracers 84
10.4.1 General remarks 84
10.4.2 Zircon chronology 87
10.4.3 Isotopic tracers 87

11 FORMATION OF THE CONTINENTAL CRUST OF WESTERN DRONNING MAUD LAND 93
11.1 Volcanic arc at 1350–1150 Ma 95
11.2 Arc-continent collision of 1100–1000 Ma 95
11.3 Post-orogenic cooling at 1000–900 Ma 96
11.4 Rodinia rifting at 800–750 Ma and amalgamation of Gondwana at 570–530 Ma 96
11.5 Gondwana break-up at 180 Ma, cooling and development of continental margin at 140–100 Ma 97

12 CONCLUDING REMARKS 98
12.1 Original thickness of the continental crust of western Dronning Maud Land 98
12.2 A xenolith suite with both orogenic and anorogenic origins 99
12.3 Thermal evolution of the crustal domain of western Dronning Maud Land 99
12.4 Tectonic evolution of the crustal domain of western Dronning Maud Land 100

ACKNOWLEDGEMENTS 100

REFERENCES 101

APPENDICES 107

1 INTRODUCTION

Over geological time, the crust of the Earth has evolved geochemically and mineralogically through magmatic differentiation and recycling within the geosphere. The geological processes affecting the bedrock commonly take a long time, and periods of 0.1–1 Ga often need to be examined to distinguish processes such as the formation and modification of oceanic and continental crust, as well as plate tectonics. The crust (both oceanic and continental) is the only direct source of minerals and metals that make modern human life possible on Earth. Moreover, the continental crust, comprising 0.5% of the mass of the Earth, is a major reservoir of incompatible elements (e.g. McLennan et al. 2006). By studying the lithological units of the continental crust it has been possible to decipher the evolution of the Earth from the Archean to the present. The essential tools used are geochemical fingerprinting, a variety of geochronological methods and palaeomagnetism. A crucial prerequisite in the interpretation of geochemical data is knowledge of the mineralogy and petrography of the rocks examined. The plate tectonic context of the rock units offers insights into the geological processes and is also the basis for numerous practical applications, including prospecting and the study of overall changes in the Earth system.

The crystalline bedrock in the current plate tectonic assembly of Antarctica is a collage of crustal units that were assembled into the supercontinent Rodinia in the Proterozoic and dispersed during the Mesozoic (e.g. Boger 2011). In Antarctica, exposed segments of Precambrian crust are also found in western Dronning Maud Land, East Antarctica. The framework of the regional geology in western Dronning Maud Land and southern Africa is based on the recognition of the entity referred to as the Kalahari craton, defined by Jacobs et al. (2008) as the Archean nuclei of the Kalahari craton and the surrounding Proterozoic mobile belts (Fig. 1). The Proterozoic and Mesozoic events indicative of supercontinent cycles of Rodinia and Gondwana have generated new crust and tectonically modified the new and the pre-existing crust of the study area. However, the basement over the wide coastal area of western Dronning Maud Land is unexposed due to ice cover and overlying Jurassic flood basalts. The interface, probably sutured, between Archean and Proterozoic geological units is hidden, probably located beneath the Jurassic formations of the Vestfjella mountain range, as indicated by aerogeophysical data (e.g. Corner 1994). Suture zones are geologically complex and tectonically disturbed, and often provide a plethora of igneous and metamorphic rocks of different ages, compositions and possible genetic interpretations.

The study area is positioned in a rifted continental margin setting. Prior to the break-up of Gondwana in the Jurassic, Vestfjella was located at or in the vicinity of the juncture of East Antarctica, Africa, the Falkland microplate and the Ellsworth-Haag microplate (Jacobs et al. 2008, Jacobs & Thomas 2004) (Fig. 1). Based on aerogeophysical data, the Archean–Proterozoic boundary is likely to transect the basement of northern Vestfjella. This probably results in the basement of Vestfjella being geologically complex, comprising a mélange of lithologies that originated in different eons. As outcrops are rare and scientific drilling has not been carried out on the land, expectations were high for the studied xenoliths, which represent inaccessible crustal levels.

In order to constrain the composition and age of the unexposed bedrock, the mineralogy, petrography, geochemistry, mineral and whole-rock Sm-Nd ages, and zircon U-Pb ages of two lamproite-hosted xenolith suites from Vestfjella, western Dronning Maud Land, were investigated in this work. On the basis of correlative trace element geochemistry and mineral equilibration

calculations, the crustal provenance and information on the ancient crustal thickness were deciphered. The origins of the xenoliths and associated geological processes that led to the present crustal architecture of western Dronning Maud Land were examined by combining whole-rock and mineral geochemical data, based on detailed petrography and mineralogy of the samples, with U-Pb zircon geochronology. This work provides direct information on the concealed Precambrian of East Antarctica, which is valuable in resolving the palaeogeography of the supercontinents Rodinia and Gondwana, the regional geology of East Antarctica and southern Africa, and related geological processes in the bedrock. The results may be used for interpreting the existing and, hopefully, forthcoming geochemical and geophysical data on the study area.

2 PROTEROZOIC CRUSTAL EVOLUTION

2.1 Proterozoic continental crust and processes therein

The formation of the continental crust is an ongoing process that demonstrably already started with zircon crystallization in the Hadean (Cavosie et al. 2004) and was followed by the formation of oceanic proto-crust in the Archean (e.g. Arndt 2013). The Hadean (4.4 Ga) zircons of Jack Hills, Western Australia, indicate the presence of differentiated source rocks (Cavosie et al. 2004, Valley et al. 2014) and are indicative of re-melting processes of the proto-crust and subsequent continental crust formation (Arndt 2013). The late Archean crust is governed by felsic, quartz- and feldspar-dominated components, e.g. the tonalite–trondhjemite–granodiorite suites (e.g. Arndt 2013) and greenstone belts where mafic-ultramafic volcanic rocks are common. It has been suggested that 75% of the continental crust was formed during the Archean and has since been recycled by subduction and sedimentation processes (e.g., McLennan et al. 2006). Our perception of the differences between the Archean and Proterozoic Earth are based on age determinations and geochemical fingerprinting, combined with seismic and heat flow studies on current geological environments (McLennan et al. 2006). Although the composition of the Archean and Proterozoic crust differs geochemically, knowledge of the Phanerozoic processes has been widely used to interpret the formation of the continental crust during the Meso- and Neoproterozoic (cf. Davidson & Arculus 2006).

Convergent margins and accreted oceanic plateaus are considered as the primary location for the production of juvenile continental crust (e.g. Davidson & Arculus 2006). Deep mantle plume and subduction-derived basalts provide the juvenile basis for continental rock types. As the continental crust is buoyant compared to the oceanic crust (which may only exist for about 200 Ma in the Phanerozoic eon), it has been subject to a variety of time-integrated modifications, including weathering, erosion, partial melting, ductile and brittle deformation, and metamorphism. The continental crust is a buoyant reservoir and the fractionation and differentiation of magmas in it produce more evolved, incompatible-element-enriched lithological units. In addition, sedimentary rocks act as crustal contaminants and a source component of anatectic melts, yielding an additional end member for the geochemical puzzle of the continental crust.

A characteristic feature of the Proterozoic continental crust is its heterogeneity and great diversity of rock types. In general, magmas that were extracted from the mantle during the Proterozoic were more likely to have been contaminated by the earlier-formed crust than their Archean counterparts. Melting and migmatisation of the pre-existing crust (magmatic, metamorphic and sedimentary rocks), together with the contribution of magmas from depleted and enriched mantle peridotite and pyroxenite reservoirs, have been important factors producing an internally differentiated continental crust characterized by increasing concentrations of incompatible elements from the deep to the shallow crust (cf. Rudnick & Gao 2004).

The dynamics of the continental lithosphere are controlled by the structural and compositional heterogeneities of the continental crust

and the subcontinental lithospheric mantle (cf. Levander et al. 2006). The resultant tectonic mixture of crustal components of different ages and recrystallization of, for example, zircon, monazite and titanite used in geochronology is evident (cf. Karlstrom & Williams 2006) and complicates unravelling of the genesis of crustal sections, particularly that of high-grade granulite terrains (e.g. Whitehouse & Kamber 2005).

Inevitably, therefore, the Proterozoic crust of the Earth that we observe today is the result of a great variety of geological processes and may be reflected by uniformitarianism. The most important environments of magma generation in the plate tectonic context are mid-ocean ridges, oceanic islands, oceanic and continental arcs, and continental rifts. Mass-balance calculations, heat flow models and seismic proxies indicate that the main process generating continental crust in the Proterozoic was arc magmatism (e.g. McLennan et al. 2006). The continental crust cannot be solely produced by melting of the mantle, but also through the melting of pre-existing crust, mixing of the mantle-derived basaltic magmas with more felsic material, and by metamorphic and metasomatic modification of the pre-existing crust. The tectonically significant force affecting the abovementioned processes was the formation of collisional orogenies through convergence. Additionally, the crust and the lithospheric mantle comprise a dynamic entity in which the varying characteristics of the crust and upper mantle, such as the composition, thickness, temperature and ability to generate heat, affect factors such as the mechanical properties and possible styles of deformation in the plate tectonic context (e.g. Rosenbaum et al. 2010, Sandiford & McLaren 2006). It has also been proposed that the plate motions and changes in lithospheric thickness govern convection in the shallow mantle (King & Anderson 1998).

2.2 Supercontinent Rodinia

The concept of supercontinents combines geological, geophysical, geodetical and biological data for palaeogeographic interpretations of the relative configuration and distribution of the Earth's continental landmass through time. Correlation between the age and composition of geological formations and tectonic features, together with information on palaeomagnetism (remanent magnetism of the magnetic minerals displaying the ancient magnetic fields), are the main tools used in continental reconstruction. Accordingly, comprehensive unitary landmasses referred to as the supercontinents Rodinia, Gondwana and Pangea have been reconstructed on the basis of the proxies preserved on the continents of today.

The Rodinia supercontinent and its precursory continental blocks were built up in orogenic processes between 1.3–0.9 Ga, one of the spatially most extensive being the 1.1 Ga Grenville-age orogeny, also known as the Kibaran orogeny in southern Africa. The age, configuration and detailed evolution of Rodinia is controversial, however, and is continuously being revised, as is common in the study of continents through time. Probably all continental blocks in existence at that time (e.g. Amazonia, Baltica, Laurentia, Australia, East Antarctica, India and Kalahari) were involved in the diachronous assembly of Rodinia, featured by the accretion or collision of continental blocks around the margin of Laurentia (Goodge et al. 2008, Li et al. 2008). Overall, Grenville-age mobile belts are widespread and found, for example, in Australia, Canada, East Antarctica, southern Africa and south-central and eastern North America (Goodge et al. 2008, Jacobs et al. 2015), mostly on the edges of continental nuclei. During its known presence, Rodinia experienced plume-induced periods of heating and continental rifting, resulting in two-stage disintegration: the rifting of western Laurentia between ca. 0.83 and 0.74 Ga and eastern Laurentia at ca. 0.6 Ga (Li et al. 2008). This process and associated regional convergence of continental blocks led to the formation of Gondwana at ca. 0.53 Ga (Li et al. 2008). In the Mesozoic, East and West Gondwana rifted apart and the continental margin of western Dronning Maud Land, East Antarctica, was formed (e.g. Jacobs & Thomas 2004).

3 GEOLOGICAL SETTING

The study area is situated in a rifted continental margin setting. Prior to the Jurassic break-up of Gondwana, Vestfjella was located at or in the vicinity of the juncture of East Antarctica, Africa, and a collage of microplates (Jacobs et al. 2008, Jacobs & Thomas 2004). The continental fragments relevant to this study are the Archean Kalahari and Grunehogna segments of Africa and Antarctica (Groenewald et al. 1995, Jacobs et al. 2008), and especially the fragments of the Mesoproterozoic collisional arc systems: the Natal-Maud Belt and presently spatially scattered Falkland and Haag-Ellsworth microplates (Jacobs et al. 2008) (Fig. 1).

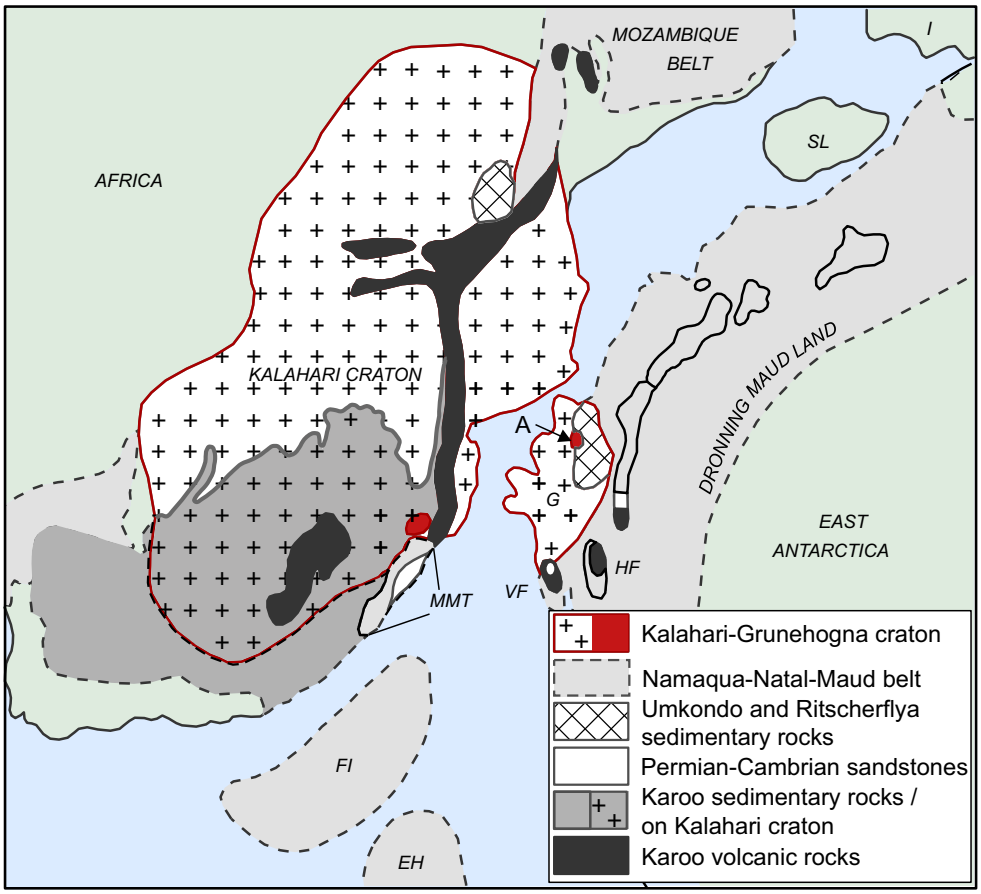

Fig. 1. The study area in a Mesozoic Gondwana reconstruction. Modified after Jacobs and Thomas (2004) and Grantham et al. (2011). Abbreviations: A, Annandagstoppane nunatak; EH, Ellsworth-Haag microplate; FI, Falkland microplate; G, Grunehogna craton; HF, Heimefrontfjella mountain range; I, India; Kalahari, Kalahari craton; SL, Sri Lanka; MMT, Mzumbe terrain, Margate terrain and Tugela terrain of the Natal belt; VF, Vestfjella mountain range.

3.1 Regional crustal domain of western Dronning Maud Land

Western Dronning Maud Land on the east coast of the Weddell Sea is broadly covered by the East Antarctic ice sheet, but some of the bedrock is exposed on nunataks, ridges and mountains (Fig. 1). Immediately to the north of Vestfjella, geophysical data indicate an Archean craton boundary as marked by a large-scale magnetic anomaly (Corner 1994, Golynsky 2007) (Fig. 2). Topographically, the Heimefrontfjella (2800 masl) and Vestfjella (900 masl) mountain ranges are separated by an ice-filled horst-graben system with basins at 400 to 1600 m below the ice (Sandhäger & Blindow 1997, Popov & Leitchenkov 1997). The exposed Vestfjella, a circa 120-km-long range of scattered ridges, is composed of the Jurassic Karoo flood basalts, which are cross-cut by associated dolerites, gabbros and rare granitic dykes (Vuori & Luttinen 2003). On a sole ridge on the northern Vestfjella, Permian sandstones are exposed (e.g. McLoughlin

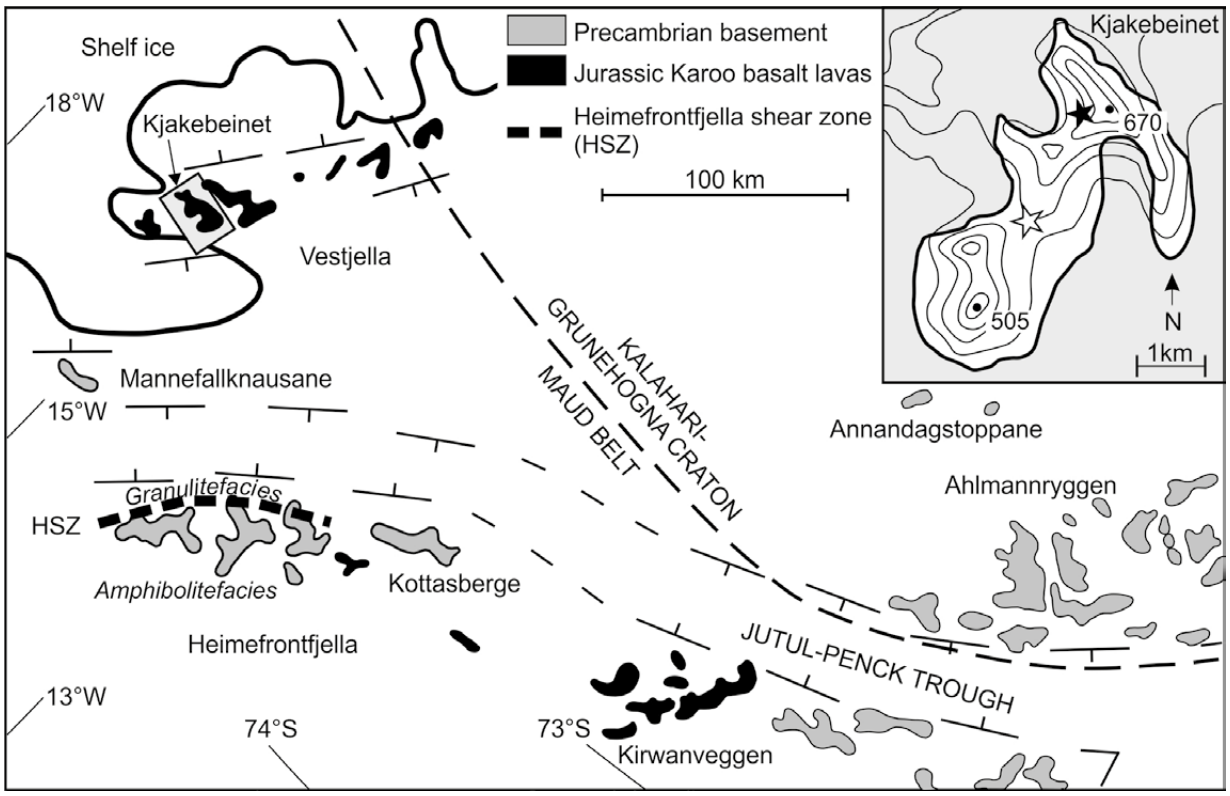

Fig. 2. Geological sketch map of western Dronning Maud Land, Antarctica, modified after Luttinen et al. (2002). On Ahlmannryggen, only dykes represent the Jurassic flood basalt magmatism (cf. Riley et al. 2005). The inset shows the sampling sites of the xenoliths on Kjakebeinet nunatak, Vestfjella mountain range: Glacial boulders (open star) 73° 47.762´ S, 014° 54.452´ W and 73° 47.650´ S, 014° 54.660´ W, lamproite dyke (filled star) 73° 47.011´ S, 014° 52.397´ W. Heimefrontfjella shear zone (HSZ) after Jacobs et al. (2003).

et al. 2005). The Heimefrontfjella mountains ca. 150 km to the southeast and the Mannefallknausane nunataks ca. 50 km to the south of Vestfjella provide insights into the unexposed basement of Vestfjella (Fig. 2).

The Precambrian bedrock of western Dronning Maud Land, exposed in the Annandagstoppane nunataks, Heimefrontfjella Mountains and nunataks south of Vestfjella (Mannefallknausane) (Fig. 1), registers major regional events related to the evolution of the supercontinent Rodinia (cf. Bauer 1995, Bauer et al. 2003a, 2003b, Rämö et al. 2008, Barton et al. 1987, Marschall et al. 2010). Rodinia was mainly built up in the ca. 1.1 Ga Grenvillian-Kibaran-Frazer orogeny, which produced Andean-type orogens of the Superior Province (Canada), the Namaqua-Natal-Maud Belt (southern Africa and East Antarctica) and Albany-Frazer (Australia). At the end of the Mesoproterozoic, the diachronous arcs of Namaqua-Natal and Maud were spatially connected (Bisnath et al. 2006). The Namaqua-Natal-Maud mobile belt fringes the Archean Kalahari-Grunehogna craton, exposed in southern Africa and Annandagstoppane, western Dronning Maud Land (Jacobs et al. 2008, Grantham et al. 2011, Marschall et al. 2010). The Grunehogna segment of the Kalahari craton is covered with ice and a ca. 1.1 Ga Ritscherflya sequence of sedimentary and volcanic rocks (Groenewald et al. 1995, Marschall et al. 2013a) (Fig. 1). The Precambrian geochronological results of the previous studies are listed later in Table 10.

The Falkland Islands (Cape Meredith complex) and Ellsworth-Haag Mountains of West Antarctica have been correlated with the Namaqua-Natal-Maud Belt rocks formed during the 1.1 Ga Grenvillian orogeny (Fig. 1) (e.g. Jacobs et al. 2003, McCourt et al. 2006). The Neoproterozoic East African-Antarctic orogenic compressional tectonic regime, related to the change from Rodinia to Gondwana, caused a major 0.95–0.45 Ga metamorphic overprint (aka. The Pan-African event) with the coeval intrusion of felsic magmas from magmatic and sedimentary sources (Li et al. 2008, Jacobs & Thomas 2004). The East Antarctic African orogeny is marked by ca. 0.65–0.5 Ga crustal anatexis and amphibolite

to granulite facies metamorphism observed at Heimefrontfjella and Kirwanveggen, western Dronning Maud Land (Fig. 2), and by ca. 0.5–0.6 Ga plutonic intrusions and granulite facies metamorphism in central Dronning Maud Land (Paulsson & Austrheim 2003, Jacobs et al. 1998, 2003, Jacobs & Thomas 2004, Bisnath et al. 2006).

Central Dronning Maud Land has also been correlated with the Mozambique Belt, Africa (Fig. 1), where the metamorphism correlated with the East Antarctic African orogeny overprints the Mesoproterozoic rocks (e.g. Jacobs 1998, Bisnath et al. 2006). The Gondwana assembly was accomplished by ca. 0.53 Ga (Li et al. 2008) and positioned western Dronning Maud Land within the frontier zone of East and West Gondwana. During the Jurassic, the Gondwana supercontinent rifted. This process was accomplished by the extrusion of the Karoo flood basalts at ca. 180 Ma. This event predated the intrusion of Vestfjella lamproites by ca. 20 Ma (Luttinen et al. 2002). The lamproite magmas transported the xenoliths studied in this work to the surface at Kjakebeinet, southern Vestfjella (Fig. 2).

3.2 The Kalahari-Grunehogna craton

The Kalahari craton includes the Archean nucleus, referred to as Proto-Kalahari by Jacobs et al. (2008), and the surrounding Mesoproterozoic Grenville collisional orogenic belt, of which the Namaqua-Natal-Maud mobile belt forms a considerable part (Jacobs et al. 2008) (Fig. 1). This once continuous fragment of stabilized continental crust disintegrated into fragments, mainly during the Jurassic.

The granitic Grunehogna craton basement, covered with ice and a ca. 1.1 Ga Ritscherflya sequence of sedimentary and volcanic rocks (Groenewald et al. 1995, Marschall et al. 2013a, 2013b), is exposed at Annandagstoppane, western Dronning Maud Land (Groenewald et al. 1995) (Figs. 1 & 2). The Annadagstoppane granite was dated at ca. 3070 Ma by the zircon U-Pb method (Marschall et al. 2010). The interiors of the Kalahari-Grunehogna craton were intruded by mafic sills and dykes at ca. 1110 Ma (Hanson et al. 2004, Hanson et al. 1998, Marschall et al. 2013a, 2013b). These basaltic magmas with intra-continental magma characteristics form the Umkondo Large Igneous Province, temporally simultaneous with the Grenville collisional orogeny, which yoked the continental fragments into the Rodinia Supercontinent (Hanson et al. 2004, Jones et al. 2003).

3.3 The Precambrian of the Natal-Maud mobile belt

3.3.1 Heimefrontfjella Mountains and Mannefallknausane nunataks

Maud Belt rocks of western Dronning Maud Land, the Antarctic extension of the Grenville-aged Namaqua-Natal Belt of southern Africa, are exposed on the Heimefrontfjella mountain range and the Mannefallknausane nunataks (Fig. 2). The Heimefrontfjella Mountains include diverse terrains, separated by tectonic discontinuities, with igneous ages between 1180–1050 Ma (Jacobs 2009). Neoproterozoic, late-orogenic magmatism was accompanied by high-grade metamorphism between ca. 1090 and 1060 Ma (Jacobs et al. 2003). On southwestern Heimefrontfjella the Heimefrontfjella shear zone (HSZ) is up to 20 km wide and comprises of a set of N–S trending shear zones (cf. Jacobs et al. 2003). The HSZ represents a significant lithospheric discontinuity. It originated at the western boundary of the East African Antarctic orogeny at ca. 1080 Ma and re-activated at ca. 500 Ma (Bauer et al. 2003b, Jacobs et al. 2003, Jacobs & Thomas 2004, Jacobs 2009, Bauer et al. 2016). The west side of the HSZ is typified by granulite facies metamorphic conditions and 950–1010 Ma mineral cooling ages (Jacobs et al. 1995). The HSZ and outcrops to the east of it record amphibolite facies assemblages and 470–570 Ma mineral cooling ages (Jacobs et al. 1995, Bauer et al. 2016).

The oldest igneous age obtained from the granulite terrain is 1135 Ma (Arndt et al. 1991), and detrital zircon ages of 1200–2000 Ma with a significant peak at 1800 Ma have been

measured from metasedimentary rocks of the granulite facies terrane (Vardeklettane; Arndt et al. 1991, Jacobs 2009). The amphibolite terrain is composed of a supracrustal sequence of metasedimentary rocks (quartzite, metapelite, marble, paragneiss) intercalated with banded mafic and felsic gneisses and intruded by several late Mesoproterozoic granitoids. This assemblage records intense polyphase deformation and metamorphism (Jacobs et al. 2003, Bauer et al. 2016) and may have originated in an extensional back-arc setting (Bauer et al. 2003b). The amphibolite facies Kottasberge nunatak (Fig. 2), northeast of the granulite terrain, is characterized by intercalated sedimentary rocks, calc-alkaline granitoids and tonalites. It has been interpreted as a fragment of a Mesoproterozoic island arc where the ca. 500 Ma Pan-African overprint is restricted to minor discrete shear zones (Bauer et al. 2003b). The Mannefallknausane nunataks (Fig. 2) are dominated by ca. 1070 Ma charnockites and K-feldspar megacrystic A-type granites indicative of a granulite facies environment (Arndt et al. 1991, Siivola et al. 1991, Rämö et al. 2008).

3.3.2 Umkondo and Ritscherflya supracrustal sequences

The ca. 1100 Ma volcano-sedimentary Ritscherflya sequence stratigraphically overlies the Archean Grunehogna craton and is exposed on Ahlmannryggen, juxtaposed to the Maud Belt rocks (Groenewald et al. 1995, Marschall et al. 2013a, 2013b) (Figs. 1 & 2). The sedimentary and volcanic rocks eroded from an active continental arc (Marschall et al. 2013a, 2013b), accumulated in a foreland basin (Groenewald et al. 1995), and are correlative with the Umkondo sequence of Zimbabwe and Mozambique (Hanson et al. 2004, Hanson et al. 1998) (Fig. 1). Clastic, immature sedimentary rocks include greywackes, arenites, siltstones, mudstones, argillites and conglomerates. The palaeocurrent directions of fluvial sediments indicate derivation from the southwest (Groenewald et al. 1995).

The volcanic rocks are basaltic to andesitic lavas, also deposited as volcaniclastic rocks, and intercalation with sediments has been observed (Watters et al. 1991 according to Groenewald et al. 1995). Detrital zircons of Ritscherflya show a dominant age peak close to the sedimentation age at ca. 1130 Ma, and older peaks at 1370 Ma, 1725 Ma, 1880 Ma, 2050 Ma and 2700 Ma (Marschall et al. 2013b). In addition, 2800–3445 Ma zircons, correlative with the Kalahari-Grunehogna basement, have been reported (Marschall et al. 2013a, 2013b). The volcano-sedimentary sequence was intruded by mafic to ultramafic, basaltic sills at ca. 1100 Ma, as indicated by the results of detrital zircon U-Pb studies combined with Rb-Sr / Sm-Nd whole-rock data by Marschall et al. (2013b) and Moyes et al. (1998). On the basis of the tholeiitic composition and palaeomagnetic data on the sills, a correlation with the Mesoproterozoic Umkondo igneous province was proposed by Hanson et al. (2004).

3.3.3 Mzumbe, Margate and Tugela accretionary terrains

The Grenvillian Natal Belt, the African continuation of the Maud Bbelt, is bounded in the north by the Kaapvaal craton. Metavolcanic gneisses, paragneisses, granitoid gneisses and younger intrusive rocks such as megacrystic granitoids, charnockites and mafic to ultramafic plutonites of the Natal Bbelt have been divided, from south to north, into the Margate, Mzumbe and Tugela terranes (e.g. Thomas et al. 1993, Jacobs et al. 1993, Eglington 2006) (Fig. 1). The Margate terrane is characterised by granulite-facies rocks, as well as A-type and S-type granitoids and ortho- and paragneisses (Eglington 2006, Jacobs et al. 1993, Thomas et al. 1993). The lithostratigraphy of the underlying Mzumbe terrane is broadly similar, but it also includes mafic intrusions and granulite facies assemblages within the amphibolite facies basement orthogneisses (Thomas & Eglington 1990, Mendonidis et al. 2009). The Tugela terrane is characterised by paragneisses and mafic metavolcanic rocks with amphibolite facies metamorphic assemblages, mafic to ultramafic plutonites and minor orthogneisses (Mendonidis et al. 2009, Eglington 2006, Jacobs et al. 1993, Thomas et al. 1993, Thomas & Eglington 1990).

The oldest inherited zircon of the Natal Belt has been dated at ca. 1800 Ma from the Portobello granite, Margate terrane (Mendonidis & Armstrong 2009). The igneous and meta-igneous rocks of the Natal Belt have igneous ages in the 1235 to 1025 Ma range (McCourt et al. 2006), and

they have been interpreted as arc-related, juvenile crust (e.g. McCourt et al. 2006, Jacobs et al. 1993, Thomas & Eglington 1990). The megacrystic A-type granitoids and related charnockites of the Margate terrain, indicating post-accretion extension within the Natal Belt, were intruded at ca. 1030–1070 Ma (Eglington et al. 2003, McCourt et al. 2006). The Mzumbe terrain pegmatites and calc-silicate rocks indicate a thermal or hydration event at ca. 900 Ma (based on K-Ar muscovite) and re-heating at ca. 530 Ma (based on titanite fission track analyses), respectively (Jacobs & Thomas 1996).

3.4 Falkland and Ellsworth-Haag microplates

The present Falkland Islands of the South Atlantic Ocean and the crustal block comprising the Ellsworth-Whitmore Mountains and the Haag Nunataks of West Antarctica have been interpreted as small fragments of Precambrian continental landmasses, referred to as micro-continents. The West Falkland Islands (Cape Meredith complex) and Ellsworth-Whitmore-Haag mountains represent exposures of the Falkland microplate (FI) and Ellsworth-Haag microplate (EH), respectively (Jacobs & Thomas 2004), which were juxtaposed to the Natal Belt and East Antarctica in the Mesoproterozoic (Fig. 1).

3.4.1 Falkland microplate

The crystalline basement of the West Falkland Islands represents the Falkland microplate (Fig. 1). The exposure along a 5-km-long coastal strip on Cape Meredith is comprised of Mesoproterozoic mafic and silicic metavolcanic gneisses intruded by granitoid orthogneisses. The silicic metavolcanic rocks of the complex have been dated at ca. 1120 Ma by zircon U-Pb and the associated mafic gneisses at ca. 1000 Ma by amphibole Ar-Ar. The metavolcanic rocks were presumably generated in an island arc setting and contain inherited zircon cores of ca. 1135 Ma (Jacobs et al. 1999). Cross-cutting intrusions of syn- to post-tectonic granodiorite and granite range in age from 1090 Ma to ca. 1000 Ma. The regional amphibolite facies metamorphism was dated to between ca. 1090 and 1070 Ma (Jacobs et al. 1999). The comparison of post-tectonic zircon crystallization ages and amphibole cooling ages indicates rapid cooling (Jacobs et al. 1999). Additionally, no evidence for Pan-African overprinting was observed by Jacobs et al. (1999). The Mesoproterozoic gneisses were intruded by lamprophyre dykes and sheets at ca. 520 Ma dated by K-Ar on biotite (Thomas et al. 1998). Nd model ages of 870 Ma and 930 Ma for picritic basalts that cross-cut the lamprophyres were also reported by Thomas et al. (1998). The 520 Ma West Falkland lamprophyres may indicate localised intracontinental extension of the Falkland microplate, possibly in the vicinity of the Natal-Maud Belt.

3.4.2 Ellsworth-Haag microplate

The Ellsworth-Whitmore Mountains and the Haag Nunataks of West Antarctica are representative of the Ellsworth-Haag microplate. The scattered exposures delineated by the Whitmore Mountains in the south, the ca. 400-km-long Ellsworth Mountain range in the middle and the Haag Nunataks in northwest represent an area of ca. 125 000 km^2 (cf. Storey & Dalziel 1987). Aerogeophysical data and geological comparisons indicate that the Ellsworth-Whitmore Mountains and the Haag nunataks form part of an extensive continental fragment (the Ellsworth-Whitmore Mountains crustal block), one of the main crustal blocks of West Antarctica (e.g. Grunow et al. 1987, Curtis & Storey 1996, Leat et al. 2018). This sub-fragment, known as the Ellsworth-Haag microplate, probably resided at the juncture of Africa and Antarctica prior to the breakup of Gondwana (Dalziel & Grunow 1992, Curtis & Storey 1996, Randall & Niocaill 2004, Jacobs et al. 2008) (Fig. 1). The Whitmore Mountains are dominated by Jurassic granitic intrusive rocks having within-plate magma characteristics (Vennum & Storey 1987b, Craddock et al. 2017). In addition, a 0.5–1.0 Ga isotopic signature and indications of crustal and juvenile magma sources of the granites were reported by Craddock et al. (2017).

The Ellsworth Mountain range is dominated by Paleozoic, deformed sedimentary rocks of marine and terrestrial origin such as sandstones,

argillites, marbles, conglomerates, quartzites, black shales and volcanoclastic sediments (Storey & Dalziel 1986, Curtis et al. 1999, Randall & Niocaill 2004). Conformable rift-related, Cambrian metavolcanic rocks crop out near the base of the Paleozoic succession (Curtis et al. 1999, Leat et al. 2018). The Paleozoic succession hosts volcanic rocks of basaltic, basaltic andesite, andesitic, rhyolitic and shoshonitic composition and is intruded by basaltic, granitic and lamprophyric dykes, and Jurassic granite plutons (Vennum & Storey 1987a, Vennum & Storey 1987b, Millar & Pankhurst 1987, Curtis et al. 1999). The basaltic lavas and dykes bear a dominant OIB-type and less commonly a MORB-type geochemical signature (Curtis et al. 1999).

The Late Mesoproterozoic basement is exposed in the Haag Nunataks of the Ellsworth-Whitmore Mountains crustal block (e.g. Millar & Pankhurst 1987, Curtis & Storey 1996) (Fig. 1). The three 50–100-m exposures are composed of foliated calc-alkaline granodioritic gneisses, probably representing a magmatic island arc complex (Millar & Pankhurst 1987, Grantham et al. 1997). The granodioritic gneiss, dated at 1176 ± 76 Ma, is intruded by granites dated at 1058 ± 53 and 1003 ± 18 Ma by the whole-rock Rb-Sr method (Millar & Pankhurst 1987). K-Ar biotite and hornblende of the granodioritic gneiss record an age of 991–1031 Ma, interpreted as a minimum age for amphibolite facies metamorphism in the Haag Nunataks (Millar & Pankhurst 1987).

4 XENOLITHS

4.1 Challenges in xenolith research

Xenoliths are foreign rock fragments in a magmatic rock and may be carried to the Earth's surface by rapidly ascending, often mantle-derived magmas (Rudnick & Fountain 1995). Generally, xenolithic samples are divided in two groups: accidental xenoliths derived from the crust or the mantle, entrained into passing host magma, and cognate xenoliths (autoliths), which represent cumulates crystallized from the host magma or a related magmatic component. In the context of the magma dynamics and rock mechanical properties of the levels of the lithosphere traversed, xenolith samples are not statistically representative of the whole lithosphere they passed through. The representativeness of the samples in terms of, for instance, middle crust, formation or intrusion is also questionable due to the accidental nature of the sampling process. Tracking of the xenolith provenance crustal level, especially for amphibolite facies xenoliths, is a challenging and sometimes impossible task, as the xenolith samples may represent any crustal level that their host magma transected (Rudnick & Gao 2004). Through detailed mineralogical study, if suitable mineral pairs are present in the sample material, the equilibration temperature and pressure of the rock may be traced and the depth of origin within the crust may accordingly be estimated.

Depending on the compositional difference between the xenolith and host rock, together with the consequent difference in the respective melting temperatures, partial melting, and dehydration or complete dissolution of the xenolithic material may occur (e.g. Tsuchiyama 1986). Additional modifications related to magmatic transport include infiltration of the host magma and associated fluids along cracks and intergrain boundaries in the xenolith. Chemical alteration caused by fluids, also known as metasomatism, results in the crystallization of metasomatic minerals (modal metasomatism) or changes in whole-rock or mineral chemistry (cryptic metasomatism). In addition to the metasomatic influence of the host magma, decompression (by tectonic uplift or polybaric transport of host magma) may modify the texture and mineralogy of xenoliths. Decompression-induced changes include the development of microcracks, partial melting of the minerals along grain boundaries and the formation of kelyphite rims (rims of dark-coloured, very fine <1 µm material) on garnets (Rudnick 1992). Xenoliths hosted by kimberlite pipes often show the development of greenschist facies assemblages due to hydrothermal alteration (Rudnick 1992).

4.2 Relevance of xenolith studies

Compositionally heterogeneous xenolith suites provide unique direct information on the regional lithosphere of their study areas (e.g. Selverstone et al. 1999). Commonly, xenoliths are samples provided by magmatic rocks and are otherwise impossible to reach. The rapid ascent of, for example, alkaline basalt, lamproite and kimberlite magma makes it possible that even samples from the mantle, hydrated samples or felsic samples with a lower melting temperature relative to the host may be preserved instead of undergoing complete dilution in the host magma (e.g. Rudnick 1992, Tsuchiyama 1986). In addition, weathering, retrograde metamorphosis and alteration effects in xenolithic samples may be modest relative to the effects occurring over in hundreds of millions of years in the Earth's atmosphere and hydrosphere. The best preserved and also the least altered, distal xenoliths have been reported in alkali basaltic hosts (e.g. Rudnick 1992). Xenoliths carried by relatively young (>1 to ca. 140 Ma) alkali basalts of non-cratonic areas such as Phanerozoic fold belts and rifts are dominated by mafic compositions, probably because they occur in areas of long-term and recent basaltic magmatism (Rudnick 1992).

Lamproite, lamprophyre, kimberlite and minette magmas, by comparison, generally erupt through stable continental regions (Rudnick 1992) and may therefore provide samples of markedly older and more complex origins. Meta-igneous lower crustal and mantle-derived xenoliths have long been of scientific interest because of the inaccessibility of the source area, its importance regarding the evolution of the Earth and economic interests, e.g. diamond exploration. Felsic, evolved and meta-sedimentary xenoliths, in contrast, have been less attractive. This is probably due to general ambivalence hampering the interpretations of such samples, e.g. the possibility of chemical imbalance within the rock, the lack of mineral assemblages suitable for precise P-T determinations that would enable tracing of their depth of origin, and the less evident economic advantage of the time-consuming studies. Consequently, xenolith studies have been more rewarding in the investigation of the mantle and the granulite facies lower crust. Studies on the middle and upper crust have concentrated on exposed crustal sections, as the lithological control of the samples reduces the uncertainty (Rudnick & Gao 2004).

5 MATERIALS

5.1 Samples

The FINNARP 1997 and 2002 expeditions collected xenolith samples from Jurassic, mica-rich dykes and boulders on the nunatak of Kjakebeinet, southern Vestfjella (Mr Arto Luttinen and Mr Saku Vuori, pers. comm. 2005). The xenolith suites were hosted by glacial boulders of mica-rich ultrapotassic rock, later in this study referred as lamproite (73° 47.762´ W, 014° 54.452´ W), and a ca. 160 Ma lamproite dyke examined on outcrop (73° 47.011´ S, 014° 52.397´ W) (Romu et al. 2008, Luttinen et al. 2002) (Fig. 2). Altogether, 27 xenolith samples, of which 24 were photographed (Fig. 3), were investigated for this thesis. The xenoliths were rounded, 3–40 cm in diameter, and the contacts towards the host were usually sharp. Some xenoliths displayed re-crystallized or molten rims. The boulders hosted a heterogeneous suite of xenoliths dominated by large (up to 40 cm in diameter) felsic samples. Smaller (4–10 cm in diameter), mafic xenoliths were less abundant. Small (1–4 cm), rounded but often nebulous felsic nodules, representing partially disintegrated xenoliths and macrocrysts of clinopyroxene and magnetite, and composite nodules of clinopyroxene, magnetite and apatite (<2 cm) were also observed. Three adjacent, narrow (<1.0 m) lamproite dykes were found to host predominantly small (3–10 cm wide), round, mafic xenoliths (Table 1). These xenolith suites also hosted cognate xenoliths, a phlogopitic autolith (P3) and a carbonatitic autolith (Xe15) (Fig. 3) (Romu 2006, unpublished M.Sc. thesis), but these were excluded from this study.

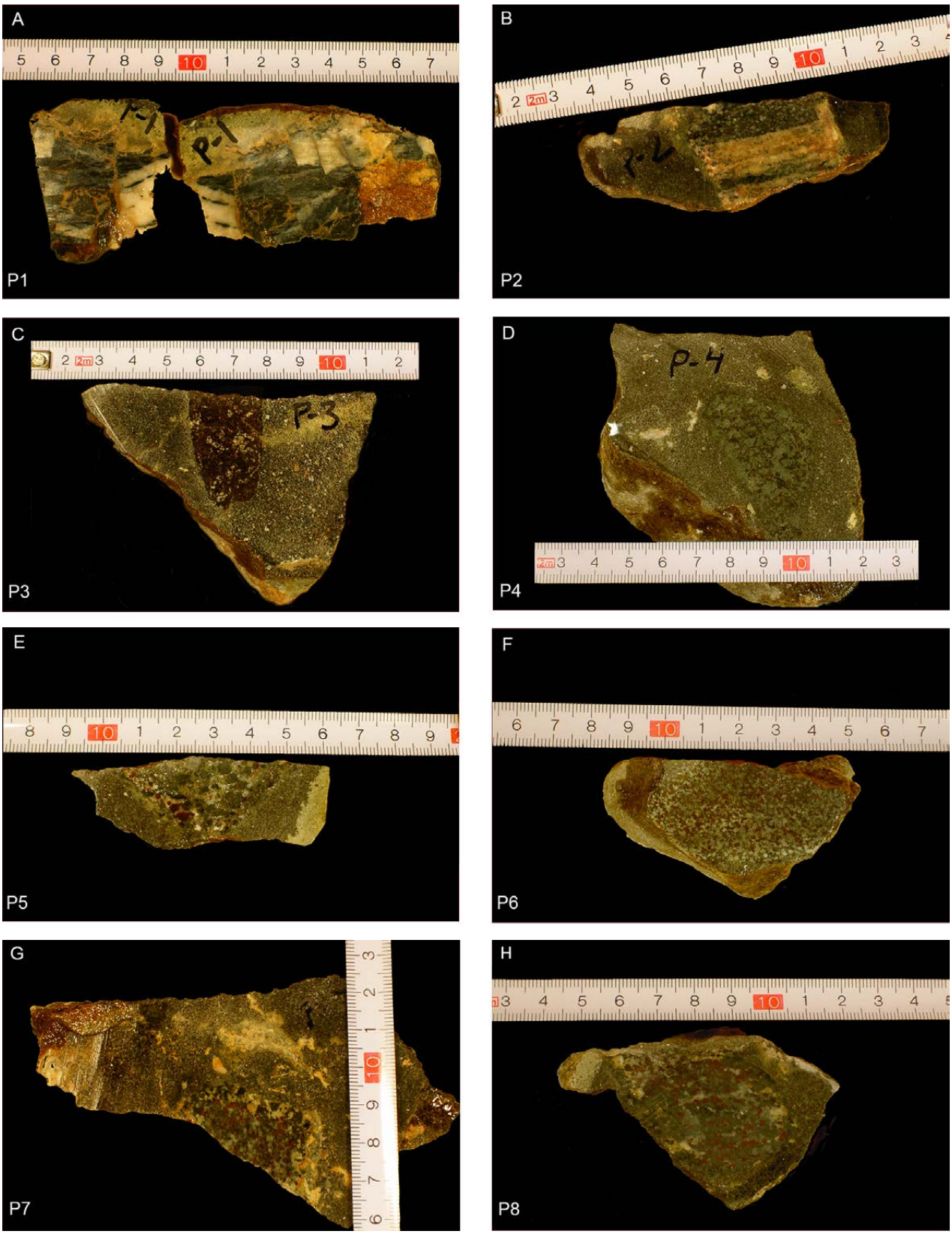

Fig. 3. The xenolith samples. Scale in centimetres. Xenoliths hosted by a lamproite dyke: (A) graphitic metashale sample P1; (B) metagabbronorite sample P2; (C) phlogopitite autolith sample P3; (D) garnet-free metagabbro sample P4; (E) metapelite sample P5; (F) metagabbronorite sample P6; (G, H) garnet-bearing metagabbro samples P7 and sample P8. Xenoliths hosted by mica-rich boulders: (I, L, Q) metatonalite samples Xe1, Xe4 and Xe9; (J, K, M) mylonitic metagranite samples Xe2, Xe3, Xe5 and Xe12; (N, O, P, T) gneissic metagranite samples Xe6, Xe7 and Xe8; (R) quartz metadiorite sample Xe10; (S) garnet-free metagabbro sample Xe11; (U) metapelite sample Xe13; (V) metagreywacke sample Xe14; (W) carbonatitic autolith sample Xe15; (X) garnet-bearing metagabbro sample Xe16.

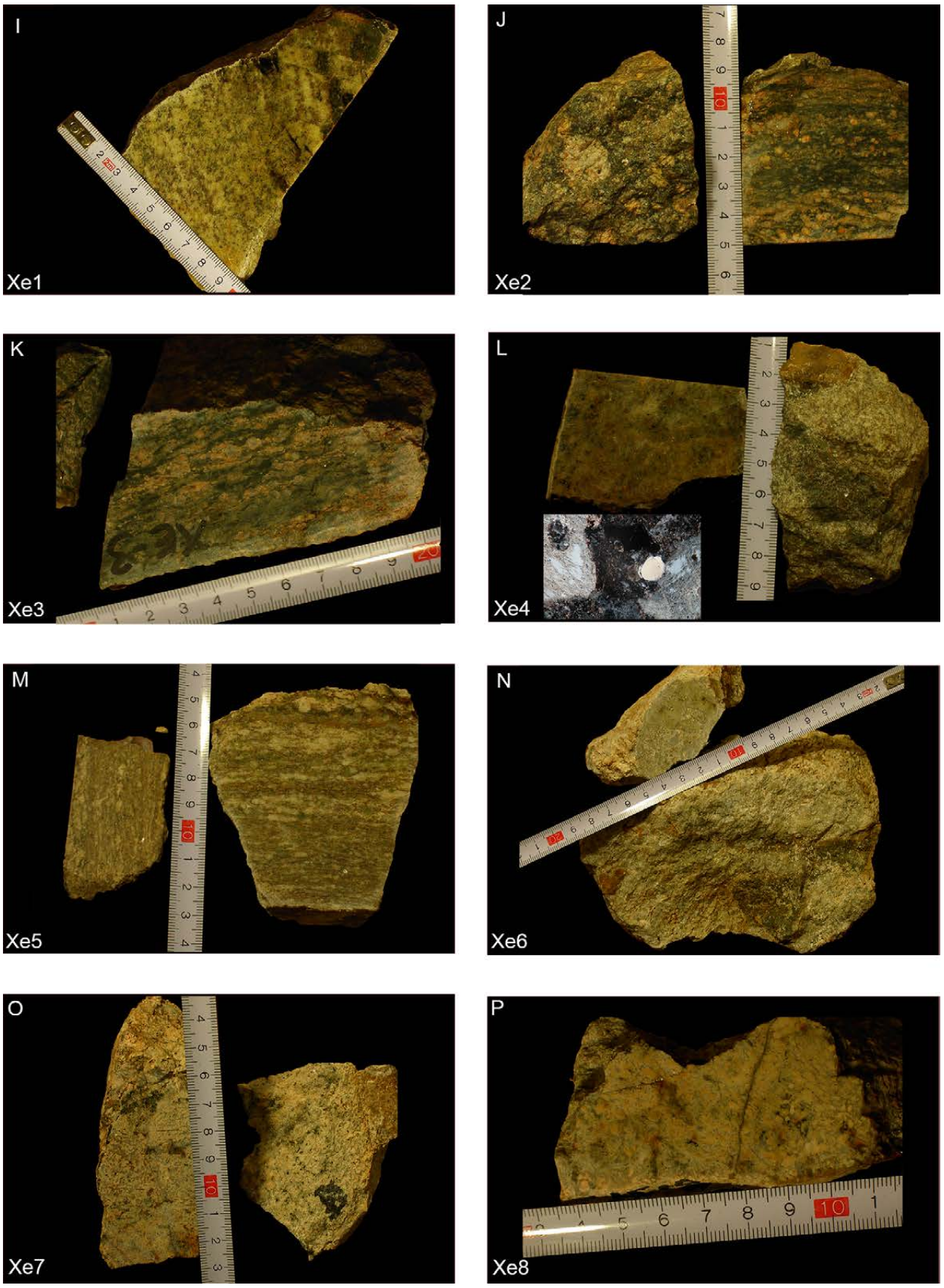

Fig. 3. Cont.

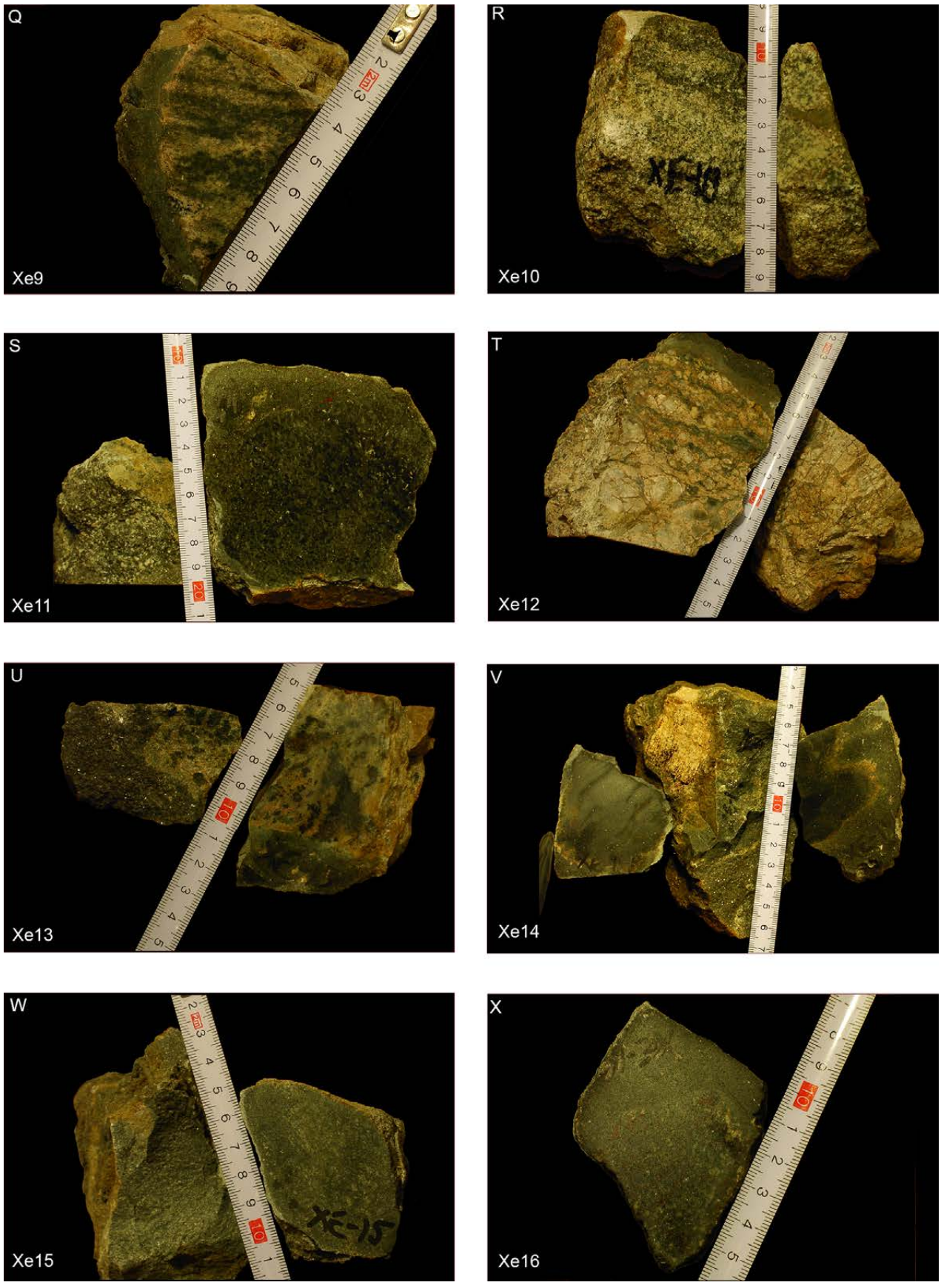

Fig. 3. Cont.

5.2 Representativeness of the samples

Vestfjella is a ca. 120-km-long range of scattered ridges located at the rifted margin of western Dronning Maud Land. The exposed ridges of Vestfjella are composed of Jurassic flood basalts cross-cut by temporally associated intrusive rock types such as dolerites, gabbros and granitic dykes. The lamproite dykes of Kjakebeinet were dated at ca. 160 Ma (Luttinen et al. 2002) and represent one of the latest magmatic phases on Vestfjella (Fig. 2). Proterozoic crystalline basement is found 80–150 km further inland at Mannefallknausane and Heimefrontfjella. The examined xenoliths are considered to mainly represent Precambrian basement beneath the basalts and continental ice. It is likely that the host lamproite intruded rapidly and along nearly vertical conduits, and the samples may therefore actually provide a cross-section of the continental lithosphere beneath Vestfjella. However, the xenolith suites may not represent different crustal levels equally, and samples of certain depths may be overrepresented (cf. Chapter 4). The practical limitations of sample collection (hammer only) may also have caused some bias, e.g. relative to the xenolith suites from mined kimberlite and lamproite occurrences. As a result, estimates of the abundance of certain rock types of the unexposed Vestfjella lithosphere are avoided. However, the studied xenoliths were generally well preserved and notably unweathered, probably due to extraction by recent glacial erosion and the prevailing dry and cold climate of East Antarctica.

6 ANALYTICAL METHODS

The 27 xenolith samples from Vestfjella lamproites selected for this study were analysed for their petrography and mineralogy. The mineral chemistry, whole-rock major and trace-element geochemistry, U-Pb geochronology and Sm-Nd and Rb-Sr isotope geochemistry of a subset of samples (Table 1) was analysed as described below.

6.1 Petrography

Standard petrographic methods, optical transmitted light microscopy, reflected light microscopy and point counting were combined with the microprobe energy dispersive method and backscattered electron imaging to determine the mineralogy and petrography of the samples. The modal mineralogy of the meta-igneous samples only was determined by point counting, as the nomenclature of the igneous rocks may also be solely based on the modal mineral abundances (Streckeisen 1974). Due to alteration and metamorphism, alkaline feldspar and plagioclase were not always reliably distinguished from each other by optical microscopy, however (see chapter 6). The author photographed the thin sections at the Geological Survey of Finland, Kuopio.

6.2 Mineral chemistry

Semi-quantitative microprobe analyses of minerals were performed using the energy dispersive technique and a JEOL JXA-8600 instrument at the Department of Geology, University of Helsinki, in 2004 and 2005. Analyses were performed with an accelerating voltage of 15 kV, a beam current of 1 nA and a beam diameter of 1 µm. Co was employed as the standard. The analytical results were corrected using the ZAF procedure (Sweatman & Long 1969). The detection limit for major elements was ca. 1 wt% (Mr Ragnar Törnroos, pers. comm. 2006). Quantitative electron microprobe analyses of minerals were performed using the wavelength dispersive technique and a Cameca SX100 instrument at the Geological Survey of Finland, Espoo, in 2009.

Data were obtained with an accelerating voltage of 15 kV, a beam current of 20 nA and a beam diameter of 5 µm. A subset of garnet and rutile, mounted in epoxy, was analysed with an accelerating voltage of 15 kV, a beam current of 30 nA and a beam diameter of 3 µm. Natural minerals and metals were employed as standards. The analytical results were corrected using the PAP on-line correction program (Pouchou & Pichoir 1986).

Feldspar molar compositions were calculated on the basis of 32 oxygen atoms and 12 cations. The molar proportions of $CaAl_2Si_2O_8$ (An), $NaAlSi_3O_8$ (Ab) and $KAlSi_3O_8$ (Or) were calculated by normalizing the composition to Ca+Na+K = 100.

Pyroxene molar compositions were calculated on the basis of 6 oxygen atoms and 4 cations ($M2M1T_2O_6$). The molar proportions of $Mg_2Si_2O_6$ (En), $Ca_2Si_2O_6$ (Wo) and $Fe_2Si_2O_6$ (Fs) were calculated according to Morimoto et al. (1989), the composition being normalized to Ca+Mg+ΣFe = 100 with ΣFe = Fe^{2+}+Fe^{3+}+Mn^{2+}.

Garnet molar compositions were calculated on the basis of 24 oxygen atoms and 16 cations ($X_3Y_2Si_3O_{12}$). The molar proportions of $Fe_3Al_2Si_3O_{12}$ (Alm), $Ca_3Al_2Si_3O_{12}$ (Grs), $Mg_3Al_2Si_3O_{12}$ (Prp) and $Mn_3Al_2Si_3O_{12}$ (Sps) were calculated by normalizing the composition to Ca+ΣFe+Mg+Mn = 100 where ΣFe = total Fe of the microanalysis.

Amphibole molar compositions were calculated on the basis of 23 oxygen atoms and 16 cations ($AB_2C^{VI}{}_5T^{IV}{}_8O_{22}(OH)_2$) and classified after the IMA recommendation of Leake et al. (1997) (Preston & Still 2001). Fe^{2+}/Fe^{3+} was determined after Droop (1987), while the total Fe content was measured by microprobe analysis (Preston & Still 2001).

6.3 Whole-rock geochemistry

XRF and ICP-MS analyses were performed at the Peter Hooper GeoAnalytical Lab, Washington State University, USA (later the GeoAnalytical Lab), in 2007. For XRF results, the detection limit for major element oxides was <1 wt% and for trace elements <1 ppm (Washington State University 2015a). For ICP-MS results, the long-term precision of the method was typically better than 5% (RSD) for the REEs (Sc, Y, La, Ce, Pr, Nd, Sm, Eu, Gd, Tb, Dy, Ho, Er, Tm, Yb, Lu) and 10% for Ba, Th, Nb, Hf, Ta, U, Pb, Rb, Cs, Sr, Zr, Ti, K and P (Washington State University 2015b).

Technical notes and the principles of these methods have been presented by Johnson et al. (1999) and Knaack et al. (1994), respectively. For whole-rock chemical analyses, xenolith material was extracted from the samples using a diamond saw and the cut surfaces were cleaned with water and fine sand paper to avoid blade-induced contamination. All samples were crushed in a steel jaw crusher and a 100–300-g aliquot of the freshest chips was handpicked and washed in an ultrasound bath of distilled water to avoid contamination from the host rock, weathered surfaces and preparation equipment. Subsequently, 50–100 g of each sample was ground in a Fe-Ni mill, homogenized, and c. 50 g aliquot was reground in a hardened steel mill. The crushing and milling were performed at the University of Helsinki, Finland, in 2007, and final re-grinding at the GeoAnalytical Lab.

6.4 U-Pb geochronology

Because of the small size of the sample material, only single-crystal U-Pb geochronology, SIMS and SHRIMP were used. For secondary ion mass spectrometry (SIMS) analysis, the selected samples were separated using conventional separation techniques (magnetic separation, heavy liquids and hand picking). A representative set of zircon crystals was selected under a microscope and mounted in epoxy, polished and gold coated. Prior to analysis, cathodoluminescence images (CL) and backscattering electron images (BEI) of sectioned zircon crystals were obtained in order to identify suitable zircon populations. The ion microprobe analyses were performed using the Cameca IMS 1270 (2008) and IMS 1280 (2009) secondary ion mass spectrometer of the NORDSIM laboratory at the Swedish Museum of Natural History, Stockholm. The spot diameter for

the ca. 4.5 nA primary $O2^-$ ion beam was ca. 25 µm, and oxygen flooding in the sample chamber was used to increase the production of Pb^+ ions. Three or four counting blocks (depending on the secondary ion signal intensity), each including four cycles of the Zr, Hf, Pb, Th and U species of interest, were measured from each spot. The mass resolution (M/D M) was 5300 (10%). The data were calibrated against a zircon standard (91500; Wiedenbeck et al. 1995) and corrected for modern common Pb (T = 0; Stacey & Kramers 1975). Decay constant errors were ignored. The procedure was essentially similar to that described in detail by Whitehouse et al. (1999) and Whitehouse and Kamber (2005). The fitting of the discordia lines and calculation of the intercept and concordia ages were carried out using the Isoplot/Ex 3.00 program (Ludwig 2003). In the concordia diagrams, all error ellipses are plotted at 2σ level. Unless otherwise indicated, the calculated age errors are at the 2σ level.

For sensitive high-resolution ion microprobe (SHRIMP) analysis, zircons were separated using conventional separation techniques (Wilfley table, magnetic separation, heavy liquids and hand picking). Prior to analysis, cathodoluminescence images (CL) of sectioned zircon crystals were obtained in order to identify suitable zircon populations. The analyses were carried out using SHRIMP II at the Research School of Earth Sciences, The Australian National University, Canberra, Australia. SHRIMP analytical methods follow those presented by Williams (1998) and references therein. The analyses consist of six scans through the mass range using a spot size of ca. 20 µm diameter. The U/Pb ratios were calibrated relative to the 1099 Ma Duluth Gabbro reference zircons (see Paces & Miller 1993) and the data were reduced using the SQUID Excel Macro of Ludwig (2000). Common Pb was corrected using the measured $^{204}Pb/^{206}Pb$ ratio following Tera and Wasserburg (1972) as described by Compston et al. (1992). Uncertainties in the measured ratios are given at the 1σ level. Weighted mean age uncertainties, however, are given at the 2σ confidence level (plots and calculation using IsoPlot/Ex software; Ludwig 1999, 2003).

6.5 Sm-Nd and Rb-Sr isotope geochemistry

The samples Xe11 and Xe16 were ground in a Fe-Ni mill. Material for mineral concentrates was sieved to fractions of <0.075 mm, 0.125–0.250 mm, 0.250–0.5 mm and >0.5 mm. Minerals were separated using a hand magnet, a Franz isomagnetic separator, heavy liquids and, finally, by hand picking at the University of Helsinki in 2005. The isotopic analyses were performed in the Unit for Isotope Geology, Geological Survey of Finland, in 2005. The mineral separates were washed with dilute HNO_3 (apatite in dilute HCl) in an ultrasonic bath. The samples were dissolved in Teflon vials in a 1:4 mixture of HNO_3 and HF for several hours. After evaporation, the samples were dissolved in HCl and a clear solution was spiked with ^{149}Sm-^{150}Nd and ^{87}Rb-^{84}Sr tracers. Rubidium, strontium and light rare earth elements were separated using standard cation exchange chromatography, after which Sm and Nd were purified on quartz columns (Richard et al. 1976).

Isotopic ratios and concentrations of Sm, Nd, and Sr were measured on a VG Sector 54 mass spectrometer (those of Nd and Sr in dynamic mode) at the Geological Survey of Finland, Espoo. Isotopic measurements on Rb were performed using a noncommercial Nier-type mass spectrometer built at the Geological Survey of Finland. Repeated analyses of the La Jolla Nd standard gave a $^{143}Nd/^{144}Nd$ ratio of 0.511847 ± 0.000008 (standardization during the sample Xe11 apatite and whole-rock analysis) and 0.511849 ± 0.000008 (mean and external 2s error of nine measurements) (standardization during the sample Xe11 plagioclase and sample Xe16 clinopyroxene, plagioclase and whole-rock analysis). The external error of the reported $^{143}Nd/^{144}Nd$ ratios was estimated to be better than 0.0025%. Repeated analyses of the NBS987 Sr standard gave a $^{87}Sr/^{86}Sr$ ratio of 0.710268 ± 0.000020 (mean and external 2σ error of eleven measurements). The $^{87}Sr/^{86}Sr$ ratios were reported relative to $^{87}Sr/^{86}Sr$ 0.71024 of NBS987, and the external error was estimated to be better than 0.002%. Sm-Nd and Rb-Sr isochrons were calculated with IsoPlot/Ex software (Ludwig 2003).

7 PETROGRAPHY AND MINERALOGY

The petrography and mineralogy of the 27 studied xenoliths, representing 12 different rock types (Table 1), are described here. An overview of the petrography of the representative samples is presented in Figure 4. The petrography and texture of the boundaries between the xenoliths and host dyke are indicated in Figure 5. The internal grain boundary characteristics of the studied xenoliths are presented in Figure 6. The xenolith samples comprise three main categories: metagabbroic and quartz metadioritic samples (n = 11), metagranitoid samples (n = 11) and metasedimentary samples (n = 5) (Table 1). Modal-based (Table 2) classification of rock types for the metaigneous samples is presented in Figure 7. The SEM-EDS semi-quantitative mineral chemical data are based on Romu (2006 unpublished M.Sc. thesis) (Appendix 1). Quantitative mineral chemical analyses (EMP study) were collected for samples predicted to be suitable for thermobarometric estimates (ALKBM1-98, ALKBM6-98, KR-07-13X, P4, Xe11 and Xe16) (Appendix 2).

Table 1. Petrography and mineralogy of the studied xenolith samples.

Rock type	Mineralogy	Texture
Metagabbroic and quartz metadioritic samples		
Garnet-bearing gabbro, samples **Xe16**, P7, P8, ALKBM8-98	Cpx Pl (An 20-23) Ap Mag-Usp ± Alm-Pyp ± Prg ± *aegirine*	Granoblastic. Fresh Alm-Pyp showed thick brown kelyphitic rims and was mainly completely replaced by dark kelyphite. Cpx showed symplectic rims. Pl un-twinned.
Garnet-free gabbro, samples **Xe11**, P4	Di Prg Pl (An 18-23) *Mag Spl Ap Cal*	Granoblastic, modally layered. Prg rich in Spl inclusions, cpx symplectic with vermicular plagioclase altered to clay. Pl albite twinned and un-twinned, showed decreasing An towards Prg.
Gabbronorite, samples P2, P6	Pl (An 21-57) Cpx *Bt Ap* ± Ol ± *Opx* ± *qtz* ± *Zrn*	Gneissic, mafic bands granoblastic. Pyroxenes chloritized and minorly uralitized. Pl albite-twinned. Minor Ol altered to Tlc and opaque minerals.
Quartz diorite, samples Xe10, ALKBM1-98	Pl (An 25-46) Qtz Aug *Ap Zrn Rt Ilm Mag*	Granoblastic, medium- to coarse-grained, modally layered. Curved grain boundaries. Qtz undulose, Aug shows narrow symplectic rims. Pl un-twinned and albite twinned.
Quartz dioritic nodule, sample KR-07-13X	Pl (An 24) Qtz Kfs *Ap Rt Alm-Pyp Sil*	Granoblastic, medium-grained, modally layered. Pl albite twinned, Qtz undulose, Sil fibrous. Fresh Alm-Pyp shows thick brown kelyphitic rims.
Metagranitoid samples		
Tonalite , samples Xe1, Xe4, Xe9	Pl (An 17-34) Qtz *Ap Mag Zrn* ± *Alm* ± *Rt* ± *Na-silicate* ±*Chl* ±*Sph*	Granoblastic, Pl un-twinned. Fibrous Kfs abundant along the grain boundaries.
Equigranular granite, sample ALKBM6-98	Anorthoclase, Kfs, Qtz, Aug, *Ap, Ilm, Rt, Zrn, Py*	Granoblastic, even- and fine-grained. Kfs cross hatch twinned and/or perthitic. Pl albite twinned, Qtz undulose.
Gneissic granite, samples Xe6, Xe7, Xe8	Kfs Qtz Zrn *Chl* ± Pl (An 2-15) ± *Ap* ± *Na-silicate*	Medium- to coarse-grained. Kfs strongly altered to clay. Minor Pl albite-twinned. Fine-grained Kfs and Cc along grain boundaries.
Mylonitic granite, samples Xe2, Xe3, Xe5, Xe12	Kfs Qtz Zrn Chl ± Pl (An 19-30) ± *Ap* ± *Na-silicate*	Augen texture, medium-grained. Kfs cross hatch twinned and/or perthitic. Qtz undulose, mainly polycrystalline. Mafic bands comprise of fine-crystalline low-Al Na-silicate.
Metasedimentary samples		
Pelite, samples P5, Xe13	Kfs Qtz Ky *Rt Spl* ± *Alm* ± *Opx* ± *Zrn*	Migmatitic, heterogenous. Coronae textures.
Greywacke, sample Xe14	Qtz Ab Kfs Gr *Chl Rt Ap Dol* opq	Aphanitic matrix encloses carbon-rich (Gr) material and angular pieces of sandstone. Richterite occur as spherulitic aggregates near by dyke contact.
Sandstone, sample P9	Pl (An 5-24) Qtz *Jd Mag Am Mnz*	Inequigranular; polygonal granoblastic Pl surrounds coarser saussuritized Pl and aggregates of undulose Qtz.
Graphitic shale, sample P1	Gr Qtz Ab	Gr layers interlayered by layers of polygonal Ab. Qtz encloses Gr dust.

P- and ALKBM-samples hosted by lamproite dyke, co-ordinates: 73° 47.011´ S, 014° 52.397´ W

Xe- and KR-samples hosted by glacial boulders of lamproite, co-ordinates: 73° 47.762´ W, 014° 54.452´ W

Mineral abbreviations after Kretz (1983); zircon U-Pb was studied samples underlined, Sm-Nd and Rb-Sr samples in **bold**, accessory minerals in *italics*

Table 2. Modal proportions (vol.%) of minerals in the meta-igneous xenolith samples.

Sample ID	**P2**	**P6**	**P4**	**P7**	**P8**	**Xe11.1**	**Xe11.2**	**Xe16**	**Xe10**	**ALKB M1-98**	**P3**	**Xe15.1**	**Xe15.2**
Mineral	Metagabbros and quartz metadiorites										Autoliths		
Qtz	22.4	–	–	–	–	–	–	–	13.6	29.3	2.1	–	–
Pl	64.5	48.8	–	50.3	25.8	–	17.9	26.9	64.8	58.6	–	–	–
Kfs	–	–	–	–	–	–	–	–	–	–	3.2	17.3	–
Afs	–	–	–	–	–	–	–	–	–	–	–	–	–
Bi	–	5.1	10.2	–	–	2.7	–	–	–	–	82.3	2.2	9.3
Cpx	1.3	23.8	55.7	15	42.7	47.8	34.6	38.4	18.3	4.9	4.7	–	23.7
Opx	10.7	–	–	–	–	–	–	–	x	–	–	–	–
Prg	–	–	24.6	10.4	–	38.2	46.4	0.1	–	–	–	–	–
Grt	–	–	–	17.2*	9.9*	–	–	21.8*	–	–	–	25.5	7.9
Carb	–	–	1.3	1.5	4.5	0.7	0.5	1	–	–	5.5	52.1	52.3
Am	–	–	–	–	–	–	–	–	–	–	0.8	–	–
Ap	0.4	0.4	0.3	1.3	1.7	0.3	0	3.6	–	–	0.5	1.5	0.9
Brt	–	–	–	–	–	–	–	–	–	–	–	1.3	–
Chl	–	–	–	1.1	–	–	–	0.6	–	–	–	–	–
Opq	0.7	4.1	6.3	3.2	15.4	10.3	0.6	7.6	3.3	–	–	–	5.9
Psm	–	17.8	1.6	–	–	–	–	–	–	7.2	–	–	–
Rt	–	–	–	–	–	–	–	–	–	–	0.9	0.1	–
Tot vol.%	100	100	100	100	100	100	100	100	100	100	100	100	100
M´	13.1	50.8	98.4	46.9	68	99	81.6	68.5	21.6	12.1	88.7	29.1	46.8
Sample ID	**Xe1**	**Xe4**	**Xe9**	**Xe2**	**Xe3**	**Xe5**	**Xe12**	**Xe6**	**Xe7**	**Xe8**	**ALKB M6-98**		
Mineral	Metatonalites			Mylonitic metagranites				Gneissic metagranites			Metagranite		
Qtz	23.5	21.4	26.5	24.8	25.1	33.8	23.2	35.9	36.5	38.8	18.7		
Pl	55.5	54.1	43.2	nd	nd	nd	nd	nd	nd	nd	nd		
Kfs	nd	nd	nd	63.6	63.6	48	59.4	61.9	50.2	51	nd		
Afs	nd	nd	nd	nd	nd	nd	nd	nd	nd	nd	72.5		
Bi	–	–	–	–	–	–	–	–	–	–	–		
Cpx	–	–	–	–	–	–	–	–	–	–	8.5		
Opx	–	–	–	–	–	–	–	–	–	–	–		
Prg	–	–	–	–	–	–	–	–	–	–	–		
Grt	–	x	1.2	–	–	–	–	–	–	–	–		
Carb	x	x	x	x	x	0.9	x	x	x	x	x		
Am	–	–	–	–	–	–	–	–	–	–	–		
Ap	0.6	0.1	0.6	x	x	0.1	x	x	x	x	x		
Brt	–	–	–	–	–	–	–	–	–	–	–		
Chl	x	x	x	–	–	1.2	–	–	–	–	–		
Opq	2.3	0.9	4.6	–	–	–	–	–	–	–	0.3		
Psm	2.5	0.4	0	–	–	–	–	–	–	–	–		
Rt	–	–	0.6	–	–	–	–	–	–	–	–		
Na-sil	–	–	9.8	11.6	–	–	–	–	–	–	–		
Gb/fibrous Kfs	15.6	23.1	13.5	–	11.3	16	17.4/ 16.9	2.2	13.3/ 12.5	10.2/ 10	–		
Tot vol.%	100	100	100	100	100	100	100	100	100	100	100		
M´	5.4	1.4	16.8	11.6	0	0.1	0	0	0	0	8.8		

Mineral abbreviations after Kretz (1983), carb, carbonate; psm, pseudomorphs; Na-sil, sodium silicate; Gb/fibrous Kfs, grain boundary material Kfs±Carb ±Rt±Psm/ vol.% fibrous K-feldspar on grain boundaries; x mineral observed < 0.1 vol%; Grt* fresh garnet and kelyphite; M´ Color index.

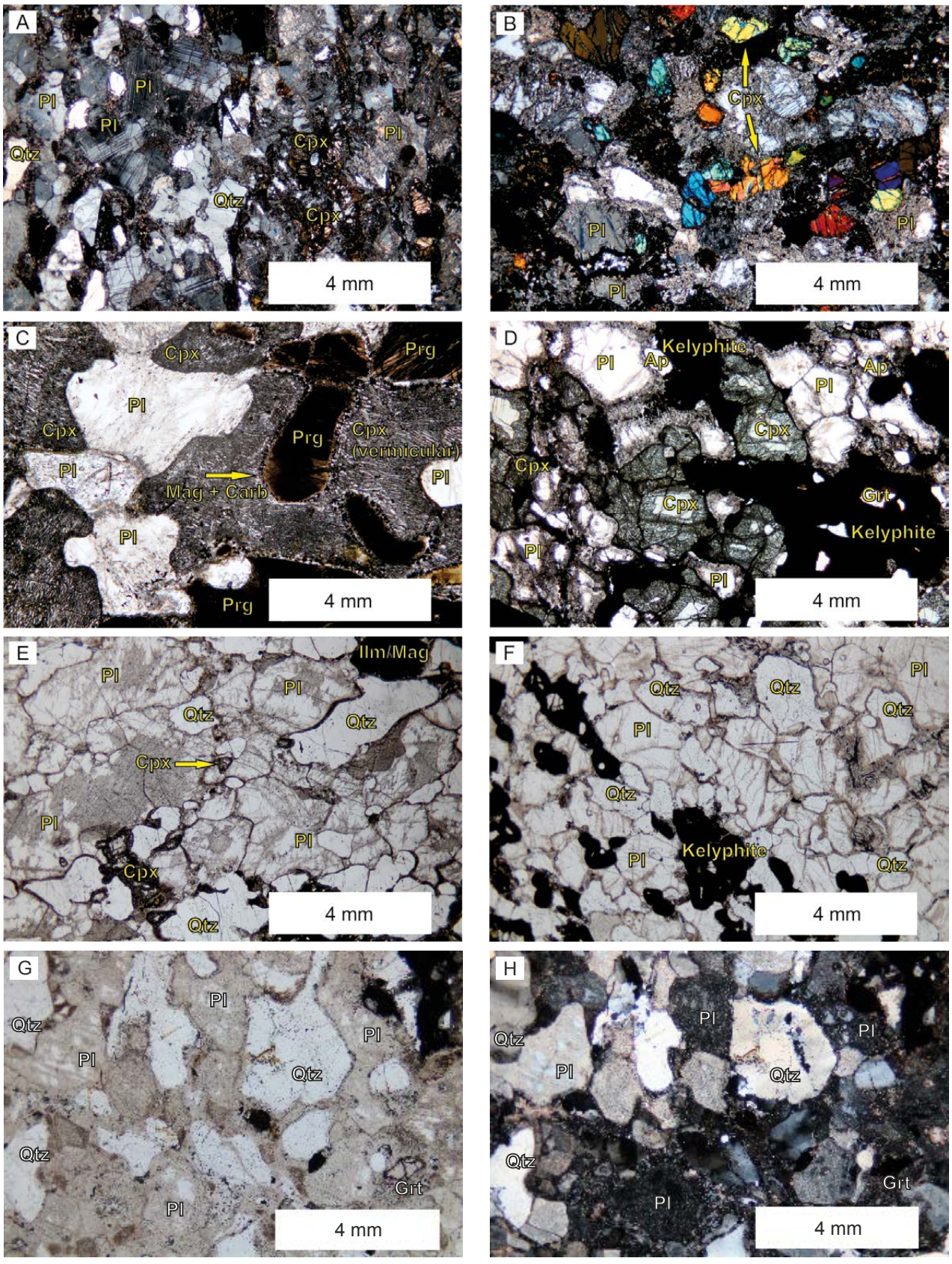

Fig. 4. A–H. Representative photomicrographs of the xenolith samples. (A) P2 metagabbronorite (xpl), felsic leucosome on the left and mafic melanosome on the right; (B) P6 metagabbronorite (xpl) is rich in cpx and seritized plagioclase; (C) Xe11 (ppl) garnet-free metagabbro includes substantial amounts of prg rich in oxide inclusions and vermicular cpx - feldspar symplectite; (D) Xe16 garnet-bearing metagabbro (xpl) is typified by kelyphite formed around grt, and reacted mineral boundaries of cpx and pl. This texture may indicate decompression-induced melting; (E) ALKBM1-98 and (F) KR-07-13X quartz metadiorites (ppl) show lobate grain boundaries, seritized plagioclase and kelyphite formed around grt and replaced grt; (G) Xe4 metatonalite (ppl,) includes minor grt associated with partially molten grain boundaries; (H) qtz of sample Xe4 (xpl) is strongly undulous and subgrains of qtz have been formed. Mineral abbreviations after Kretz (1983).

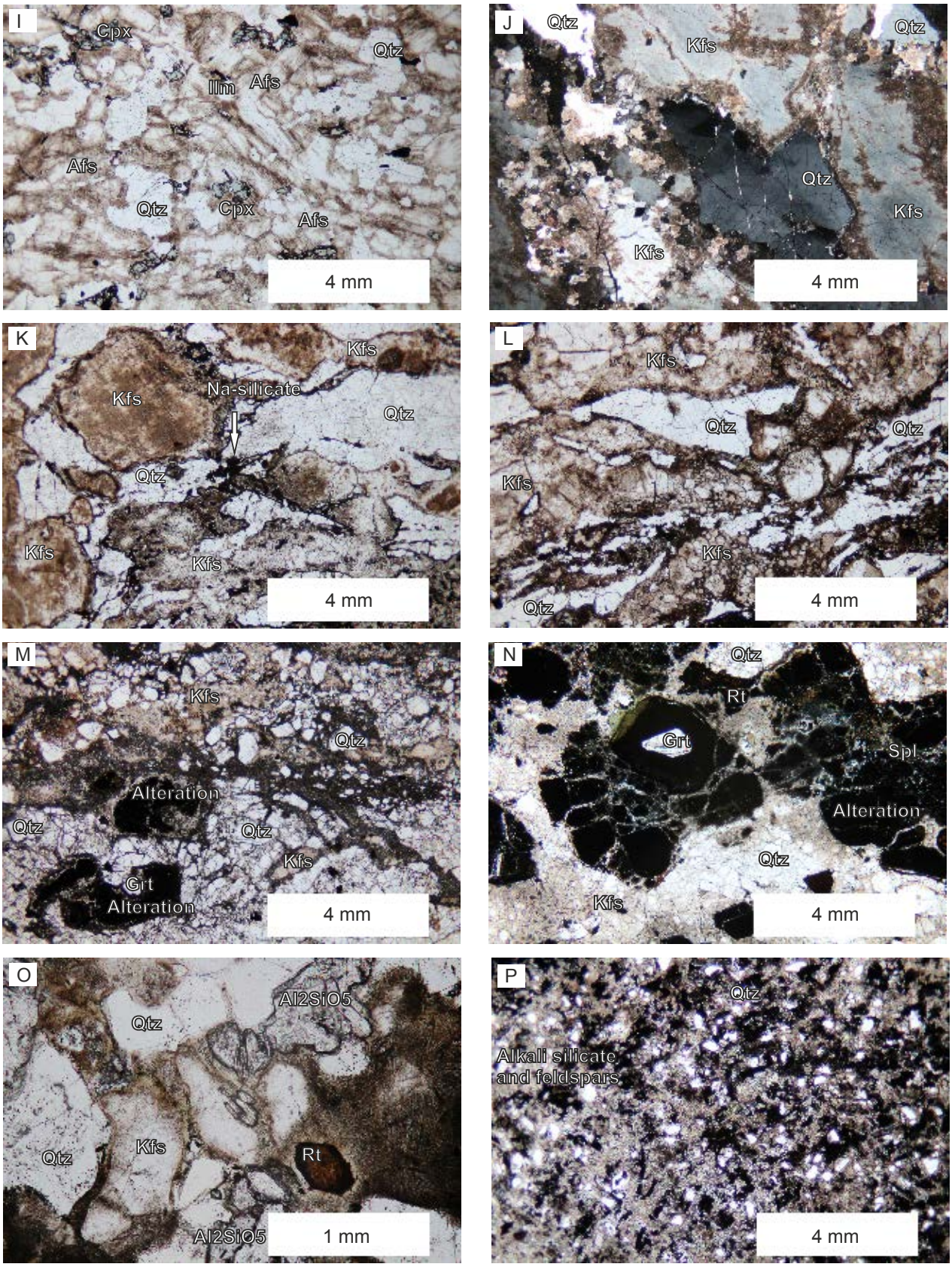

Fig. 4. I–P. Representative photomicrographs of the xenolith samples. (I) ALKBM6-98 metagranite (ppl) is equigranular and notably undeformed relative to the other metagranite samples; (J) Xe6 gneissic metagranite (xpl) is leucocratic and dominantly medium-grained; (K,L) Xe2 and Xe3 mylonitic metagranites (ppl) show well-developed ribbon-augen textures; (M, N) Xe13 metapelite (ppl) is dominated by angular qtz clasts and spl-altered alm-grt; (O) P5 metapelite (ppl) shows a high-T assemblage Kfs+Rt+Al_2SiO_5 (Sil); (P) Xe14 metagreywacke (ppl) is typified by subangular qtz clasts in a matrix of alkali silicate, feldspar minerals and gr. Mineral abbreviations after Kretz (1983).

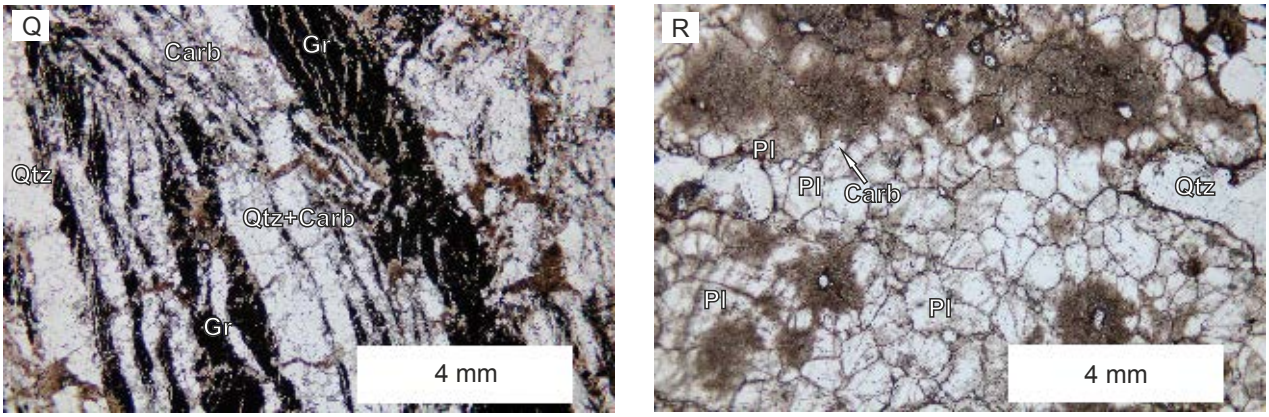

Fig. 4. Q–R. (Q) P1 graphitic metashale (ppl) includes qtz+cb veins; (R) P9 metasandstone (ppl) is typified by polygonal plagioclase, marking recrystallization of the rock. Mineral abbreviations after Kretz (1983); xpl, cross-polarized light; ppl, plane polarized light.

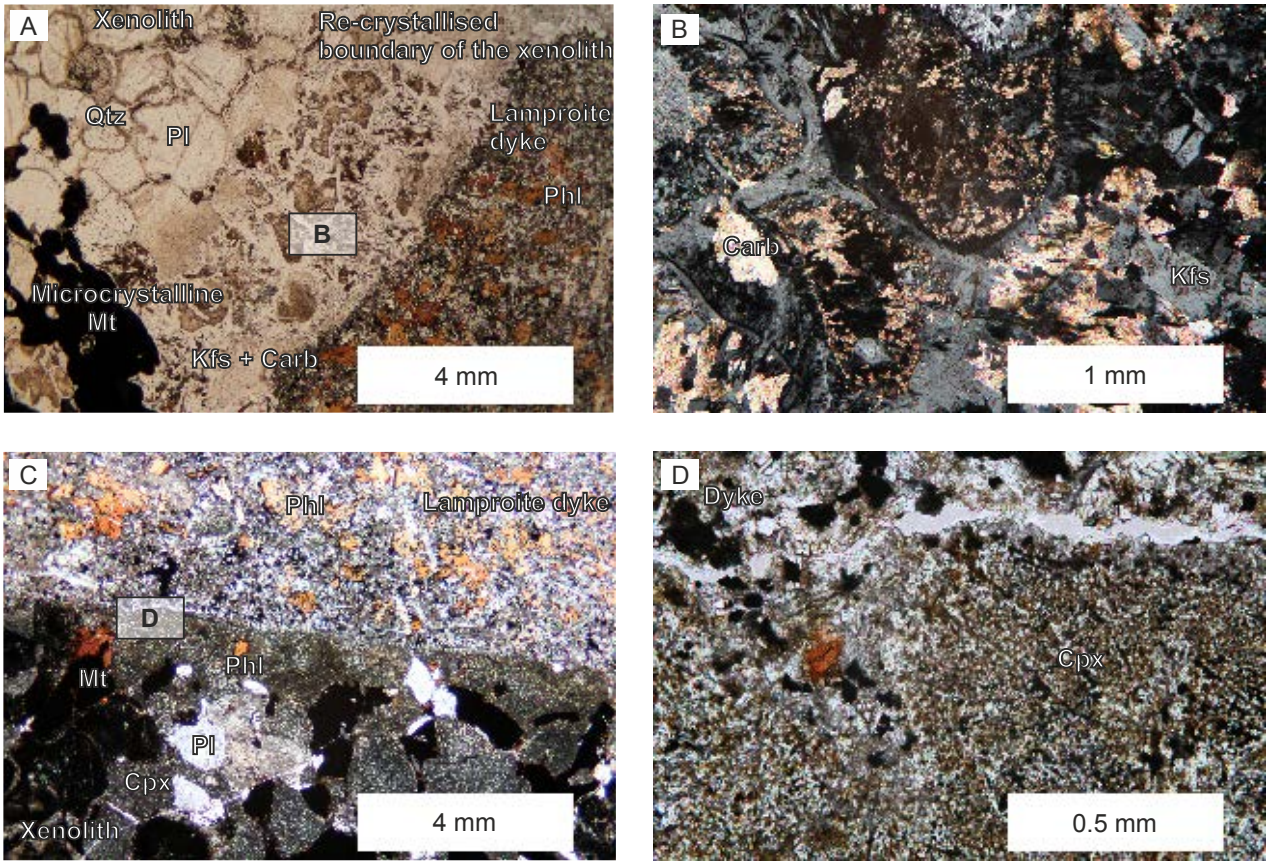

Fig. 5. Petrography of the contact boundary between the xenolith and phlogopite-rich host lamproite. (A, B) Sample KR-07-13X quartz metadioritic nodule (ppl) shows a partially molten boundary with quenched kfs-cb minerals adjacent to the phl-rich hosting lamproite dyke. (C) Sample P8 garnetiferous metagabbro (ppl) shows a sharp contact towards the phl-rich lamproite. (D) Sample P8 does not show signs of modal metasomatism or recrystallization adjacent to the host lamproite. Mica and Mag on the left of the picture are related to lamproite-melt propagation along a crack. Mineral abbreviations after Kretz (1983).

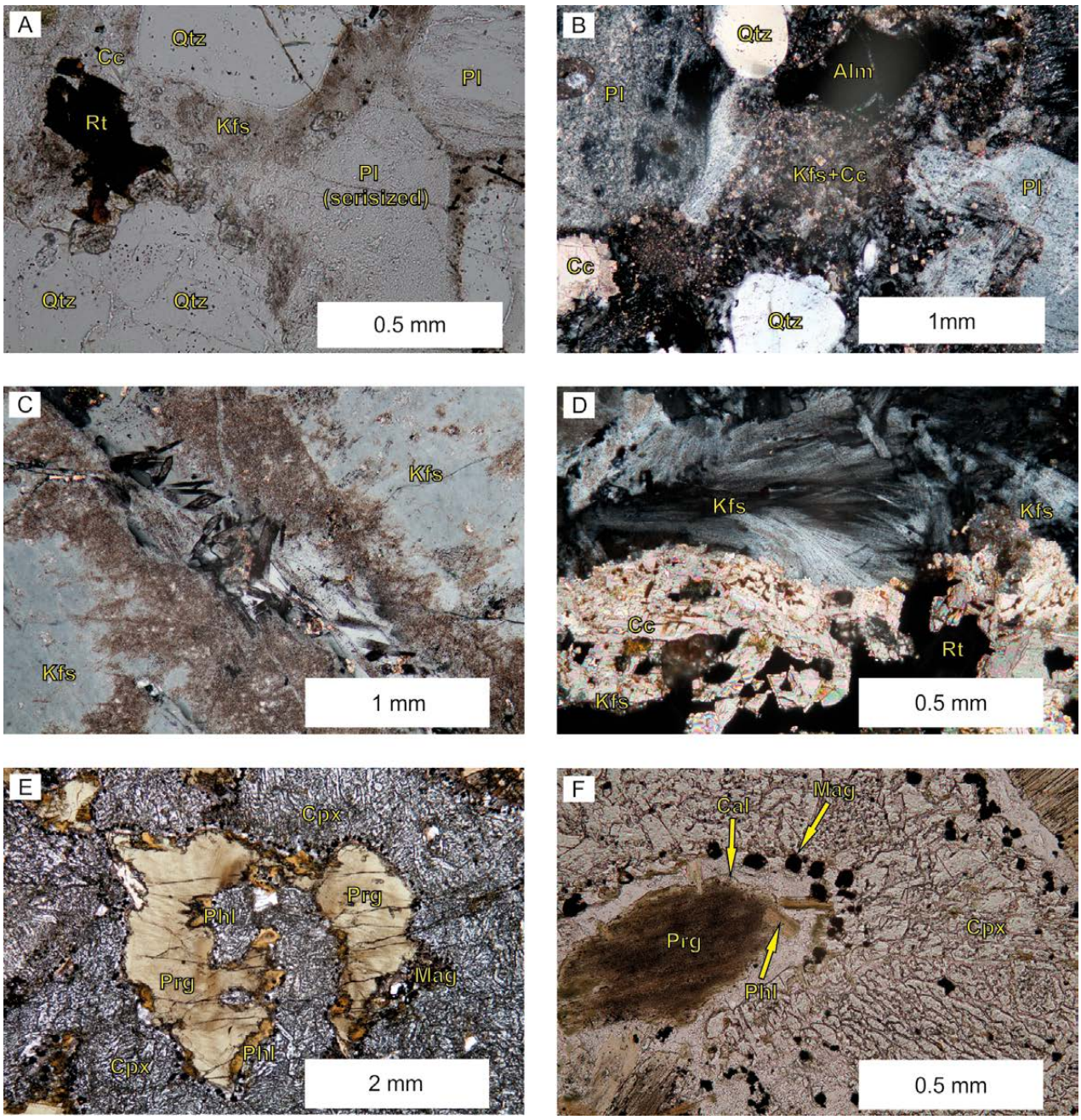

Fig. 6. Petrography of the internal grain boundaries within the xenoliths. (A) Metatonalite Xe1 is characterized by seritized plagioclase (Pl) and fibrous potassium feldspar (Kfs) + calcite (Cc) ± rutile (Rt) at grain boundaries between the quartz (Qtz) and Pl (ppl). (B) Metatonalite Xe4 is similar to Xe1, although accessory amounts of almandine-pyrope garnet (Alm) are found along the partially molten grain boundaries rich in fibrous Kfs (xpl). (C) Quench crystals of quartz and feldspar at grain boundary between Kfs and Kfs in gneissic metagranite Xe6 xenolith (xpl). (D) Close-up photo of fibrous Kfs, Cc and Rt within gneissic metagranite xenolith Xe7 (xpl). (E) Metagabbro P4 (ppl) and (F) metagabbro Xe11 (ppl) are typified by vermicular clinopyroxene (Cpx) - feldspar symplectite and pargasitic hornblende (Prg), which is rich in micron-scale oxide inclusions. (E) The Prg within xenolith P4 is often rimmed by retrograde phlogopite-mica (Phl), optically clear and inclusion-free, relatively Ti-rich Prg, and magnetite (Mag) (ppl). (F) Close-up photo of retrograde Mag, Phl and calcite (Cal) at the grain boundary between the Prg and vermicular Cpx - feldspar symplectite, xenolith Xe11 (ppl). Mineral abbreviations after Kretz (1983).

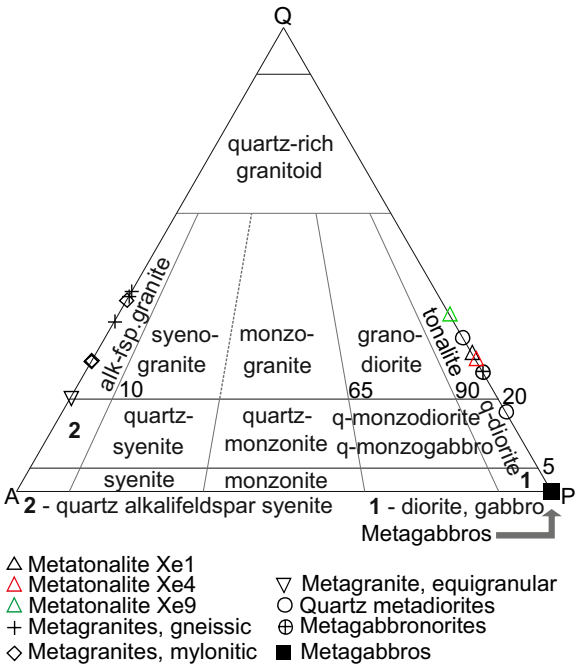

Fig. 7. Mineral mode based QAPF classification of the meta-igneous xenoliths (Streckeisen 1974). The fields are representative of igneous rocks and are for reference only, as the mineralogy of the samples has been modified by metamorphic and possibly by magmatic processes. Modal proportions of quartz (Q), alkali feldspar (A), plagioclase (P) and foid minerals (F), as identified by optical microscopy and point counting, were normalized to Q+A+P+F=100.

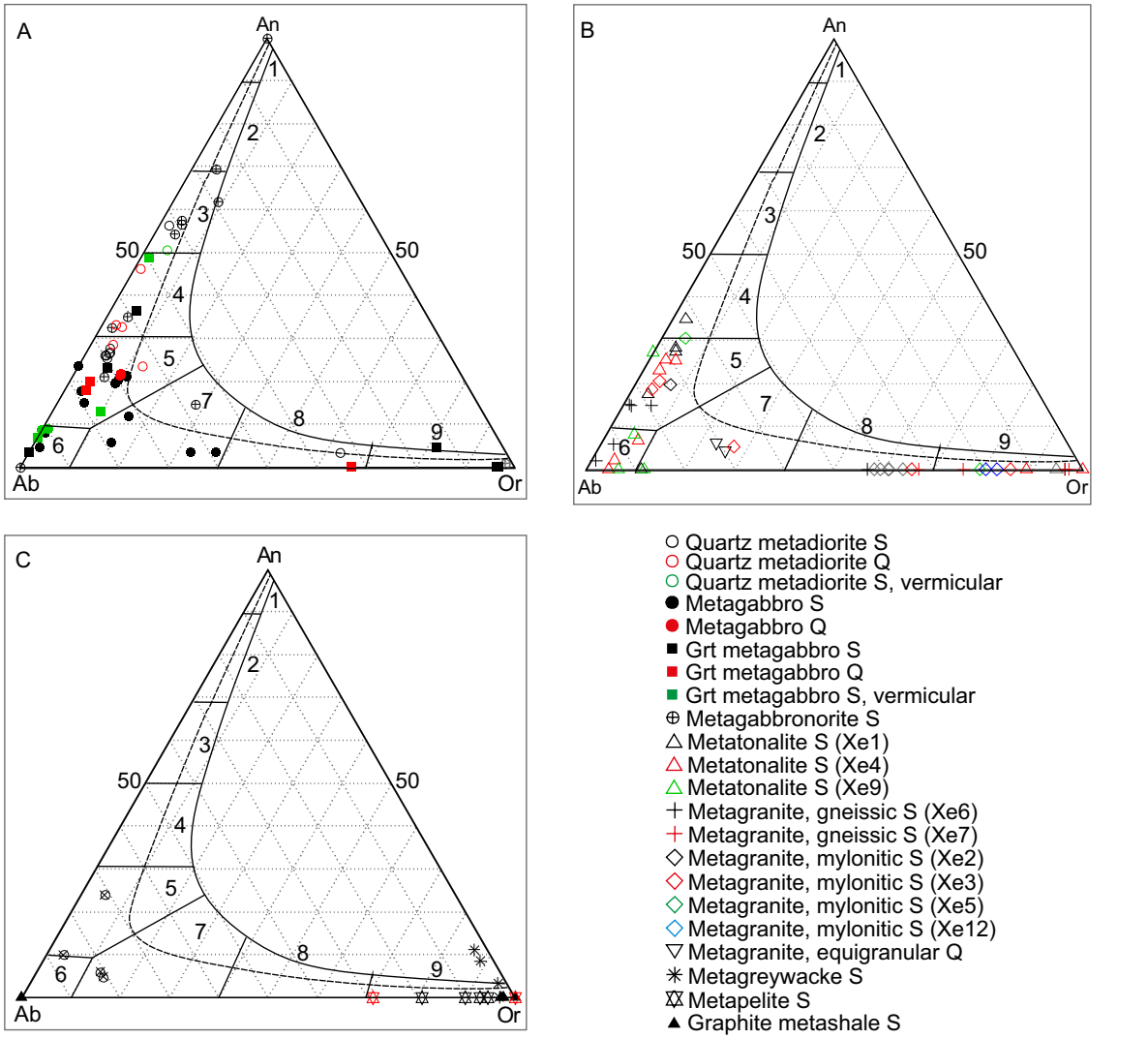

Fig. 8. The feldspar composition of the xenoliths. (A) Metagabbroic and quartz metadioritic xenoliths; (B) metagranitoid xenoliths; (C) metasedimentary xenoliths. Quantitative analyses (Q, red symbols) and semiquantitative analyses (S, black symbols). The An-Ab-Or diagram was produced after Smith (1974). 1 = anorthite; 2 = bytownite; 3 = labradorite; 4 = andesine; 5 = oligoclase; 6 = albite; 7 = anorthoclase; 8 = K- Na feldspar; 9 = K-rich feldspar.

Table 3. Representative quantitative silicate mineral analyses.

	Anorthoclase		Clinopyroxene						Garnet				
	ALKBM6-98 / r1 / 3	**ALKBM6-98 / r2 / 2b**	**ALKBM1-98/1**	**ALKBM6-98/r2/1**	**P4/r1/3a**	**P4/r2/4a**	**Xe11.2/ r1/3a**	**Xe11/ r2/3a**	**Xe16/ r3/1**	**KR-07-13X/r1/5**	**KR-07-13X/r1/6**	**Xe16/I2/ r2/r11**	**Xe16/ r4/1**
SiO_2	65.05	66.18	50.41	52.22	52.44	48.93	49.87	47.19	51.12	39.16	39.09	38.36	39.28
TiO_2	n.d.	n.d.	0.80	0.78	0.25	0.85	0.71	1.46	0.48	0.27	0.19	bdl	0.15
Al_2O_3	19.21	18.74	5.57	2.60	1.61	5.32	4.26	7.28	4.76	21.39	21.00	21.60	21.25
Cr_2O_3	n.d.	n.d.	bdl	bdl	0.18	0.21	bdl	0.12	0.00	bdl	bdl	bdl	bdl
FeO	0.15	0.22	11.25	12.54	7.94	7.70	9.34	8.60	12.04	21.59	21.61	23.73	23.57
MnO	n.d.	n.d.	0.16	0.41	0.31	0.27	0.29	0.27	0.13	2.61	2.65	0.75	0.99
MgO	n.d.	n.d.	12.45	10.11	14.10	13.05	12.41	11.49	11.68	9.07	9.20	8.77	8.90
CaO	1.28	0.90	17.82	19.29	22.19	21.53	22.49	21.21	18.02	5.97	5.96	6.21	5.76
Na_2O	7.99	7.94	1.55	2.08	0.78	1.01	0.84	1.26	1.66	0.00	0.00	0.00	0.00
K_2O	3.99	4.47	0.00	0.00	0.00	0.00	0.00	0.00	0.00	0.00	0.00	0.00	0.00
SrO	n.d.	n.d.	n.d.	0.00	n.d.	n.d.	n.d.	n.d.	n.d.	n.d.	n.d.	n.d.	n.d.
BaO	0.49	0.41	bdl	n.d.	bdl	bdl	bdl	bdl	bdl	0.00	0.00	0.00	0.00
F	n.d.	n.d.	0.00	n.d.	0.00	0.00	0.00	0.00	0.00	0.00	0.00	0.00	0.00
Cl	n.d.	n.d.	0.00	n.d.	0.00	0.00	0.00	0.00	0.00	0.00	0.00	0.00	0.00
Total	98.16	98.85	100.02	100.04	99.79	98.85	100.22	98.89	99.90	100.06	99.70	99.66	99.89
	Mica				Par-gasite				Plagio-clase				
	P4 / r2 / 2	**Xe11.2/ r1 / 5**	**Xe11.2 / r2 / 3**	**Xe16 / r3 / 2b**	**P4 / r3 / 4**	**Xe11.2/ r2 / 4**	**Xe11.1/ r1 / 3**	**Xe16 / r1 / 4**	**ALKB-M1-98 / 3**	**ALKB-M1-98 / r3 / 4b**	**KR-07-13X/r1/8**	**Xe11.2 / r2 / 2**	**Xe11.2 / r1 / 1**
SiO_2	37.04	41.62	39.13	34.94	41.56	40.11	40.23	41.04	61.40	56.33	61.75	63.20	62.54
TiO_2	2.77	2.29	3.56	6.94	1.97	2.53	4.60	3.26	0.00	0.00	0.00	0.00	0.00
Al_2O_3	13.63	9.03	9.30	13.57	13.26	16.12	12.78	11.82	23.08	25.90	22.06	21.88	22.67
Cr_2O_3	bdl	bdl	bdl	bdl	0.21	0.02	0.09	0.02	0.00	0.00	0.00	0.00	0.00
FeO	16.44	15.13	18.58	17.15	12.13	13.92	9.42	15.63	0.21	0.85	0.15	0.12	0.13
MnO	0.23	0.24	0.35	0.11	0.18	0.27	0.16	0.05	0.00	0.00	0.00	0.00	0.00
MgO	14.92	15.87	13.48	11.33	12.27	9.88	13.87	10.98	0.00	0.00	0.00	0.00	0.00
CaO	0.01	0.06	0.20	0.07	9.77	9.52	11.92	9.90	6.00	9.64	5.03	3.80	4.28
Na_2O	0.31	0.07	0.00	0.58	3.16	3.09	3.33	2.50	7.76	6.05	7.50	9.06	9.01
K_2O	9.56	10.06	9.91	7.73	2.09	1.40	0.23	1.51	0.78	0.22	2.32	0.80	0.75
BaO	0.00	0.00	0.00	2.79	bdl	bdl	bdl	bdl	0.03	0.00	0.00	0.03	0.00
F	0.76	1.19	0.67	0.78	0.35	0.17	0.42	0.45	0.00	0.00	0.00	0.00	0.00
Cl	bdl	bdl	bdl	bdl	bdl	bdl	bdl	0.22	0.00	0.00	0.00	0.00	0.00
Total	95.74	95.26	95.22	96.28	96.59	96.84	96.64	96.71	99.25	98.99	99.22	98.88	99.39

bdl below detection limit; n.d. not detected

Detection limits: SiO_2 0.1 wt.%, TiO_2 0.10 wt.%, Al2O3 0.10 wt.%, $Cr_2O_3$0.07 wt.%, V2O3 0.11 wt.%, FeO 0.11 wt.%, MnO 0.09 wt.%, MgO 0.09 wt.%, CaO 0.07 wt.%, Na_2O 0.05 wt.%, K2O 0.04 wt.%, BaO 0.19 wt.%, SrO 0.15 wt.%, NiO 0.06 wt.%, P_2O_5 0.12 wt.%, F 0.17 wt.%, and Cl 0.04 wt.%.

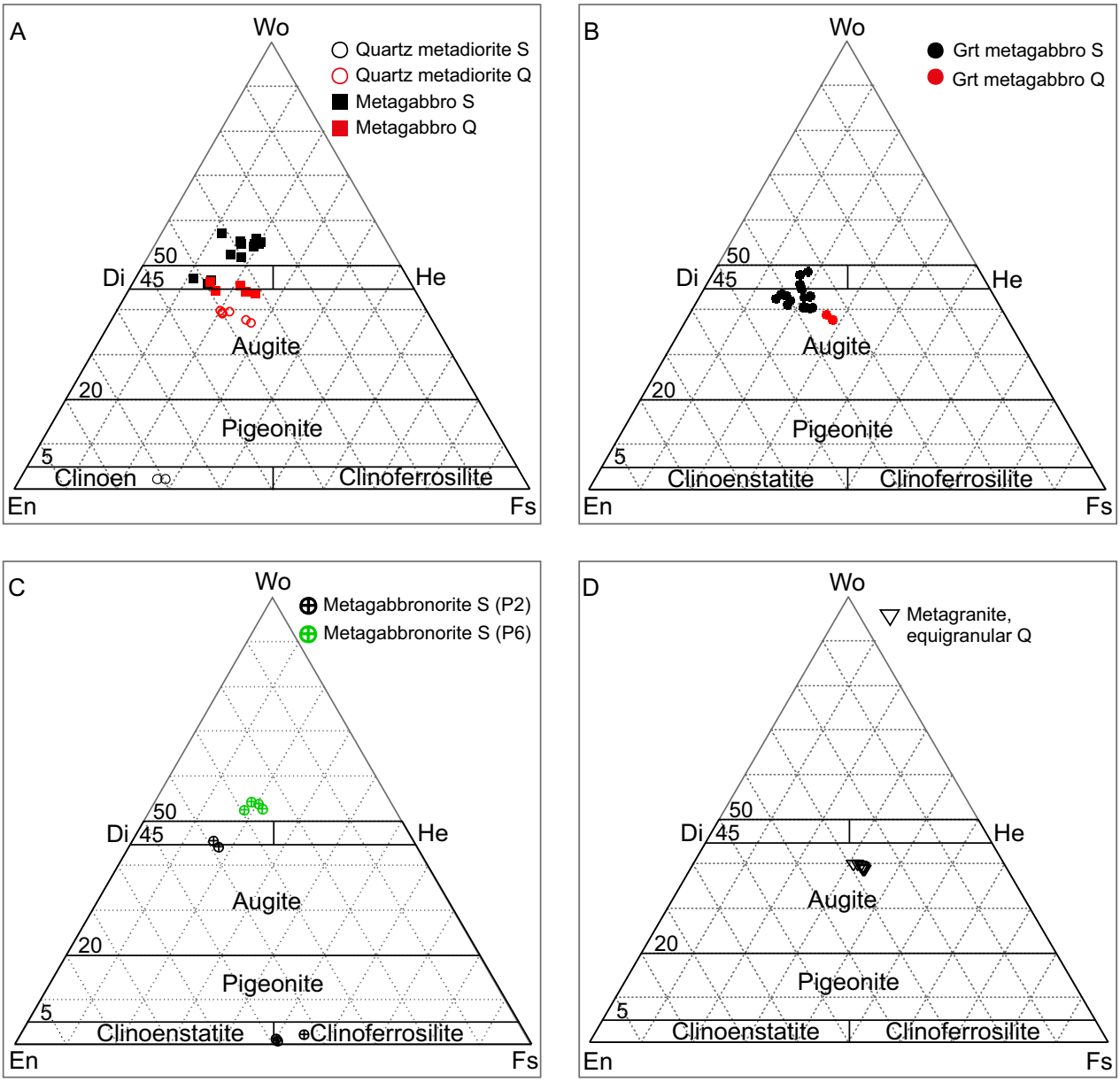

Fig. 9. The pyroxene composition of the xenoliths. (A) Clinopyroxene and orthopyroxene of metagabbroic and quartz metadioritic xenoliths. (B) Clinopyroxene of garnet-bearing metagabbros. Quantitative analyses (Q, red symbols) and semi-quantitative analyses (S, black symbols). (C) Clinopyroxene and orthopyroxene of metagabbronorites, semi-quantitative analyses. (D) Augite of equigranular metagranite ALKBM6-98, quantitative analyses. Pyroxene classification after Morimoto et al. (1989).

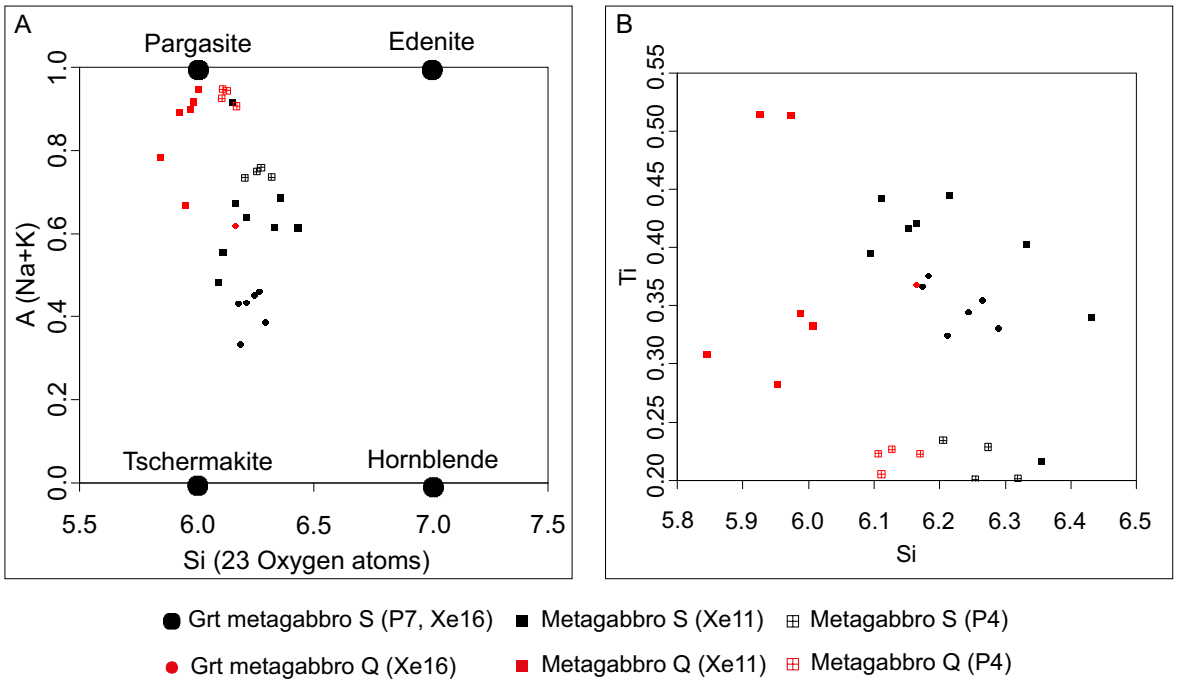

Fig. 10. The Ca-amphibole of the metagabbroic xenoliths. (A) Amphibole was classified after Leake et al. (1997). (B) Amphibole composition in terms of molar Si and Ti in the formula unit (based on 23 oxygen atoms). The highest Ti was observed in the amphibole overgrowth over amphibole. Quantitative analyses (Q, red symbols) and semi-quantitative analyses (S, black symbols).

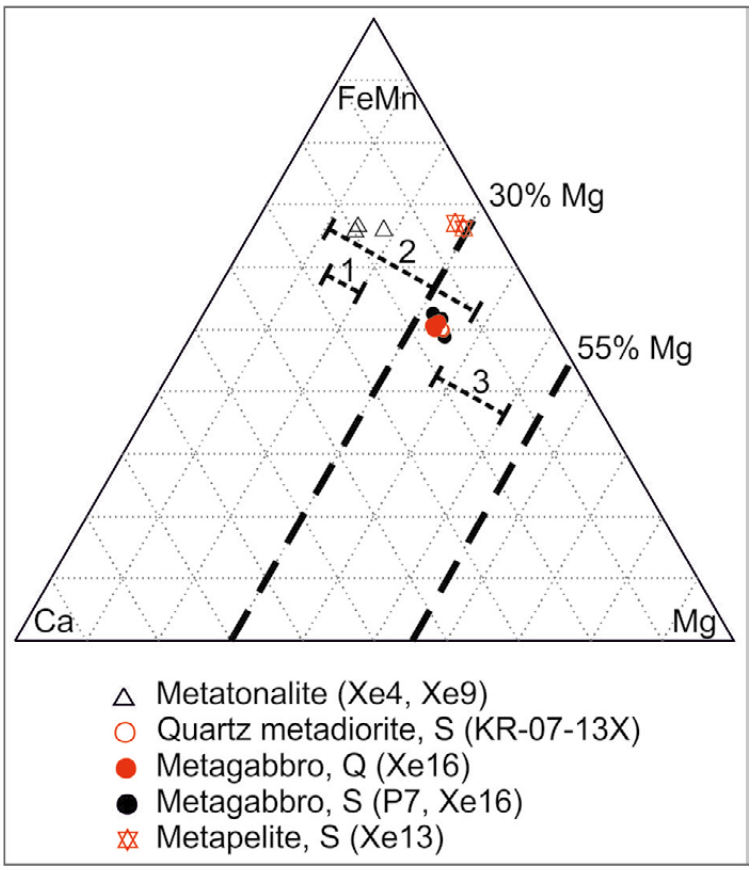

Fig. 11. The garnet composition of the metagabbroic, metapelitic and metatonalitic xenoliths. Ca (Mn+Fe2+) and Mg in the formula unit (based on 24 oxygen atoms). Quantitative analyses (Q, red symbols) and semi-quantitative analyses (S, black symbols). As a reference, average values for the garnet composition from amphibolites (1), from charnockites and granulites (2) and from eclogites occurring in gneissic or migmatite terrain (3) are given (Tröger 1959, cited in Coleman et al. 1965) (modified after Coleman et al. 1965).

7.1 Metagabbroids and quartz metadiorites.

Eight samples (ALKBM8, P2, P4, P6, P7, P8, Xe11 and Xe16) were classified as metagabbroids and three samples as quartz metadiorites (ALKBM1, KR-07-13X and Xe10) (Tables 1 and 2, Fig. 7). All the samples show a granoblastic texture and frequently exhibit modal banding. The metagabbroids and quartz metadiorites represent three main types: metagabbro, metagabbronorite and quartz metadiorite. The plagioclase composition of the metagabbroids is illustrated in Figure 8A, pyroxene in Figures 9A-C and amphibole in Figure 10.

7.1.1 Metagabbros

Samples P4, P7, P8, Xe11 and Xe16 (Figs. 3D, G, H, X; 4C, D; 5E, F; Table 2) are medium to coarse grained and composed of clinopyroxene (Figs. 9A, B) ± pargasitic hornblende (Fig. 10) ± plagioclase (Fig. 8A) ± garnet. The inferred metamorphic grade for these xenoliths is granulite facies. The samples are typified by retrograde clinopyroxene-plagioclase symplectite. When garnet is present, it shows distinctive dark kelyphitic rims (Fig. 4D). The grain boundaries of the minerals are retrograde and often include fine <1 mm carbonate, magnetite ± mica (Figs. 6E, F).

Samples P7, P8 and Xe16 are characterized by kelyphitic alteration of garnet. The xenoliths mainly consist of plagioclase [An_{4-20} Ab_{59-94} Or_{1-38}] (26–50 vol.%), augite [$Wo_{35-49}En_{32-43}Fs_{14-27}$ Ac_{0-6}] (Mg# 55-78) (15-43 vol.%), garnet (10–22 vol.%), magnetite-ulvöspinel (8–15 vol.%) and pargasitic hornblende (Mg# 56-58) (1–10 wt.%). Apatite (<4 vol.%), pyrite, rutile, Na-pyroxene, Na-amphibole, Ti- and Ba-rich phlogopite and calcite are minor and accessory phases. Augite has symplectic contacts against plagioclase and garnet. Garnet is mainly altered to dark kelyphite; small relics of almandine-pyrope garnet ($Alm_{48-49}Gro_{15-17}Prp_{33-34}Sp_{1.6-2.1}$) were observed. The kelyphite consists of fine <1 µm magnetite-silicate material. The average composition corresponds to almandine in water-free bulk composition, as described by Romu (2006) (unpublished M.Sc. Thesis).

Samples P4 and Xe11 exhibit modal and textural banding (Table 2). Sample P4 is composed of relatively coarse (up to ca. 4 mm) magnesian (Mg# 72–79) diopside-augite [$Wo_{43-46}En_{37-41}Fs_{11-18}$ Ac_{2-4}] (56 vol.%) and pargasitic hornblende (Mg# 64-65) (35 vol.%) with fine (<<1 mm) Fe-Ti-Al-spinel and magnetite (6 vol.%) along hornblende rims. Clinopyroxene is symplectic with potassium-bearing plagioclase [An_{13} Ab_{77} Or_{10}], occasionally altered to clay (Mr Lassi Pakkanen, pers. comm. 2009). Brown pargasitic hornblende (Figs. 6E, F; 10) encloses a disseminated fine opaque mineral, probably magnetite. Accessory annite-phlogopite is found on the grain boundaries of amphibole and clinopyroxene and occasionally as inclusions of amphibole (Fig. 6F). Sample Xe11 shows banding of ultramafic (M´ = 99) and mafic (M´ = 81.6) mineral layers (Table 2). The ultramafic part is quite similar to P4, but plagioclase is absent, and the texture is comparatively more even grained. The mafic part of sample Xe11 is composed of brown pargasitic hornblende (Mg# 43-45) (46 vol.%), symplectitic diopside [$Wo_{35-57}En_{25-35}Fs_{16-26}Ac_{0-5}$] (Mg# 55–73; 35 vol.%), potassium-bearing plagioclase [$An_{3.5-23}Ab_{71-95}$ Or_{0-10}] (18 vol.%) and minor Ti-magnetite, calcite and apatite. Plagioclase has lobate grain boundaries with diopside, occurs as round inclusions in the mafic minerals, and has Na-enriched rims against hornblende. Brown hornblende shows staining of fine-grained opaque oxide and has overgrowths of relatively Ti-enriched and K-depleted pargasite with oxide exsolutions. Annite–phlogopite is found between plagioclase and clinopyroxene (Fig. 6F).

7.1.2 Metagabbronorites

Samples P2 and P6 are medium-grained and mainly composed of plagioclase (49–65 vol.%) (Fig. 8 A) + clinopyroxene (1–24 vol.%) (Fig. 9 C) ± orthopyroxene (0–11 vol.%). Talc-magnetite pseudo-morphs in sample P6 have been interpreted as pseudomorphed orthopyroxene while classifying these samples. Alternatively, the pseudomorphs may be after olivine. The inferred metamorphic grade for these xenoliths is from upper amphibolite to granulite facies (Tables 1 and 2).

Sample P6 is composed of plagioclase [An_{54-69} Ab_{26-42} Or_{4-9}] (49 vol.%), augite [$Wo_{53-54}En_{26-29}Fs_{18-22}$] (Mg# 55-62) (24 vol.%) and pseudomorphs comprised of talc and magnetite (18 vol.%). Minor and accessory phases

include brown hornblende (5 vol.%), magnetite (4 vol.%), apatite (0.4 vol.%), biotite and zircon. Sample P-2 contains two distinctive parts, mafic and felsic (Fig. 3B). The studied thin section included a narrow mafic band but was dominantly felsic (M´ = 13.1). Resulting mineral mode was zoned plagioclase [An_{21-100} Ab_{0-76} Or_{0-6}] (65 vol.%), elongated orthopyroxene [$Wo_{1-2}En_{52-56}Fs_{42-45}$] (Mg # 54-57) (11 vol.%), magnesian augite [$Wo_{44-45}En_{39}Fs_{16-17}$] (Mg# 70-72) (1 vol.%) and veinlets of strongly deformed quartz (22 vol. %). Thin mafic bands of orthopyroxene (weakly altered to chlorite and quartz) and quartz veinlets result in a weakly foliated texture. Accessory phases include magnetite (0.7 vol.%), apatite (0.4 vol.%), biotite, chlorite, carbonate and zircon. The felsic part, probably a cross-cutting leucosome vein, is composed of calcic plagioclase [An_{21-100}], strongly altered K-feldspar and quartz with lobate grain boundaries.

7.1.3 Quartz metadiorites

Samples Xe10 and ALKBM1-98 are medium grained and granoblastic. The inferred metamorphic grade for these xenoliths is granulite facies. Sample ALKBM1-98 shows compositional banding: Mafic minerals comprise distinctive 1–10-mm-thick bands, which were interpreted as igneous layering (Fig. 4F). The samples are composed of plagioclase [An_{25-56} Ab_{42-70} Or_{1-4}] (59–65 vol.%) (Fig. 8A), Mg-rich (Mg# 57–67) augite [$Wo_{35-38}En_{34-38}Fs_{19-26}$ Ac_{4-6}] (5–18 vol.%) (Fig. 9A) and weakly deformed quartz (14–29 vol.%). Pseudomorphs (3–7 vol.%) comprised of dark, fine-grained (<1 µm) material, possibly after garnet, enclose plagioclase [An_{33-46} Ab_{52-64} Or_{1-3}] and orthopyroxene [En_{70}] (Mg# 71-73). Accessory phases include ilmenite, magnetite, zircon and rutile. Augite has narrow clinopyroxene-plagioclase [An_{51} Ab_{45} Or_4] symplectic coronae. Sample KR-07-13X is a small felsic, quartz dioritic xenolith referred as a nodule. The sample is granoblastic, medium grained and modally layered. Plagioclase [An_{24} Ab_{64} Or_{13}] (Fig. 8A) is albite twinned, quartz shows undulose extinction, and minor sillimanite is fibrous. Fresh garnet ($Alm_{45}Gro_{16}Prp_{34}Sp_5$) shows brown kelyphitic rims. Potassium feldspar [$An_{0.2}$ $Ab_{1.8}Or_{98}$] is probably secondary and apatite and rutile are the minor phases.

7.2 Metagranitoids

Eleven samples (Xe1, Xe2, Xe3, Xe4, Xe5, Xe6, Xe7, Xe8, Xe9, Xe12 and ALKBM6-98) can be classified as metagranitoids. The metagranitoids represent four main types: metatonalites, metagranites, gneissic metagranites and mylonitic metagranites. The metatonalites and gneissic metagranites exhibit microscopically observable traces of probably decompression-induced partial melting, which was followed by relatively rapid crystallization of fibrous K-feldspar ± calcite ± rutile at grain boundaries (Figs. 6A–D). The mylonitic and intensively deformed augen-ribbon texture of the mylonitic metagranites hampers the above-mentioned interpretations (Figs. 4K, L). Metagranite xenolith ALKBM6 is notably homogeneous and even grained (Fig. 4I). The feldspar compositions of the samples are shown in Figure 8B.

7.2.1 Metatonalites

Samples Xe1, Xe4 and Xe9 are medium grained (Figs. 3I, L, Q), and show inequigranular, weakly-foliated or granoblastic textures (Figs. 4G, H). All the samples show moderate to strong alteration of plagioclase and partially molten grain boundaries, rich in fibrous potassium feldspar.

Samples Xe1 and Xe4 may be also referred to as leucotonalites or trondhjemites. The samples consist of polygonal plagioclase [An_{2-35} Ab_{68-95} Or_{3-3}] (57–60%), strongly deformed, lenticular polycrystalline quartz (29–32%), accessory magnetite, pyrite, apatite, hematite, chlorite, carbonate and zircon ± minor garnet. Garnet is relatively almandine rich ($Alm_{55-56}Gro_{16-20}Prp_{14-18}Sps_{10-11}$). Fibrous potassium feldspar ($Ab_{0-11}Or_{79-100}$) is found along the grain boundaries. Sample Xe9 resembles samples Xe1 and Xe4, but quartz is relatively undeformed and apatite, rutile, alkali silicate and Ti-magnetite make up irregular, dark bands. Garnet is almandine rich ($Alm_{55}Gro_{20}Prp_{15}Sp_{10}$) and identical to the garnet in samples Xe1 and Xe4. In addition to fibrous potassium feldspar, alkali silicate mineral is found along grain boundaries.

7.2.2 Equigranular metagranite

Sample ALKBM6-98 is fine grained and equigranular, and notably un-deformed relative to the other samples (Fig. 4I). The grain boundaries are clear and free of fibrous potassium feldspar or other indications of decompressional partial melting. The major phases are anorthoclase (72.5 vol.%) (Fig. 8B), quartz (18.7 vol.%) and augite [$Wo_{36-37}En_{26-27}Fs_{29-31}$ Ac_7] (Mg# 45-49) (8.5 vol.%) (Fig. 9D). Anorthoclase shows cross-hatch twinning and perthitic exsolutions. Quartz is slightly undulose. Augite is clear and unaltered and slightly Na bearing "acmitic" (ca. 2 wt% Na_2O). Accessory minerals are subhedral, albite-twinned plagioclase, anhedral apatite, rutile, zircon, ilmenite and pyrite. The opaque phases comprise 0.3 vol.% of the mode. Ilmenite contains minor amounts of vanadinium (0.3 wt% V_2O_3), manganese (1.0 wt% MnO) and magnesium (1.0 wt% MgO).

7.2.3 Gneissic metagranites

Samples Xe6, Xe7 and Xe8 represent gneissic metagranites. These xenoliths are medium to coarse grained and leucocratic gneissic rocks (Figs. 3N-P). They mainly consist of coarse-grained (>5 mm) potassium feldspar [$Ab_{3-33}Or_{67-97}$] (50–62 vol.%), quartz (36–39 vol.%) and minor plagioclase [$An_{2-15}Ab_{83-97}Or_{1-6}$] (only identified by scanning electron microscopy) (Table 2). Large, optically uniform potassium feldspar crystals are divided into subgrains by recrystallized zones (Fig. 4J). Veins of weakly deformed quartz and <1 mm polygonal-sutured quartz and feldspar make up the matrix between deformed crystals. Accessory phases include apatite, magnetite, chlorite, muscovite, carbonate and zircon. Fibrous potassium feldspar occurs along grain boundaries (2–13 vol.%).

7.2.3. Mylonitic metagranites

Samples Xe2, Xe3, Xe5 and Xe12 represent mylonitic metagranites (Figs. 3J, K, M, T). These xenoliths have a macroscopic augen texture and mainly consist of (<2 cm) cross-hatched potassium feldspar augen and thin bands of chlorite, epidote and/or amphibole. Potassium feldspar augen are set within a matrix of quartz veins typified by ribbon-quartz texture (Figs. 4K, L). Polygonal feldspar is strongly altered. The feldspar includes matrix plagioclase [An_{5-30} Ab_{65-77} Or_{4-27}] (only identified by scanning electron microscopy) and potassium feldspar [$Ab_{15-52}Or_{58-85}$] (total of 48–64 vol.%). Quartz (total of 23–34 vol.%) is frequently mantled with very fine-grained acicular alkali silicate mineral (total of 0–12 vol.%), possibly aegirine-augite, which is also found within quartz as inclusions. Other minor and accessory phases include chlorite (0–1 vol.%), apatite (≤0.1 vol.%), carbonate minerals (≤1 vol.%), magnetite and zircon. Fibrous potassium feldspar is found along grain boundaries (0–17 vol.%).

7.3 Metasedimentary rock types

Five samples (P1, P5, P9, Xe13 and Xe14) are of sedimentary origin on the basis of their petrography and mineralogy. This is a heterogeneous group of xenoliths: Two samples represent metapelitic compositions and re-crystallisation in granulite facies, and three samples are rocks of lower metamorphic grade.

7.3.1 Metapelites

Samples P5 and Xe13 are migmatitic and their texture indicates partial melting and brittle deformation after the (re)crystallization of quartz and potassium feldspar (Figs. 3E, U). The samples have a high-pressure mineral assemblage of kyanite, rutile, K-feldspar, hercynitic spinel ± garnet ± orthopyroxene, distinctive for metapelitic granulites.

Sample P5 is granoblastic. The main phases are undulose and microfractured quartz, undulose orthopyroxene and anhedral kyanite, which occasionally show undulose extinction. Kyanite is slightly rounded in shape. Orthopyroxene [En_{37-51}] (Mg# 37-53) (only identified by scanning electron microscopy) coexists with dark green, hercynitic spinel forming coronae around clots of 1–3 mm in diameter, probably former garnet (Fig. 4O). Spinel, rutile, magnetite, ilmenite and metamictic rounded zircon are the accessory minerals. Orthoclase of fibrous habit

is abundant all over the rock, and the texture implies alteration and brittle deformation. Ti-magnetite has reaction boundaries with kyanite and fibrous orthoclase. Indications of decomposed garnet are present: a completely altered clot is rimmed by iron-rich chlorite and the core consists of magnetite, spinel and aluminium silicate. The dyke host has probably strongly affected this sample; euhedral potassium feldspar, fibrous sodium pyroxene, carbonate and pyrite occur near the dyke contact. Carbonate is dolomitic in composition. Sample Xe13 is brecciated and strongly infiltrated by secondary carbonate. Garnet porphyroblasts ($Alm_{65}Gro_{10}Prp_{25}$) with lobate grain boundaries are largely replaced by Fe-rich chlorite + magnetite + spinel + Al-silicate. Undulose quartz and anhedral, relatively fresh potassium feldspar has broken into clasts. Rutile is rounded. The rounded shape and undulose extinction of kyanite indicate deformation (Figs. 4M, N).

7.3.2 Other metasedimentary xenoliths

Sample P1 is fine-grained, graphitic shale. It has a strong fabric and is mainly comprised of graphite and quartz (Fig. 3A). Polygonal albite has crystallized between the graphite layers. A veinlet of polycrystalline quartz shows undulose extinction and contains very fine-grained graphite dust (Fig. 4Q). Sample P9 is granoblastic metasandstone (Fig. 4R). Relatively large aggregates of weakly deformed quartz (ca. 30 vol.%), with lobate grain boundaries, and sparse plagioclase porphyroblasts are set in fine-grained matrix (ca. 70 vol.%) dominated by polygonal plagioclase [An_{5-24}]. Accessory phases include jadeite, Ti-magnetite, amphibole, and monazite. Sample Xe14 (Fig. 3V) is fine-grained, matrix-dominated metagreywacke. Well-rounded, corroded, undulose, possibly originally volcanic quartz is present (Fig. 4P). In a hand specimen, grading caused by quartz crystals was observed. Granoblastic albite is also present. Accessory minerals are epidote, barite, apatite, chlorite, magnetite, dolomite and zeolite. There are minor volcanic rock fragments, which contain fine-grained simple-twinned feldspar. Brownish-green to olive green pleochroic sodium pyroxene, slightly altered to chlorite, is observed next to the dyke contact.

7.4 Rutile in quartz metadiorite and equigranular granite xenoliths

The rutile concentrates were side products of heavy mineral separation of zircon in quartz metadiorite (ALKBM1-98) and equigranular metagranite (ALKBM6-98) samples. Altogether, 37 spots of 21 rutile crystals were analysed. The analyses revealed variable Zr and Nb concentrations (1260–3350 ppm, <38600 ppm, respectively), low Cr (<830 ppm) and fairly constant V_2O_3 (0.7–0.9 wt%) (Table 4). The rutile concentrates from quartz metadiorite ALKBM1-98 (fraction a) and equigranular metagranite ALKBM6-98 (fractions b and c) include a) amber-coloured, V- and Fe-bearing rutile (n = 7), b) black, V-, Fe- and Nb-bearing rutile (n = 8) and c) amber-coloured, Nb- and Fe-rich rutile (n = 6).

Rutile in sample ALKBM1-98 is compositionally relatively uniform and homogeneous. It shows fairly low Nb (<3050 ppm) and high Zr (2464–3030 ppm). Instead, the rutile is more heterogeneous and notably Nb rich (17 700–38 600 ppm) in ALKBM6-98. In ALKBM6-98, there are three chemically distinctive groups of rutile: A single crystal (b1) is distinguished by extremely high Zr (3351–4110 ppm). Two crystals (b2) are typified by high Zr (1234–1486 ppm) combined with relatively low Nb (1234–1744 ppm), whereas the remaining 7 crystals (c) exhibit exceptionally high Nb (17 730–38 641 ppm), variably high Zr (1256–2829 ppm) and high FeO (1.3–2.1 wt.%).

The low Cr combined with a low Nb concentration observed in quartz metadioritic rutile is characteristic of rutile derived from metapelitic metamorphic rocks (Zack et al. 2004b, Triebold et al. 2007). The high Zr contents of the quartz metadioritic and metagranitic rutile are both indicative of a high equilibration temperature of the rutile (Zack et al. 2004a) (Table 4).

Table 4. Quantitative rutile analyses of quartz metadiorite ALKBM1 and equigranular metagranite ALKBM6.

ZR IN RUTILE THERMOMETRY

Quartz metadiorite ALKBM1	Zr ppm	T(°C)*	T(°C)**	SiO_2	TiO_2	Al_2O_3	Cr_2O_3	V_2O_3	V ppm	FeO	MnO	BaO	Nb_2O_5	Nb ppm	Ta_2O_5	ZrO_2	Total
a) black																	
r14 / 9.1	2570	993	857-860	b.d.l.	96.37	n.a.	b.d.l.	0.84	5700	1.02	b.d.l.	n.a.	0.19	1330	b.d.l.	0.35	98.77
r14 / 9.2	2580	994	857-861	b.d.l.	96.96	n.a.	0.10	0.83	5600	0.96	b.d.l.	n.a.	b.d.l.	bdl	b.d.l.	0.35	99.19
r14 / 10.1	2820	1005	869-872	b.d.l.	96.36	n.a.	b.d.l.	0.93	6300	0.98	b.d.l.	n.a.	0.16	1130	b.d.l.	0.38	98.80
r14 / 10.2	2740	1002	865-868	b.d.l.	97.26	n.a.	b.d.l.	0.94	6400	0.97	b.d.l.	n.a.	b.d.l.	bdl	b.d.l.	0.37	99.54
r14 / 11.1	3030	1014	878-881	b.d.l.	96.65	n.a.	b.d.l.	0.83	5600	1.00	b.d.l.	n.a.	0.44	2060	b.d.l.	0.41	99.32
r14 / 11.2	3030	1014	878-881	b.d.l.	96.44	n.a.	b.d.l.	0.88	6000	1.03	b.d.l.	n.a.	0.41	2870	b.d.l.	0.41	99.17
r14 / 12.1	2460	988	852-855	b.d.l.	96.29	n.a.	b.d.l.	0.68	4600	1.06	b.d.l.	n.a.	b.d.l.	bdl	b.d.l.	0.33	98.36
r14 / 12.2	2510	990	854-857	b.d.l.	97.79	n.a.	b.d.l.	0.71	4800	1.08	b.d.l.	n.a.	b.d.l.	bdl	b.d.l.	0.34	99.92
r14 / 13.1	2960	1011	875-878	b.d.l.	96.13	n.a.	b.d.l.	0.85	5800	0.98	b.d.l.	n.a.	b.d.l.	bdl	b.d.l.	0.40	98.36
r14 / 13.2	2900	1009	872-875	b.d.l.	97.70	n.a.	b.d.l.	0.93	6300	0.98	b.d.l.	n.a.	0.16	1150	b.d.l.	0.39	100.16
r14 / 14	2800	1004	868-871	b.d.l.	96.39	n.a.	b.d.l.	0.72	4900	0.99	b.d.l.	n.a.	0.39	2720	b.d.l.	0.38	98.86
r14 / 15	2690	999	862-866	b.d.l.	97.68	n.a.	b.d.l.	0.79	5400	0.77	b.d.l.	n.a.	0.16	1150	b.d.l.	0.36	99.78
Equigranular metagranite ALKBM6	Zr ppm	T(°C)*	T(°C)**	SiO_2	TiO_2	Al_2O_3	Cr_2O_3	V_2O_3	V ppm	FeO	MnO	BaO	Nb_2O_5	Nb ppm	Ta_2O_5	ZrO_2	Total
b) black																	
r8 / 5.1	3350	1027	892-894	b.d.l.	96.81	n.a.	b.d.l.	0.71	4800	0.50	b.d.l.	n.a.	0.33	2340	b.d.l.	0.45	98.80
r8 / 5.2	4110	1053	920.00	b.d.l.	97.51	n.a.	b.d.l.	0.86	5800	0.49	b.d.l.	n.a.	0.42	2960	b.d.l.	0.56	99.84
r8 /6.1	1370	913	782-789	b.d.l.	97.28	n.a.	b.d.l.	0.71	4800	0.69	b.d.l.	n.a.	0.97	6800	b.d.l.	0.19	99.84
r8 /6.2	1490	924	791-797	b.d.l.	96.28	n.a.	b.d.l.	0.73	5000	0.68	b.d.l.	n.a.	0.84	5860	b.d.l.	0.20	98.73
r8 / 7	b.d.l.	-	-	0.08	97.96	n.a.	b.d.l.	0.79	4900	0.37	b.d.l.	n.a.	b.d.l.	7050	b.d.l.	b.d.l.	99.21
r8 / 8.1	1230	899	770-778	b.d.l.	96.68	n.a.	b.d.l.	0.81	5500	0.61	b.d.l.	n.a.	0.77	5370	b.d.l.	0.17	100.37

Table 4. Cont.

Equigranular metagranite ALKBM6	Zr ppm	T(°C)*	T(°C)**	SiO_2	TiO_2	Al_2O_3	Cr_2O_3	V_2O_3	V ppm	FeO	MnO	BaO	Nb_2O_5	Nb ppm	Ta_2O_5	ZrO_2	Total
c) amber																	
r14 /1.1 core	1480	923	791-797	b.d.l.	90.99	n.a.	b.d.l.	0.74	5060	2.09	b.d.l.	n.a.	5.15	36000	0.15	0.20	99.03
r14 /1.2 core	2550	992	856-860	b.d.l.	91.30	n.a.	b.d.l.	0.80	5400	2.09	b.d.l.	n.a.	5.10	35700	b.d.l.	0.34	99.33
r14 /1.3 rim	2050	965	828-833	0.09	90.76	n.a.	b.d.l.	0.79	5400	2.05	b.d.l.	n.a.	5.05	35300	0.20	0.28	99.64
r14 / 2	1540	928	795-801	b.d.l.	91.41	n.a.	b.d.l.	0.78	5300	2.09	b.d.l.	n.a.	5.12	35900	b.d.l.	0.21	99.22
r14 / 3.1	2830	1006	869-872	b.d.l.	90.79	n.a.	b.d.l.	0.79	5300	2.07	b.d.l.	n.a.	5.08	35500	0.19	0.38	99.61
r14 / 3.2	1910	956	820-825	b.d.l.	90.38	n.a.	b.d.l.	0.76	5200	1.97	b.d.l.	n.a.	5.08	35500	0.20	0.26	99.30
r14 / 4.1	1720	942	808-813	b.d.l.	94.86	n.a.	b.d.l.	0.78	5300	1.26	b.d.l.	n.a.	2.59	18100	b.d.l.	0.23	98.66
r14 / 4.2	1260	902	772-779	b.d.l.	94.83	n.a.	b.d.l.	0.79	5400	1.28	b.d.l.	n.a.	2.54	17700	b.d.l.	0.17	99.73
r14 / 5.1 core	2190	973	837-841	b.d.l.	90.37	n.a.	b.d.l.	0.86	5800	2.13	b.d.l.	n.a.	5.44	38100	0.23	0.30	99.61
r14 / 5.2 core	1590	932	799-805	b.d.l.	90.52	n.a.	0.12	0.77	5200	2.06	b.d.l.	n.a.	5.36	37500	b.d.l.	0.21	99.33
r14 / 5.3 rim	1700	941	806-812	b.d.l.	90.69	n.a.	b.d.l.	0.83	5600	2.06	b.d.l.	n.a.	5.53	38600	0.24	0.23	99.04
r14 / 5.4 rim	1690	940	806-812	b.d.l.	90.49	n.a.	0.09	0.73	5000	1.98	b.d.l.	n.a.	5.34	37300	0.22	0.23	99.57
r14 / 7	2040	964	828-833	b.d.l.	92.11	n.a.	b.d.l.	0.75	5100	1.68	b.d.l.	n.a.	4.30	30100	b.d.l.	0.28	99.08
r14 / 8	1720	942	808-813	b.d.l.	92.95	n.a.	b.d.l.	0.66	4500	1.48	b.d.l.	n.a.	3.61	25200	b.d.l.	0.23	99.12

Detection limits: SiO_2 0.07; TiO_2 0.14; Cr_2O_3 0.09; V_2O_3 0.12; FeO 0.08; MnO 0.08; Nb_2O_5 0.15; Ta_2O_5 0.15; ZrO_2 0.14 wt%.

37 spots of 21 rutile crystals were analysed; one spot out of 32 gave Zr content lower than the detection limit 1000 ppm.

Temperature of equilibration for co-existing Rt, Qtz, and Zrn was determined by equations T(°C)*=127.8*ln(Zr in ppm)-10 (Zack et al. 2004a) and T(°C)**=[4470±120/(7.36±0.10)-log(Zr in ppm)]-273 (Watson et al. 2006).

7.5 Petrographic peculiarities and indications of melting of the studied xenoliths

The studied metagranitoid and metagabbroic xenoliths show microscopic textural evidence of partial melting and recrystallization (Figs. 5, 6). On a macroscopic scale, the xenoliths are not like classic migmatitic rocks. The textures or mineralogy cannot be explained by a straightforward simple model of, for example, H_2O-fluid saturated gabbro, granite or tonalite partial melting. In outcrops at western Heimefrontfjella and further at Natal belt felsic plutonic rocks record signs of partial melting and charnockitisation (cf. Bauer et al. 2009, Mendonidis et al. 2015).

Based on the mineral chemistry of the xenoliths and the host lamproite, one of the agents affecting them agents was probably a K-enriched fluid. The middle to lower crustal granulite terrains are thought to dominantly represent water-deficient environments, but periods of fluid activity may have occurred. For dehydration melting, potassium feldspar films covering quartz, plagioclase, and biotite were described by Rajesh et al. (2011). For the leucocratic metatonalite and gneissic metagranite xenoliths, the presence of interstitial fibrous K-feldspar + euhedral calcite ± rutile on grain boundaries between plagioclase-quartz, K-feldspar-quartz, and quartz-quartz (Fig. 6) is probably due to disequilibrium dehydration melting in the presence of H_2O-CO_2 fluid followed by quench crystallization. The lack of mafic minerals indicates that the fluid source was most probably predominantly external, as dehydration melting of biotite would have led to the stabilization of, for example, peritectic orthopyroxene (Clemens & Droop 1998). The presence of interstitial fibrous K-feldspar is not solely defined in ultrapotassic-dyke-hosted xenoliths, as a similar texture was observed by the author in tonalitic xenoliths hosted by boulders of basaltic composition. Therefore, the presence of fibrous K-feldspar probably relates to the protolith composition, melting and subsequent rapid crystallization, rather than the type of host rock. The traces of melting observed may have originated in situ in bedrock prior to xenolith entrainment into magma, during the ascent, or even during the cooling of the host. It is, however, speculative whether the leucocracy of the metatonalite and metagranite gneiss xenoliths is a feature induced by primary or later dehydration melting. In some studies, leucocratic granitoids have been reported to occur by fault zones where the fluid activity is higher relative to the regions where rock formations are solid and less fractured.

7.6 Data evaluation and interpretation

7.6.1 QAPF classification

Secondary, low-grade mineral assemblages were absent from the studied xenoliths. There is no evidence of low-grade hydrothermal overprinting of any of the samples, and the xenoliths predominantly represent high-grade metamorphosed rock types. To distinguish the protolith of metaigneous rock types, the samples were grouped according to the modal composition of minerals (Table 2 and Fig. 7). In point counting, minerals resulting from partial melting were counted separately, and the amount of fibrous potassium feldspar was not used in the determination of the protolith rock type. The strongly oriented mylonitic texture probably increased the systematic error within the respective point counting results. The identification of minor plagioclase from alkaline feldspar in gneissic and mylonitic metagranite samples by optical microscopy was obscure. This result is demonstrated by the clustering of these samples in the alkali-feldspar granite field of Figure 7. The ultramafic mineralogy of the metagabbroic samples may have resulted from the original igneous mineral layering or metamorphic redistribution of the mineral phases (Table 2). This was pronounced in sample Xe11, in which two thin sections were studied, one of a plagioclase-free part (Xe11.1) and the other of a plagioclase-rich part (Xe11.2) (Table 2). Also, as the plagioclase chemistry of the metagabbroic samples systematically shows a low (<50 wt%) anorthite content (Table 1, Fig. 8), classification diagrams used for unaltered gabbros and ultramafic rocks were not used, and the generalizing term ‘metagabbro’ was adopted. Later, the results of modal mineralogy-based rock type classification are dissected with classification schemes based on geochemical data and discussed.

7.6.2 Mineral microanalyses

Quantitative microanalyses were only available for a subset of the samples. The samples for which mineral chemistry was quantitatively studied included mafic minerals to provide P-T estimates. Most xenoliths showed textural disequilibrium, which hampers their use in P-T determinations. Most of the feldspar analyses (Fig. 8) were semi-quantitative. Evaluation of the available semi-quantitative and quantitative mineral chemical data is presented in Figures 8–11. However, as the data are scattered and no parallel analyses of precisely the same analysis spots are available, the semi-quantitative data need to be considered descriptive and interpreted with some caution. The results of the SEM analyses were normalised to 100 wt%, which also has a small effect, as minor elements and water are then neglected. As discussed below, semi-quantitative analyses can be used in the classification of the mineral species and to exemplify the petrological differences between the samples and rock types.

The clinopyroxene analyses with a higher $Ca_2Si_2O_6$ (Wo) component are semi-quantitative analyses from homogeneous clinopyroxene for sample P6 and completely symplectic clinopyroxene for sample Xe11 (Fig. 9). Samples P6 and Xe11 were analysed in different sessions in 2005 and 2004, respectively. No quantitative EMP mineral data are available for the metagabbronorite sample P6. The Ti content of clinopyroxene is similar in the samples (1–2 wt% and 1.5 wt%, respectively), however. The semi-quantitative analyses of P6 clinopyroxene (n = 4, 2 areas) show an Al content of 2–3 wt% Al_2O_3 and a Ti content ca. 1 wt% TiO_2, and Na was not detected. In metagabbro sample Xe11, the semi-quantitative analyses revealed no Na, while the quantitative analyses indicated ca. 1 wt% Na_2O. The accuracy of the semi-quantitative analyses has been estimated to range from 1–2 wt%. Due to the cobalt standardization used and the sensitivity of the EDS sensor, the heavier elements show better accuracy than the lighter elements, such as Na. The quantitative analyses of sample Xe11 indicate considerable compositional variation in Al, and slight variation in Fe, Ca and Na within one clinopyroxene crystal (i.e. symplectic aggregate comprised of clinopyroxene, plagioclase and clay minerals), for example, 4.9–7.3 wt% Al_2O_3, 8.5–9.3 wt% FeO, 21.2–22.3 wt% CaO and 0.8–1.3 wt% Na_2O. The Al contents from the semi-quantitative analyses are on average lower (mainly 3–4 wt% Al_2O_3) than those from the quantitative analyses (5–7 wt% Al_2O_3). The number of semi-quantitative analyses was higher (n = 10, from different crystals), and they represent a more extensive area (6 areas) than the quantitative dataset (n = 11 from 3 crystals, 2 areas). Accordingly, the compositional anomaly shown by the semi-quantitative clinopyroxene analyses (Fig. 9) probably indicates slight Ca enrichment of clinopyroxene (i.e. excess Ca^{2+} relative to the Fe^{2+} and Mg^{2+} cations on site M2) rather than analytical error alone (cf. Morimoto 1988).

The garnet of garnet metagabbro Xe16 was analysed both semi-quantitatively and quantitatively (Fig. 11). In terms of the major cations Ca, Fe, Mn and Mg, the semi-quantitative analysis also correlated well with the quantitative analysis. Accordingly, the use of the semi-quantitative garnet analysis is acceptable for robust P-T estimates of the xenoliths (indicated with the presented P-T estimates if used). On the basis of the semi-quantitative and quantitative microanalysis of the brown Ca-amphibole of the mafic metagabbroic samples, the amphibole is pargasitic in composition (Fig. 10). The quantitative microanalysis implies relatively high Ti, Na and K (2–3 wt% TiO_2, 2.5–4 wt% Na_2O, 1–2 wt% K_2O). The amphibole overgrowth of sample Xe11 displayed the highest amphibole Ti analysed (Fig. 10B) and was higher in Ti (4–5 wt% TiO_2) relative to the major amphibole rich in oxide inclusions. The range of compositions implies both natural compositional variation and analytical error of the semi-quantitative analysis. As predicted, due to the normalization to 100 wt%, the SEM data for the water-bearing minerals in general are less accurate than for the water-free minerals.

Overall, the semi-quantitative analyses in this work were used here for robust petrological purposes, e.g. to characterize the samples. Crucial information on the petrography and homogeneity of the samples was also obtained using BSE imaging. Accordingly, quantitative analyses were primarily used in thermobarometric modelling.

8 GEOCHEMISTRY

Geochemical whole-rock data for the host lamproites and the xenolith samples representative of their rock type are listed in Table 5. Nine xenolith samples (IDs P1–P9) were not processed for geochemical analysis because they were so small (<0.1 dm^3). Due to textural heterogeneity, two subsamples from the samples ALKBM1-98 (modal layering) and Xe14 (clasts) were analysed. The small size, metamorphism and possible contamination with host-derived magmatic fluids hamper the interpretation of the xenolith whole-rock data and fluid-mobile incompatible element data in particular (cf. Chapter 4). Accordingly, detailed interpretation of possibly preserved primary igneous features would be rather speculative. Also, the whole-rock data alone cannot be used to interpret the petrogenetic relationships, as the tectonic setting of the xenoliths is unknown and metamorphic modification of the whole-rock geochemistry has occurred (cf. Wilson 1989). The figures presented are descriptive and interpretations indicative of the origins of the xenoliths.

8.1 The studied Kjakebeinet xenoliths and their hosts

The studied Kjakebeinet xenoliths are hosted by Jurassic ultramafic, ultrapotassic and incompatible trace element-enriched dyke rocks, referred to as lamproites by Luttinen et al. (2002). These are phlogopite-rich, and their primary carbonate-bearing mineralogy implies the presence of H_2O and CO_2 in the magma (Romu et al. 2008). On average, the hosts are high in potassium (ca. 5.3 wt% K_2O) and show strong enrichment in incompatible elements, e.g. Ba (3596 ppm), Sr (2697 ppm), La (254 ppm) and Zr (937 ppm), and LREE such as Ce (482 ppm) and Nd (211 ppm) (Table 5). The chemistry of the lamproite host (ALKB1-25-03, red symbols) and the representative xenolith samples (black symbols) are presented side by side in Figures 12 and 13. All of the samples may show metamorphic and metasomatic modification from their primary geochemical composition.

The whole-rock major and trace element compositions of the xenoliths primarily reflect the mineralogical mode of the samples (Chapter 7). The dataset (Table 5, Figs. 12 and 13) shows that there is no clustering of the xenolith compositions around the lamproite-host composition. This indicates that sample preparation was successful in that the analysed material did not contain substantial amounts of the host magma. This is also consistent with the finding that the interiors of the xenolith samples appeared, while processing the crushed rock, to be devoid of the host magma. The potassium content of the gneissic and mylonitic metagranites is unlikely to have been affected by the host-derived fluids, as the K_2O concentration of these samples is higher than ca. 6 wt% in the host-lamproite sample ALKB1-25-03. The low TiO_2, FeO and MgO concentrations of intermediate-silicic samples (Figs. 12A, C, D), together with relatively high A/CNK (molar $Al_2O_3/CaO+Na_2O+K_2O$) (Fig. 12J), reflect a low amount of mafic minerals. The P_2O_5 of the xenoliths is constantly low (<0.4 wt%), except for metapelite Xe13 (0.7 wt%) and metagabbro Xe16 (0.9 wt%) (Fig. 12H), indicative of the amount of phosphate minerals. The variable LOI values (0.8–3.0) (Table 5) of the mica and amphibole-free silicic samples, however, indicate that secondary carbonate is present in the metatonalites and some of the gneissic metagranites. Host-derived mineral chemical cryptic metasomatosis (cf. Chapter 4) is, however, possible for all xenolith samples, although it cannot be reliably determined from the whole-rock compositions. The critical major elements for host-derived contamination, solely on the basis of the major element composition of the studied samples, are titanium, magnesium, calcium and phosphorus for all samples and potassium for the metagabbroids, -diorites, -tonalites and equigranular metagranite (Fig. 12G), as the concentration of the mentioned elements is higher in the host lamproite than in the xenoliths.

Potassium is a fluid-mobile large-ion lithophile element, which was probably a major constituent of lamproite-derived fluids. Accordingly, the trace element composition of the xenoliths and the host were plotted against their K_2O concentration (Fig. 13). The presented

Table 5. Major and trace element compositions of the crustal xenoliths and their host lamproites.

Rock type	Lamproite dyke* (host, P-samples)	Lamproite boulder (host, Xe-samples))	Lamproite host average	Metatonalite	Metatonalite	Mylonitic metagranite	Mylonitic metagranite	Gneissic metagranite	Gneissic metagranite	Equigranular metagranite	Quartz metadiorite	Quartz metadiorite	Quartz metadiorite	Metagabbro	Metagabbro	Metagabbro	Metapelite	Metagreywacke	Metagreywacke
Sample	ALKB6-98*	ALKB1-25-03	Average ALKB6-98* and ALKB1-25-03	Xe1	Xe4	Xe2	Xe5	Xe6	Xe7	ALKBM6-98	ALKBM1.1-98	ALKBM1.2-98	Xe10	ALKBM8-03	Xe11	Xe16	Xe13	Xe14.1	Xe14.2
	Unnormalized Major Elements (Weight %):									**Unnormalized Major Elements (Weight %):**									
SiO_2	39.86	34.11	37.0	65.02	66.75	68.79	69.10	72.42	72.71	67.08	61.36	61.40	59.62	41.61	43.08	42.39	60.04	66.58	63.52
TiO_2	4.35	2.73	3.5	0.340	0.299	0.224	0.289	0.023	0.035	0.451	0.370	0.373	0.402	2.726	1.708	2.633	1.017	0.533	0.600
Al_2O_3	8.5	7.37	7.9	14.52	14.22	13.28	12.76	13.74	12.26	14.45	16.36	16.36	16.01	12.37	14.19	13.49	12.44	13.16	13.87
FeO*	9.01	9.20	9.1	3.13	3.00	1.76	1.84	0.16	0.43	1.89	3.37	3.34	3.98	17.60	10.42	13.55	6.76	3.40	3.48
MnO	0.2	0.211	0.2	0.058	0.051	0.025	0.031	0.003	0.017	0.040	0.055	0.055	0.076	0.281	0.209	0.260	0.103	0.044	0.046
MgO	9.29	10.65	10.0	0.73	0.60	0.40	0.32	0.02	0.14	0.97	2.61	2.62	3.06	5.56	7.96	5.31	1.89	1.02	1.06
CaO	16.25	14.54	15.4	3.08	2.92	1.34	1.48	0.86	1.04	2.59	6.63	6.61	7.15	8.04	11.92	9.52	3.66	0.29	0.35
Na_2O	0.54	0.56	0.6	3.79	3.82	2.17	1.83	2.40	0.74	5.11	4.54	4.54	4.03	1.68	2.83	2.60	0.94	0.76	0.90
K_2O	5.18	5.47	5.3	4.27	4.10	8.58	7.57	7.94	9.78	4.17	1.91	1.91	2.41	3.70	2.54	3.31	6.16	9.81	10.22
P_2O_5	3.79	3.37	3.6	0.097	0.100	0.057	0.077	0.026	0.018	0.159	0.148	0.147	0.139	0.225	0.328	0.943	0.693	0.053	0.075
Sum	96.97	88.21	92.6	95.03	95.87	96.64	95.30	97.59	97.16	96.92	97.37	97.35	96.88	93.78	95.18	94.01	93.69	95.65	94.11
SO_3 >/=	na	0.27			0.06		0.03							0.26	0.09		0.14		
LOI (%)	8.03	8.08	8.1	3.00	2.72	1.28	1.94	0.88	1.11	0.85	1.64	1.70	1.55	2.78	2.87	2.33	3.49	1.91	2.59
Sum	105.00	96.57	100.8	98.02	98.65	97.91	97.27	98.47	98.27	97.77	99.00	99.05	98.43	96.82	98.14	96.34	97.32	97.56	96.70
Mg# molar	68	71	70	33	29	32	27	23	40	52	62	62	62	40	62	45	37	39	39
MgO/(FeO+MgO)	51	54	52	19	17	19	15	12	24	34	44	44	43	24	43	28	22	23	23
Na_2O+K_2O	10	10	10	8	8	11	9	10	11	9	6	6	6	5	5	6	7	11	11

Table 5. Cont.

Rock type	Lamproite dyke* (host, P-samples)	Lamproite boulder (host, Xe-samples))	Lamproite host average	Metatonalite	Metatonalite	Mylonitic metagranite	Mylonitic metagranite	Gneissic metagranite	Gneissic metagranite	Equigranular metagranite	Quartz metadiorite	Quartz metadiorite	Quartz metadiorite	Metagabbro	Metagabbro	Metagabbro	Metapelite	Metagreywacke	Metagreywacke
Sample	ALKB6-98*	ALKB1-25-03	Average ALKB6-98* and ALKB1-25-03	Xe1	Xe4	Xe2	Xe5	Xe6	Xe7	ALKBM6-98	ALKBM1.1-98	ALKBM1.2-98	Xe10	ALKBM8-03	Xe11	Xe16	Xe13	Xe14.1	Xe14.2
	XRF Unnormalized Trace Elements (ppm):									**XRF Unnormalized Trace Elements (ppm):**									
Ni	117	188	152	5	3	4	1	1	2	9	25	25	33	49	58	25	24	19	22
Cr	291	281	286	56	76	85	72	51	51	41	110	110	119	29	122	94	147	109	110
Sc	11	18	15	5	5	4	4	1	2	4	12	12	15	49	37	33	19	10	13
V	196	135	166	29	28	12	15	2	7	39	70	71	92	607	268	257	114	116	134
Ba	4293	2900	3596	432	498	968	1388	607	562	2771	335	336	422	863	1138	1731	1092	1296	1632
Rb	75	107	91	69	75	126	144	191	165	27	22	22	26	73	48	42	96	165	180
Sr	2584	2810	2697	280	272	225	277	253	93	2001	598	596	610	381	723	1288	819	227	303
Zr	1208	666	937	154	156	207	283	47	57	41	66	66	69	127	111	98	330	244	255
Y	43	41	42	14	17	15	13	6	29	7	8	8	10	38	27	60	48	16	21
Nb	174	119	147	8	7	9	9	1	7	16	7	7	11	20	17	18	28	12	15
Ga	19	13	16	16	17	14	16	15	12	14	15	16	15	20	18	18	16	20	20
Cu	54	37	46	6	4	7	8	2	3	42	7	8	7	73	17	22	28	6	11
Zn	101	105	103	49	47	33	35	0	4	23	42	43	43	164	116	177	86	53	58
Pb	19	11	15	13	13	30	26	39	23	13	4	2	3	5	2	11	17	12	19
La	263	244	254	20	21	52	46	15	6	34	11	13	23	24	23	84	102	33	51
Ce	465	499	482	35	38	107	79	31	10	52	23	27	34	57	44	156	199	66	93
Th	22	16	19	3	6	33	17	20	9	1	2	1	2	4	1	6	21	6	10
Nd	208	215	211	14	15	45	31	10	6	20	12	12	13	33	29	78	80	30	44
U	4	6	5	2	1	3	2	8	9	2	2	0	1	3	1		5	6	9

Table 5. Cont.

Rock type	Lamproite dyke* (host, P-samples)	Lamproite boulder (host, Xe-samples))	Lamproite host average	Metatonalite	Metatonalite	Mylonitic metagranite	Mylonitic metagranite	Gneissic metagranite	Gneissic metagranite	Equigranular metagranite	Quartz metadiorite	Quartz metadiorite	Quartz metadiorite	Metagabbro	Metagabbro	Metagabbro	Metapelite	Metagreywacke	Metagreywacke
Sample	ALKB6-98*	ALKB1-25-03	Average ALKB6-98* and ALKB1-25-03	Xe1	Xe4	Xe2	Xe5	Xe6	Xe7	ALKBM6-98	ALKBM1.1-98	ALKBM1.2-98	Xe10	ALKBM8-03	Xe11	Xe16	Xe13	Xe14.1	Xe14.2
	ICPMS Unnormalized Trace Elements (ppm):									**ICPMS Unnormalized Trace Elements (ppm):**									
La ppm		256.7		20.1	22.1	56.3	46.6	15.1	3.6	32.8	13.5	13.4	20.8	24.6	19.7	84.4	104.3	35.3	50.0
Ce ppm		510.9		36.1	39.7	110.9	87.3	30.4	7.3	53.7	24.3	24.5	36.1	55.3	45.0	163.9	202.7	65.5	91.1
Pr ppm		59.7		4.0	4.4	12.8	9.8	3.4	1.0	5.8	2.8	2.8	4.0	7.4	6.3	20.0	23.0	8.5	11.5
Nd ppm		220.4		14.5	15.7	46.8	34.3	11.8	4.0	21.1	10.6	10.6	14.8	31.8	27.6	80.8	85.0	31.7	43.0
Sm ppm		33.9		2.9	3.3	9.6	6.2	2.2	1.5	3.6	2.0	2.0	2.7	8.3	6.5	16.0	14.7	5.9	7.8
Eu ppm		9.2		0.9	0.9	1.4	1.6	0.5	0.2	2.2	0.8	0.7	0.9	2.4	2.2	5.3	3.5	2.3	3.2
Gd ppm		22.4		2.8	3.1	7.8	4.5	1.5	2.4	2.5	1.8	1.8	2.3	8.4	6.4	14.5	12.1	4.7	6.0
Tb ppm		2.6		0.4	0.5	1.0	0.6	0.2	0.5	0.3	0.3	0.3	0.4	1.4	1.0	2.1	1.8	0.6	0.8
Dy ppm		11.9		2.7	3.1	4.2	2.9	1.0	4.1	1.5	1.5	1.5	2.0	8.1	5.7	12.1	10.4	3.3	4.4
Ho ppm		1.9		0.6	0.6	0.6	0.5	0.2	0.9	0.2	0.3	0.3	0.4	1.6	1.1	2.3	2.0	0.6	0.8
Er ppm		3.9		1.6	1.8	1.3	1.2	0.6	3.0	0.6	0.7	0.7	1.0	4.2	2.9	5.7	5.4	1.6	2.0
Tm ppm		0.4		0.2	0.3	0.2	0.1	0.1	0.5	0.1	0.1	0.1	0.1	0.6	0.4	0.8	0.8	0.2	0.3
Yb ppm		2.2		1.4	1.7	1.0	0.8	0.6	3.3	0.4	0.6	0.6	0.9	3.5	2.4	4.4	4.8	1.6	1.8
Lu ppm		0.3		0.2	0.3	0.2	0.1	0.1	0.5	0.1	0.1	0.1	0.1	0.5	0.4	0.6	0.7	0.3	0.3
Ba ppm		2927.8		436.9	503.8	990.2	1437.4	620.2	577.6	2878.0	332.4	334.8	417.8	869.7	1156.0	1742.2	1111.5	1341.2	1700.2
Th ppm		17.6		2.5	5.8	36.1	19.2	21.7	11.3	0.6	1.4	1.5	1.7	2.6	0.7	4.2	22.2	9.0	10.7
Nb ppm		121.9		8.3	7.9	10.0	9.1	2.5	8.1	15.9	7.4	7.5	11.7	21.2	17.1	21.4	30.5	12.4	15.1
Y ppm		44.6		14.5	16.9	15.3	12.4	5.7	28.6	6.1	7.2	7.2	10.1	39.6	27.4	58.7	50.9	16.3	20.9
Hf ppm		17.6		3.9	3.8	6.1	6.9	1.6	1.4	0.7	1.6	1.7	1.7	3.1	3.1	2.8	8.3	6.9	7.1
Ta ppm		8.4		0.3	0.3	0.6	0.3	0.5	1.4	0.4	0.3	0.3	0.3	1.1	0.9	1.1	1.1	0.7	0.8
U ppm		3.7		1.2	1.8	4.0	2.3	8.1	7.9	1.7	0.9	0.9	1.2	1.8	0.8	3.2	5.5	7.2	9.0
Pb ppm		12.7		14.2	15.2	33.6	31.7	42.9	27.3	15.3	4.7	4.7	4.9	6.3	3.7	12.5	18.7	18.4	24.5
Rb ppm		104.1		70.9	75.8	125.8	144.6	192.0	165.8	27.4	21.3	21.3	26.1	74.7	48.1	43.6	99.4	165.4	179.1
Cs ppm		0.4		0.2	0.3	0.2	0.4	2.8	1.2	0.0	0.1	0.1	0.1	1.6	3.1	1.1	0.4	0.9	1.0
Sr ppm		2858.5		286.6	275.1	223.9	277.8	255.6	92.7	1934.0	594.9	597.5	627.4	395.7	729.5	1372.6	857.8	228.2	302.0
Sc ppm		14.6		4.7	4.2	4.2	3.1	0.3	1.8	4.1	11.1	10.9	14.4	48.7	35.1	32.5	19.2	11.6	15.0
Zr ppm		647.5		143.8	135.1	199.8	263.5	43.7	55.4	40.3	62.2	63.1	66.5	123.7	106.3	98.0	324.6	238.9	245.2
Ti ppm	26078.3	16393.2	21235.7	2037.8	1792.4	1340.8	1729.6	140.5	207.8	2704.5	2217.2	2235.3	2408.0	16340.2	10238.5	15783.0	6097.8	3196.1	3596.8
K ppm	42999.2	45397.3	44198.2	35419.4	34043.8	71252.2	62829.9	65919.2	81209.5	34582.5	15881.2	15873.3	19988.0	30707.8	21091.1	27515.7	51099.9	81439.4	84799.7
P ppm	16539.6	14697.1	15618.3	425.4	434.6	250.2	337.1	112.9	77.8	692.1	646.5	641.9	607.2	982.8	1432.5	4117.1	3022.4	231.1	325.6

*Data from Luttinen et al. 2002
Major elements and Ni, Cr, Sc, V, Ga, Cu, Zn, Pb, XRF-data. Rest of the trace elements, ICP-MS data.

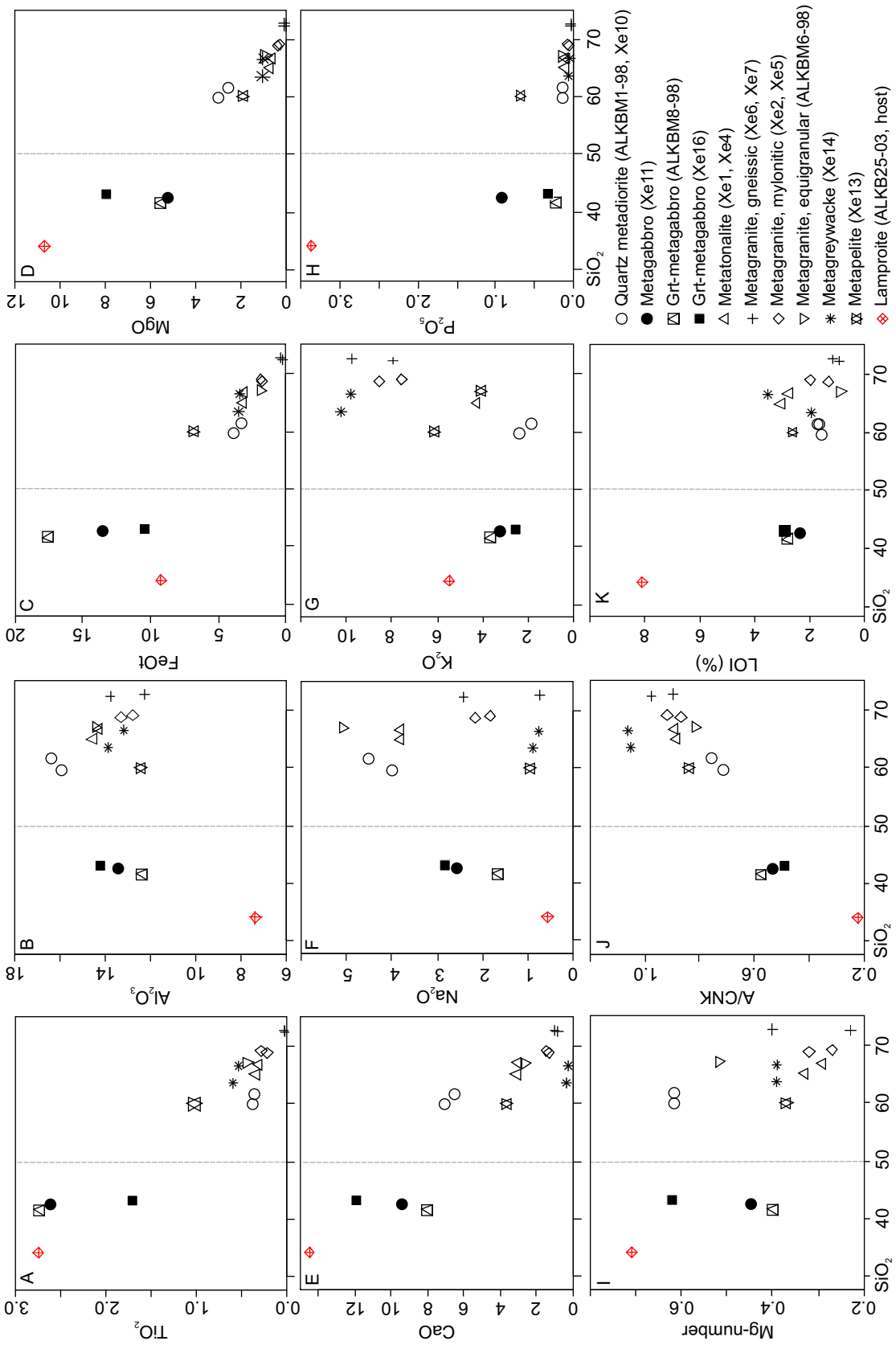

Fig. 12 A–K. Whole-rock major (wt%) element composition and loss-on-ignition (LOI) value versus SiO_2 (wt%) (Table 5). Values for the host-lamproite sample ALKB25-03 are indicated by red symbols and values for the studied xenolith samples by black symbols. (A) TiO_2 vs. SiO_2, (B) Al_2O_3 vs SiO_2, (C) FeO(tot) vs SiO_2, (D) MgO vs SiO_2, (E) CaO vs. SiO_2, (F) Na_2O vs. SiO_2, (G) K_2O vs. SiO_2, (H) P_2O_5 vs. SiO_2, (I) Mg number [molar (Mg/Mg+Fe(tot))] vs. SiO_2, (J) A/CNK [molar Al/Ca+Na+K] vs. SiO_2, and (K) LOI (wt.%) vs. SiO_2.

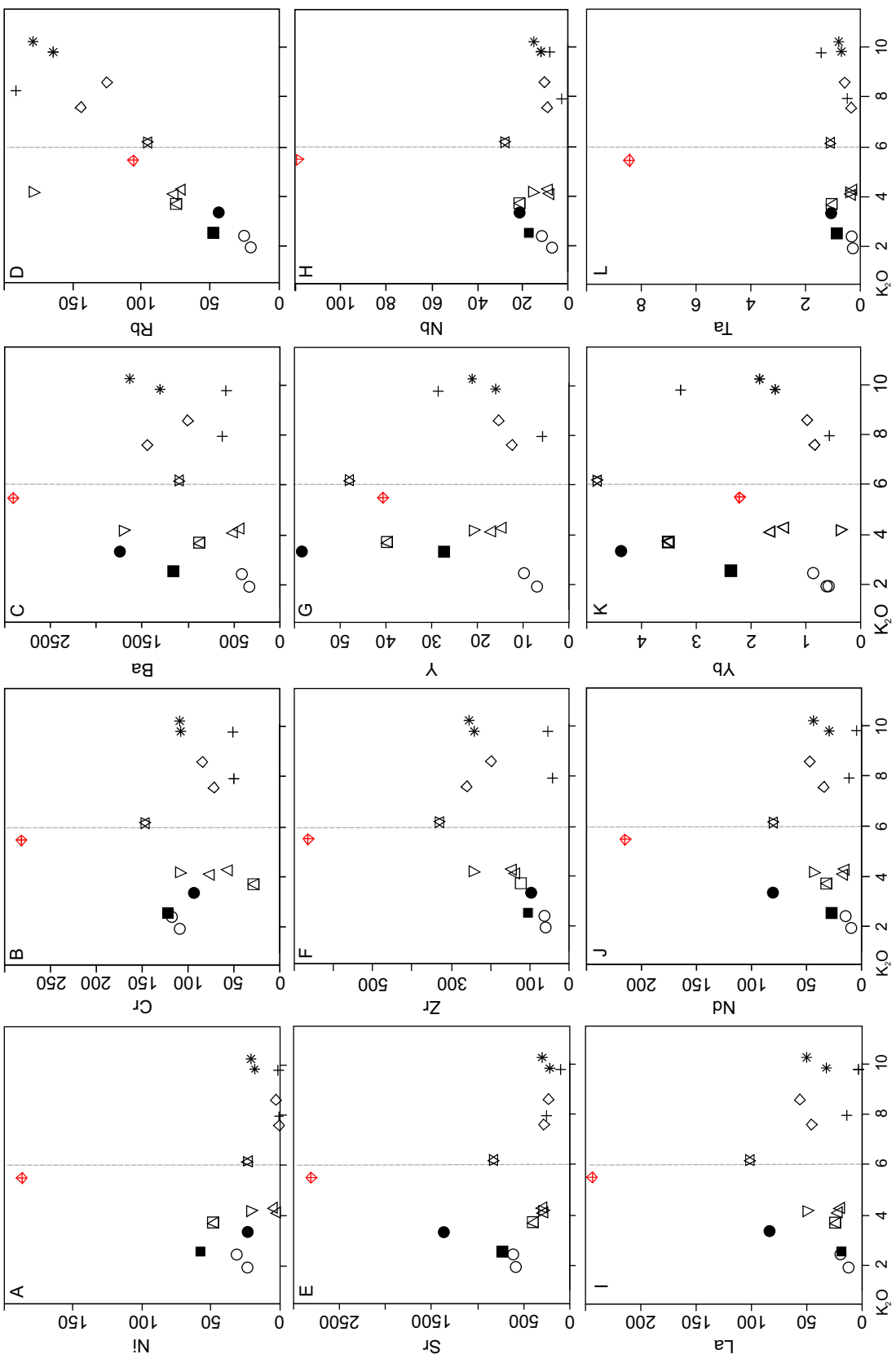

Fig. 13 A–L. Whole-rock trace element (ppm) composition versus K2O (wt%) (Table 5). The host-lamproite sample ALKB25-03 values are indicated by red symbols and the values for the studied xenolith samples by black symbols. Symbols as in Fig. 12. (A) Ni (ppm) vs. K_2O, (B) Cr (ppm) vs. K_2O, (C) Ba (ppm) vs. K_2O, (D) Rb (ppm) vs. K_2O, (E) Sr (ppm) vs. K_2O, (F) Zr (ppm) vs. K_2O, (G) Y (ppm) vs. K_2O, (H) Nb (ppm) vs. K_2O, (I) La (ppm) vs. K_2O, (J) Nd (ppm) vs. K_2O, (K) Yb (ppm) vs. K_2O and (L) Ta (ppm) vs. K_2O. Ni, Cr, Ba, Rb, Sr, Zr, Y, Nb, La and Nd, XRF data, Yb, and Ta, ICP-MS data.

trace element contents of the host are uniformly higher than in the xenoliths (apart from the rubidium content of gneissic and mylonitic metagranites, and metagreywacke Xe14; yttrium of metagabbro Xe11 and metapelite Xe13). Accordingly, if the geochemical characteristics of the following elements are not considered in detail, the critical minor elements possibly causing geochemical modification for all the studied samples are nickel, chromium, barium, strontium, zirconium, niobium, lanthanum, neodymium and tantalum (Fig. 13). As rubidium and strontium are commonly associated with potassium feldspar and plagioclase, respectively, the positive K_2O-Rb and negative K_2O-Sr correlations of the whole sample set (Figs. 13D, E) mainly indicate the presence of potassium feldspar and plagioclase as major mineral phases in metagranitoids and metagabbroic and -dioritic samples, respectively. The relatively high yttrium concentrations of samples Xe16 and Xe13 (60 ppm and 48 ppm, respectively) may indicate the presence of monazite, as the samples also show elevated P_2O_5 relative to the other samples. All of the xenolith samples display constantly low Nb (<30 ppm) and Ta (<2 ppm).

8.2 Geochemical classification of the studied metaigneous xenoliths

All of the samples may show metamorphic and metasomatic modification from their primary geochemical composition. The total alkali-silica (SiO_2 versus NaO + K_2O) (TAS) diagram (Cox et al. 1979) (Fig. 14A) and Si, Na, K, Fe, Ti, Al, Mg, Ca cation proportion diagram (De La Roche et al. 1980) (Fig. 14B) were used to estimate the protolith rock type of the metaigneous xenoliths and to dissect the results based on QAPF classification (Fig. 7, Chapter 7) and geochemical classification presented here. The multielement cation proportion diagram was used, as it gives less weight to the elements Si and K, the values of which may have been modified by metamorphic redistribution of quartz and metasomatism of the samples; this is more of a problem with the traditional TAS diagram (Fig. 14A). For the metatonalites (Xe1, Xe4) and equigranular metagranite (ALKBM6-98), the geochemical rock type classification differs from classification based on modal mineralogy. For the metatonalites, this shows in the presence of abundant fibrous potassium feldspar on grain boundaries, and for equigranular metagranite, anorthoclase feldspar. The metagabbro compositions (samples Xe11, Xe16, ALKBM8-98) are alkaline, but there is no named rock type for these specific compositions in TAS-based classification (Fig. 14A). Furthermore, the metagabbros are defined as quartz-deficient gabbroic rock types in classification based on cation proportions (Fig. 14B). These results are consistent with their quartz-free, alkaline and nepheline-normative mineralogy (cf. Chapter 7). However, due to mineral layering resulting in an ultramafic composition for sample Xe11 and pervasive metamorphism of the metagabbros, the rock type definitions of syenogabbro for sample ALKBM8-98, nepheline monzodiorite for sample Xe11 and nepheline gabbro for Xe16 (Fig. 14B) would be incorrect.

The classifications of Figures 14B and 14D have been developed for studies on fresh, homogeneous samples of aphanitic volcanic rocks, and they are consequently not optimal for the metaigneous, originally plutonic samples of this study. The diagrams based on incompatible trace elements (Figs. 14C-F), however, were selected from many available ones, as they do not involve common fluid-mobile elements such as Rb, K, Sr and Ba (cf. Chapter 4), which may have been modified by secondary processes. For metaigneous samples, the Nb/Y vs. Zr/Ti binary diagram (Fig. 14C) was used to compare their geochemical composition with that of volcanic rock types. The result is relatively consistent with the SiO_2, K_2O and Na_2O contents of the xenoliths shown in the TAS classification diagram (Fig. 14A): most of the samples show compositions plotting on the transition between subalkalic and alkalic rock types, and the metagranitoids record increasing alkalinity and silicity from metadiorites to gneissic metagranites. Accordingly, the metagabbroic xenoliths show basaltic affinity, quartz metadiorite trachyandesitic affinity, metatonalites andesitic-basaltic andesite affinity, equigranular and mylonitic metagranites trachytic affinity, gneissic metagranite Xe7 rhyolitic-dacitic affinity, and gneissic metagranite Xe6 alkali rhyolitic affinity. In order to make interpretations about the tectonic setting of the

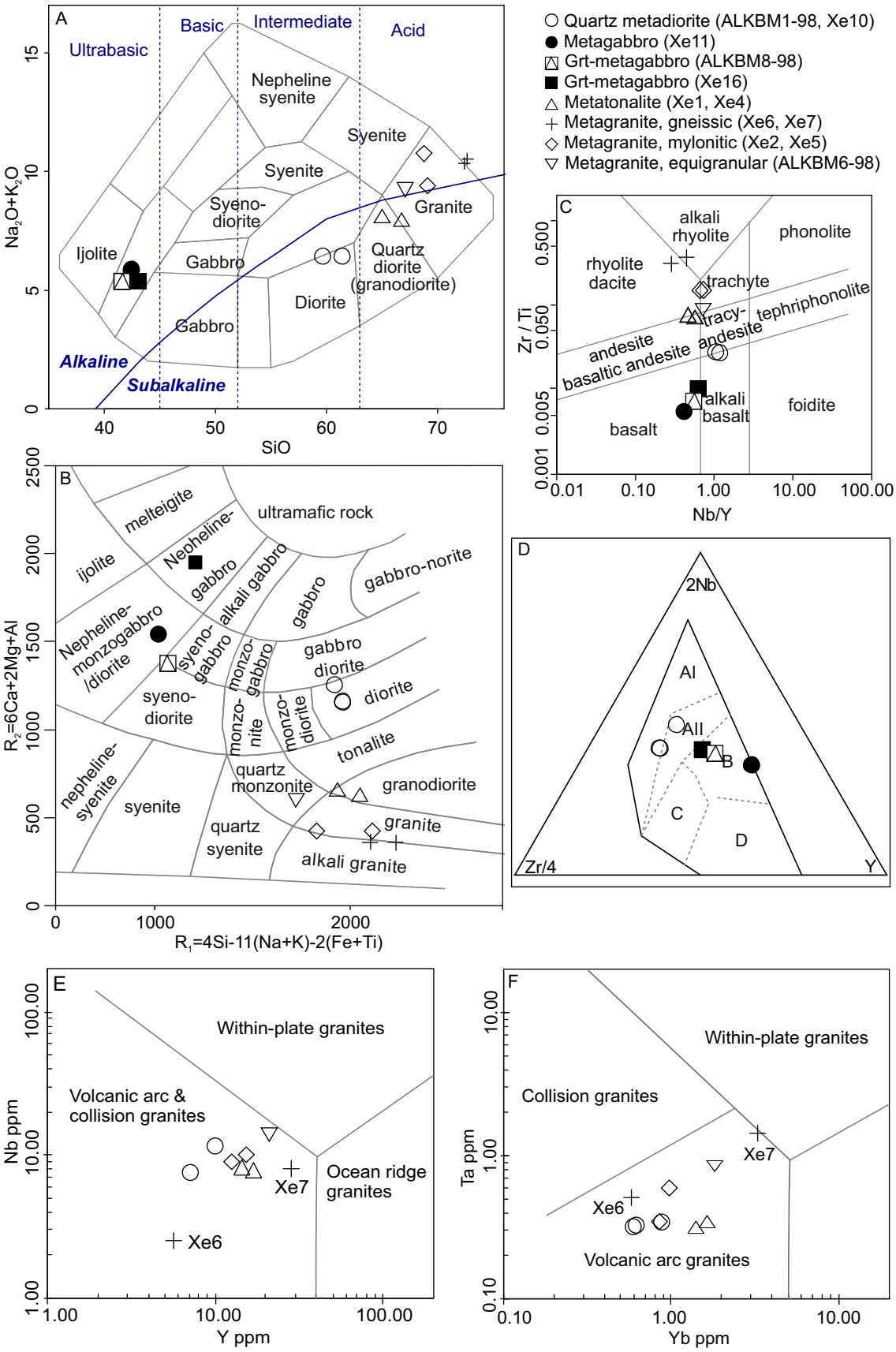

Fig. 14. Chemical composition of the meta-igneous xenoliths examined in this study shown in (A) the total alkali-elements (K_2O+Na_2O) vs silica (SiO_2) (TAS) diagram of Cox et al. (1979), (B) multielement binary diagram of De La Roche et al. (1980), (C) the Nb/Y vs. Zr/Ti diagram of Pearce (1996), (D) the Zr-Nb-Y tectonic discrimination diagram of Meschede (1986), (E) the Y vs. Nb tectonic discrimination diagram of Pearce et al. (1984) and (F) the Yb vs. Ta tectonic discrimination diagram of Pearce et al. (1984). Abbreviations in (D): AI-II and C, within-plate basalts; B, P-type mid-ocean ridge basalts; D, N-type mid-ocean ridge basalts; C-D, volcanic arc basalts.

analysed xenoliths, the ternary Zr, Nb and Y diagram (Fig. 14D) was used for metagabbroids and metadiorites and Y vs. Nb and Yb vs. Ta discrimination diagrams (Figs. 14E, F) for metagranitoids. The quartz metadiorites show affinity to within-plate basaltic rocks and the metagabbros to P-type mid-ocean ridge basaltic rocks (Fig. 14D). The metagranites show affinity to granites of volcanic arcs and collisional orogenies (Fig. 14E), more precisely the volcanic arc granites (Fig. 14F).

Nb, Y, and Zr are highly incompatible in mantle melting and the crystal fractionation of basic to silicic magmas (e.g. Pearce 1996). The heavy rare earth elements Sc, V and Y are only compatible with garnet and zircon in basaltic and andesitic magmas (cf. Kelemen et al. 2004). Ti, instead, behaves compatibly during the fractional crystallization of intermediate-silicic magma (Pearce 1996). Although metamorphosis ideally is an isochemical process the size and xenolithic origin of the studied samples restricts the representativeness of the whole-rock data. The mineral fractionation or metamorphic redistribution of the minerals may have affected the observed whole-rock trace element concentrations. These modifications are relevant for this study dealing with high-grade metamorphosed samples:

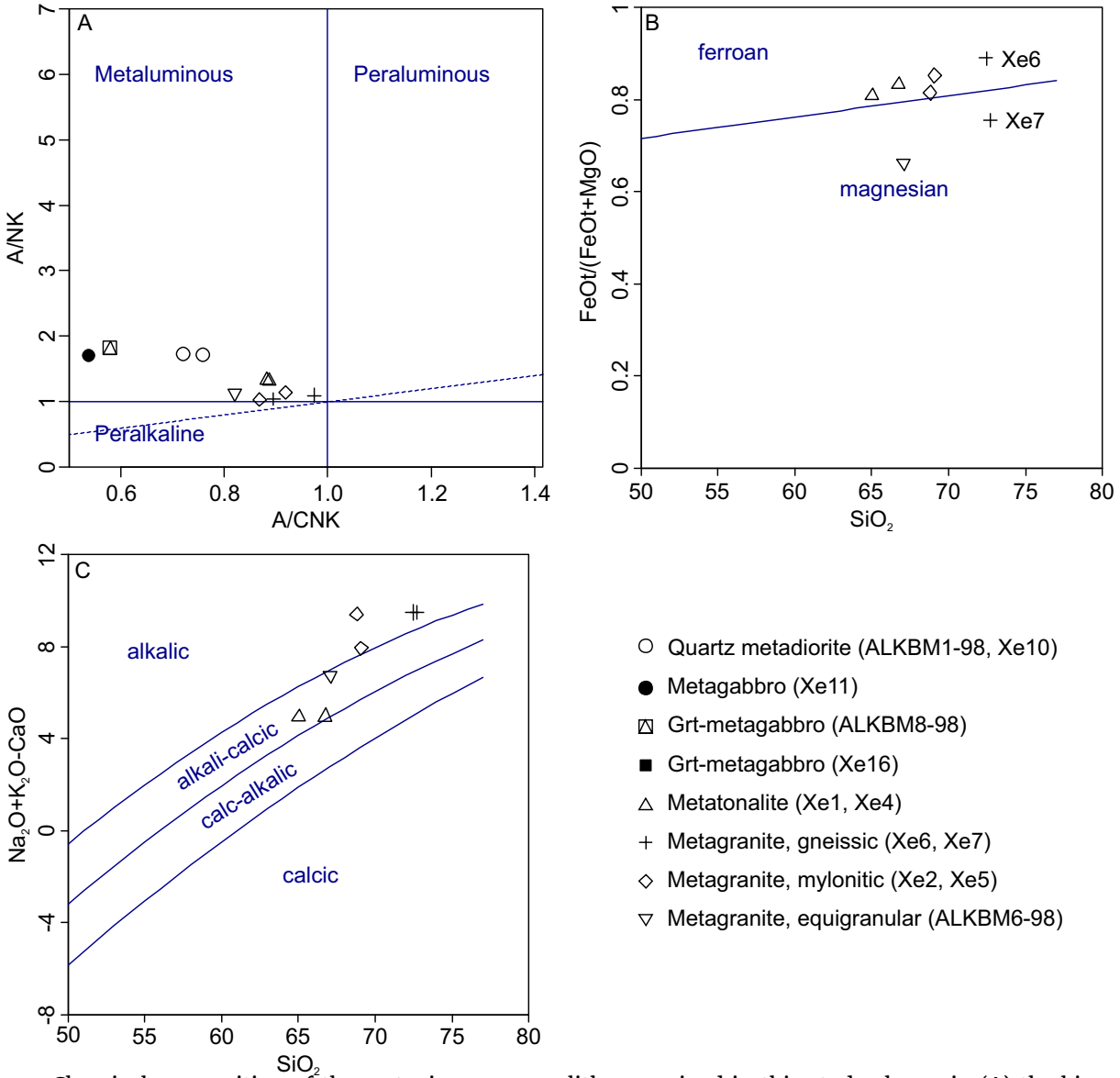

Fig. 15. Chemical composition of the meta-igneous xenoliths examined in this study shown in (A) the binary alumina saturation diagram A/CNK vs. A/NK (cf. Shand 1943), (B) the SiO_2 vs. Fe-number diagram of Frost (2001) (metagranitoids), (C) the SiO_2 vs. Na_2O+K_2O-CaO (modified alkali-lime index) alkalinity diagram of Frost (2001) (metagranitoids). Abbreviations: A/NK= molar $[(Al_2O_3/Na_2O) + K_2O]$; A/CNK = molar $[Al_2O_3/(CaO+Na_2O+K_2O)]$. Symbols as in Figure 14.

the common high-grade, weathering-resistant minerals garnet and rutile, present in several samples, are major sinks for Nb and Y, and zircon for Zr. Possible modification and re-distribution of these minerals may have fractionated the tectonic discrimination results of the metagabbro and quartz metadiorite xenoliths.

In terms of molar Al/Na+K (A/NK) vs. Al/Ca+Na+K (A/CNK), discriminating metaluminous, peraluminous and peralkaline compositions, the metaigneous samples are metaluminous character (Fig. 15A). This is consistent with the modal mineralogy of the metaigneous samples, which is free of muscovite, cordierite, and Al_2SiO_5-minerals. Garnet is mostly present only in minor amounts (0–1.2 vol% in metagranitoids). In metagabbros, the modal amount of garnet may exceed 20 vol%, but the mode calculation is obscured by voluminous kelyphite formation, as kelyphite was included into the garnet (Table 2). The metagranitoids are ferroan, except gneissic metagranite Xe7 and equigranular metagranite ALKBM6-98, which are magnesian (Fig. 15B). The metatonalites and equigranular metagranite are alkali-calcic and the gneissic and mylonitic metagranites alkalic (Fig. 15C).

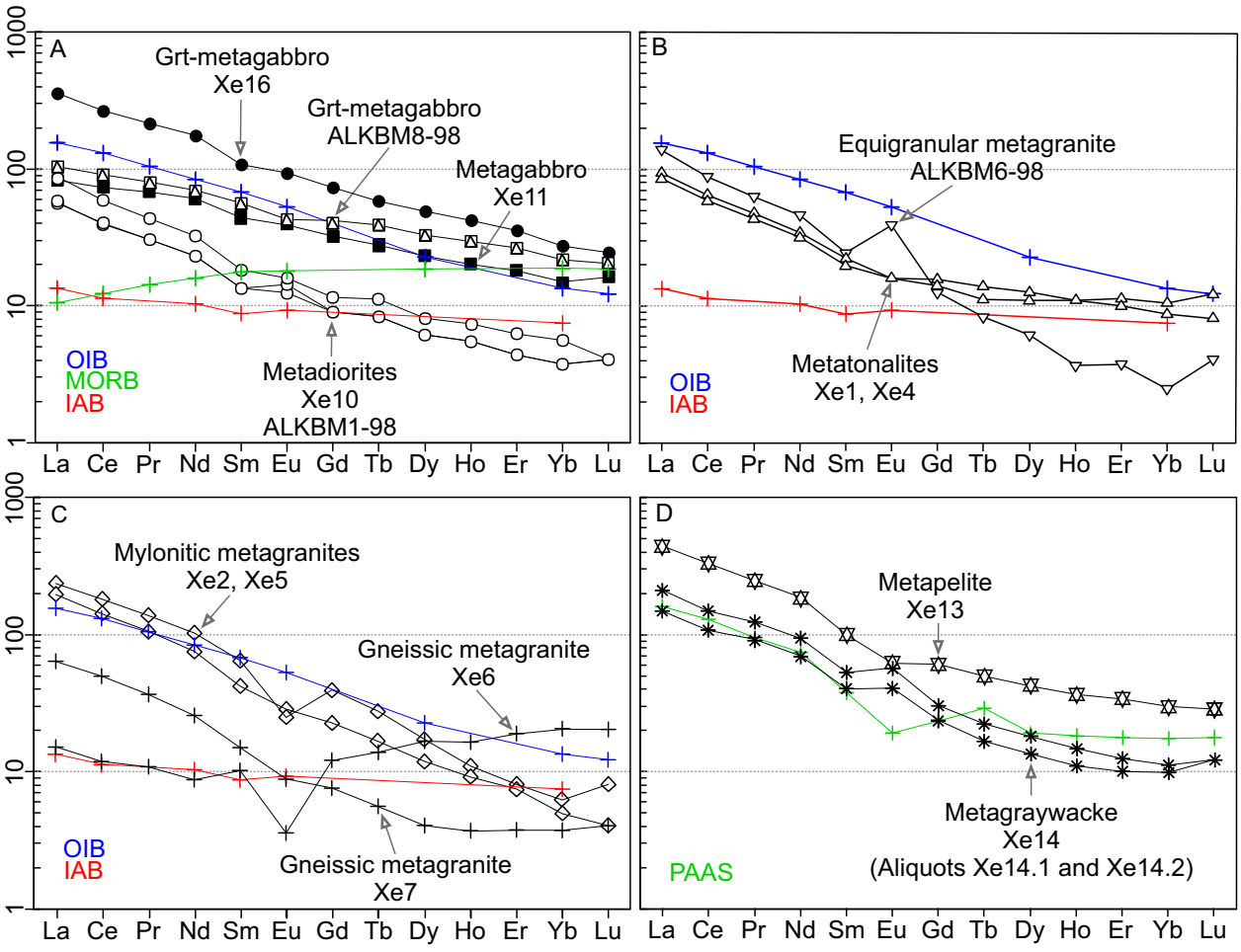

Fig. 16. Rare earth element (REE) composition of the meta-igneous and metasedimentary xenoliths examined in this study normalised to the CI chondritic reservoir of McDonough and Sun (1995). (A) Metagabbroic and -dioritic xenoliths and reference values of N-MORB, OIB and IAB. (B) Metatonalites and equigranular metagranite xenoliths and reference values of OIB and IAB. (C) Gneissic and mylonitic metagranite xenoliths and reference values of OIB and IAB. (D) Metasedimentary xenoliths and reference value of PAAS. Abbreviations and references: N-MORB, normal mid-ocean ridge basalt (Sun & McDonough 1989); OIB, ocean island basalt (Sun & McDonough 1989); IAB, island arc basalt, Central Aleutians (Nye & Reid 1986); PAAS, Post-Archean Australian Shale (McLennan 1989).

8.3 Metagabbros and metadiorites

The major element composition of metadiorites corresponds to the field of diorites on the TAS classification diagram (Fig. 14A). In contrast, Cox et al. (1979) defined no plutonic rock type name for the analysed metagabbro compositions (Fig. 14A). The metagabbros and -diorites, however, show affinity to quartz deficient gabbros and diorites in the multielement binary diagram of De La Roche et al. (1980) (Fig. 14B). The incompatible trace element concentrations are broadly similar, with basaltic affinity (Figs. 14C & D). Relatively low concentrations of MgO (ca. 3–8 wt%), Ni (25–58 ppm) and Cr (29–122 ppm), and low Mg numbers [molar $Mg/(Mg+0.85Fe_t)$] (0.40–0.62) (Table 5, Figs. 12 & 13) are different from primary, unfractionated basalts and suggest that the samples do not represent primary magmas. Petrography and mineralogy dominated by reacted mineral phases such as vermicular, symplectic clinopyroxene, garnet surrounded by kelyphitic rims, and the constantly low anorthite content (An) of untwinned plagioclase are indicative of metamorphism and secondary processes. Accordingly, the presented figures based on geochemical composition are descriptive and interpretations are indicative of the origins of the xenoliths.

8.3.1 Metagabbros

The metagabbro samples display low, relatively unvarying SiO_2 (41.6–43.1 wt%) and high K_2O (2.5–3.7 wt%), with alkaline affinity (Figs. 14A & B). Sample Xe11 shows the highest Mg number of 0.62 (Fig. 12I). The abundance of plagioclase is indicated by higher Al_2O_3 and CaO relative to samples ALKBM8-98 and Xe16 (Figs. 12B & E). These samples, however, have lower Mg numbers (0.40 and 0.45, respectively). The garnet-bearing gabbro Xe16 has a distinctively high P_2O_5 content of 0.9 wt% (Fig. 12H), which shows in the exceptionally abundant apatite in this sample (ca. 4 vol.%). The concentrations of K_2O (2.5–3.7 wt%), Ba (863–1731 ppm), Sr (723–1288 ppm) and Nb (17–21 ppm) (Table 5) are high relative to average primitive mid-ocean ridge basalt, average oceanic arc basalt and average continental arc basalt compositions, considered as representative of unaltered volcanic rocks (Kelemen et al. 2004). The Zr/Ti (0.01) and Nb/Y (0.37–0.63) values are low, pointing to basaltic affinity (Fig. 14C). The discrimination diagram 2Nb, Zr/4, Y (Fig. 14D) refers to field B, a composition with affinity to the mid-ocean ridge basalt type having a plume signature, defined using samples of Icelandic mid-ocean ridge basalts by Meschede (1986). The rare earth elements (REE) exhibit smooth chondrite-normalised patterns (Fig. 16A). Concentrations of REE are variable but consistently high with, for example, chondrite-normalised La_N varying from 83 up to 356. The light REE are enriched relative to heavy REE, with $(La/Yb)_N$ ranging from 5 to 13.

8.3.2 Quartz metadiorites

The quartz metadiorite samples are metaluminous [Al/(Na+K) >1; Al/(Ca+Na+K) <1)] (Fig. 15A) intermediate rocks and equivalent to diorites in geochemical composition (Cox et al. 1979, La Roche et al. 1980, Pitcher et al. 1985) (Figs. 14A & B). The Mg numbers are relatively high (0.61–0.62) and reflect the presence of magnesian augite and a low abundance of opaque minerals in these samples (Fig. 12I). The concentrations of Cr (110–119 ppm), Sr (596–610 ppm) and Nb (17–21 ppm) (Table 5) are high relative to dioritic and monzodioritic plutonic arc rocks of the Coastal batholith, Peru (Agar & Le Bel 1985). The Zr/Ti (0.028) and Nb/Y (1.03–1.15) values are intermediate and point to alkali basaltic to trachyandesitic affinity (Fig. 14C). The within-plate basaltic composition for quartz metadiorites is indicated by the ternary discrimination diagram 2Nb, Zr/4, Y of Meschede (1986) (Fig. 14D). The chondrite-normalised REE patterns are uniform and smooth (Fig. 16A). The light REE are enriched relative to heavy REE, with $(La/Yb)_N$ ranging from 15 to 16. There is a slight positive Eu anomaly with an Eu/Eu* value of ca. 1.2.

8.4 Metagranitoids

The metagranitoids include metatonalites as well as mylonitic, gneissic and equigranular metagranite samples. They show silicic (65–73 wt% SiO_2), metaluminous [Al/(Na+K) >1; Al/(Ca+Na+K) <1)] compositions (Figs. 12 & 15A) and geochemically correspond to granodiorites, granites and quartz monzonites (Cox et al. 1979, De La Roche 1980) (Figs. 14A & B). In the classification of Frost et al. (2001), they are ferroan to mildly magnesian [$FeO_t/(FeO_t+MgO)$ = 0.66–0.88], their magnesium number ranges from 0.23 to 0.53, and (Na_2O + K_2O – CaO) vs SiO_2 from alkali-calcic to alkalic (Figs. 15B & C). The metagranitoids display high Rb concentrations relative to the other studied samples, and accordingly it is unlikely that the Rb content would have been significantly increased by lamproite-host-derived fluid (Fig. 13D). The discrimination diagrams based on Y vs. Nb and Yb vs. Ta (Figs. 14E & F) suggests a volcanic arc-type composition for the metagranitoids.

8.4.1 Metatonalites

The geochemical rock type classification of the metatonalites indicates a granodioritic whole-rock composition (Figs. 14A & B). The difference in the results between QAPF classification (Streckeisen 1974, Le Maitre 1989) based on modal mineralogy (Fig. 7) and whole-rock geochemical classifications (Figs. 14A & B) stems from the abundant fibrous potassium feldspar of the grain boundaries being excluded from the mineralogical classification used to decipher the protolith rock type (Table 2). The metatonalites show mildly potassic compositions (K_2O/Na_2O ca. 1.1) and a medium ferroan character indicated by [$FeO_t/(FeO_t+MgO$] (0.81–0.83), and magnesium numbers from 0.29 to 0.33 (Fig. 15B). The modified alkali-lime index ((Na_2O + K_2O – CaO) vs SiO_2) (Frost et al. 2001) for the metatonalites indicates alkali-calcic compositions (Fig. 15C). The metatonalites can be distinguished from the other metagranitoids by their lower SiO_2 (65–67 wt%) (Table 5). The chondrite-normalised REE patterns of two samples are uniform and smooth (Fig. 16B). The light REE are enriched relative to the heavy REE with $(La/Yb)_N$ of 9 to 10. The light REE are more fractionated ($(La/Sm)_N$ = 4) relative to the heavy REE ($(Gd/Yb)_N$ = 1.5).

8.4.2 Mylonitic and gneissic metagranites

The geochemical rock type classification of the mylonitic and gneissic metagranites indicates an alkaline granitic whole-rock composition (Figs. 14A & B). They are strongly potassic (K_2O/Na_2O > 3), relatively high in SiO_2 (69–73 wt%) and notably low in FeO_t (0.16–1.8 wt%) and MgO (<0.4 wt%) (Table 5). Based on the modified alkali-lime index (Na_2O + K_2O – CaO vs SiO_2) (Frost et al. 2001), the mylonitic and gneissic alkali-feldspar granites are alkalic. All samples, except gneissic metagranite Xe7, are ferroan with [$FeO_t/(FeO_t+MgO)$ = 0.82–0.88] and a magnesium number of 0.23–0.32 (Figs. 15B & C). Sample Xe7 is distinguishable from other mylonitic and gneissic metagranites by its high K_2O/Na_2O (13.2) and relatively high magnesium number (0.40). The concentrations of REE are mainly high with chondrite-normalised La_N varying from 64 to 237. The chondrite-normalised REE patterns of the gneissic metagranite Xe6 and mylonitic metagranite Xe5 are smooth (Figs. 16C & D). The light REE of the mylonitic metagranites are enriched relative to the heavy REE with $(La/Yb)_N$ of 37 to 39, and the gneissic metagranite Xe6 with $(La/Yb)_N$ of 18. Samples Xe7 (gneissic) and Xe2 (mylonitic) show negative Eu anomalies with Eu/Eu* values of ca. 0.3 and 0.8, respectively. Sample Xe7 displays a distinctive flat chondrite-normalised REE pattern (Fig. 16C), which is enriched in heavy REE and depleted in light REE, having a $(La/Yb)_N$ value of 0.7.

8.4.3 Equigranular metagranite

The equigranular metagranite is alkaline granitic and quartz monzonitic based on its whole-rock geochemical composition (Cox et al. 1979, De La Roche 1980, respectively) (Figs. 14A & B). In terms of alkalinity, it is more sodic (K_2O/Na_2O ca. 0.8) than the other metagranitoids. According to the modified alkali-lime index (Na_2O + K_2O – CaO vs SiO_2) (Frost et al. 2001), it is alkali-calcic (Fig. 15B). It also shows the highest MgO (0.97 wt%), a magnesium number of 0.52 and a magnesian [$FeO_t/(FeO_t+MgO)$ = 0.66] character (Fig. 15C). These features are consistent with the modal mineralogy of anorthoclase, quartz and diopsidic clinopyroxene. The difference in the results

between QAPF classification (Streckeisen 1974, Le Maitre 1989) based on modal mineralogy (Fig. 7) and whole-rock geochemical classification after De La Roche (1980) (Fig. 14B) stems from the presence of anorthoclase (sodium-bearing potassium feldspar, in this case with albite exsolution texture), which was only observable by electron microscopy. Modal mineral abundances were defined under a transmitted-light polarization microscope and the Na-bearing anorthoclase was counted as Na-free potassium feldspar. Overall, the major element composition is similar to A-type granites (Whalen et al. 1987), although the trace elements show extreme enrichment in Ba (2771 ppm) and Sr (2001 ppm), together with relatively low concentrations of Rb (27 ppm) and Zr (41 ppm), which is not typical of A-type granites (Table 5, Figs. 12 & 13). The chondrite-normalised pattern of REE shows a positive Eu anomaly (Eu/Eu* = 2.3) (Fig. 16B). The concentration of REE is high, with La_N = 138. The light REE are enriched relative to heavy REE, with a $(La/Yb)_N$ value of 58.

8.5 Geochemical classification of the metasedimentary xenoliths

Two of the four metasedimentary samples were analysed for major and trace elements (Table 5). The K_2O content of the analysed samples is higher (>6 wt%) than that of the host lamproite, and it has probably not been significantly increased due to host-derived fluids (Fig. 12). The samples show low Na_2O/K_2O values (0.08–0.15). However, the SiO_2, Na_2O and K_2O contents, used for the discrimination of arkoses, arenites and wackes (e.g. Herron 1988), may have changed due to metamorphic and metasomatic modifications. Geochemical classification schemes, in which high Al_2O_3 relative to SiO_2 indicates a more immature and less weathered composition akin to wackes and lithic arenites, were applied (cf. Pettijohn et al. 1972, Herron 1988). These classifications are commonly used for sandstones and shales.

8.5.1 Metapelite

The high-grade, migmatised sample Xe13 displays high SiO_2 (60 wt%) and low TiO_2 (1 wt%), MgO (1 wt%), CaO (3.7 wt%) and Na_2O (0.8 wt%) (Table 5, Figs. 12B, D, E & F). The sample is characterized by high Cr, Zr and Y contents relative to the other xenolith samples, and the Y content is higher than that of the host lamproite (Figs. 13D, H & I). The loss-on-ignition value (3.5 wt%) and concentrations of Ba (1092 ppm) and Sr (819 ppm) are relatively high (Figs. 13E & G), probably due to the presence of potassium feldspar and secondary carbonate. According to the geochemical classification for sandstones and shales, the sample shows affinities to arkoses [$\log(SiO_2/Al_2O_3)$ 0.7 and $\log(Na_2O/K_2O)$ -0.8] (Pettijohn et al. 1972) and wackes [$\log(Fe_2O_3/K_2O)$ 0.09] (Herron 1988). In terms of SiO_2 and $\log K_2O/Na_2O$ (1.1), the sample shows affinity to sandstones and mudstones in an island-arc environment (Roser & Korsch 1986). The chondrite-normalised REE pattern is smooth (Fig. 16D). The concentration of REE is high with, for example, chondrite-normalised La_N = 440, which may reflect the small degree of melting of the sedimentary protolith. The light REE are enriched relative to heavy REE with $(La/Yb)_N$ = 15. However, the geochemical composition is dominated by leucosome of quartz and potassium feldspar and, accordingly, at least the Al_2O_3 and K_2O of the xenolith have been modified from a protolith sediment composition. Thus, the interpretation is nebulous and only suggestive of the geo-environment of genesis.

8.5.2 Metagreywacke

The greywacke sample Xe14 is heterogeneous. It included fragments of sandstone (not included in whole-rock analysis) and regularly distributed, irregularly shaped patches of graphitic material. Microscopic fragments interpreted as volcanic material were also observed. The heterogeneity is also visible in the geochemistry of the two aliquots Xe14.1 and Xe14.2 of the sample. The loss-on-ignition values observed are between 1.9 and 2.6 wt%. In the major and trace element compositions (Fig. 12), the variation is slight. The SiO_2 content is relatively high (63.5 and 66.6 wt%). Concentrations of Al_2O_3 (13–14 wt%) and K_2O (ca. 10 wt%) imply the presence of feldspars and the immature nature of the

sample relative to quartz arenites, for example. High Ba (1296–1632 ppm) may reflect the composition of the sedimentary protolith, possibly lost Ba-rich minerals precipitated from seawater into the sediment, or may relate to modification by the host lamproite. The major element composition of the samples show greater affinity to the acid xenoliths than the basic ones. Notably, Ni and Cr contents are similar to the quartz metadiorite samples. The $\log(SiO_2/Al_2O_3)$ value (0.66–0.70) indicates a relatively immature character. According to the classifications of Pettijohn et al. (1972) and Herron (1988), the samples show a geochemical affinity to arenites [log Na_2O/K_2O (-1.1) and log Fe_2O_3/K_2O (0.4)] rather than litharenites or subarkoses. In terms of SiO_2 and [log (K_2O/Na_2O) (1.06)], the sample shows affinity to sandstones and mudstones in an island-arc environment (Roser & Korsch 1986). The chondrite-normalised pattern for the REE indicates a small positive Eu anomaly (Eu/Eu* = 1.35) (Fig. 16D). The concentration of REE is high with, for example, chondrite-normalised La_N = 149–211. The light REE are enriched relative to heavy REE, with $(La/Yb)_N$ values of 15–18. These parameters are indicative of felsic upper crustal source material, and the heavy REE pattern shows slight affinity towards the shale reference value of Australian Post-Archean shales (PAAS; McLennan 1989) (Fig. 16D).

8.6 Data evaluation and interpretation

8.6.1 Geochemical modification of the studied xenoliths

The geochemical properties of the trace elements vary and depend on the geochemical environment. It is challenging if not impossible to precisely determine the prevailed geochemical environment, especially for ancient rock samples. The interpretations in this study are predominantly based on the geochemical behaviour of the elements under intermediate to high metamorphic and magmatic conditions. Secondary processes are more likely to take place in environments where hydrothermal activity is high, and rocks may have been affected by multiple processes through their lifespan.

Xenolith samples are often mineralogically or chemically modified during magmatic transport and associated uplift from their provenance. Consequently, it is likely that especially the K, Ba and Sr values of the lamproite-hosted xenoliths studied here were modified during transport and the crystallization of the host (cf. Rudnick 1992). Fenitization, i.e. metasomatism caused by alkaline elements, is a widely observed phenomenon related to alkaline rock intrusions. The rocks of the surroundings, e.g. felsic basement gneisses, intruded by plutons or dykes of alkaline rock types, may show increased alkali-element concentrations and metasomatic mineralization of alkali-bearing minerals such as alkaline pyroxenes and amphiboles. The alkaline fluids may also propagate further through fractures and faults within the bedrock. These types of later modification may interfere with the protolith compositions of the studied xenoliths.

No significant secondary low-grade or hydrothermal mineral assemblages were observed within the studied xenoliths. Accordingly, there was no mineralogical evidence of significant low-grade hydrothermal overprinting of any of the samples. The protoliths of the xenoliths metamorphosed prior to transport, and especially metasomatism by mantle-derived melts with a low degree of melting and alkaline fluids may have occurred, as the bedrock of Vestfjella has experienced at least one period of tension and rifting, namely the Jurassic. Early stages of rifting are often associated with alkaline basaltic magmatism, and related fluids may have affected the protoliths of the xenoliths. Potassium is a fluid-mobile large ion lithophile element, and it is predicted that it was a significant constituent of lamproite-derived fluids (Table 5, Fig. 13). On the basis of the potassium content of the gneissic and mylonitic metagranites (K_2O higher than ca. 6 wt% of the host lamproite sample ALKB1-25-03), it is unlikely that the host-derived fluids would have increased their K_2O concentrations. The metagabbros, metadiorites, metatonalites and equigranular metagranite instead are lower in K_2O relative to the host, and may accordingly have been more prone to K-metasomatic modification. The concentration of potassium

in fluid, however, may have been different from that indicated by the lamproite whole-rock K_2O concentration.

8.6.2 The geochemical rock type classifications

Differences between the results from QAPF classification (Streckeisen 1974, Le Maitre 1989) based on modal mineralogy (Fig. 7) and whole-rock geochemical classifications (Figs. 14A & B) were observed for metatonalite and equigranular metagranite samples. For the metatonalites, geochemical classification resulted in a granodioritic composition. This observation stems from the amount of fibrous potassium feldspar of the grain boundaries being determined by point counting. It was excluded from the mineralogical classification used to decipher the protolith rock type due to possibly secondary origin (Table 2). The equigranular metagranite resulted in a quartz monzonitic composition (Fig. 14B). This observation is due to the presence of anorthoclase (sodium-bearing potassium feldspar, in this case with albite exsolution texture), which was only observable by electron microscopy. Modal mineral abundances were defined under a transmitted-light polarization microscope and the Na-bearing anorthoclase was counted as Na-free potassium feldspar. The observed whole-rock major and trace element concentrations may also have been modified by magmatic fractionation or metamorphic redistribution of the major plagioclase, potassium feldspar, clinopyroxene and hornblende. Generalizing, mineral mode-based classifications for samples with metasomatic or other subtle secondary mineralogical and geochemical modifications may be more useful in protolith rock-type determination than solely geochemical classifications.

8.6.3 The use of tectonic discrimination diagrams based on incompatible trace elements

Primarily, magmatic processes have affected the geochemical composition, and the different tectonic settings displaying characteristic geochemical features are presented in tectonic discriminant diagrams. In this study, elements that were least susceptible to metamorphism and element mobility, active in processes such as burial, magmatism and subduction, were used. Nb, Ta, Y and Zr are highly incompatible in mantle melting and the crystal fractionation of basic to silicic magmas, but rather immobile in subduction (e.g. Pearce 1996), and accordingly, fingerprints of these elements may have preserved in evolved and hydrothermally altered rocks. Heavy rare earth elements (such as Yb), Sc, V and Y are only compatible with garnet and zircon in basaltic and andesitic rocks (cf. Kelemen et al. 2004). Ti instead behaves compatibly during fractional crystallization of intermediate-silicic magma (Pearce 1996). While using trace element data, the increase in systematic analytical error related to extremely low concentrations of trace elements, and possible contamination during sample processing, needs to be remembered and overinterpretation of the geochemical data avoided.

The trace element contents of the xenoliths were plotted against K_2O to estimate the possible host-derived contamination, as tectonic discrimination diagrams based on Zr, Nb, Y, Yb and Ta concentrations were used (Fig. 14). The critical elements on the basis of composition of the host were potassium, nickel, chromium, barium, strontium, zirconium, niobium, lanthanum, neodymium and tantalum for all samples (Fig. 13). Rubidium was not considered as a possible contaminant for the metagranitoid and metagreywacke Xe14 samples (Fig. 13D) nor yttrium for garnet-bearing metagabbro Xe16 and metapelite Xe13 samples (Fig. 13G). Ytterbium concentrations of the metagabbros, metapelite and gneissic metagranite sample Xe7 were also higher in the xenolith than in the host (Fig. 13K). Accordingly, it is unlikely that the above-mentioned trace element concentrations of the respective samples would have been modified by lamproite-derived fluids. The exact composition of the fluid is, however, unknown, although the lamproite whole-rock composition provides an approximation that was used in this study.

The elements Zr, Nb, Y, Yb and Ta are principally set in the minerals zircon, rutile and garnet in magmatic and metamorphic rocks. These minerals are highly resistant to weathering and considered as inert in most natural environments. Therefore, the host-derived, K-H_2O-CO_2 fluids were unlikely to have affected the concentrations of these elements in the studied xenoliths. However, mineral fractionation

or metamorphic redistribution of zircon, rutile and garnet may have affected the observed concentrations of Zr, Nb, Y, Yb and Ta. These possible modifications are relevant for this study dealing with high-grade metamorphosed samples. Accordingly, the tectonic discrimination results of the metagabbros and quartz metadiorites may have been fractionated on the basis of their petrography. The characteristics of the metagranitoid samples may also have been affected by rutile distribution, if rutile had been fractionated at some point during evolution and retained the elements Nb, Ta and Y (Figs. 14E & F). In addition, the concentrations of Nb, Yb and Ta are generally low (Figs. 13H, K & L). Although Yb and Ta were determined by ICP-MS analysis, possible modification by host-derived fluids or contamination during sample preparation may increase the error.

8.6.4 REE geochemistry of the studied xenoliths

The RE elements La, Ce, Pr, Nd, Pm, Sm, Eu, Gd, Tb, Dy, Ho, Er, Tm, Yb and Lu are useful in petrogenetic studies, as they are geochemically similar to each other (cf. Wilson 1989). They are trivalent under most geological conditions, except Eu and Ce. Eu shows two oxidization stages, 2+ and 3+, and Ce 3+ and 4+, depending on the oxygen fugacity and oxidization conditions (cf. Wilson 1989). To avoid problems caused by paired and unpaired elemental numbers (cf. Wilson 1989) and to diminish the effect of the different analytical setups and calibrations (cf. Rollinson 1993), REE concentrations are usually normalized relative to some established standard concentrations. Here, I used CI chondrite after McDonough and Sun (1995), commonly used for evolved and Precambrian rocks, to depict the different REE patterns of the samples. The chondrite-normalized REE diagrams show that the metagabbros, samples ALKBM8-98 and Xe11, are alike, and metagabbro sample Xe16 also shows light REE enrichment and heavy REE depletion with weak affinity towards the REE patterns of island-arc basalts (IAB) and ocean island basalts (OIB) rather than mid-ocean ridge basalts (MORB) (Nye & Reid 1986, Sun & McDonough 1989) (Fig. 16A). The quartz metadiorite samples ALKBM1-98 and Xe10 somewhat resemble the metatonalite samples Xe1 and Xe4 (Figs. 16A & B). Their enriched light REE and depleted heavy REE patterns show similarities to IAB and island arc basaltic andesite (Nye & Reid 1986, Bacon et al. 1997), but are different from tholeitic IAB (Nye & Reid 1986). The metagranites show distinctive patterns (Chapter 8.2), with light REE enrichment and heavy REE depletion, except for the gneissic metagranite sample Xe7 (Fig. 16 C). The metasedimentary samples (Fig. 16D) show general affinity to upper crustal compositions, e.g. Post-Archean Australian Shale (PAAS) (McLennan 1989). It needs to be emphasized that the basalt compositions used as a reference in Figures 16A–C represent primary magmas and, as a result, the fractionated and metamorphosed character of the studied samples is pronounced.

The REE patterns of the metagabbroids may indicate a lower degree of partial melting of the metagabbros Xe16 and ALKBM8-98 relative to the metagabbro Xe11, if possible post-protolith crystallization enrichment by lithospheric fluids is excluded. Also, Arculus and Ruff (1990) noted that most studies on granulite and eclogite xenoliths by the 1990s had reported variable contamination of the studied xenolith compositions by pre-existing crust enriched in incompatible elements. As the studied xenoliths represent high-grade, granulitic rock types and the mylonitic granites and metapelite has been intensively deformed, these modifications from the protolith compositions also need to be assessed. Pan and Fleet (1996) reported REE enrichment within mafic gneisses during their prograde granulite facies metamorphism, and precipitation of fluorapatite and other REE-rich minerals such as allanite, monazite and zircon in peak metamorphic conditions. Their study indicates that in orthopyroxene and clinopyroxene-rich mafic gneisses, REE were enriched in granulite facies metamorphism. This REE enrichment was accompanied by mobile fluorine-bearing fluid. The petrography of the apatite of metagabbros indicates that the inclusion-rich apatite may have precipitated at a late stage. Rolland et al. (2003) reported that changes in REE concentrations of the granites deformed in shear zones are ascribed to the alteration of pre-existing magmatic REE-bearing minerals and the syntectonic precipitation of these minerals, including monazite, bastnäsite, aeschynite and tombarthite.

Minor proportions (<2%) of these minerals, commonly of <20 µm in diameter, may even result 5-fold enrichment of the REE relative to the initial granite whole-rock composition. This type of enrichment is not related to the deformation style of the rock, but to the fluid characteristics and precipitation of the REE minerals (Rolland et al. 2003). Also, REE mobility in an specific hydrothermal environment appears to be case sensitive and the behaviour is still poorly understood (Rolland et al. 2003 and references therein).

9 U-PB, RB-SR AND SM-ND ISOTOPE GEOLOGY

Of the 27 xenolith samples examined, eight representative silicic and mafic ones were selected for U-Pb zircon dating and Rb-Sr and Sm-Nd isotope study to gain information on the chronology and origin of the xenoliths. Zircon was recovered from six representative silicic metaigneous xenoliths (Xe1, Xe2, Xe4, Xe6, ALKBM1 and ALKBM6). These xenoliths were selected on the basis of their size, Zr concentration, positive observation of zircon in thin section, and the common experience that zircon is more often recoverable from silicic rock types than mafic ones. The results of the isotope analysis are presented in Tables 6, 7 and 8. Samples Xe1 and Xe4 (Figs. 7I & L) were analysed using SHRIMP II in Canberra and the data were provided by Mr Joachim Jacobs (written communication Mr Joachim Jacobs). The rest of the samples were analysed at the SIMS laboratory in Stockholm by Ms Ilona Romu and Mr Matti Kurhila. The six silicic samples were omitted from Rb-Sr and Sm-Nd analysis because of their evolved nature and possible host lamproite-derived contamination. Two representative ultramafic-mafic xenolith samples (Xe11, Xe16) were analysed for mineral and whole-rock Rb-Sr and Sm-Nd at the Geological Survey of Finland, Espoo, by Ms Ilona Romu. No zircon, allanite, titanite, rutile or monazite of sufficient size was observed in thin section and the overall size of the mafic samples was small relative to the silicic samples. Whole-rock, plagioclase, apatite and clinopyroxene fractions of two metagabbroids (Xe11, Xe16) were analysed for their Sm-Nd and Rb-Sr isotopic compositions to obtain information on their ages and the nature of their source materials (Table 8).

Table 6. SHRIMP U–Pb results.

Sample/ spot #	Description[a]	Derived ages (Ma)						Corrected ratios						ρ [b]	Disc. [c]	Elemental data			Th/U	$^{206}Pb/^{204}Pb$
		$^{207}Pb/^{206}Pb$	±1σ	$^{207}Pb/^{235}U$	±1σ	$^{206}Pb/^{238}U$	±1σ	$^{207}Pb/^{206}Pb$	±1σ (%)	$^{207}Pb/^{235}U$	±1σ (%)	$^{206}Pb/^{238}U$	±1σ (%)		(%)	[U] (ppm)	[Th] (ppm)	[Pb] (ppm)	(meas.)	(meas.)
KBM1																				
n3302-01a	st., rnd, CL white rim	473	109	620	25	661	11	0.057	5.10	0.841	5.40	0.108	1.75	0.33	1.4	38	14	5	0.377	2.07E+3
n3302-01b	st., CL dark (BSE light) core	731	23	621	8	591	7	0.064	1.07	0.844	1.65	0.096	1.26	0.76	0.1	303	52	32	0.173	1.70E+4
n3302-02a	st., euh. osc z core	720	37	676	12	662	11	0.063	1.76	0.945	2.45	0.108	1.69	0.69	conc.	150	59	19	0.392	6.95E+3
n3302-02b	st., euh., CL white rim	no data	no data	no data	no data	104	19	no data	no data	no data	no data	0.016	18.32	no data	no data	25	15	[0]	0.602	2.26E+1
n3302-03a	euh., el., osc z bright (core?)	373	107	384	16	386	5	0.054	4.91	0.460	5.06	0.062	1.26	0.25	conc.	64	23	5	0.362	3.20E+3
n3302-03b	euh., el. osc z. (rim?)	719	52	722	15	723	10	0.063	2.51	1.036	2.88	0.119	1.42	0.49	conc.	81	23	11	0.282	4.18E+3
n3302-04a	st., anh., CL dark core	838	20	669	10	620	11	0.067	0.96	0.933	2.06	0.101	1.82	0.88	-25.0	646	117	73	0.180	4.11E+4
n3302-05a	st., anh., CL white area	766	57	673	15	645	8	0.065	2.73	0.940	3.03	0.105	1.31	0.43	0.2	70	21	8	0.305	6.28E+3
n3302-06a	st., euh., CL dark core	1221	44	1322	22	1385	22	0.081	2.27	2.677	2.88	0.240	1.77	0.62	2.4	84	23	23	0.271	3.00E+4
n3302-06b	st., euh., osc z rim	753	95	528	21	478	9	0.064	4.62	0.682	5.03	0.077	1.99	0.40	conc.	25	14	2	0.585	n/a
n3302-07a	st., euh., osc z	1230	71	1333	33	1399	29	0.081	3.72	2.718	4.37	0.242	2.29	0.52	1.6	68	12	19	0.179	1.74E+4
n3302-08a	rnd, CL bright zone	658	137	402	25	359	11	0.062	6.66	0.486	7.32	0.057	3.05	0.42	1.6	48	16	3	0.327	2.17E+3
n3302-09a	anh., splinter, CL bright.	432	216	1010	71	1297	33	0.055	10.40	1.705	10.77	0.223	2.77	0.26	conc.	4	1	1	0.234	1.74E+3
n3302-10a	rnd, CL dark (core?)	879	31	835	21	818	25	0.068	1.51	1.276	3.58	0.135	3.25	0.91	3.8	229	132	38	0.580	2.50E+4
n3302-10b	rnd, CL bright (rim?)	667	153	806	43	857	11	0.062	7.52	1.212	7.64	0.142	1.36	0.18	2.1	7	11	1	1.463	3.17E+3
n3302-11a	euh., CL brigth tip (rim?)	418	299	323	42	310	6	0.055	14.70	0.375	14.83	0.049	2.00	0.14	conc.	15	10	1	0.686	9.54E+2
n3302-12a	rnd, splinter, CL bright	699	88	742	27	756	20	0.063	4.24	1.077	5.06	0.124	2.76	0.55	-6.1	27	10	4	0.374	4.98E+3
n3302-13a	st., euh., osc z	840	32	863	12	872	12	0.067	1.56	1.340	2.13	0.145	1.45	0.68	conc.	77	25	13	0.329	6.75E+4
n3302-14a	euh., osc z. dark	940	64	547	20	457	15	0.070	3.20	0.714	4.69	0.074	3.42	0.73	conc.	85	13	7	0.159	7.26E+3
n3302-15a	euh., CL bright core	1359	178	1188	76	1096	38	0.087	9.77	2.222	10.47	0.185	3.76	0.36	conc.	23	6	5	0.279	2.11E+2
n3305-01a	st., rnd, CL-zoned	746	68	675	19	653	13	0.064	3.31	0.943	3.91	0.107	2.09	0.54	conc.	43	17	5	0.403	1.05E+4
n3305-02a	st., anh., CL pale (core?)	852	69	873	30	882	31	0.067	3.40	1.363	5.10	0.147	3.79	0.74	conc.	32	12	6	0.391	3.34E+3
n3305-03a	st., rnd, rim z in CL	1205	36	1346	19	1436	21	0.080	1.87	2.763	2.48	0.249	1.63	0.66	9.4	48	16	14	0.336	1.22E+4
n3305-04a	euh., osc. z, tip	753	39	581	11	538	9	0.064	1.88	0.773	2.53	0.087	1.68	0.67	-14.1	102	27	10	0.262	7.43E+3
n3305-04b	euh., CL bright core	540	66	526	17	522	13	0.058	3.10	0.678	4.02	0.084	2.56	0.64	conc.	68	16	6	0.237	4.98E+3
n3305-05a	Euh. (etched), CL bright core	912	104	745	30	691	13	0.069	5.24	1.083	5.62	0.113	2.04	0.36	conc.	25	13	3	0.528	4.80E+3
n3305-05b	Euh. (etched), CL dark middle z.	699	98	649	24	635	8	0.063	4.72	0.895	4.92	0.104	1.38	0.28	conc.	19	17	3	0.924	2.79E+3
n3305-06a	euh., osc. Z	646	56	478	14	444	10	0.061	2.66	0.602	3.55	0.071	2.35	0.66	-7.6	68	17	6	0.254	7.16E+3
n3305-07a	st., rnd, CL dark zone	592	100	573	25	569	16	0.060	4.79	0.759	5.57	0.092	2.85	0.51	conc.	16	19	2	1.167	3.45E+3
n3305-09a	rnd, CL bright zone	64	158	216	14	230	5	0.047	6.98	0.237	7.30	0.036	2.14	0.29	conc.	40	7	2	0.176	2.62E+3
n3305-10a	euh., osc. Z	575	44	451	9	427	6	0.059	2.05	0.559	2.55	0.068	1.50	0.59	-5.8	84	30	7	0.361	8.90E+3

Table 6. Cont.

Sample/ spot #	Description[a]	Derived ages (Ma)						Corrected ratios						ρ [b]	Disc. [c]	Elemental data			Th/U	$^{206}Pb/^{204}Pb$
		$^{207}Pb/^{206}Pb$	±1σ	$^{207}Pb/^{235}U$	±1σ	$^{206}Pb/^{238}U$	±1σ	$^{207}Pb/^{206}Pb$	±1σ (%)	$^{207}Pb/^{235}U$	±1σ (%)	$^{206}Pb/^{238}U$	±1σ (%)		(%)	[U] (ppm)	[Th] (ppm)	[Pb] (ppm)	(meas.)	(meas.)
n3305-12a	euh., CL osc z. core	930	71	893	23	878	12	0.070	3.54	1.410	3.83	0.146	1.44	0.38	conc.	17	7	3	0.420	3.56E+3
n3305-12b	euh., CL homog tip	815	93	779	32	767	25	0.066	4.56	1.154	5.72	0.126	3.44	0.60	conc.	70	19	10	0.268	9.35E+3
n3305-13a	st., anh., CL white homog.	803	69	857	21	877	11	0.066	3.38	1.325	3.66	0.146	1.40	0.38	conc.	20	14	4	0.714	5.85E+3
n3305-14a	st., euh., osc z, CL gray	-1034	678	299	75	492	16	0.031	27.70	0.342	27.91	0.079	3.41	0.12	18.8	8	7	1	0.845	5.01E+2
KBM6																				
n3303-1a	clss, rnd, homog.	1044	64	1079	26	i	22	0.074	3.26	1.895	3.90	0.185	2.14	0.55	conc.	42	49	11	1.164	2.57E+4
n3303-02a	brn, euh., st., sect z	103	59	156	4	160	2	0.048	2.56	0.166	2.90	0.025	1.35	0.47	conc.	249	149	8	0.601	1.52E+4
n3303-03a	clss, rnd, osc z	150	71	161	5	162	2	0.049	3.08	0.172	3.36	0.025	1.34	0.40	conc.	236	118	7	0.501	9.82E+3
n3303-03b	clss, rnd, sect z, (homog.)	0	81	157	5	167	2	0.046	3.05	0.168	3.34	0.026	1.35	0.40	conc.	309	239	10	0.773	5.25E+3
n3303-04a	yllw, rnd osc z	84	59	156	4	161	2	0.048	2.55	0.166	2.88	0.025	1.35	0.47	conc.	265	121	8	0.457	8.99E+3
n3303-05a	clss rnd osc z (core?)	-80	80	149	5	164	2	0.045	3.43	0.158	3.68	0.026	1.35	0.37	conc.	225	99	7	0.440	4.69E+3
n3303-05b	clss rnd homog rim	26	94	156	6	165	2	0.047	4.01	0.167	4.26	0.026	1.41	0.33	conc.	133	52	4	0.391	6.42E+3
n3303-06a	yllw, st., euh, homog. Core	-1	76	155	5	165	2	0.046	3.24	0.165	3.53	0.026	1.39	0.39	conc.	220	125	7	0.568	7.95E+3
n3303-06b	yllw, st., euh., sect z rim	136	59	162	4	164	2	0.049	2.54	0.173	2.88	0.026	1.35	0.47	conc.	244	111	7	0.456	8.84E+3
n3303-07a	brn rnd osc z	-27	80	154	5	166	2	0.046	3.36	0.163	3.63	0.026	1.35	0.37	conc.	215	89	7	0.417	6.41E+3
n3303-07b	brn rnd osc z	182	56	169	4	168	2	0.050	2.44	0.181	2.79	0.026	1.35	0.48	conc.	289	195	10	0.674	6.62E+3
n3303-08a	yllw rnd homog.	464	107	468	20	469	7	0.056	5.00	0.585	5.23	0.075	1.53	0.29	conc.	34	13	3	0.391	2.44E+3
n3303-09a	yllw rnd homog. rim	-181	181	142	10	162	2	0.043	7.67	0.150	7.79	0.025	1.38	0.18	conc.	78	32	2	0.405	2.34E+3
n3303-09b	yllw, rnd sect z	87	64	159	5	164	2	0.048	2.74	0.170	3.05	0.026	1.34	0.44	conc.	214	94	7	0.439	8.10E+3
n3303-10a	brn rnd osc z	22	85	158	6	168	2	0.046	3.63	0.169	3.87	0.026	1.35	0.35	conc.	193	80	6	0.413	3.87E+3
n3303-11a	yllw, rnd osc z	-45	84	153	5	166	2	0.045	3.54	0.163	3.78	0.026	1.35	0.36	conc.	183	75	6	0.409	5.23E+3
n3303-12a	clss rnd sect z	-49	49	152	4	166	2	0.045	2.60	0.162	2.93	0.026	1.36	0.46	conc.	225	123	7	0.547	1.46E+4
n3303-13a	yllw, euh, osc z	0	91	157	5	166	2	0.046	3.26	0.167	3.54	0.026	1.38	0.39	conc.	210	95	6	0.453	6.38E+3
n3303-14a	yllw, euh, st. z core	-12	64	153	4	164	2	0.046	2.70	0.163	3.02	0.026	1.35	0.45	conc.	273	145	9	0.529	6.33E+3
n3303-14b	yllw, euh, st., homog. rim	-207	207	141	12	162	2	0.042	8.77	0.148	8.89	0.025	1.47	0.17	conc.	51	21	2	0.422	2.70E+3
n3303-14c	yllw, euh, st., osc z rim	-9	99	156	6	167	2	0.046	4.21	0.166	4.42	0.026	1.36	0.31	conc.	144	62	4	0.426	6.14E+3
n3303-15a	yllw rnd homog (core?)	175	99	164	7	163	2	0.050	4.36	0.175	4.56	0.026	1.36	0.30	conc.	96	34	3	0.354	5.27E+3
n3303-15b	yllw, rnd osc z (rim?)	-126	96	148	6	165	2	0.044	4.01	0.157	4.25	0.026	1.42	0.33	conc.	145	51	4	0.351	4.10E+3
n3303-16a	yllw rnd homog core	24	133	174	10	185	3	0.047	5.79	0.187	6.04	0.029	1.71	0.28	conc.	93	44	3	0.471	2.54E+3
n3303-16b	yllw, rnd osc z rim	59	70	158	5	164	2	0.047	2.99	0.168	3.28	0.026	1.35	0.41	conc.	233	102	7	0.436	6.73E+3
n3303-17a	clss rnd osc z	43	54	155	4	162	2	0.047	2.29	0.164	2.67	0.025	1.38	0.52	conc.	256	121	8	0.474	1.71E+4

Table 6. Cont.

Sample/ spot #	Description[a]	Derived ages (Ma)						Corrected ratios						ρ [b]	Disc. [c]	Elemental data			Th/U	$^{206}Pb/^{204}Pb$
		$^{207}Pb/^{206}Pb$	±1σ	$^{207}Pb/^{235}U$	±1σ	$^{206}Pb/^{238}U$	±1σ	$^{207}Pb/^{206}Pb$	±1σ (%)	$^{207}Pb/^{235}U$	±1σ (%)	$^{206}Pb/^{238}U$	±1σ (%)		(%)	[U] (ppm)	[Th] (ppm)	[Pb] (ppm)	(meas.)	(meas.)
Xe2	**Optical**																			
n3306-01a	bl. st., sect z	752	21	443	6	386	5	0.064	0.98	0.547	1.70	0.062	1.39	0.82	-41.4	2084	314	148	0.151	7.15E+2
n3306-02a	bl. euh, osc z	649	168	365	26	321	5	0.061	8.28	0.432	8.44	0.051	1.62	0.19	conc.	3515	564	201	0.160	4.23E+2
n3306-03a	bl. euh, weak z	983	11	880	9	839	11	0.072	0.55	1.378	1.46	0.139	1.35	0.93	-11.2	1054	312	163	0.296	2.37E+3
n3306-04a	bl. euh, osc z (rim?)	742	37	458	8	403	5	0.064	1.75	0.569	2.24	0.065	1.40	0.62	-31.8	1870	261	134	0.139	4.85E+2
n3306-04b	bl. euh, osc z (core?)	906	21	658	8	588	8	0.069	1.02	0.912	1.69	0.096	1.35	0.80	-29.1	1428	131	150	0.092	1.58E+3
n3306-05a	bl. euh, osc z (rim?)	1006	8	995	9	990	12	0.073	0.39	1.665	1.40	0.166	1.34	0.96	conc.	832	72	152	0.087	1.35E+4
n3306-05b	bl. euh, osc z (core?)	659	164	443	30	403	6	0.062	8.07	0.547	8.21	0.064	1.50	0.18	conc.	1909	143	133	0.075	5.53E+2
n3306-06a	bl. st., homog	710	20	466	6	418	5	0.063	0.93	0.582	1.63	0.067	1.35	0.82	-34.1	2473	340	183	0.138	1.18E+3
n3306-07a	bl. thin euh, osc z	997	27	882	11	836	11	0.072	1.33	1.383	1.89	0.138	1.34	0.71	-8.2	967	145	150	0.150	7.65E+2
n3306-07b	bl. thin euh, homog	692	139	380	22	331	4	0.063	6.84	0.454	6.98	0.053	1.37	0.20	conc.	1915	274	113	0.143	1.27E+2
n3306-08a	bl. euh, osc z	973	84	824	26	770	13	0.072	4.22	1.251	4.60	0.127	1.83	0.40	conc.	1275	205	181	0.160	4.14E+2
n3306-09a	bl. St., osc z rim	804	33	446	8	380	5	0.066	1.60	0.552	2.11	0.061	1.38	0.65	-40.8	2413	419	166	0.174	5.59E+2
n3156-1	bl. euh, osc z	877	102	765	31	727	18	0.068	5.11	1.124	5.76	0.119	2.67	0.46	conc.	2051	357	277	0.174	2.40E+2
n3156-2	bl. euh, homog	1004	9	1013	9	1018	13	0.073	0.45	1.713	1.41	0.171	1.33	0.95	conc.	965	93	182	0.096	4.28E+4
n3156-3	bl. euh, osc z	880	54	634	14	567	7	0.068	2.64	0.866	2.96	0.092	1.34	0.45	-17.6	1826	337	188	0.184	9.53E+2
n3156-4	bl. euh, osc z	963	18	690	9	609	8	0.071	0.89	0.973	1.69	0.099	1.44	0.85	-32.0	1731	260	192	0.150	3.23E+3
n3156-5	bl. euh, osc z	756	25	487	7	432	6	0.064	1.21	0.616	1.84	0.069	1.38	0.75	-33.8	2662	354	206	0.133	6.29E+2
n3156-6	bl. euh, homog	644	86	346	13	303	4	0.061	4.10	0.406	4.35	0.048	1.43	0.33	-13.6	2945	264	154	0.090	3.49E+2
n3156-7	bl. euh, osc z	860	21	558	7	487	6	0.068	1.02	0.733	1.71	0.078	1.37	0.80	-36.9	1820	239	158	0.131	1.07E+3
n3156-8	bl. euh, osc z	974	42	685	13	600	9	0.072	2.07	0.963	2.57	0.098	1.53	0.59	-25.7	1201	379	136	0.316	5.44E+2
n3156-9	bl. euh, osc z	847	32	447	8	373	5	0.067	1.56	0.553	2.12	0.060	1.43	0.68	-44.7	1992	129	130	0.065	6.91E+2
n3156-10	bl. euh, osc z	750	189	478	37	423	6	0.064	9.50	0.601	9.61	0.068	1.40	0.15	conc.	1905	295	147	0.155	7.04E+1
n3156-11	bl. euh, osc z	1055	86	826	27	743	12	0.074	4.38	1.255	4.69	0.122	1.67	0.36	-3.3	1330	104	181	0.078	1.58E+2
n3156-12	bl. euh, osc z	873	66	598	17	528	10	0.068	3.24	0.802	3.76	0.085	1.90	0.50	-16.7	3101	618	307	0.199	1.41E+2
Xe6																				
n3301-01a	brng, st., osc z cracked	781	30	453	13	391	13	0.065	1.43	0.562	3.64	0.063	3.34	0.92	-38.8	3302	182	224	0.055	1.82E+3
n3301-02a	brng, euh, osc z core	878	31	626	8	559	5	0.068	1.53	0.853	1.77	0.091	0.89	0.50	-26.5	681	101	69	0.149	5.81E+2
n3301-02b	brng, euh, osc z rim	449	314	431	57	428	11	0.056	15.64	0.529	15.87	0.069	2.67	0.17	conc.	3961	216	288	0.054	8.15E+1
n3301-03a	brng, euh, osc z rim	731	55	368	9	313	3	0.064	2.64	0.436	2.82	0.050	1.01	0.36	-34.4	4809	246	261	0.051	2.92E+2
n3301-03b	brng, euh, homog core	625	141	196	14	162	5	0.061	6.85	0.213	7.62	0.025	3.33	0.44	-0.4	14030	2568	404	0.183	1.15E+2
n3301-04ax	brng, euh, homog core	1163	46	888	16	782	10	0.079	2.36	1.398	2.71	0.129	1.34	0.50	-20.4	306	253	55	0.826	3.19E+2
n3301-04b	brng, euh, osc z rim	529	565	351	97	324	15	0.058	30.99	0.412	31.33	0.052	4.62	0.15	conc.	2753	141	158	0.051	7.58E+1

Table 6. Cont.

Sample/ spot #	Description[a]	Derived ages (Ma)						Corrected ratios						ρ [b]	Disc. [c]	Elemental data			Th/U	$^{206}Pb/^{204}Pb$
		$^{207}Pb/^{206}Pb$	±1σ	$^{207}Pb/^{235}U$	±1σ	$^{206}Pb/^{238}U$	±1σ	$^{207}Pb/^{206}Pb$	±1σ (%)	$^{207}Pb/^{235}U$	±1σ (%)	$^{206}Pb/^{238}U$	±1σ (%)		(%)	[U] (ppm)	[Th] (ppm)	[Pb] (ppm)	(meas.)	(meas.)
n3301-05b	brng, euh, homog (core?)	265	52	204	5	199	3	0.052	2.29	0.223	2.65	0.031	1.34	0.51	conc.	16307	1361	550	0.083	1.83E+2
n3301-06a	brng, euh, homog core	994	31	860	12	809	10	0.072	1.54	1.332	1.99	0.134	1.27	0.63	-9.4	292	171	49	0.584	1.17E+3
n3301-06b	brng, euh, osc z (rim?)	617	61	330	9	290	4	0.060	2.88	0.384	3.18	0.046	1.36	0.43	-24.4	4640	261	239	0.056	2.32E+2
n3301-07a	brng, euh, homog core	181	129	185	10	185	2	0.050	5.78	0.200	5.91	0.029	1.24	0.21	conc.	10673	568	333	0.053	6.84E+2
n3301-07b	brng, euh, osc z rim	782	212	471	43	409	10	0.065	10.81	0.590	11.13	0.066	2.64	0.24	conc.	2617	90	185	0.035	1.70E+2
n3301-08a	brng, euh, osc z (rim?)	840	39	~~521~~	~~10~~	451	6	0.067	1.92	0.671	2.39	0.073	1.42	0.60	-32.5	3533	156	287	0.044	4.25E+2
n3301-09a	brng, euh, homog core	907	89	714	24	654	8	0.069	4.44	1.019	4.61	0.107	1.25	0.27	conc.	299	133	41	0.443	2.24E+2
n3301-09b	brng, euh, homog core	1016	40	1072	16	1100	13	0.073	2.00	1.874	2.36	0.186	1.25	0.53	conc.	85	70	21	0.825	2.51E+3
n3301-09c	brng, euh, osc z rim	288	379	384	62	400	6	0.052	18.69	0.460	18.76	0.064	1.66	0.09	conc.	3718	152	253	0.041	9.55E+1
n3301-10a	brng, euh, osc z	139	168	197	14	202	3	0.049	7.53	0.215	7.66	0.032	1.38	0.18	conc.	7999	380	271	0.047	3.28E+2
n3301-11a	brng, euh, homog middle	968	31	1915	17	2902	29	0.071	1.51	5.596	1.96	0.569	1.24	0.63	221.2	300	301	198	1.005	2.32E+2
n3301-11b	brng, euh, homog core	1009	26	1132	14	1198	17	0.073	1.31	2.050	2.05	0.204	1.58	0.77	10.8	3547	1890	839	0.533	1.18E+3
n3301-12a	brng, euh, osc z	637	47	397	9	357	6	0.061	2.21	0.478	2.73	0.057	1.61	0.59	-23.5	4653	187	284	0.040	4.37E+2
n3301-13a	brng, euh, osc z	1008	19	846	10	786	10	0.073	0.92	1.301	1.65	0.130	1.37	0.83	-17.0	669	633	117	0.946	3.28E+3
n3301-14a	brng, euh, homog core	1101	22	1110	11	1114	13	0.076	1.10	1.983	1.67	0.189	1.25	0.75	conc.	126	123	33	0.972	1.49E+4
n3301-14b	brng, euh, osc z rim	765	88	744	26	737	16	0.065	4.31	1.081	4.88	0.121	2.29	0.47	conc.	3880	464	533	0.120	7.28E+1
n3301-15a	brng, euh, homog zone	1113	20	1099	11	1092	13	0.077	1.01	1.952	1.61	0.185	1.25	0.78	conc.	145	131	36	0.905	2.96E+4
n3301-15b	brng, euh, osc z zone	1093	25	1076	12	1068	13	0.076	1.27	1.886	1.81	0.180	1.29	0.71	conc.	94	64	22	0.680	1.66E+4

[a] brn=brown, brng=brownish gray, brkn=broken, clss= colorless, light=light-coloured or clss, lbrn=light brown, rbrn=reddish brown, prism=prismatic, rnd=rounded, el=elongate, st=stubby, z=zoned, h=homogeneous, c=core, r=rim, CL=cathodoluminescence

[b] Rho, error correlation for $^{207}Pb/^{235}U$ versus $^{206}Pb/^{238}U$ ratios

[c] Degree of discordance is calculated at the closest 2 σ limit. Conc. mark concordant data.

Table 7. SIMS U–Pb results.

SHRIMP U-Pb zircon results for sample XE 1.

							Total Ratios						Radiogenic Ratios					Age (Ma)				
Grain. spot	U (ppm)	Th (ppm)	Th/U	Pb* (ppm)	$^{204}Pb/^{206}Pb$	f_{206} %	$^{238}U/^{206}Pb$	±	$^{207}Pb/^{206}Pb$	±	$^{206}Pb/^{238}U$	±	$^{207}Pb/^{235}U$	±	$^{207}Pb/^{206}Pb$	±	ρ	$^{206}Pb/^{238}U$	±	$^{207}Pb/^{206}Pb$	±	% Disc
1.1	730	137	0.19	103	0.000	0.04	6.079	0.064	0.071	0.000	0.165	0.002	1.622	0.019	0.071	0.000	0.888	982	10	972	11	-1
1.2	124	93	0.75	17	0.000	0.31	6.101	0.079	0.073	0.001	0.163	0.002	1.595	0.036	0.071	0.001	0.580	976	12	951	37	-3
1.3	528	197	0.37	79	0.000	0.04	5.713	0.062	0.075	0.000	0.175	0.002	1.810	0.023	0.075	0.000	0.866	1039	10	1070	13	3
2.1	499	223	0.45	73	0.000	0.06	5.916	0.065	0.074	0.000	0.169	0.002	1.701	0.022	0.073	0.000	0.857	1006	10	1015	13	1
2.2	302	187	0.62	42	0.000	0.16	6.193	0.070	0.074	0.001	0.161	0.002	1.612	0.025	0.073	0.001	0.719	964	10	1001	22	4
3.1	751	615	0.82	143	0.000	0.01	4.523	0.048	0.083	0.000	0.221	0.002	2.518	0.029	0.083	0.000	0.918	1288	12	1260	9	-2
3.2	362	102	0.28	51	0.000	0.03	6.112	0.066	0.075	0.001	0.163	0.002	1.654	0.022	0.073	0.001	0.823	975	10	1027	15	5
4.1	2617	109	0.04	438	0.000	0.01	5.132	0.057	0.077	0.000	0.195	0.002	2.069	0.023	0.077	0.000	0.979	1148	12	1121	5	-2
4.2	290	231	0.80	40	0.000	0.14	6.222	0.070	0.073	0.001	0.160	0.002	1.580	0.024	0.071	0.001	0.749	959	10	969	20	1
5.1	324	195	0.60	62	0.000	0.05	4.491	0.051	0.083	0.001	0.223	0.003	2.631	0.036	0.085	0.001	0.823	1299	15	1326	15	2
5.2	180	145	0.81	24	0.000	0.23	6.453	0.082	0.072	0.001	0.155	0.002	1.502	0.033	0.070	0.001	0.578	927	11	942	37	2
6.1	191	222	1.17	27	0.000	0.23	5.957	0.090	0.073	0.001	0.167	0.003	1.652	0.032	0.072	0.001	0.771	998	14	972	26	-3
7.1	1142	46	0.04	222	0.000	0.01	4.411	0.049	0.080	0.000	0.227	0.003	2.498	0.029	0.080	0.000	0.951	1317	13	1195	7	-10
7.2	424	261	0.61	60	0.000	0.05	6.102	0.079	0.073	0.001	0.164	0.002	1.647	0.025	0.073	0.001	0.864	978	12	1011	15	3
8.1	586	179	0.31	98	0.000	0.06	5.116	0.056	0.080	0.001	0.195	0.002	2.146	0.034	0.080	0.001	0.683	1150	11	1189	23	3
8.2	425	145	0.34	57	0.000	0.08	6.361	0.071	0.073	0.001	0.157	0.002	1.558	0.021	0.072	0.001	0.806	941	10	985	17	4
9.1	481	191	0.40	93	0.000	0.06	4.422	0.048	0.085	0.000	0.226	0.002	2.670	0.033	0.086	0.001	0.879	1316	14	1328	12	1
9.2	316	133	0.42	47	0.000	0.13	5.754	0.084	0.075	0.001	0.174	0.003	1.772	0.032	0.074	0.001	0.814	1032	14	1042	21	1
10.1	234	133	0.57	44	0.000	0.11	4.523	0.062	0.086	0.001	0.221	0.003	2.587	0.044	0.085	0.001	0.812	1286	16	1315	19	2
10.2	690	279	0.40	101	0.000	0.03	5.885	0.065	0.073	0.000	0.170	0.002	1.702	0.021	0.073	0.000	0.878	1011	10	1005	12	-1
11.1	855	267	0.31	157	0.000	0.07	4.669	0.053	0.080	0.000	0.214	0.002	2.402	0.030	0.081	0.000	0.924	1253	13	1227	9	-2
11.2	120	126	1.04	16	-	<0.01	6.326	0.086	0.073	0.001	0.158	0.002	1.616	0.033	0.074	0.001	0.667	947	12	1044	31	9

Table 7. Cont.

SHRIMP U-Pb zircon results for sample XE 4.

							Total Ratios						Radiogenic Ratios					Age (Ma)				
Grain. spot	U (ppm)	Th (ppm)	Th/U	Pb* (ppm)	$^{204}Pb/^{206}Pb$	f_{206} %	$^{238}U/^{206}Pb$	±	$^{207}Pb/^{206}Pb$	±	$^{206}Pb/^{238}U$	±	$^{207}Pb/^{235}U$	±	$^{207}Pb/^{206}Pb$	±	ρ	$^{206}Pb/^{238}U$	±	$^{207}Pb/^{206}Pb$		% Disc
1.1	307	196	0.64	59	0.000	0.10	4.496	0.051	0.085	0.001	0.222	0.003	2.578	0.039	1.518	0.084	0.742	1293	13	1296	20	0
1.2	979	58	0.06	154	0.000	0.02	5.473	0.066	0.076	0.000	0.183	0.002	1.906	0.025	1.302	0.076	0.931	1082	12	1087	10	0
1.3	208	152	0.73	35	0.001	1.21	5.075	0.066	0.079	0.001	0.195	0.003	1.841	0.074	4.040	0.069	0.330	1147	14	886	79	-29
2.1	664	48	0.07	102	0.000	0.05	5.610	0.060	0.075	0.000	0.178	0.002	1.836	0.023	1.246	0.075	0.855	1057	10	1061	13	0
2.2	117	137	1.17	17	0.000	0.22	6.059	0.080	0.072	0.001	0.165	0.002	1.654	0.032	1.930	0.073	0.682	985	15	1004	29	2
3.1	332	187	0.56	45	0.000	0.05	6.271	0.075	0.071	0.001	0.159	0.002	1.559	0.023	1.502	0.071	0.792	953	11	955	19	0
4.1	588	141	0.24	91	0.000	0.04	5.555	0.069	0.074	0.000	0.180	0.002	1.857	0.026	1.374	0.075	0.899	1068	13	1062	12	-1
4.2	130	75	0.58	20	0.000	0.23	5.620	0.104	0.074	0.001	0.178	0.003	1.848	0.042	2.260	0.075	0.821	1057	20	1075	26	2
5.1	121	80	0.67	17	0.000	0.10	6.149	0.081	0.074	0.001	0.162	0.002	1.592	0.032	2.020	0.071	0.656	968	13	964	31	-0
5.2	1531	56	0.04	242	0.000	0.03	5.436	0.056	0.075	0.000	0.184	0.002	1.899	0.022	1.140	0.075	0.907	1088	10	1066	10	-2
6.1	2080	39	0.02	345	0.000	0.01	5.174	0.060	0.077	0.000	0.193	0.002	2.054	0.025	1.212	0.077	0.952	1139	12	1123	7	-1
6.2	276	144	0.52	41	0.000	0.14	5.851	0.068	0.075	0.001	0.171	0.002	1.742	0.026	1.518	0.074	0.770	1016	11	1042	20	2
7.1	277	74	0.27	52	-	<0.01	4.543	0.052	0.082	0.001	0.220	0.003	2.525	0.035	1.388	0.083	0.828	1284	14	1272	15	-1
7.2	105	78	0.75	15	-	<0.01	6.182	0.083	0.071	0.001	0.162	0.002	1.588	0.032	2.041	0.071	0.658	967	12	963	31	-0
8.1	240	107	0.45	40	0.000	0.10	5.194	0.061	0.079	0.001	0.192	0.002	2.070	0.032	1.531	0.078	0.770	1134	12	1148	19	1
8.2	173	173	1.00	25	0.000	0.17	5.902	0.097	0.073	0.001	0.169	0.003	1.678	0.034	2.032	0.072	0.809	1008	18	984	24	-2
9.1	657	92	0.14	104	-	<0.01	5.441	0.063	0.076	0.001	0.184	0.002	1.934	0.030	1.574	0.076	0.738	1088	12	1103	21	1
9.2	913	751	0.82	184	-	<0.01	4.270	0.055	0.083	0.000	0.234	0.003	2.704	0.037	1.369	0.084	0.933	1357	16	1286	10	-6
10.1	1024	191	0.19	173	0.000	0.00	5.072	0.054	0.078	0.000	0.197	0.002	2.132	0.025	1.156	0.078	0.913	1160	11	1158	9	-0
10.2	408	251	0.61	56	0.000	0.08	6.281	0.070	0.072	0.001	0.159	0.002	1.558	0.022	1.432	0.071	0.782	952	10	958	18	1
11.1	192	118	0.61	28	0.000	0.22	5.844	0.070	0.075	0.001	0.171	0.002	1.721	0.029	1.662	0.073	0.722	1016	11	1016	23	0
12.1	269	125	0.46	40	0.000	0.13	5.795	0.072	0.073	0.001	0.172	0.002	1.713	0.030	1.754	0.072	0.709	1025	12	988	25	-4

1. Uncertainties given at the one σ level.
2. Error in FC1 Reference zircon calibration was 0.36% for the analytical session.
3. f_{206} % denotes the percentage of ^{206}Pb that is common Pb.
4. Correction for common Pb made using the measured $^{204}Pb/^{206}Pb$ ratio.
5. For % Disc, 0% denotes a concordant analysis.

Table 8. Sm–Nd and Rb–Sr results.

Sample	Rock type	Sm ppm	Nd ppm	Sm/ Nd	$^{147}Sm/^{144}Nd$	$^{143}Nd/^{144}Nd$	εNd (180Ma)	εNd (0)	Rb ppm	Sr ppm	$^{87}Rb/^{86}Sr$	$^{87}Sr/^{86}Sr$	εSr (180Ma)	εSr (0)	T_{DM}	$εNd_{init}$
Xe11 WR	Metagabbro	6.3	27.3	0.23	0.139	0.512455±9	-2.3	-3.6	49.0	730.7	0.193	0.704369±15	-5.9	-1.9	1204	7.09 (1450)
Xe11 Ap	Metagabbro	115.3	731.8	0.16	0.096	0.512419±11	-2.0	-4.3	15.9	4330.9	0.011	0.703271±14	-14.9	-17.4	816	14.5
Xe11 Pl	Metagabbro	0.5	4.0	0.13	0.079	0.511880±10	-12.1	-14.8	44.1	1643.6	0.077	0.703815±14	-9.6	-9.7	1310	7.1
Xe16 WR	Metagabbro	15.3	79.7	0.19	0.116	0.512108±13	-8.5	-10.4	44.1	1375.0	0.092	0.704712±19	2.6	3.0	1456	-8.53 (180)
Xe16 Cpx	Metagabbro	15.6	59.5	0.26	0.159	0.512139±9	-8.9	-9.8	11.7	194.6	0.174	0.704829±13	1.3	4.7	2535	-8.5
Xe16 Pl	Metagabbro	2.6	17.9	0.14	0.088	0.512053±11	-9.0	-11.5	44.4	1959.2	0.065	0.704916±13	6.5	5.9	1199	-8.96

Estimated error for $^{147}Sm/^{144}Nd$ and $^{87}Rb/^{86}Sr$ is 0.4%. $^{143}Nd/^{144}Nd$ is normalized to $^{146}Nd/^{144}Nd=0.7219$, $^{87}Sr/^{86}Srto\ ^{86}Sr/^{84}Sr=0.1194$. εNd and εSr values are calculated using present day values $^{143}Nd/^{144}Nd=0.51264$ and $^{147}Sm/^{144}Nd=0.1966$, and $^{87}Sr/^{86}Sr=0.7045$ and $^{87}Rb/^{86}Sr=0.0816$ for CHUR (Chondrite Uniform Reservoir) according to Hamilton et al. (1983). Depleted mantle model-age (T_{DM}) after DePaolo (1981). Abbreviations: WR=whole rock powder; ap=apatite; cpx=clinopyroxene; and pl=plagioclase.

9.1 Metagranitoids

9.1.1 Metatonalites Xe1 and Xe4

The lamproite-hosted metatonalite samples Xe1 and Xe4 are petrographically and geochemically nearly identical and may even come from the same intrusion. Tonalite sample Xe1 contains elongate to rounded, zoned zircons, with a diameter of ca. 100–250 µm. The maximum length-width ratio is 3:1. Cathodoluminescence (CL) images show oscillatory-zoned cores that are surrounded by complex and in part relatively wide zircon overgrowths (Fig. 17A). The most apparent of these rims are relatively low in U (100–400 ppm). The distinctive inner part of the zircon crystals is hereafter referred as the core and the surrounding continuous overgrowth of varying width as the rim. Twenty-two spots from eleven crystals were analysed. Most of the zircon cores have $^{207}Pb/^{206}Pb$ ages ranging from 1250–1330 Ma, but two cores are younger with $^{207}Pb/^{206}Pb$ ages of ca. 1150 Ma. Most of the low-U rims have $^{207}Pb/^{206}Pb$ ages ranging from 940–1000 Ma, while three analyses have $^{207}Pb/^{206}Pb$ ages of ca. 1040 Ma. The two young ages and the most concordant spot analysis provide the minimum age for this metatonalite of 966 ± 7 Ma (Fig. 18A).

Tonalite sample Xe4 has elongate to rounded, stubby zircons with a size ranging from 100–200 µm (Fig. 17B). Many of these zircons have oscillatory-zoned cores that are surrounded by thin zircon overgrowths (Fig. 18B). In CL images (Fig. 17B), the cores show oscillatory zoning and are overgrown by mostly relatively thin zircon rims with low U values (100–400 ppm) but relatively high Th/U (Table 7). Twenty-two spots from twelve zircon crystals were analysed for Xe4. The spots from the core define three distinct $^{207}Pb/^{206}Pb$ age groups at ca. 1280 Ma, ca. 1130–1150 Ma and 1060 Ma. The rims gave $^{207}Pb/^{206}Pb$ ages of mainly 950–990 Ma. Two zircon overgrowth analyses provided $^{207}Pb/^{206}Pb$ ages of ca. 1040–1080 Ma (Fig. 18B).

In these two metatonalite samples (Xe1 and Xe4), no indication of later lead loss is seen, so the obtained $^{207}Pb/^{206}Pb$ ages yield the crystallization ages of the respective zircon crystals and domains (Figs. 19A & B). The U contents are all within the range typical of granitoids (Xiang et al. 2011). No systematic Th/U patterns were observed within the different morphological or age groups that would have been significant in distinguishing between a magmatic and metamorphic origin of zircon. The oldest groups of core ages, 1250–1330 and 1130–1150 Ma, probably represent inherited zircon. The rims are concordant at 960 Ma and have fairly high Th/U (0.6–0.8), similar to that of the oldest cores, whereas the metamorphic zircon typically shows Th/U of <0.1 (Hoskin & Schaltegger 2003). The 1040–1070 Ma and 940–1000 Ma ages may represent emplacement and recrystallization in granulite facies, respectively, of these metatonalite xenoliths.

9.1.2 Mylonitic metagranite Xe2

The zircons from mylonitic metagranite Xe2 are dark grey, prismatic and mostly stubby. The crystals are in most cases oscillatory zoned, severely altered and cracked (Figs. 17C & D). Some crystals seem to display a multiple crystallization history, but these features are not clear. Overall, the zircon crystals are so intensely cracked that it was not easy to find targets for the ion beam. Altogether, 24 domains from 21 zircon crystals were measured. On average, the zircons are high in U (ca. 2000 ppm) and the crystals are often metamict with Pb loss and resultant high degree of discordance. However, all of the data points can be attributed to the same crystallization upper intercept age of 1021 ± 30 Ma (MSWD 2.1; Fig 19E). Many of the analysis spots represent zircon with high common Pb but fall on the same discordia line, irrespective of this. Hence, we have used them in age calculations. The lead loss seems to have been episodic, pointing to a lower intercept of 193 ± 22 Ma. This probably relates to the widespread Jurassic mafic magmatism during the break-up of Gondwana.

9.1.3 Gneissic metagranite Xe6

The zircons from the gneissic metagranite Xe6 are large and euhedral. Visible light does not penetrate the crystals and they show a white or light bluish grey tint under an optical microscope. These features are typical of zircons recovered from granitic pegmatites. In BSE images, the crystals are intensely cracked, relatively

altered and display well-defined "spongy" metamictic zones (Fig. 17E). In CL images, oscillatory zoning is often visible (Fig. 17F). Altogether, 26 domains from 15 zircon crystals were analysed. The U contents vary considerably (from 64 to 2568 ppm), being mostly >1000 ppm. The range is indicative of considerable Pb loss (Fig. 19D). The few concordant spots show a weighted mean $^{207}Pb/^{206}Pb$ age of 1094 ± 11 Ma (Fig. 18D). If a discordia line is fitted through the analytically acceptable data points, a similar upper intercept age for the reference line is attained (Fig. 19C). The relatively low common-Pb spots ($^{207}Pb/^{206}Pb$ > 1000) define a discordia line with an upper intercept age of 1081 ± 25 Ma (MSWD 1.7), which is also similar to the concordia age. The lower intercept for this discordia is 204 ± 26 Ma, partly contemporaneous with the recorded Jurassic mafic magmatism during the break-up of Gondwana.

9.1.4 Equigranular metagranite ALKBM6

Compared to the other metagranitoid samples, the equigranular metagranite ALKBM6 is notably more massive and more even grained. Altogether, 26 domains from 17 zircon crystals were analysed. The zircons from metagranite ALKBM6 are fairly large, euhedral, stubby and often oscillatory zoned. Sector zoning can also be seen in some crystals (Fig. 17G). The U levels are low, being 30–300 ppm, commonly 200–300 ppm. The Th/U value ranges from 0.35 to 1.2, being predominantly <0.55 (Table 7). The age indicated by the Thera-Wasserburg plot (Fig. 18G) is unequivocally Jurassic, with an average $^{206}Pb/^{238}U$ age of 165 ± 1 Ma (MSWD 1.04) (Figs. 18G & H). This also sets the maximum age for the host lamproite dyke. In three zircon crystals, the measurements provided spot ages of ca. 1090, ca. 470 and ca. 185 Ma. In appearance, these measured crystals show a conspicuously homogeneous internal structure, as opposed to the typically zoned Jurassic zircons (Fig. 17G). These spot ages correspond to orogenic Grenvillian-Kibaran (ca. 1090 Ma), orogenic East Antarctic–African aka. Pan-African (ca. 470 Ma), and extensional Karoo (185 Ma) thermal events (Fig. 18G), and were therefore regarded to be zircon of inherited origin.

9.2 Metagabbroids and metadiorites

Only the quartz metadiorite sample ALKBM1 yielded zircon that could be measured for its U-Pb isotope composition. Zircon was not recovered from the metagabbros. The two metagabbroic samples, Xe11 and Xe16, were examined using the Rb-Sr and Sm-Nd mineral isochron methods (Table 8).

9.2.1 Quartz metadiorite ALKBM1

In terms of its zircon population, the quartz metadiorite is notably heterogeneous. The recovered zircons are mostly very large, colourless and stubby. Both prismatic and anhedral rounded crystals are present (Fig. 17F). Some crystals appear to have a structure displaying a core and continuous overgrowth referred to later on as a rim, but these are not particularly prominent. Many crystals display oscillatory zoning, but homogeneous zircons are also present.

Altogether, 38 spots from 29 zircon crystals were analysed. The structure of the zircons is variable and mainly complex. Some of the crystals display a thin overgrowth (<<25 µm), but this is not a prominent feature among the population. Average U, Th and Pb contents are low, in some instances to the point of having no observed Pb signal, indicative of later Pb loss. The U-Pb results spread over a wide range (Fig. 18F), but are mostly concordant, although relatively imprecise due to low elemental concentrations and hence low precision. The youngest spot age is 230 Ma and the oldest is 1350 Ma. There is no constant connection between the identified structural feature groups and the age results. Notably, the results show a wide gap between the Phanerozoic and Proterozoic ages. The heterogeneous zircon fraction probably includes a significant detrital/inherited component discussed in detail in Chapter 10.

9.2.2 Garnet-free metagabbro Xe11

The gabbroic xenolith Xe11 was examined using the Rb-Sr and Sm-Nd mineral isochron method. Sample Xe 11 is dominated by clinopyroxene and

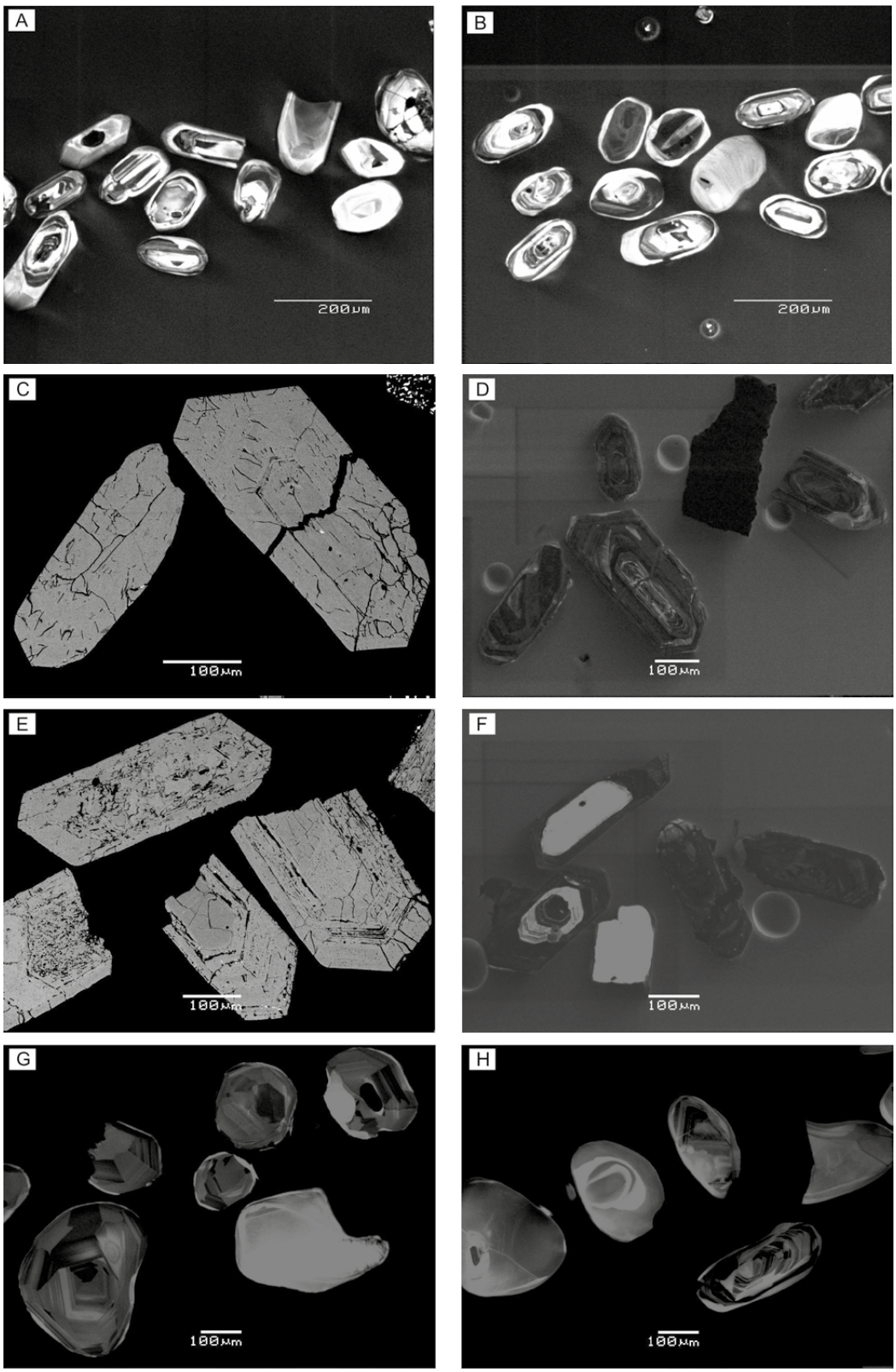

Fig. 17. (A-H) Representative cathodoluminescence (CL) and back scattered electron (BSE) images of the zircon crystals in the studied silicic xenoliths. The zircons of (A) metatonalite Xe1 and (B) metatonalite Xe4 show commonly oscillatory normal zoned euhedral cores and bright, relatively low-U rims on CL images. The zircons in (C, D) gneissic metagranite Xe2 and (E, F) mylonitic metagranite Xe6 are commonly euhedral, showing oscillatory normal zoned cores, but (C) intensive cracking is clearly visible in BSE images, and (E) "spongy" metamict zones are also well defined. (D, F) Typically, the zircon of xenoliths Xe2 and Xe6 is high in U, except for some rims that are low in U, indicated by high reflectivity in CL images. (G) The zircons from equigranular metagranite ALKBM6 are fairly large, euhedral, stubby and often oscillatorily zoned. Some homogeneous crystals are low in U, indicated by high reflectivity in CL images. (H) The zircons from quartz metadiorite ALKBM1 are mostly large but also huge, colourless and stubby. Both prismatic and anhedral rounded crystals are present, representative of the large zircon aliquot. Copyright for images: Images A and B provided by Dr Joachim Jacobs; images C–H provided by Ms Ilona Romu and Dr Matti Kurhila.

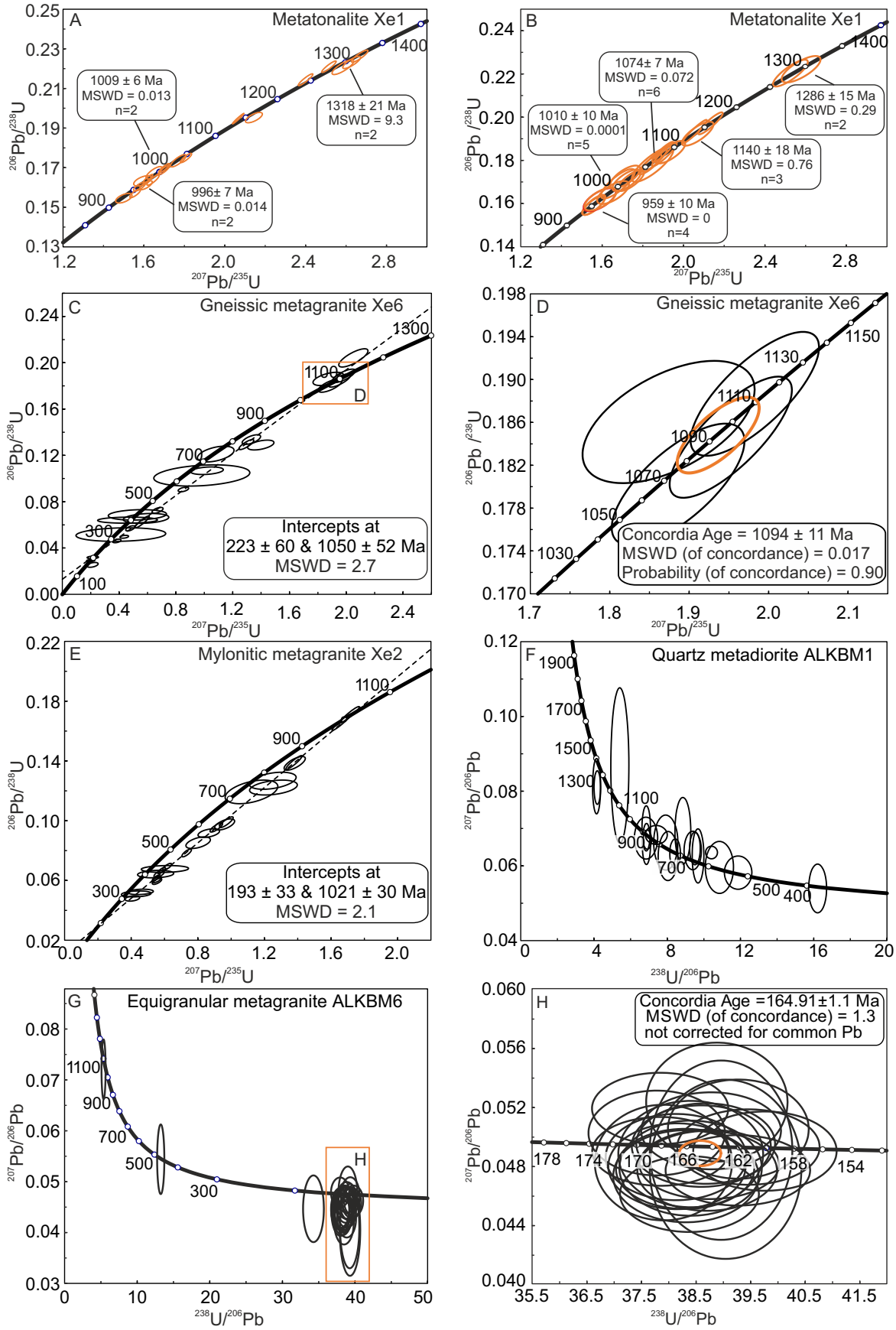

Fig. 18. (A–E) Zircon $^{206}Pb/^{238}U$-$^{207}Pb/^{235}U$ and (F–H) $^{207}Pb/^{206}Pb$-$^{238}U/^{206}Pb$ diagrams. The analysed concordant zircons of the (A) metatonalite Xe1 and (B) metatonalite Xe4, Wetherill plot. (C) Gneissic metagranite Xe6, intercept ages, Wetherill plot. (D) Gneissic metagranite Xe6, concordant analyses of the upper intercept, Wetherill plot. (E) Mylonitic metagranite Xe2, intercept ages, Wetherill plot. (F) Quartz metadiorite ALKBM1, concordant analyses, Tera-Wasserburg plot. (G) Equigranular metagranite ALKBM6, Tera-Wasserburg plot. (H) Equigranular metagranite ALKBM6, concordant analyses (common-Pb uncorrected) pointing to igneous crystallization in the Jurassic. The data-point error ellipses are 2 σ.

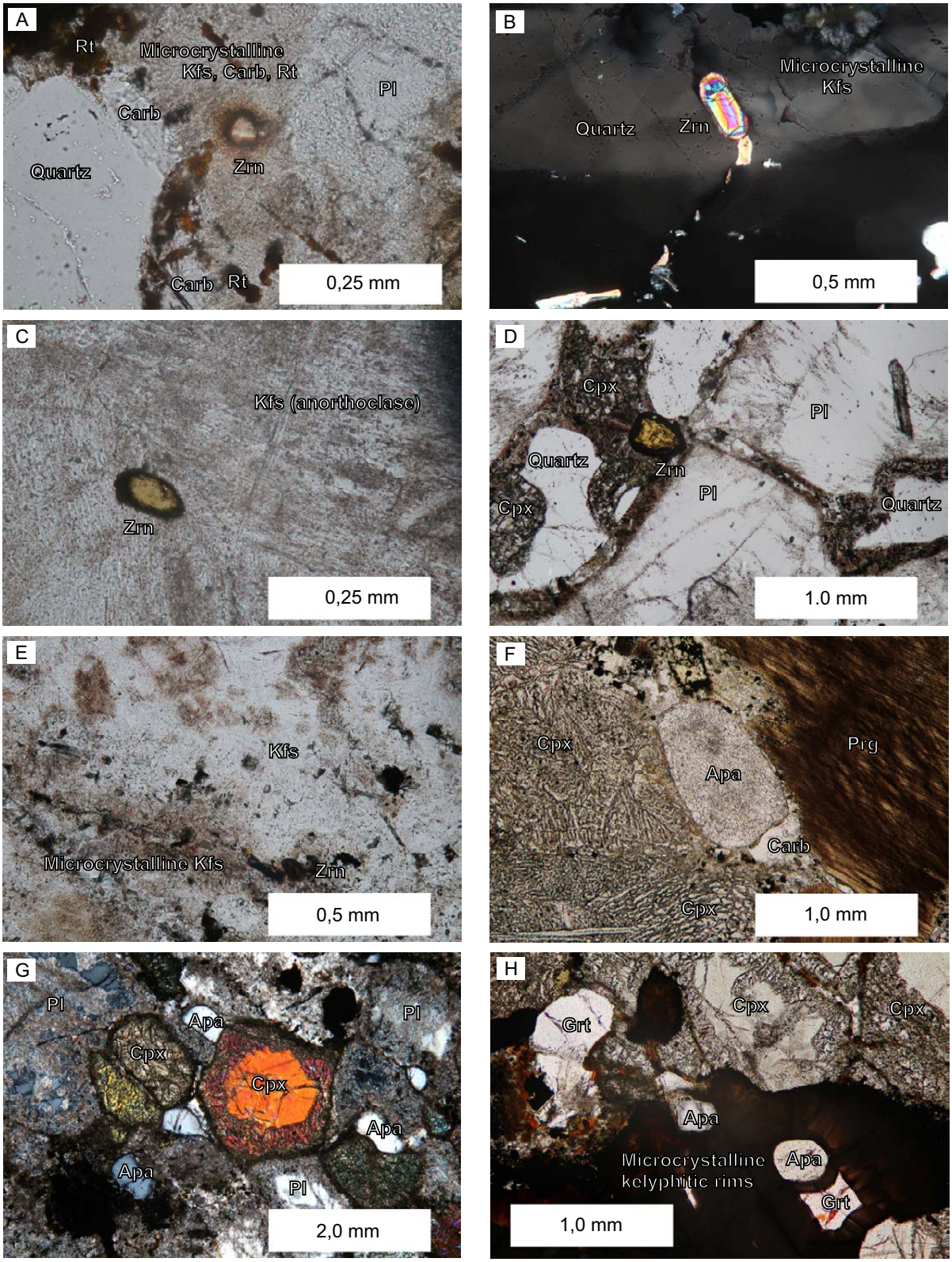

Fig. 19. Photomicrographs of the zircon, apatite, clinopyroxene, garnet and plagioclase in situ. (A) Metamict zircon of metatonalite xenolith Xe1. A halo produced by radiation damage within the surrounding microcrystalline matrix dominated by fibrous Kfs is well developed (photomicrograph, ppl). (B) Zoned euhedral zircon of the metatonalite xenolith Xe4 surrounded by deformed undulose quartz. The normal zoned core is overgrown by a rim (photomicrograph, xpl). (C) Distinctively yellowish Phanerozoic zircon of the equigranular metagranite ALKBM6 (photomicrograph, ppl). (D) Yellowish, probably Phanerozoic zircon of the quartz metadiorite ALKBM1 set between clinopyroxene, plagioclase and quartz crystals (photomicrograph, ppl). (E) Dark-coloured zircon of the gneissic metagranite Xe2. (F) Clinopyroxene of the metagabbro Xe11 is vermicular in habit, apatite is rich in fluid inclusions, and pargasite is stained and full of oxide inclusions (ppl). (G) Clinopyroxene and plagioclase of the metagabbro Xe16 show reacted, vermicular outer boundaries and apatite is rich in fluid inclusions (xpl). (H) Garnet of the metagabbro Xe16 is surrounded by microcrystalline, kelyphitic rims (ppl). Abbreviations: Xpl, cross-polarized light; ppl, plane polarized light.

pargasite, which comprise 80–90% of the volume of the xenolith (Table 2; Figs. 3S, 4C & 19F). This modally layered xenolith is in part plagioclase free. Apatite and plagioclase were recovered, but clinopyroxene and pargasite could not be separated from each other. The measured whole-rock composition, however, gives an estimate of the composition of the clinopyroxene-pargasite mixture.

Clinopyroxe is vermicular with microscopic feldspar exsolutions and pargasite is rich in oxide inclusions (Fig. 19F). Dominantly anhedral, zoned plagioclase is unaltered in thin section, but the recovered crystals are mostly cloudy and contain minor quantities of magnetite. A quantity of translucent plagioclase was also present in the analysed plagioclase fraction. Apatite contains micron-sized fluid inclusions and is distinctive in its petrography (Fig. 19F): the anhedral rounded shape combined with inclusion-rich texture indicate that it may have precipitated or re-crystallized after the magmatic crystallization of the protolith. This would be consistent with the behaviour of phosphate phases in high-grade metamorphosed crustal rocks (Pan & Fleet 1996, Vavra & Schaltegger 1999). To summarize, the apatite is unlikely to represent an igneous composition and the sample probably contained both igneous and metamorphic plagioclase, which may result in mixed isotopic compositions (Romu 2006, unpublished M.Sc. Thesis). The xenolith whole-rock however, may have behaved as a closed system, retaining the igneous whole-rock isotope composition.

Three-point errochrons imply an incomplete state of equilibrium of Rb-Sr and Sm-Nd systems between plagioclase, apatite and whole rock (Figs. 20A & B). The two-point Rb-Sr isochron of apatite and plagioclase may record metamorphic opening of the Rb-Sr system (Fig. 20C). The Rb-Sr system closure temperatures are lower relative to the Sm-Nd system. On the basis of petrographic evidence, the Rb-Sr system of apatite (anhedral, fluid-inclusions, Fig. 19F) and plagioclase may have reset or partially reset after Sm-Nd diffusion closure, possibly during the Neoproterozoic ca. 600 Ma. The plagioclase-whole-rock pair yields an age of 1400–1480 Ma, which may be indicative of igneous crystallization (Fig. 20D) (cf. Rubie & Brearley 1987). The whole-rock depleted mantle model age (T^{DM}) after DePaolo (1981) is Proterozoic, ca. 1200 Ma, correlative with present-day epsilon values of -4.3 for apatite, -3.6 for whole rock and -14.8 for plagioclase (Table 8). The partial opening of the Sm-Nd system, indicated by the apatite results, increases the material-based error for the plagioclase-whole-rock age. Overall, the Sm-Nd results are suggestive of a Mesoproterozoic Sm-Nd closure and possibly crystallization of this metagabbro.

9.2.3 Garnet-bearing metagabbro Xe16

The gabbroic xenolith Xe16 was examined using the Rb-Sr and Sm-Nd mineral isochron method. Unlike xenolith Xe11, this sample does not show modal layering. Ca. 85 vol.% of the sample consists of clinopyroxene, plagioclase, garnet and kelyphitic rims of garnet. Inclusion-rich apatite is a relatively abundant minor phase, whereas the pargasite is rare (Table 2; Figs. 3X, 4D & 19G–H). The recovered plagioclase is mostly cloudy and contains some magnetite. A quantity of translucent plagioclase was also present in the analysed plagioclase fraction. The recovered clinopyroxene contains some magnetite. In thin section, clinopyroxene shows reacted vermicular margins (Fig. 19G). Garnet is surrounded by microcrystalline kelyphitic rims (Fig. 19H). Apatite is rich in fluid inclusions and was recovered but could not be analysed (Figs. 19G & H). The petrography suggests at least one re-equilibration of the protolith, the kelyphitic rims of the garnet being indicative of decompression (cf. Rudnick 1992).

Three-point errochrons imply an incomplete state of equilibrium of Rb-Sr and Sm-Nd systems between plagioclase, whole rock and clinopyroxene (Figs. 20E & F). The Rb-Sr errochron (Fig. 20E) exemplifies that the two point "age" of ca. 100 Ma for the whole rock and clinopyroxene diagram is highly speculative (Fig. 20G), as Rb-Sr of clinopyroxene and plagioclase have not attained the state of equilibrium. It may, however, mark the approximate cooling age of the xenolith and the host dyke. The analysed fractions plot roughly along a 200 Ma Sm-Nd isochron, and the plagioclase-clinopyroxene pair yields an age of 184 ± 30 Ma (Fig. 20H). The whole-rock T^{DM} age after DePaolo (1981) is Proterozoic, ca. 1460 Ma, and the present-day epsilon values are

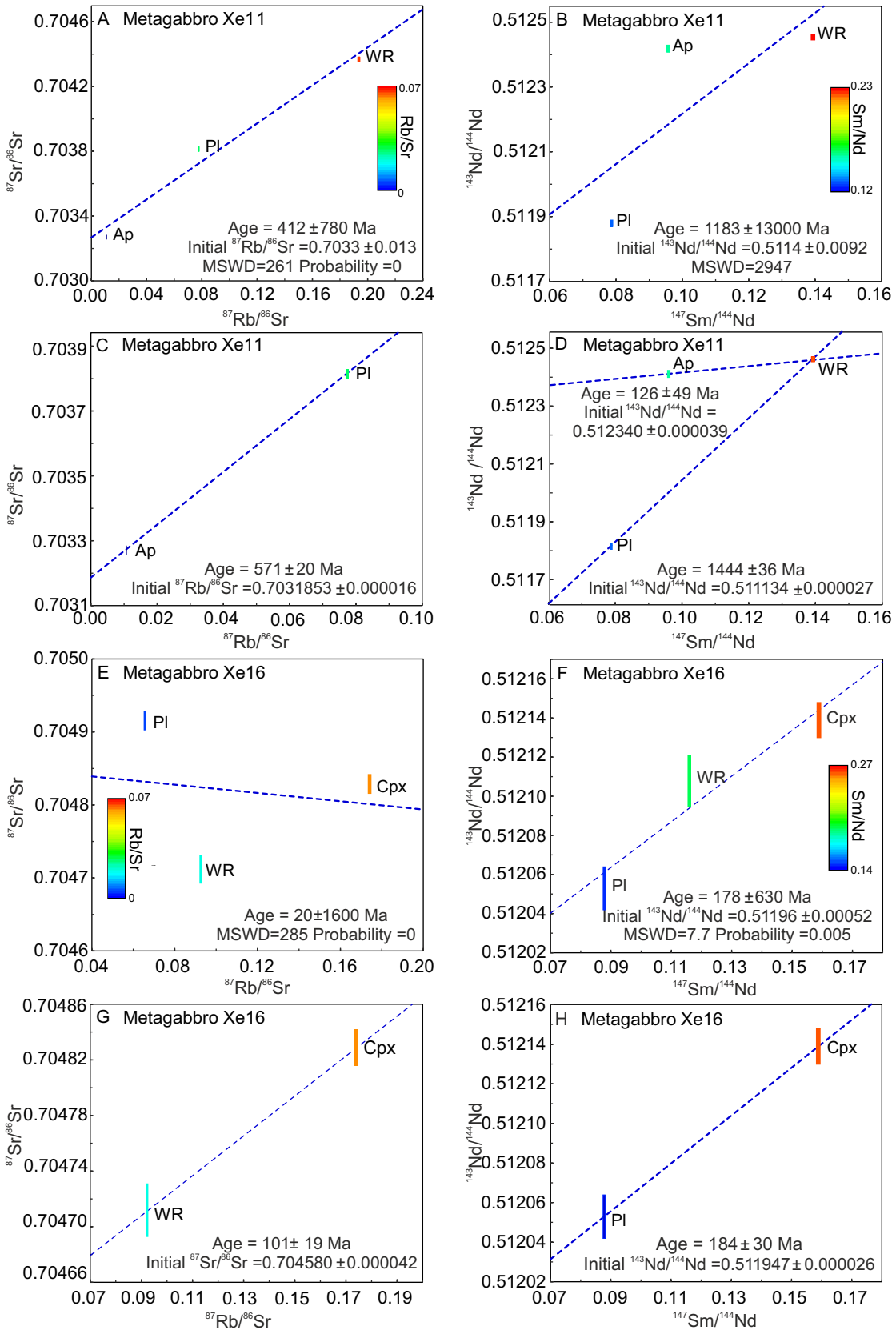

Fig. 20. $^{87}Sr/^{86}Sr$-$^{87}Rb/^{86}Sr$ and $^{143}Nd/^{144}Nd$-$^{147}Sm/^{144}Nd$ diagrams for mineral fractions and whole rocks of the metagabbro xenoliths Xe11 and Xe16. An increase in Rb/Sr and Sm/Nd (ppm) (colour coded) correlates positively with an increase in $^{87}Sr/^{86}Sr$ and $^{147}Sm/^{144}Nd$ ratios. (A) A three-point ap-pl-whole-rock Rb-Sr errochron of the xenolith Xe11. (B) A three-point ap-pl-whole-rock Sm-Nd errochron of xenolith Xe11. (C) A two-point ap-pl Rb-Sr isochron of xenolith Xe11. (D) A two-point ap-whole-rock and pl-whole-rock Sm-Nd isochron of xenolith Xe11. (E) A three-point cpx-pl-whole-rock Rb-Sr errochron of xenolith Xe16. (F) A three- point cpx-pl-whole-rock Sm-Nd errochron of xenolith Xe16. (G) A two-point cpx-whole-rock isochron of xenolith Xe16. (H) A two-point pl-cpx isochron of xenolith Xe16. Recalculated after Romu (2006). Mineral abbreviations after Kretz (1983).

-10.4 for whole rock, -9.8 for clinopyroxene and -11.5 for plagioclase (Table 8). The εNd (180 Ma) values are within analytical error, (-8.5)–(-8.6). The two-point Sm-Nd mineral age for plagioclase-clinopyroxene of 184 ± 30 Ma implies Phanerozoic equilibration of the garnet-bearing metagabbro Xe16, which may be correlated with the Jurassic break-up of Gondwana and the subsequent period of cooling. Overall, the Sm-Nd results are suggestive of Phanerozoic Sm-Nd closure of this garnet-bearing metagabbro.

9.3 Isotopic data evaluation

The interior parts of the xenolith samples, studied in thin sections, were solid and crystalline. The samples were also free of microscopic fractures or micro-cracks, except the metapelitic samples Xe13 and P5. Accordingly, there was a good reason to suppose that the isotopic composition remained undisturbed during the Jurassic intrusion of the host lamproite. The zircon used in uranium lead geochronology is extremely resistant to weathering and the crystallization temperature and closure temperature of U-Pb-system within zircon is over 900 °C (cf. Hodges 2004, Johannes & Holtz 1987). However, the cracks and porosity seen in back-scattered electron images and low uranium content implied by high reflectance in cathodoluminescence images appear to correlate with an increased size of the error ellipsoids. This was the case with samples Xe2 and Xe6. The Pb content of the analysed zircon was on average low in samples Xe1, Xe4 and ALKBM1. This increases the analytical uncertainty, as displayed by increased error of the spot analyses, and hampers the interpretation. On the whole, due to the sample size, the amount of recovered zircon was relatively small, and unfortunately there were only a limited number of concordant analyses, as many of the analysed zircons were metamict. The Rb-Sr and Sm-Nd results are even more prone to material-based geological errors. Cryptic metasomatosis, i.e. chemical enrichment of minerals, after igneous crystallization is possible, as the elemental concentrations of Rb, Sr and Nd are higher in the high-temperature host lamproite melt than in the studied xenoliths. Also, vice versa, the xenolith minerals may have been depleted in incompatible elements through melt extraction relative to their original composition.

9.3.1 Secondary ion mass spectrometry in zircon U-Th-Pb studies

Due to its precision, secondary ion mass spectrometry (SIMS) of zircon U-Th-Pb age determinations is the best option for studies in which the scope is to determine geologically meaningful periods of time. The method provides accurate ages but is not as precise as, for instance, the ID-TIMS method (Ireland & Williams 2003). However, for multiphase zircon, observation of precise ages is only possible with SIMS measurements targeted at single zircon interiors. SHRIMP and the Cameca 1270/1280 secondary ion microprobes mainly differ in secondary ion focusing, which governs the way in which the ion optics are tuned (see Ireland & Williams 2003). These authors also noted that the secondary ion yield of Cameca 1270/1280 is considerably increased with an increase in the partial pressure of oxygen, whereas for SHRIMP the effect is moderate. Consequently, with the Cameca instrument, oxygen bleeding into the source chamber during operation is used, as it increases the yield of the measured particles. In both instruments, spot positioning with reflected light is used; additionally, ion imaging may be used with the Cameca 1270/1280. In general, however, spot positioning is more difficult with the Cameca 1270 (Ireland & Williams 2003), which may sometimes result in mixed isotopic ratios generated by heterogeneous zircon. The analytical precision of SHRIMP and the Cameca 1270 based on the normal maximum sensitivity of zircon U-Th-Pb analysis is, however, similar (Ireland & Williams 2003).

The age data provided in this study were obtained using the SIMS single-zircon method at the NordSIMS and SHRIMP II facilities in Stockholm and Canberra, respectively. The precision issue with secondary ion mass spectrometers in zircon U-Th-Pb studies arises from the molecular isobaric interferences caused by the molecular secondary ions generated via the ion bombardment of the natural solid zircon sample. The analytical matrix of SIMS measurements is more complex relative to the ID-TIMS method, as an extremely small quantity (ca. 2 ng) (Ireland and Williams 2003) of solid natural zircon is sputtered towards the collector of the mass spectrometer, while in ID-TIMS analytics, chemically purified solutions made of natural zircon concentrates are used.

9.3.2 Rb-Sr and Sm-Nd results

In an attempt to determine the igneous crystallization age for the metagabbroic xenoliths, mineral-whole-rock diagrams were used. First, as the Rb-Sr and petrography implies mineral disequilibrium, these results need to be interpreted with caution. During prograde metamorphism and magmatic stages, $^{87}Sr/^{86}Sr$ isotopic homogenization of the protolith, mixing and isotopic exchange may take place (Wickham 1987). Secondly, the Sm-Nd system of the minerals is less prone to re-equilibrate compared to the Rb-Sr system. This results from the relative durability of the major Sm- and Nd-hosting mafic minerals and slower elemental diffusion rates relative to the Rb and Sr. The rate of intracrystalline diffusion may be so slow, even in eclogite facies metagabbros showing disequilibrium in thin section, that adjacent reactant minerals such as plagioclase and augite can react almost as closed systems and preserve their Sm-Nd isotopic composition (cf. Rubie & Brearley 1987). Thirdly, even the geologically meaningful Rb-Sr and Sm-Nd ages were derived from two-point "isochrones", which are based on low probability-of-fit regressions (Ludwig 2012). As only a few analyses and determined analytical errors were available, only the lower band of the true errors is provided (Ludwig 2012). Accordingly, the reliability of these ages is low due to statistically poor coverage of the samples. On this basis, only a difference between Proterozoic (xenolith Xe11) and Phanerozoic (xenolith Xe16) resetting of the Sm-Nd system can be interpreted.

10 CRUSTAL PROVENANCE OF THE VESTFJELLA XENOLITHS

The current crustal thickness (the depth of Moho) in western Dronning Maud Land is considerable, ranging from 52 to 44 km at Heimefrontfjella. It decreases towards the coast to 30 km and reaches 14 km further off the coast (Bayer et al. 2009; Kudryavtzek et al. 1991 as referred in Bayer et al. 2009). In comparison, crustal thickness in the Namaqua-Natal Belt and Kaapvaal Craton of southern Africa varies from 46–50 km and 34–42 km, respectively (Nair et al. 2006). On a global scale, the typical crustal thickness for rifted margins is ca. 30 km (Rudnick & Fountain 1995).

Western Dronning Maud Land has obviously experienced several episodes of crust formation and heating in the course of its evolution. The latest, extensive rifting period during the Jurassic affected the thermal state of the region and the protoliths of the xenoliths, now hosted by Jurassic intrusions. The coverage of geophysical data in the vicinity of Vestjella is poor. Also, the Vestfella mountains, surrounded by the lobes of continental ice sheets, are covered by Jurassic flood basalts that prevent us from observing and sampling the underlying basement. Therefore, many proxies usually used to constrain the bedrock geological interpretation, such as the style of intrusion and intrusive and stratigraphic relationships, are not available. The xenoliths examined provide an *a priori* window into the unexposed continental crust of study area.

The mineral chemistry of rutile, whole-rock trace elements, mineral assemblages, mineral chemistry and isotope geochemistry were used to trace the origins, composition and crustal provenance of the xenoliths studied. This includes interpretations of the geological setting and the PT conditions indicative of the depth in crust and secondary processes that may have modified the geochemistry of the xenoliths.

Whole-rock major and trace elements were analysed for representative samples from the 27 xenoliths covering, in total, seven rock types. The petrography and mineral assemblages of the 27 xenoliths were studied optically and by SEM-EDS. Rutile was recovered from quartz metadiorite and equigranular metagranite samples as a by-product of zircon mineral separation. The mineral chemistry of representative phases was studied using an electron microprobe in search of material for thermobarometric analysis. The isotope geochemistry of two mafic-ultramafic metagabbroic xenoliths and zircon U-Pb geochronology of metatonalite, metagranite and quartz metadiorite xenoliths (six samples in total) were studied as described in Chapter 9.

10.1 Zr-in-rutile and Zr-in-whole-rock saturation temperatures

To estimate the equilibration temperatures for the metagranitoids and quartz metadiorite, whole-rock zircon saturation temperatures were calculated (Watson & Harrison 1983) and the Zr-in-rutile thermometer was applied (Watson et al. 2006, Zack et al. 2004a) (Tables 4 and 9). Rutile was recovered as a by-product of zircon mineral separation from two silicic xenoliths, quartz metadiorite ALKBM1 and equigranular metagranite ALKBM6. From the other metagranitoids, -diorites and -gabbros, rutile was not recovered. The calculated zircon-saturation temperatures, 770–920 °C (Table 9), are compatible with granulite facies metamorphism and supra-solidus conditions in granitoid systems overall (e.g. Holland & Powell 2000). Evaluation of the whole-rock zircon saturation results is, however, difficult due to the relatively small and potentially unrepresentative xenolithic samples and possible pro- and retrograde reactions that may have redistributed Zr in the Zr-bearing minerals such as zircon, rutile, and amphiboles.

In general, rutile is a high-temperature mineral, resistant to retrograde reactions, and may retain information on the source rock history, melt generation and prograde metamorphic reactions producing rutile (together with other Ti-rich phases, such as dissociation of Ti-biotite and amphiboles) (e.g. Xiong et al. 2005, Triebold et al. 2007). As rutile is also resistant to weathering and may even survive subduction, it may have been inherited, however, and it may have crystallized in matrix differing from its *in situ* context. It was, however, reasonable to assume that rutile was crystallized in a quartz- and zircon-bearing, silica saturated system, which usually corresponds to granitoids and quartz dioritoids, as well as quartzofeldspathic metamorphic rocks (cf. Ferry & Watson 2007). Accordingly, equation log(Zr) = (7.36 ± 0.10) – (4470 ± 120)/T (K), calibrated by Watson et al. (2006), was applied. This equation was considered to be more representative than, for example, the equation of Zack et al. (2004a). The thermometer of Zack et al. (2004a) is calibrated on rutile enclosed by garnet and clinopyroxene and yielded considerably higher temperatures (Table 4) above the solidus of the studied silica oversaturated rock types (Fig. 21). Pressure corrections (cf. Tomkins et al. 2007) were not used on either of the thermometers applied because of the poorly constrained pressure conditions during rutile crystallization.

Altogether, 37 spots from rutile in the xenoliths were analysed. Rutile analyses and respective results of the thermometric calculations are shown in Chapter 7.4, Table 4. The rutile in the sample ALKBM1 (quartz metadiorite) is black and compositionally relatively uniform. It shows fairly low Nb (<3050 ppm) contents typical of metapelite and possible for metabasite-derived rutile (cf. Zack et al. 2004b, Zack et al. 2002; Fig. 21) and gives crystallization temperatures of 857–881 °C (Watson et al. 2006, Table 9). The equigranular metagranite ALKBM6 contains two types of rutile: black, V-, Fe- and Nb-bearing, and amber-coloured, Nb- and Fe-rich (Table 4). Three chemically distinctive groups were observed: A single crystal is distinguished by extremely high Zr (3351–4110 ppm) (b1 in Table 9). Two crystals are high in Zr (1234–1486 ppm) and relatively low in Nb (1234–1744 ppm) (B2 in Table 9), whereas the remaining 7 crystals exhibit exceptionally high Nb (17 700–38 600 ppm) and also high FeO (1.3–2.1 wt%) (C in Table 9). The respective rutile equilibration temperatures for metagranite ALKBM6 are 892–920 °C (b1), 770–815 °C (b2) and 791–872 °C (c) (Watson et al. 2006; Table 9). The exceptionally Nb-rich rutile in the equigranular metagranite

(ALKBM6) is compositionally similar to rutile from felsic granulite facies rocks (cf. Zack et al. 2004b, Fig. 21, Zack et al. 2002).

Given that the rutile data were recovered from mineral concentrates, textural features could not be used to constrain the interpretation. The concentrates did not include mixed grains with garnet or clinopyroxene, and neither was inclusion rutile found. The considerable variations in the Zr and Nb contents in rutile probably reflect the overall mineral assemblage and conditions of crystallization. Specifically, the variations in the Nb content probably depend on the presence or absence of adjacent amphibole and biotite during high-grade metamorphosis and anatexis. Both amphibole and biotite are absent from the studied quartz metadiorite and equigranular metagranite xenoliths. The presence of inherited zircon in the samples used for temperature estimates is compatible with rutile also being inherited. This seems probable in the case of equigranular metagranite ALKBM6, given the heterogeneous nature of the rutile population in this sample, and of quartz metadiorite ALKBM1 due to the average metapelite-like composition of the rutile (Fig. 21).

These two thermometry methods use different approaches (whole-rock composition of a crystallizing magma vs. equilibration of the rutile). The rutile in quartz metadiorite xenolith ALKBM1 yielded high granulite facies temperatures of 880–860 °C (cf. Watson et al. 2006). Whole-rock zircon-saturation temperature for the same sample is considerably lower (650 °C) (cf. Watson & Harrison 1983). The rutile in equigranular metagranite ALKBM6 is compositionally heterogeneous and records a temperature range between 770 and 920 °C (cf. Watson et al. 2006). The whole-rock zircon-saturation temperature for the same sample, 780 °C (cf. Watson & Harrison 1983), is similar to the lower range of the rutile results. Under the above-mentioned temperatures, the silicic protoliths of the xenoliths have probably been partially molten, even without an aquatic fluid. Under a moderate pressure of 5 kbars, 8–12.5% melt may have been generated (Rubie & Brearley 1987).

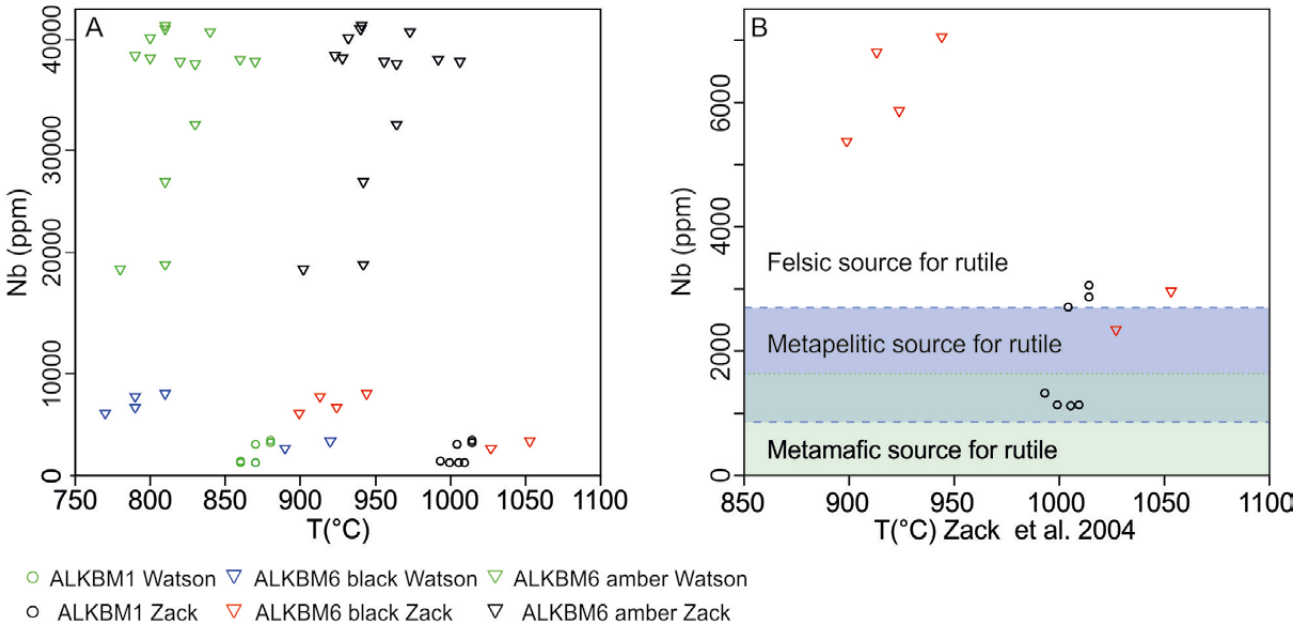

Fig. 21. Results of Zr-in-rutile thermometry. (A) Comparison of the temperatures obtained with calibration after Zack et al. (2004) and Watson et al. (2006). (B) Estimate of the rutile provenance rock type on the basis of the Nb concentration in rutile. Lower limit for metapelitic rutile 900 ppm and upper limit 2700 ppm (cf. Zack et al. 2004b).

Table 9. Results of the thermo- and barometry.

Metagabbroids	P(kbar)	T(°C)	Method	Depth in km / mixed burden*	Depth in km/ granite burden**
P-4, Xe-11	<11	1100	Basalt-eclogite transition (Green & Ringwood 1962)	<36	<41
Xe-16	19	1040	TWQ v. 2.34 (Berman 1991, Berman & Aranovich 1996, Berman et al. 1995, Berman & Aranovich 1997)	63	70
Xe-16	19.9	1050	Thermocalc 3.33 1) prp+2grs=3di+3cats 2) prp+2grs+3qtx=3an+3di 3) 2grs+ alm+3qtz=3an+3hed (Powell & Holland 2009, Powell & Holland 1988)	66	74
Quartz metadiorite					
ALKBM1		857-881	Zr in Rt, fraction a (Watson et al. 2006)		
		657	Zrn saturation (Watson & Harrison 1983)		
Xe-10	>6		Opx+Pl±Spl=Grt±Cpx±Qtz (Griffin & Heier 1973)	>20	>22
		651	Zrn saturation (Watson & Harrison 1983)		
Metatonalites					
Xe-1		749	Zrn saturation (Watson & Harrison 1983)		
Xe-4		747	Zrn saturation (Watson & Harrison 1983)		
Metagranites					
ALKBM6, equigranular		892-920	Zr in R, fraction b1		
		770-815	Zr in Rt, fraction b2		
		791-872	Zr in Rt, fraction c		
		785	Zrn saturation (Watson & Harrison 1983)		
Xe-6, gneissic		679	Zrn saturation (Watson & Harrison 1983)		
Xe-7, gneissic		690	Zrn saturation (Watson & Harrison 1983)		
Xe-2, mylonitic		781	Zrn saturation (Watson & Harrison 1983)		
Xe-5, mylonitic		816	Zrn saturation (Watson & Harrison 1983)		
Metasedimentary rock types					
Xe-13, P-5	≥10	≥800	Bt+Pl+Crd±Qtz=Grt+Als+Kfs+melt (Koester et al. 2002), Bt+Pl+Qtz=Opx+Kfs+melt (Spear 1993)	≥33	≥37
P-5	17.8		Thermocalc 1) sp + qtz = mgts 2) en + 2spl + 2kya = 4mgts 3) fs + 2kya = 2herc + 4qtz (Powell & Holland 2009, Powell & Holland 1988)	59	66

*Pressure gradient 3.3 kbar/km d=2970 g/cm^3 **Pressure gradient 3.7 kbar/km d=2800 g/cm^3

10.2 Thermobarometry and metamorphism

In the following, I will review the PT conditions of the metagabbros, metatonalites, quartz metadiorites and metasedimentary xenoliths. The temperature and pressure conditions of recrystallization of the xenoliths are difficult to decipher due to the lack of suitable minerals or mineral pairs and the observed textural and mineral chemical disequilibria in the metagabbroic samples and metapelitic sample Xe13 (Table 9). Also, the equilibration in granulite facies indicates diffusion closure rather than the precise formation P and T (Thompson 1990). However, the texture and mineralogy, particularly of the meta-igneous samples, is consistent with a high metamorphic grade (Fig. 3). Consistent with this are the signs of partial melting within the silicic xenoliths (Fig. 6). Textural evidence of slow decompression, the kelyphitic rims of garnet (cf. Rudnick 1992) and symplectic clinopyroxene, was observed within the metagabbros (Figs. 19F–H). This may be indicative of uplift; further, deep crustal granulites may be tectonically transported to higher crustal levels (cf. Moorbath & Taylor 1986, Treloar et al. 1990). The accidental nature (cf. Chapter 4) of the xenoliths also implies that the studied samples may not represent the different crustal levels in an equal manner.

10.2.1 Metagabbros

Pressure estimates using the basalt-eclogite transformation diagrams of Green and Ringwood (1967) for quartz tholeiitic and alkali basalt compositions at 1100 °C imply a pressure range of 11–17 kbar (ca. 36–56 km) for the garnet-bearing metagabbro (Xe16) and notably lower pressures of 5–8 kbar (ca. 17–26 km) for the garnet-free metagabbros (Xe11, P4). To obtain semi-quantitative pressure and temperature results for the garnet-bearing metagabbro Xe16, TWQ 2.34 (Berman 1991) and Thermocalc 3.33 (Powell & Holland 2009, Powell & Holland 1988) multi-reaction equilibria programs were used. To obtain semi-quantitative results using Thermocalc, an assemblage grt + cpx + pl + qtz was used, although quartz was not observed in the metagabbro Xe16. It was further assumed that sample Xe16 had been affected by secondary K_2O enrichment (see chapter 6) and the K_2O content of plagioclase was adjusted from 1.6 to 0.5 wt% K_2O to calculate the activities of anorthite and albite. In TWQ calculation, the assemblage grt + cpx + pl + phl + qtz was used. The results of the TWQ and Thermocalc calculations suggest nearly identical temperatures (1050 °C and 950–1050 °C, respectively) and pressures (19 kbars and 20 kbars, respectively). These conditions correspond to a depth of 63–66 km.

Based on mineralogy rich in garnet, plagioclase and pyroxene with minor or absent amphibole and biotite, sample Xe16 may represent a lower crustal granulitic restite (cf. Clements 1990). However, the mafic lower crustal xenoliths have commonly been interpreted to represent intra- or underplated mafic magmas instead of restitic leftover material after the extraction of granitic melt (Arculus & Ruff 1990). Given the equilibration of the Sm-Nd isotopic system of sample Xe16 in the Phanerozoic, the xenolith may represent lower crustal material (Rudnick 1992). This would be consistent with the recorded pressure and temperature (Table 9). Therefore, the garnet-bearing metagabbro probably represents lower crust, whereas the garnet-free metagabbros may have been derived from shallower depths (cf. Moorbath & Taylor 1986).

10.2.2 Metatonalites and quartz metadiorites

The metatonalite Zr-in-whole-rock saturation temperature, 750 °C, is consistent with the textural evidence of partial melting (Chapter 7.5). The reaction relationship opx + pl = grt +cpx + qtz observed for the quartz metadiorite xenolith Xe10 also suggests high granulite facies conditions for the quartz metadioritic samples. The presence of almandine-rich garnet in the metatonalites refers to pressures higher than 13 kbar (Allen & Boettcher 1983, Schmidt & Thompson 1996) and, overall, granulite facies (Table 9).

10.2.3 Metasedimentary rock types

Based on the assemblage of qtz, kfs ±ky ± opx ± spl, the metapelitic xenoliths P5 and Xe13 probably re-crystallized at 8–11 kbar (cf. Spear 1993) (Table 9). This corresponds to a depth of 26–36 km.

10.3 Incompatible element geochemical constraints

Previously (Chapters 10.1 and 10.2), mineralogical evidence of the crustal provenance of the xenoliths has been presented. Here, the geochemical composition of incompatible elements of the xenoliths is used to decipher their origins and depth in the continental crust. This complements the PT -data presented in Chapters 10.1 and 10.2. The characterization of the three-layer continental crust consisting of upper, middle, and lower layers (Rudnick & Fountain 1995) is based on extensive geological and seismic datasets. The research on this topic is on-going, but, modifications for the established elemental abundances have recently been rather moderate (cf. Rudnick & Gao 2004, McLennan et al. 2006). To compare the incompatible element composition of the Vestfjella xenolith samples with the globally representative values of the upper, middle and lower crust, I normalized the whole-rock data relative to the data given in Rudnick and Fountain (1995). In addition to the resulting averaged compositions, they presented data typical of different tectonic provinces, of which I used the continental arc and rifted margin data. In the following, the abbreviation LCC denotes the average lower continental crust, MCC is the average middle continental crust, and UCC is the average upper continental crust (Rudnick & Fountain 1995). A common feature for the continental crust-normalized metagabbro, metatonalite, metagranite and metasedimentary xenoliths studied is a moderate (1–4-fold) positive K anomaly (Fig. 22), which may be indicative of xenolith-based or regional K-metasomatosis of the xenolith protoliths derived from the depths of 10–66 km (cf. Rudnick 1992, Moorbath & Taylor 1986). Figure 22 is a summary of the best-fit incompatible element fingerprints relative to established crustal compositions.

10.3.1 The continental crust reference values used

Knowledge of the geochemical and mineralogical characteristics of the continental crust is based on large, diverse datasets (e.g. Rudnick & Fountain 1995). These include both geological (geochemical and mineralogical) and seismological datasets from different geological environments such as convergent and divergent plate margins and continental areas subject to compressive and extensive tectonic regimes. The interpretations for the composition and characteristics of the bulk continental crust and different levels of the continental crust (upper crust, middle crust, lower crust) is are based on the actual rock materials studied: clastic sedimentary rocks, shales, granulite terrains, xenolith samples, deep continental drilling core samples, and proxies such as the geochemical composition of magmas derived from and erupted through the crust. The role of seismic data is crucial, as the exposed crustal sections only open a window to scattered and sometimes controversial geological evidence. Once the seismic properties of the crustal rock types have been determined, the seismic reflection data, showing the characteristic seismic velocity for each rock type in their present status (such as the mineral mode, degree of partial melting and crystal orientation), are used to interpret the division and thickness of the rock units of distinctive seismic velocities within the crust.

In particular, the depth of the transition zone between the crust and the mantle, the Moho, is determined via seismic data. The Moho is a place where the seismic velocity exceeds a certain value (e.g. Levander et al. 2006), but it cannot be considered as a solid, unchangeable reference surface (Levander et al. 2006). It is useful to note that the Moho evolves through time and its significance differs between tectonic settings. For example, the seismic Moho may locate higher relative to the petrologically determined crust-mantle boundary, and the metamorphic reactions (such as eclogitization) and magmatic underplating may cause the Moho to shift downward (Levander et al. 2006). Due to the buoyancy and complex crustal dynamics, the continental crust is not destroyed as the oceanic crust is (ca. 200 Ma) (e.g. Davidson & Arculus 2006). Accordingly, the continental crust is more heterogeneous and has been subject to multiphase evolution and differentiation, whereas the oceanic crust is less complex in character.

The established values for average continental crust (e.g. Rudnick & Fountain 1995, Rudnick & Gao 2003, Taylor & McLennan 1995) are based on studies in which several factors have been considered. These include the seismic and geological

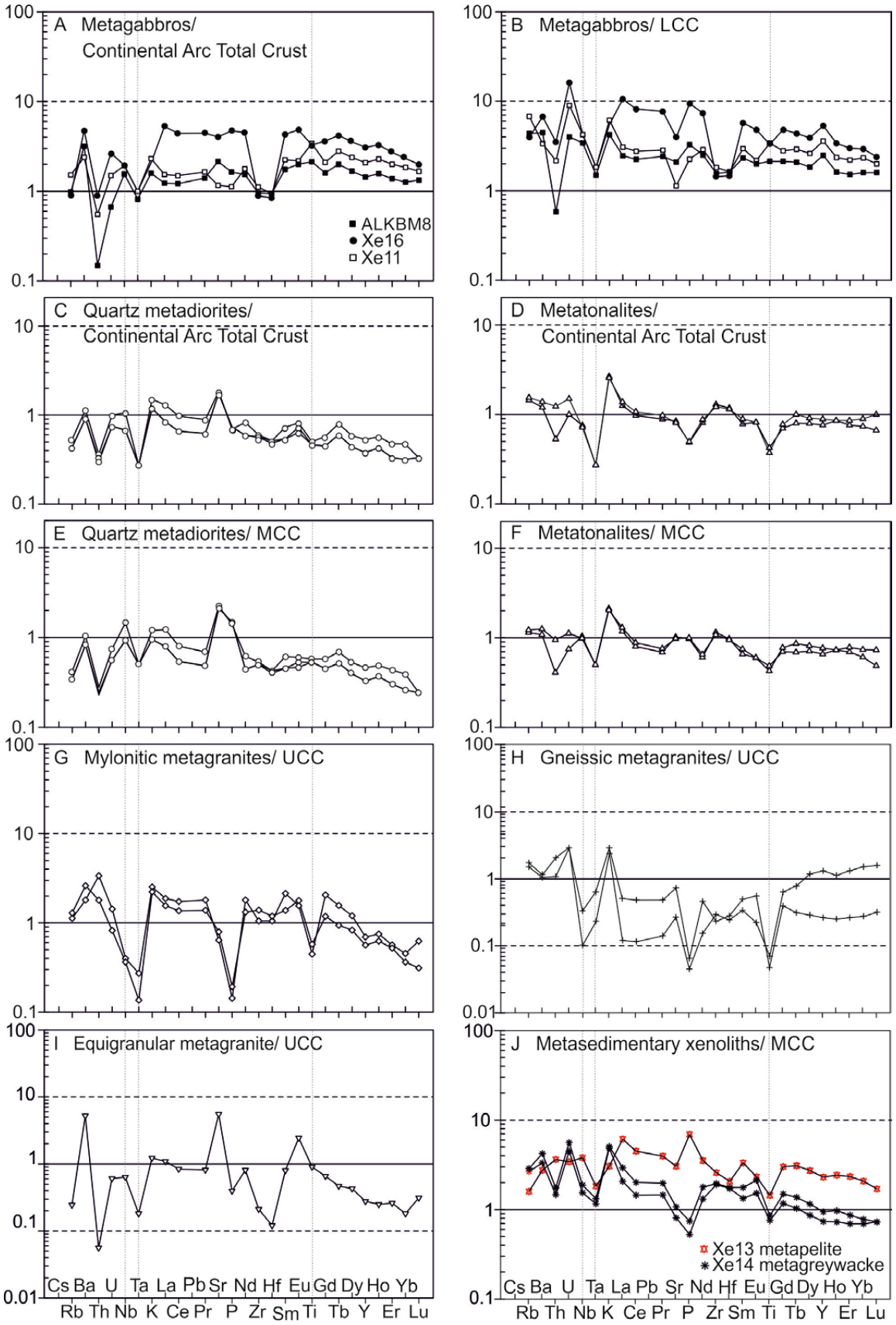

Fig. 22. The incompatible trace elements of the xenolith samples normalized against the selected averages of the continental crust (cf. Rudnick & Fountain 1995). (A) Metagabbros vs. average continental arc crust; (B) metagabbros vs. average lower continental crust; (C) quartz metadiorites vs. average continental arc crust; (D) metatonalites vs. average continental arc crust quartz; (E) quartz metadiorites vs. average middle continental crust; (F) metatonalites vs. average middle continental crust; (G) mylonitic metagranites vs. average upper continental crust; (H) gneissic metagranites vs. average upper continental crust; (I) equigranular metagranite vs. average middle continental crust; (J) metapelite and metagreywacke vs. average middle continental crust.

properties of crustal segments and the nature and timing of the crust-forming processes. The element abundances, especially the trace element contents, are strongly dependent on the geochemical composition of the rock types interpreted to dominate the specific crustal levels. The formation of felsic crust during the Proterozoic was dominated by magma production on destructive plate margins, i.e. arc environments. The most voluminous felsic magmatism has been recorded in continental arcs, where the mafic oceanic lithosphere is subducted beneath previously formed continental crust. The hypothesis is often referred to as the "Andesitic model".

The trace element signature of the granitic samples shows considerable variation. This is typical of granitic rocks, as their sources are more diverse and mainly indicate the heterogeneity of their crustal sources, including magma mixing, assimilation, fractional crystallization and the degree of partial melting. In addition, the trace element composition of the granitic samples is considered relative to the model average crustal compositions after Rudnick and Fountain (1995). In the andesitic model and modern volcanic arc systems, granitic magmas are voluminously minor relative to the basaltic, andesitic and dasitic magmas. Therefore, the granite compositions have less weight when modelling and calculating the average crustal compositions.

10.3.2 Metagabbros

The trace element patterns of the metagabbro xenoliths best fit the total continental arc crust and average LCC (Figs. 22A & B). The metagabbros are, however, slightly enriched relative to the above-mentioned reference values and display a smooth REE pattern relative to standardization values, with only 2-3-times higher concentrations. The lower crust shows depletion in the heat-producing elements U, Th and K because of their incompatible nature. The metagabbros show depletion of Th relative to the total continental arc crust (Fig. 22A) and average LCC (Fig. 22B), which supports the idea of lower crustal origins. However, the samples are enriched in the LREE relative to the average LCC (Fig. 22B). Comparison with rifted margin lower crust (Rudnick & Fountain 1995) shows that the Rb concentration of the metagabbros is 7–10 times higher. The metagabbros show notable enrichment in incompatible elements relative to the rifted margin lower crust and continental arc lower crust (cf. Rudnick & Fountain 1995). Relative to MCC and UCC, the samples are generally depleted but the K content of the metagabbros is similar or slightly enriched relative to the MCC (cf. Rudnick & Fountain 1995).

The continental lower crust is thought to be depleted in heat-producing and fluid-mobile elements due to its residual nature. The incompatible element signature of the Vestfjella metagabbro xenoliths is more like the total continental arc crust composition, which implies that the protoliths have not been severely depleted by melt extraction or fluxing by reductive fluid (cf. Clements 1990). This may be because the trace element geochemistry reflects the protolith magmatic compositions or that the xenolith protoliths were (re)-enriched in trace elements and REE at some point of their evolution by metamorphic and/or metasomatic fluids (cf. Moorbath & Taylor). On the basis of petrographic evidence, it is likely that the whole-rock composition is a composite of primary and metamorphic and/or metasomatic features.

10.3.3 Metatonalites and quartz metadiorites

The incompatible element patterns of the metatonalite xenoliths best fit the total continental arc crust and average MCC (Figs. 22D & F), although the HREE concentrations of these are similar to the average continental arc lower crust. The metatonalites are, however, slightly enriched relative to the total continental arc crust and average MCC; Th, Ta, P and Ti show negative anomalies, pronounced relative to the continental arc crust. The incompatible element patterns of the quartz metadiorite xenoliths best fit with those of the total continental arc crust and average MCC (Figs. 22C & E). The general trend of the quartz metadiorites is slight depletion relative to the above-mentioned reference values. Only Sr shows enrichment, by a factor of 2, and Rb, Th and Ta show negative anomalies in both cases. In terms of major and trace elements compatible in plagioclase and clinopyroxene, the quartz metadiorites are quite similar to those of the average MCC with, for example, SiO_2 of 60–61 wt%, Ni of 25–33 ppm, Cr of 110–119 ppm, Ba of 332–418 ppm and Sr 595–627 ppm, whereas incompatible element

concentrations, e.g. Zr (62–67 ppm), are lower (cf. Rudnick & Fountain 1995).

Relative to the rifted margin lower crust and continental arc lower crust the xenoliths are, however, relatively enriched, and only slightly depleted relative to UCC (cf. Rudnick & Fountain 1995). These results emphasize the volcanic arc affinities of the xenoliths and also suggest that these four xenoliths are genetically related. The difference in their HREE enrichment relative to chondrite (Fig. 16) may indirectly refer to the depth of magma generation (source mineralogy) or degree of melting. Metatonalites (ca. 10 times enriched) may have been generated at a shallower depth relative to quartz metadiorites, enriched <10 times relative to chondrite. The combination of high whole-rock Mg numbers, high SiO_2 and within-plate basalt-type affinity indicated by the discrimination diagram of Meschede (1986) (Fig. 5C) is compatible with generation of the quartz metadiorites by crustal contamination of a mafic magma, possibly in an island arc environment (cf. Pitcher et al. 1985).

10.3.4 Metagranites

The mylonitic metagranites are nearly identical and show slightly enriched compositions relative to those of the average UCC (Fig. 22G), but pronounced negative Ta, P and Ti anomalies. Their REE pattern resembles that of ocean island basalts (Fig. 16). The gneissic metagranites (Fig. 22H) are typified by variably low incompatible element contents. The LREE pattern of sample Xe6 resembles the one of island arc basalts, and enrichment of HREE relative to the chondrite may be indicative of a magma source above garnet stability in the crust (Fig. 16). Sample Xe7, in contrast, is different from IAB and shows HREE depletion, which may be indicative of a magma source within the garnet stability field in the crust. These features may, however, also originate from the fractionation or removal of mafic minerals during the evolution of the xenoliths. The gneissic metagranites are suspiciously leucocratic, which may refer to alteration due to secondary processes, e.g. fluids. Equigranular metagranite shows varying concentrations and resembles neither average UCC nor MCC (Fig. 22J).

10.3.5 Metasedimentary rock types

Metapelite xenolith Xe13 also geochemically resembles granulite facies metapelite xenoliths, although the K_2O, P_2O_5, REE, U and Th values are clearly higher (cf. Rudnick & Fountain 1995). Sample Xe13 is dominated by leucosome material derived by partial melting, which may explain the increase in LIL elements K, U and Th. Metagreywacke xenolith Xe14 best fits the MCC (Fig. 22J), especially in its HREE. The REE pattern of Australian shale composite PAAS (cf. McLennan 1989) is notably similar but differs in its negative Eu anomaly, which is not present in the metagreywacke.

10.4 Control points from geochronology and isotopic tracers

10.4.1 General remarks

The zircon ages determined for meta-igneous xenolithic rock types represent both inherited ages derived from the source rocks of the magmas and ages that mark crystallization of the zircon and subsequent re-equilibration. Some of the zircon shows rims of high reflectivity in cathodoluminescence images but could only be measured for the metatonalite xenoliths, as the majority of the rims were too narrow to analyse (<25).

The observed zircon ages and Sm-Nd results add to the regional geological context of the western Dronning Maud Land. Early Mesoproterozoic zircon cores of the metatonalites pre-date the 1.1 Ga Grenville-age thermal event. Mesoproterozoic zircon coincides with the major 1.1 Ga phase of the Grenvillian orogeny. Neoproterozoic zircon of the metatonalites and metagranites post-date the 1.1 Ga major Grenvillian thermal event (Fig. 23). Scattered zircon ages of the quartz metadiorite coincide with the Pan-African thermal event related to the vast East African Antarctic orogeny of Mozambique belt, Madagascar, and central Dronning Maud Land (Fig. 23, Table 10). The zircon of the equigranular metagranite post-dates the major phase of the Jurassic Karoo event. Also, quasi-linear discordance arrays of the gneissic and mylonitic

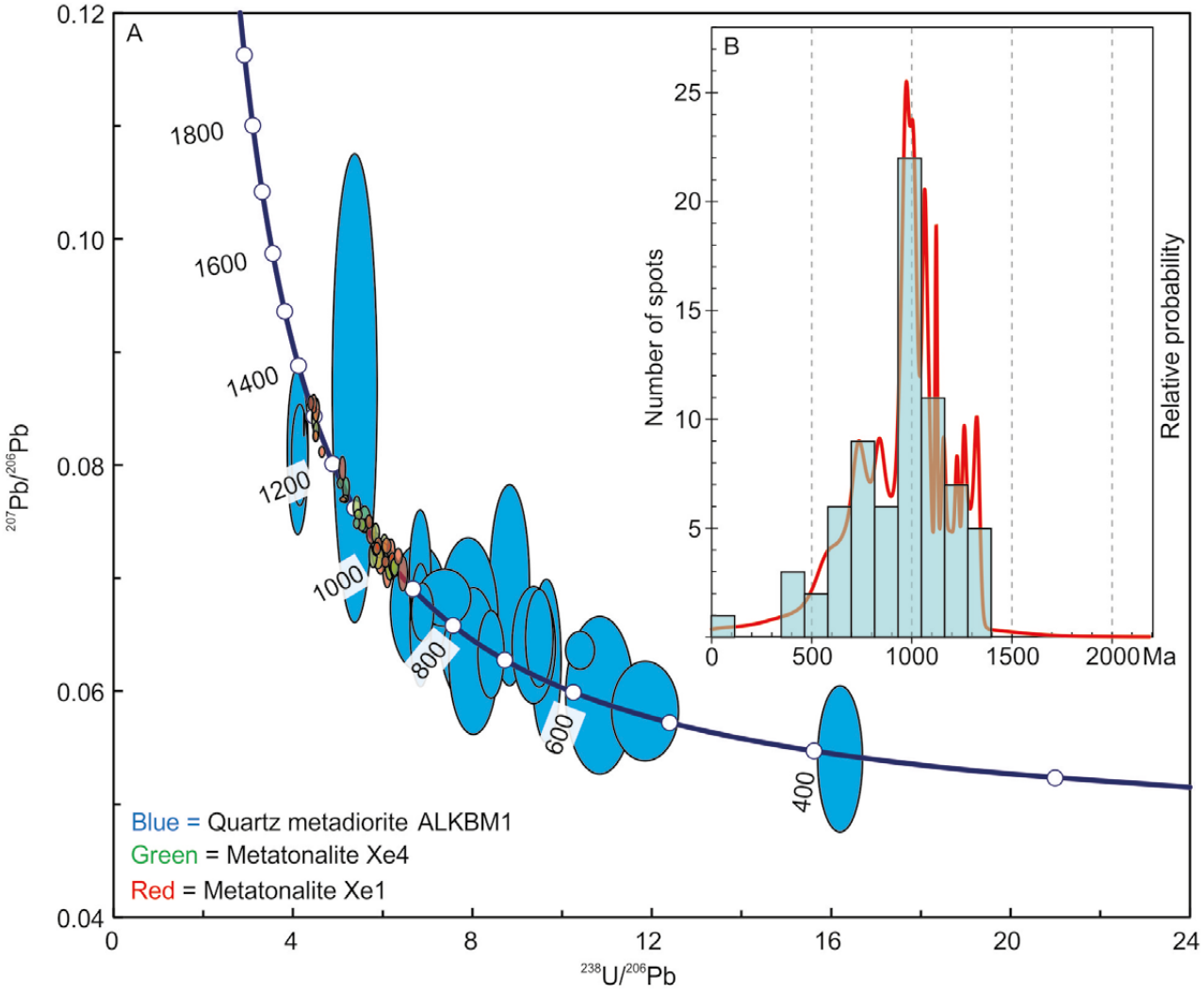

Fig. 23. Combined zircon data for quartz metadiorite ALKBM1 and metatonalites Xe1 and Xe4, indicative of a prolonged period of zircon crystallization in silicic arc-affinity rocks of Vestfjella. Tera-Wasserburg $^{238}U/^{206}Pb$ versus $^{207}Pb/^{206}Pb$ diagram, ALKBM1 (blue), Xe1 (red) and Xe4 (green). Error ellipsoids plotted at the 2σ level, red and green rescaled for visibility. Inset: Probability density plot of the combined dataset.

metagranites record the approximate timing of the major thermal events among the concordant data: the Meso-Neoproterozoic and Triassic-Jurassic.

The Sm-Nd isotope composition of the mafic xenoliths is indicative of Mesoproterozoic and Phanerozoic thermal events, such as those reported in numerous studies on Grenville-age metavolcanic rocks and Karoo volcanic rocks and associated intrusive rock types at western Dronning Maud Land and southern Africa. The strongest affinity of incompatible trace elements of the studied metagabbroic xenoliths is towards continental arc total crust (cf. Rudnick & Fountain 1995), which includes the lower, middle and upper crust (LCC, MCC and UCC, respectively). Relative to the average lower crust, the metagabbros are only slightly more enriched (Fig. 22). The incompatible trace element concentrations of these xenoliths indicate more pronounced enrichment relative to the lower crust of rifted margins and continental arcs (cf. Rudnick & Fountain 1995). The heat-producing LILE elements Rb, Th, U and K show 3–12-fold and 1–10-fold enrichment, respectively. Relative to the middle and upper continental crust, these xenoliths are generally depleted, but relative to potassium content of the MCC the metagabbro xenoliths are similar or slightly enriched. Enrichment in Rb and K may derive from lamproite or crustally derived metasomatism (cf. Rudnick 1992, Moorbath & Taylor 1986).

The observation of abundant pargasitic, Na-bearing and K-rich hornblende in xenolith Xe11

and untypically high K of plagioclase (up to 1.7 wt% K_2O) in both of the studied metagabbroic xenoliths is consistent with the alkali-enriched nature of the samples, also indicated by their whole-rock compositions (Figs. 14A & B). The notably REE-enriched signature of the garnet-bearing metagabbro Xe16 (Figs. 16, 22A & B) is consistent with occurrence of garnet but may also originate from apatite, untypically abundant for average gabbroic rocks (3.5 vol.%). The apatite in the metagabbro xenoliths Xe11 and Xe16 has probably been affected by secondary processes such as heating of the western Dronning Maud Land continental crust, as it is anhedral and full of fluid inclusions (cf. Figs. 19F–H).

The Rb-Sr and Sm-Nd isotopic composition measured for the Vestfjella xenoliths may represent mixtures of regionally derived partial melts and fluids. The εNd (180 Ma) values of the metagabbros are quite different from each other, being -2.3 (Xe11) and -8.5 (Xe16) (Table 8). The ages of 1450 and 180 Ma indicated by the Sm-Nd two-mineral diagrams (Fig. 20) were used to determine initial εNd for the samples: εNd(init) +7.1 (Xe11) and -8.5 (Xe16). These inferred initial values resemble mantle-derived magmas and enriched crustal compositions, respectively, and are different from uncontaminated mantle-derived mafic magmas such as N-MORB. However, whether this εNd signature was magmatic or due to secondary enrichment, e.g. by lithospheric mantle-derived fluids or melts, would require in situ isotope analysis of the minerals of these metamorphosed xenoliths, for example. As a reference, the εNd (160Ma) value of the Vestfjella lamproite dyke, the best representative of the western Dronning Maud Land lithospheric mantle, is ca. -6 (cf. Luttinen et al. 2002). The whole-rock present-day Sm-Nd isotopic composition of the metagabbros shows affinity to Karoo province gabbroic rocks and granulite xenoliths (Fig. 24), although the interpretation is hampered by the large uncertainty involved in granulite facies xenolith age determinations.

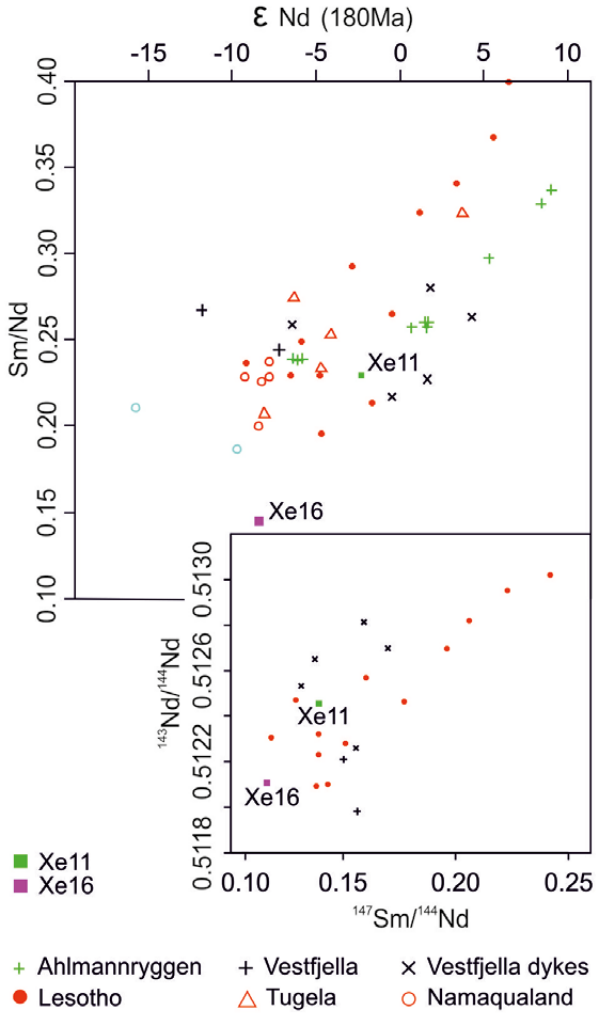

Fig. 24. εNd (180 Ma) versus Sm/Nd of the Vestfjella metagabbro xenoliths with data from Northern Lesotho, Namaqualand (Markt) and Tugela Terrain (Letsen-la-Terae) mafic granulite xenoliths of variable and uncertain age, Ahlmannryggen Jurassic quartz tholeiitic gabbros, and Vestfjella Jurassic gabbroic rocks. εNd calculated relative to CHUR = 0.512640, ^{137}Sm decay constant = 0.00654 (DePaolo 1981). Inset: ^{137}Sm/^{144}Nd versus ^{143}Nd/^{144}Nd diagram of Vestfjella gabbroic rocks and Lesotho mafic granulite xenoliths. Reference data after Riley et al. (2005), Rogers and Hawkesworth (1982), Schmitz and Bowring (2004), Huang et al. (1995) and Luttinen et al. (2015).

10.4.2 Zircon chronology

The ca. 1300 Ma Mesoproterozoic zircon cores of Vestfjella metatonalites are older than the Neo- to Mesoproterozoic Natal-Maud mobile belt zircon ages obtained in earlier studies (Table 10). This age group may record mafic magmatism of the volcanic arcs before accretion of the arc terrains to form the Grenvillian Natal-Maud Belt and, possibly, emplacement of tonalite intrusions. These crystals may have derived from the amphibolitic source of the tonalites, and the younger 950–1020 Ma zircon would possibly mark the slow tonalite magma crystallization within the middle crust. The majority of the zircon of the quartz metadioritic xenolith ALKBM1 was crystallized between 850 and 500 Ma, as recorded by the concordant spot analyses, although they were low in precision due to the zircon quality (Fig. 23A). On the basis of its texture, geochemistry, presence of magnesium-rich clinopyroxene, and highly variable zircon ages, the sample is likely a plutonic rock which contains detrital zircons. The detrital zircon was obtained by assimilation of older rock material. The zircon ages, however, may indicate that the high-temperature event, repeatedly causing the U-Pb system of the zircon to open, was long-lasting and coeval with the Pan-African event involved in Rodinia rifting and subsequent Gondwana assembly. The primary crystallization of zircon as a result of local rifting, causing crustal thinning and related magmatism, cannot be excluded, either. The quartz metadiorite ALKBM1 zircon population and its $^{207}Pb/^{206}Pb$ ages differ from those of the geochemically similar metatonalite xenoliths of this study (Fig. 23A) and also from Neo- to Mesoproterozoic Natal-Maud Belt zircon U-Pb ages of earlier studies (Table 10). The quartz metadiorite age results of this study are more similar to the Pan-African zircon ages of central Dronning Maud land and Mozambique belt correlated to the magmatism during the East African–Antarctic orogeny.

The Vestfjella metagranites show two age groups: Mesoproterozoic and Jurassic (Fig. 18). The zircon in deformed, gneissic and mylonitic metagranites is metamict and mainly discordant. The upper intercept ages indicate Mesoproterozoic crystallization of the zircon at 1094 ± 11 Ma (4 concordant spots) and 1021 ± 30 Ma, respectively. The concordant upper intercept of the gneissic metagranite Xe6 may record granite crystallization during arc-continent collision. The tectonic event that produced the mylonitic texture of xenolith Xe2 caused zircon crystallization during the cooling of the continental crust at 1021 ± 30 Ma. The Concordia age 165 ± 1 Ma of the equigranular metagranite ALKBM6 probably records granite crystallization and also sets the minimum age of the host lamproite dyke. This Jurassic xenolith is also distinctive relative to the other xenoliths due to its REE and trace element composition, which probably reflects a different source.

10.4.3 Isotopic tracers

Even though the Rb-Sr and Sm-Nd data and texture of the metagabbro xenoliths Xe11 and Xe16 imply mineral disequilibrium, some of the mineral pairs yield geologically meaningful ages that reflect equilibration of the Rb-Sr and Sm-Nd systems in the xenoliths (Fig. 20). However, to gain more confident age results, at least five data points per sample (Ludwig 2012) or per group of cogenetic samples would be preferred. Initial εNd values were calculated for these two metagabbro xenoliths on the basis of information gained from the whole-rock mineral diagrams (Table 8.). The εNd values calculated at 1450 Ma for the metagabbro Xe11 and at 180 Ma for the garnet-bearing metagabbro Xe16 are compatible with the samples having been equilibrated during the Proterozoic and the Phanerozoic, respectively. Rb-Sr closure of apatite and plagioclase (571 ± 20 Ma) in metagabbro Xe11 may record metasomatism of this xenolith (Fig. 20). The high initial εNd value of xenolith Xe11 (+7.1) refers to mantle-derived origins, and the low initial εNd value of xenolith Xe16 (-8.5) refers to a possibly older crustal source, but isotopic mixing may have occurred (see 10.3.2). As plagioclase of xenolith Xe16 has been a reactant phase to form garnet under higher pressure relative to the equilibration of the garnet-free xenolith Xe11, it seems likely that the Sm-Nd system of xenolith Xe16 was re-equilibrated during the Jurassic, but its protolith possibly originated earlier. Also, the present-day whole-rock Sm-Nd isotopic composition does not significantly differ from those of the Jurassic Karoo province gabbroic rocks and granulite xenoliths of Proterozoic to Phanerozoic age (Vuori 2004, Rogers & Hawkesworth 1983) (Fig. 24).

Table 10. The regional zircon chronology of western Dronning Maud Land and adjacent areas.

All the ages are zircon U-Pb unless otherwise stated. N refers to number of grains analyzed.

Western Dronning Maud Land

Area	Reference	Rock type	Method	Age (Ma)	Interpretation
Vestfjella xenoliths					
Kjakebeinet	This work	Metatonalite Xe1	SHRIMP 207/206 n=2	966±7	Crystallization
"	"	"	SHRIMP 207/206 n=2	1009±6	Crystallization
"	"	"	SHRIMP 207/206 n=2	1318±21	Inherited
Kjakebeinet	"	Meta-tonalite Xe4	SHRIMP 207/206 n=4	959±10	Crystallization
"	"	"	SHRIMP 207/206 n=5	1010±10	Crystallization
"	"	"	SHRIMP 207/206 n=6	1074±7	Crystallization
"	"	"	SHRIMP 207/206 n=3	1140±18	Crystallization
"	"	"	SHRIMP 207/206 n=2	1286±15	Inherited
Kjakebeinet	"	Equigranular metagranite ALKBM6	SIMS 207/206	165±1	Igneous
Kjakebeinet	"	Gneissic metagranite Xe6	SIMS 207/206 n=3	1094±11	Igneous
	"	"	SIMS upper intercept	1050±52	Igneous, all zircons
	"	"	SIMS lower intercept	223±60	heating, all zircons
Kjakebeinet	"	Mylonitic metagranite Xe2	SIMS 207/206 n=2	1009±15	Small zircons concordia
	"	"	SIMS upper intercept	1021±30	deformation, all zircons
	"	"	SIMS lower intercept	193±33	heating, all zircons
Kjakebeinet	"	Quartz metadiorite ALKBM1	SIMS 207/206 n=1	230	heating/lead loss see Figs. 23 and 25
	"	"	SIMS 207/206 n=1	1350	Inherited see Figs. 23 and 25
Kjakebeinet	"	Garnet-metagabbro Xe16	T_{DM}	1204	
	"	"	Sm-Nd [Pl-Cpx]	184±45	Sm-Nd closure
	"	"	Rb-Sr [Cpx-whole rock]	101±19	
Kjakebeinet	"	Garnet-free metagabbro Xe11	T_{DM}	1456	
	"	"	Sm-Nd [Pl-whole rock]	1444±36	Sm-Nd closure
	"	"	Rb-Sr [Pl-Ap]	571±20	
West-Muren	Luttinen & Furnes 2000	Metagranitoids X4 and X3	T_{DM}	3240-3270	
West-Muren	Luttinen & Furnes 2000	Metasandstone X5	T_{DM}	1550	
Vestfjella outcrops					
Muren, Utpostane	Vuori 2004	Gabbro	ID-TIMS 207/206 Zrn, Bad	~180	
Utpostane	"	Bt-granite A1649	ID-TIMS 207/206	180±4	
"	"	"	"	185±5	
Mannefallknau-sane					
	Arndt et al. 1991	Charnockite 12.2/1	ID-TIMS 207/206, upper intercept	1073±8	
	Rämö et al. 2008	Wiborgite	LAMS	1073±6	Igneous
	Rämö et al. 2008	Pyterlite	LAMS	1084±8	Igneous
Heimefrontfjella (HF) (direction N-S)					
Kottasberge (NE-HF)	Bauer et al. 2003a	Felsic meta-volcanite S1-55	SHRIMP 207/206	1161.2±9.5	Igneous
"	"	Felsic meta-volcanite S1-49	"	1129±31	Igneous
Sivorgfjella	"	Mafic meta-volcanite S1-32	"	1086±10	Igneous

Table 10. Cont.

Area	Reference	Rock type	Method	Age (Ma)	Interpretation
Kottasberge	Bauer et al. 2003b	Tholeiite dyke KB156	SHRIMP 207/206	1033.4±7	Igneous
Sivorgfjella	"	EMORB dyke KB136	SHRIMP 207/206, n=1	586±7	Igneous
Milorgfjella (NE-HF)	Arndt et al. 1991	Garnet amphibolite 17.1/7	SHRIMP 207/206	1060±8	Metamorphic, amphibolite terrain
"	"	Granitic pegmatite 3.1/2	"	1060±8	Igneous
"	"	Augen gneiss A7.1/1	ID-TIMS 207/206	1088±10	Igneous, main episode of felsic magmatism
Tottanfjella (SW-HF)	"	Granodiorite 9.2/22	ID-TIMS 207/206	1045±9	Igneous, after the main metamorphic event
Vardeklettane (SW-HF)	"	Charnockite 10.2/2	ID-TIMS 207/206	1135±8	Igneous
"	"	Quartzite 10.2/1	SHRIMP 207/206	1104±5	Metamorphic, granulite terrain
"	"	"	"	1215±15	Detrital
"	"	"	"	~2000	Detrital
Kirwanveggen					
Polaris Ridge	Kleinschmidt et al. 1996	Granitoid sheet Z 2-2	Single grain evaporation TIMS	1073±35	
	"	Granitoid sheet Z 5-2	"	1058±18	
Central Dronning Maud Land (direction W-E)					
Area	Reference	Rock type	Method	Age (Ma)	Interpretation
Annandagstoppane					
	Marschall et al. 2010	Granite, granodiorite, Bt-enclaves	Ion microprobe	3067±8	Igneous, Grunehogna basement
Ahlmannryggen					
Ritscherflya supergroup	Marschall et al. 2009	80 detrital zircon grains	LA-ICP-MS 207/206 histograms	1110-1170	Detrital
				1350	Detrital
				1700	Detrital
				1880	Detrital
				2040	Detrital
				2700	Detrital
Borgmassivet					
Jekselen	Allsopp & Neethling 1970	Subvolcanic quartz diorites	Rb-Sr	1672±79	Isochron
"	Barton & Copperthwaite 1983	"	"	948±120	Isochron
Gjelsvikfjella					
Jutulsessen	Paulsson & Austrheim 2003	Migmatite	SIMS 206/207	1163±6	Igneous
"	"	Syenite	SIMS 206/207	504±6	Igneous
Gjelsvikfjella	Jacobs et al. 2003	Granite 3112/2	SHRIMP 206/238	486.9±3.8	Igneous
Stabben	"	Meta-gabbro 0501/2	SHRIMP 206/238 titanite	483±11	Igneous cooling
"	"	Lamprophyre 2312/2	SHRIMP 206/238	523.2±4.8	Igneous
Mühlig-Hofmann-gebirge	"	Hbl-leucosome	SHRIMP 206/238	1088±49	Metamorphism
"	"	"	SHRIMP 206/238	557±13	Migmatitization
"	"	Charnockitic gneiss	SHRIMP 207/206	1000-1150	Protolith
		"	SHRIMP 207/206	521±3.4	Charnockisation

Table 10. Cont.

Area	Reference	Rock type	Method	Age (Ma)	Interpretation
Portnipa	Bisnath et al. 2006	Aplite ABA/69		498±5	Igneous, min for Pan-African deformation
Stabben	"	Metagabbro ABA/64	SHRIMP 207/206	487±4	Igneous, late-post tectonic
Portnipa	"	Banded gneiss ABA/32	SHRIMP 207/206	1120±9	Detrital, Max age for sed protolith
Nupskammen	"	Mylonitic augen gneiss ABA/10B	SHRIMP 207/206	1104±8	Igneous
Von Essenskarvet	"	Augen gneiss ABA/10A	SHRIMP 207/206	1124.4±11	Igneous
Wohlthatmassiv					
Petermannketten	Jacobs et al. 1998	Metarhyolite J1838	SHRIMP 207/206	1130±12	Igneous
	"	"	SHRIMP 206/238	575±10	Metamorphism, rim
Petermannketten	"	Charnockite J1 6	SHRIMP 206/238	608±9	Igneous
	"	"	"	544±15	Metamorphic
Orvinfjella					
Dallmannberge	"	Metarhyolite J1704	SHRIMP 207/206	1137±21	Igneous
	"	"	"	529±8	Metamorphism, rim
	"	"	"	1084±8	Metamorphic
Dallmannberge	"	Metarhyolite J1795	SHRIMP 207/206	1076±14	Igneous
	"	"	SHRIMP 206/238	557±11	Metamorphism, rim
Conradgebirge	"	Augen orthogneiss J1736	SHRIMP 207/206	1086±20	Igneous
	"	"	SHRIMP 206/238	570±25	Migmatization, rim
Conradgebirge	"	Metagranodiorite J1698	SHRIMP 206/238	527±8	Igneous & metamorphic
Conradgebirge	"	Tonalitic leucosome J1745	"	516±5	Migmatization
Conradgebirge	"	Meta-leucogranite J1695	SHRIMP 206/238	527±6	Igneous
Zimbabwe					
	Hanson et al. 1998	Dolerite (granophyre)	zircon n= 3	1105±2	Igneous
Coats Land, Antarctica					
	Gose et al. 2006	Granophyre, rhyolite	zircon	1112±4	Igneous
Haag nunatak, Antarctica					
	Millar & Pankhurst 1987	Granodioritic gneiss	Rb-Sr	1176 ± 76	
	"	Granite	Rb-Sr	1058 ± 53	
	"	Granite	Rb-Sr	1003 ± 18	
Falkland Islands					
Area	Reference	Rock type	Method	Age (Ma)	Interpretation
Cape Meredith Complex	Jacobs et al. 1999	Meta-rhyolite CM94	SHRIMP 204/206	1118±8	Igneous
		Meta-rhyolite CM94	SHRIMP 204/206	~1000 n=2	Metamorphic over-growth
	"	Granodiorite orthogneiss CM93	SHRIMP	~1090	Igneous
	"	Granite augen gneiss CM51	SHRIMP 207/206	1135±11	Inherited cores
	"	Granite augen gneiss CM51	SHRIMP 207/206	1067±9	Igneous, syntectonic
	"	Granite CM87	SHRIMP 207/206	1003±16	Igneous, post-tectonic

Table 10. Cont.

Area	Reference	Rock type	Method	Age (Ma)	Interpretation
	"	Amphibolite	40Ar/39Ar hornblende	1009±14	
	"	Amphibolite	40Ar/39Ar hornblende	1015±6	
	"	Pegmatite	40Ar/39Ar muscovite	989±3	
	"	Pegmatite	40Ar/39Ar biotite	989±7	
Cape Meredith Complex	Thomas et al. 1998	Lamprophyre C20	K-Ar biotite	503±6	
Cape Meredith Complex	"	Lamprophyre CM67	K-Ar biotite	520±5	
Cape Meredith Complex	"	Basalt (picritic) CM83	T_{DM}	~930	Cross-cut ~500 Ma lamprophyres
Cape Meredith Complex	"	Basalt (picritic) CM84	T_{DM}	~930	Cross-cut ~500 Ma lamprophyres
Cape Meredith Complex	"	Basalt (picritic) CM85	T_{DM}	~870	Cross-cut ~500 Ma lamprophyres
Natal Belt, RSA					
Area	Reference	Rock type	Method	Age (Ma)	Interpretation
Natal	Eglington & Armstrong 2003	Biotite gneiss WE 1/66	SHRIMP 207/206	1134±15	Igneous
Natal	"	Biotite gneiss WE 1/66	T_{DM}	~2400	
Tugela Terrane (accreted to Calahari Craton margin)					
Kotongweni	Johnston et al. 2001	Meta-tonalite STJ96T4	SHRIMP	1209±5	Igneous
Mkondene	"	Meta-diorite, meta-anorthosite	ID-TIMS	~1181	Intrusion
	"	Meta-granitoids	SHRIMP	1155±1	
Dulumbe	"	Paragneiss	SHRIMP, re-calculated	1276±10	Detrital, deposition of the sed
	"	"	"	1240±10	Detrital, Sambridge & Compston 1994
	"	"	"	1175±9	Detrital
Mzumbe Terrane (south of Tugela Terrane) = amphibolite facies					
Mzumbe Terrane	Thomas & Eglington 1990	Tonalite gneiss RT 832	ID-TIMS	1207±10	Igneous
Mpambanyoni River	Cornell et al. 1996	Meta-andecite/dacite RT 1071	SHRIMP 207/206	1163±12	Igneous
"			SHRIMP 207/206	1071±26	Metamorphic
"			SHRIMP lower intercept	172±32	Metamorphic
Fafa River	Jacobs & Thomas 1996	Granite	Titanite fission-track	481± 55	Cooling
Mpambanyoni River		Metarhyolite	K-Ar muscovite	918±20	Metamorphic
Mpambanyoni River	"	Calc-silicate rock	Titanite fission-track	687 90	Cooling
Mucklebraes Klippe	"	Spodumene pegmatite	K-Ar muscovite	905±22	Metamorphic
Mzumbe River	"	Tonalitic gneiss	Titanite fission-track	517± 39	Cooling
Mtwalume River	"	Tonalitic gneiss	Titanite fission-track	558± 45	Cooling
Quha River	Thomas et al. 1999	Meta-greywacke Q6	SHRIMP 207/206	1235±9	Igneous
"			SHRIMP 207/206	1065±15	Metamorphism, rim
"	Jacobs & Thomas 1996	Muscovite-pegmatite	K-Ar muscovite	954±23	Metamorphic

Table 10. Cont.

Area	Reference	Rock type	Method	Age (Ma)	Interpretation
Margate Terrane (south of Mzumbe Terrane)					
Palm Beach	Mendonidis et al. 2009	Monzonorite PM07/1		1091±7.1	Igneous
	"	"		1074±27	Metamorphism, rim
Munster headland	"	Mafic granulite PM07/4		1093±5.8	Igneous?
				±	
Banana Beach	Cornell & Thomas 2006	Quartz diorite gneiss RT 845	SIMS	1065±10	Igneous
			SIMS	1021±24	Metamorphic
Mbizana	Thomas et al. 1993	Microgranite dykes		1026±3	Igneous
Port Edward	Eglington et al. 2003	Enderbite, UND 175	SHRIMP 207/206	1025±8	Igneous
Fafa	"	A-type granite, UND 199	SHRIMP 207/206 upper intercept	1037±10	Igneous
Oribi Gorge	"	A-type granite, B1	SHRIMP 207/206	1070±4	Igneous
				1029±8	Metamorphism, rim
Glenmore	Mendonidis et al. 2002	S-type Bt-Grt-granite	SHRIMP 207/206	1091±9	Igneous
Sikombe	Thomas et al. 2003	S-type Bt-granite gneiss	SHRIMP 207/207	1181±15	Igneous
Northern Lesotho, xenoliths in kimberlites					
Area	Reference	Rock type	Method	Age (Ma)	Interpretation
Mothae	Schmitz & Bowring 2004	Granulite, metasedimentary KX23-3	ID-TIMS, monazite	1045±2	
Letsang-la-Terae	"	"	"	1001±2	
"	"	Grt-Kya-opx-granulite KX-20-1	ID-TIMS, zircon	~1017 - 1000	
"	"		ID-TIMS, monazite n=2	1098±3	
"	"	Felsic granulite KX20-5	ID-TIMS, zircon	997±6	metamorphic
		Mafic granulite KX20-8	ID-TIMS, zircon	1092±2	
Namaqualand, RSA (western continuation of Natal belt)					
Area	Reference	Rock type	Method	Age (Ma)	Interpretation
Bitterfontein	Thomas et al. 1996	Granite CBD 574		1065±2	
Okiep Copper District					
Nababeep	Robb et al. 1999	Granitic orthogneiss NAM6	SHRIMP 207/206	1824±36	Igneous
"	"	"	"	1032±18	metamorphic
Springbok	"	Orthogneiss NAM1	"	1199±12	igneous
"		Mafic-intermediate granulite NAM3	"	1168±9	Igneous
		"	"	1063±16	metamorphic
		Diorite NAM10		1057±8	igneous
Eastern Namaqualand, xenoliths in kimberlite					
Witberg pipe	Schmitz & Bowring 2004	2-pyroxene granulite KX10-4	ID-TIMS, zircon n=3	1100±3	metamorphic
Markt	"	Granitic gneiss KX4-28	ID-TIMS, zircon	1150±3	Igneous
	Huang et al. 1995	Mafic granulite HSA12	Sm-Nd mineral-whole-rock	604±36	
	"	Mafic granulite HSA32	Sm-Nd mineral-whole-rock	851±53	

11 FORMATION OF THE CONTINENTAL CRUST OF WESTERN DRONNING MAUD LAND

The results of the zircon geochronology and Sm-Nd and Rb-Sr isotope studies draw a picture of an old, at least Mesoproterozoic, tectonically and thermally modified continental domain, reworked by events related to the Mesoproterozoic Rodinia assembly and Neoproterozoic break-up followed by ca. 530 Ma Gondwana assembly (Li et al. 2008) and finally break-up in Jurassic. Overall, combined compositional and geochronological data on the studied xenoliths indicate that the Kjakebeinet area in southern Vestfjella is underlain by Proterozoic basement composed of mafic and felsic granulites and high-grade metapelites, together with lower-grade supracrustal rock types. A central thesis of this work is that a Proterozoic granulite domain, possibly an extension of the granulite terrane exposed at Heimefrontfjella and Mannefallknausane (Fig. 1), is registered by the examined xenoliths in the subsurface of Vestfjella.

A wide range of concordant zircon $^{207}Pb/^{206}Pb$ ages from 1350 Ma, representing inherited zircon cores from metatonalitic-quartz metadioritic xenoliths, down to the 165 Ma igneous crystallization age of metagranitic xenolith were obtained (Fig. 25). The ages mainly correlate with the previously established tectono-magmatic events in the Namaqua-Natal-Maud Belt, but previously unknown ages of the western Dronning Maud Land were also obtained. Combined with pre-existing data, the Vestfjella xenoliths allow a refinement of the origin and subsequent evolution of the continental crust of western Dronning Maud Land.

Interpretation of the isotopic and geochemical data for the metagabbro xenoliths is not straightforward. The REE and incompatible trace element data indicate that these xenoliths could be cogenetic. However, the two Sm-Nd ages, discussed in Chapter 9.2, refer to different, Mesoproterozoic and Phanerozoic, equilibration events of the xenoliths. Consequently, these samples represent granulite facies mafic rocks and their protoliths may have originated in a collisional setting during the Proterozoic, or from crustally contaminated Jurassic mafic magmas.

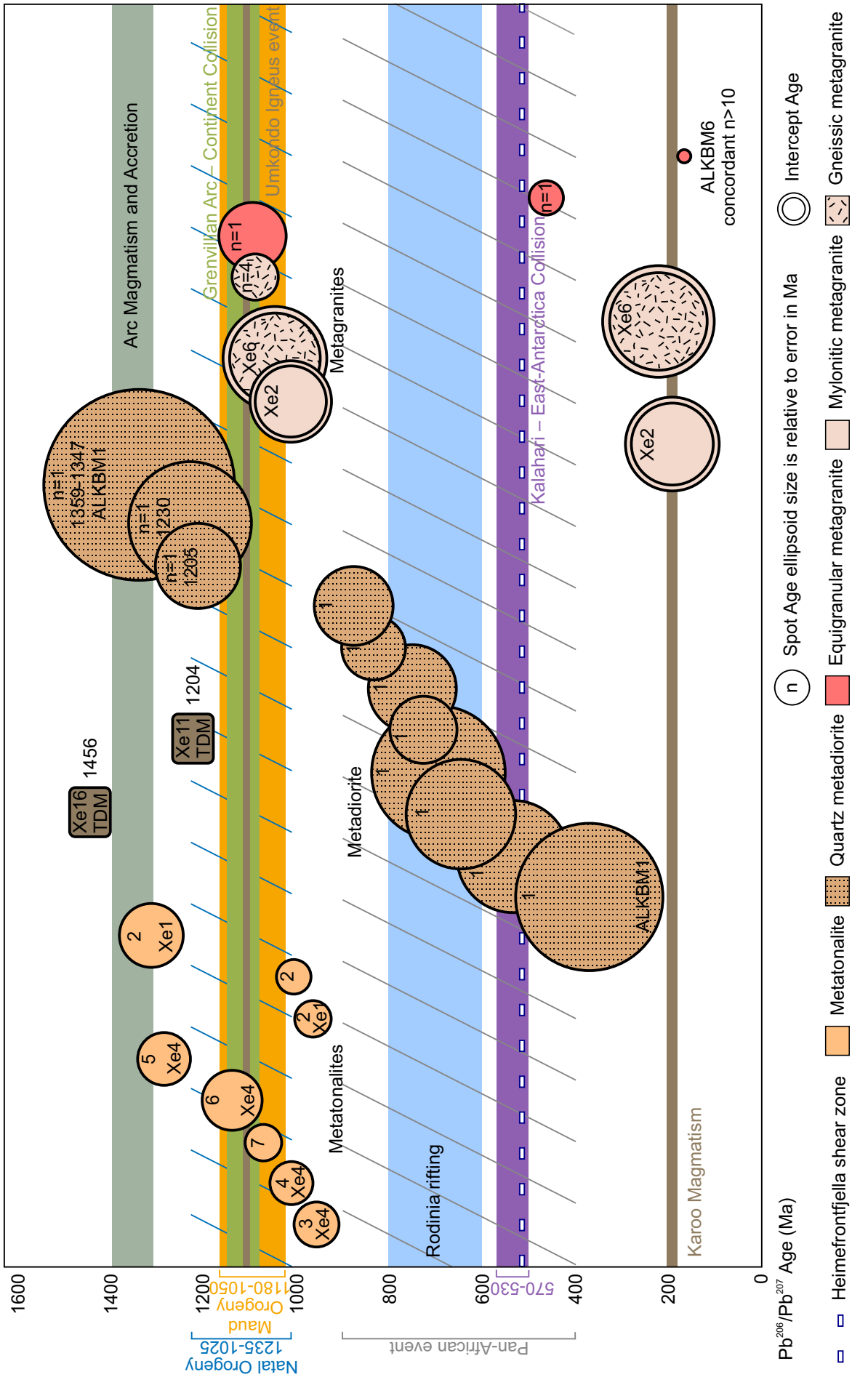

Fig. 25. Zircon $^{207}Pb/^{206}Pb$ ages of the studied xenoliths in the context of the regional geology of western Dronning Maud Land.

11.1 Volcanic arc at 1350–1150 Ma

On the basis of the overall zircon population of the metatonalite and quartz metadiorite xenoliths, the oldest concordant zircons dated at 1340–1150 Ma may represent inherited material. This age range coincides with the period of juvenile crust formation recorded along the Namaqua-Natal-Maud Belt before the Grenville-age collision (Table 10, Fig. 25). Equally old or older inherited zircons have been reported from Ahlmannryggen (ca. 1350 Ma, Marschall et al. 2009), Heimefrontfjella (ca. 2000–1200 Ma, Arndt et al. 1991, Jacobs et al. 2009), Falkland (Cape Meredith; 1135 ± 11 Ma; Jacobs et al. 1999), and Natal (1130–1200 Ma; Eglington & Armstrong 2003, Thomas & Eglington 1990). The crystallization ages of felsic arc-related magmas in Heimefrontfjella (1170 Ma, 1135 ± 8 Ma; Bauer et al. 2009, Jacobs et al. 2009) and Natal (1235 ± 9 Ma; Thomas et al. 1999, 1209 ± 5 Ma; Johnston et al. 2001, 1207 ± 10 Ma; Thomas & Eglington 1990, 1166 ± 12 Ma; Cornell et al. 1996, 1161 ± 9 Ma; Bauer et al. 2003b) coincide with the oldest zircon in the Vestfjella xenolith suite (Table 10).

The presence of 1350-1150 Ma zircon within the zircon population of metatonalites, quartz metadiorites, and of the equigranular metagranite (Fig. 25) suggests the presence of juvenile crust beneath the supracrustal formations of Vestfjella. This concealed crust was partially molten and produced some of the arc-affinity protoliths of the studied xenoliths (Figs. 14 & 16). Geochemical data for the metasedimentary xenoliths are compatible with sandstone and mudstone protoliths in island arc settings (cf. Roser & Korsch 1986), also marked by the presence of volcanic arc rock types in the vicinity. The plagioclase – whole-rock Sm-Nd "age" of 1444 ± 36 Ma for metagabbro Xe11 probably records juvenile mafic magmatism (Figs. 20D & 25).

11.2 Arc-continent collision of 1100–1000 Ma

The collision of the Kaapvaal-Grunehogna craton and a further continental landmass (Coats Land block; Jacobs et al. 2008) led to a high-grade metamorphic event in the juvenile crust of Vestfjella. In Heimefrontfjella and southern Natal, the peak of the collision has been dated between 1090 Ma and 1060 Ma using syn-tectonic granitoids and overgrowths (e.g. Jacobs et al. 1993, Cornell et al. 1996, Thomas et al. 1999, Mendonidis et al. 2002). The gneissic metagranite (Xe6; 1094 ± 11 Ma) and a single grain in Jurassic equigranular metagranite (ALKBM6; ca. 1090 Ma) can be associated with syn-tectonic magmatism in southern Natal (cf. Eglington et al. 2003, Mendonidis et al. 2002). The ages of this study are marginally older, just within error, than those of 1073 ± 6 Ma and 1084 ± 8 Ma for late-tectonic rapakivi-type coarse, megacrystic granites south of Kjakebeinet (Mannefallknausane; Arndt et al. 1991, Rämö et al. 2008) and 1070 ± 4 Ma for southern Natal Province (Oribi Gorge; Eglington et al. 2003). One concordant age group at 1074 ± 7 Ma (n = 6) for the metatonalite sample Xe4 (Fig. 18) is compatible with the ages indicative of arc-continent collision, and implies heating of the crust during the late stage of the Grenville-age orogeny in the Vestfjella region.

The mylonitic metagranite samples are geochemically uniform and different from the gneissic and equigranular metagranite samples. The upper intercept age observed from the mylonitic metagranite xenolith (Xe2; 1021 ± 30 Ma) overlaps with the transitional period from late-tectonic to post-tectonic granite magmatism of the Namaqua-Natal belt. The K-feldspar augen of this mylonitic metagranite xenolith may record a relict megacrystic texture, which is typical of these late-tectonic intrusions. In Natal, the younger suite of late-tectonic enderbites and A-type granites took place at ca. 1020–1050 Ma (Margate terrane; 1025 ± 8 Ma, 1037 ± 10 Ma; Eglington et al. 2003) and the undeformed 1026 ± 3 Ma Mbizama microgranite of the Margate terrain gives the minimum age of ductile deformation (Thomas et al. 1993). In Heimefrontfjella, mafic dykes (1033 ± 7 Ma; Bauer et al. 2003a) are associated with post-tectonic events.

11.3 Post-orogenic cooling at 1000–900 Ma

The last stages of the Grenville-age orogen in the Natal-Maud Belt have been associated with sinistral shearing along terrane boundaries in Natal and exhumation in the Maud Belt (e.g. Jacobs & Thomas 1994, Jacobs et al. 1996). In Natal, pegmatites and calc-silicate rocks indicate a thermal or hydration event at ca. 900 Ma (based on K-Ar muscovite) (Jacobs & Thomas 1996). In the Maud Belt, widespread evidence of cooling at 1010–900 Ma is recorded by K-Ar closure in, for example, muscovite porphyroblasts in quartzites and pegmatites (960 ± 20, 962 ± 20 Ma; Jacobs et al. 1995) and granites (886 ± 19 Ma; Jacobs et al. 1996). In the Falkland Islands, a metarhyolite U-Pb zircon metamorphic overgrowth was dated at ca. 1000 Ma, contemporaneous with hornblende Ar-Ar cooling ages of 1021–986 Ma and Ar-Ar pegmatite mica of 996–982 Ma (Jacobs et al. 1999). Rare evidence of igneous activity includes an Ar-Ar muscovite age of 954 ± 23 Ma for a late-tectonic pegmatite in Natal (Mzumbe; Jacobs &Thomas 1996), U-Pb zircon of 1003 ± 16 Ma for post-tectonic granite in the Falkland Islands (Cape Meredith; Jacobs et al. 1999) and sparse detrital 980 Ma zircons in quartzite, Heimefrontfjella (Jacobs et al. 2009).

The younger 1020–950 Ma zircon in metatonalite xenoliths (Xe1, Xe4) from Vestfjella may mark recurrent tonalite evolution within the middle crust. These geochemically and petrographically nearly identical samples exhibit geochemical affinities to continental arcs (Fig. 22). Bearing in mind the relatively small size of the samples and possible metasomatic overprint, however, the geochemical data available are not unequivocally representative of the magma compositions. These metatonalites are typified by inherited zircon cores (1350–1060 Ma) and record melting or thermal modification of Maud Belt Mesoproterozoic crust in response to post-orogenic exhumation. The xenoliths could represent pluton-size intrusions, leucosome veins in migmatites, or something between.

It is probably significant that the ages recorded by the metatonalite (Xe1, Xe4) and quartz metadiorite (ALKBM1) zircon populations (Fig. 23) practically cover the igneous and metamorphic zircon ages reported in the Maud Belt, Mzumbe, Margate and Tugela terrains of Natal (references in Table 10), Northern Lesotho granulite xenoliths (Schmitz & Bowring 2004) and the Falkland Islands (Thomas et al. 1998, Jacobs et al. 1999) (Fig. 1). The detrital zircons of Ahlmannryggen and Heimefrontfjella metasediments (Marschall et al. 2009, Arndt et al. 1991) are older on average.

11.4 Rodinia rifting at 800–750 Ma and amalgamation of Gondwana at 570–530 Ma

Rodinia breakup is documented along the southwestern, western and northwestern margins of the Kalahari Craton (Fig. 1), where rift sediments and volcanic rocks indicate rifting and breakup at ca. 800–750 Ma (Li et al. 2008). The metatonalite and quartz metadiorite xenoliths contain zircons that yield a remarkably wide age range from 1350 Ma to ca. 150 Ma. The oldest ages of these xenoliths are associated with pre-Rodinia arc magmatism (1350 Ma group), whereas the ca. 800–900 Ma ages fall between the purported time of post-orogenic exhumation (1000–900 Ma) and anorogenic rifting (800–750 Ma). There is, however, no overlap between the zircon 1100–1000 Ma spot ages of the metatonalites and the quartz metadiorite spot ages during the previously mentioned 1100–1000 Ma arc-continent collision period (Fig. 23A).

The few low-precision Mesozoic ages of the quartz metadiorite xenolith are ascribed to lead loss, whereas the ages of ca. 500 Ma determine the lower intercept of the quartz metadiorite zircon population (Fig. 23). Therefore, despite their geochemical similarities, the quartz metadiorite, with significant detrital zircon component, is probably different from the metatonalite magmatism. Accordingly, the quartz metadiorite xenolith may represent a crustally contaminated layered magmatic rock younger than the metatonalites. The challenge of age determination for this xenolith may derive from its complex origins: rutile recovered from this sample shows a bimodal distribution with respect to the Nb content and is dominated by rutile with metapelite affinity. Therefore, it is likely that the zircon population also bears a significant detrital

component. The combined data on the metatonalites and quartz metadiorite indicate a long-lasting positive thermal anomaly at Vestfjella (Figs. 23 & 25).

The ca. 500–600 Ma Pan-African overprint, related to the East African Antarctic orogeny and amalgamation of Gondwana, has been recorded in the Kottasberge amphibolite facies terrane east of the Heimefrontfjella shear zone (cf. Meert 2003) (Fig. 1) and also by the syenite, granite and lamprophyre intrusions of central Dronning Maud Land and lamprophyre dykes of the Falkland Islands (Jacobs et al. 1998, 1999, 2003). The minimum age for Pan-African deformation in Dronning Maud Land is recorded by 489 ± 5 Ma aplite on Gjelsvikfjella (Bisnath et al. 2006).

In contrast, Pan-African ages have not been reported from the granulite facies terrane west of the Heimefrontfjella shear zone (includes Mannefallknausane) or from the Tugela, Mzumbe and Margate terrains of the Natal Belt. The Mzumbe terrain pegmatites and calc-silicate rocks do indicate re-heating at ca. 530 Ma, as evidenced by titanite fission track analyses (Jacobs & Thomas 1996), which is post-dated by the lamprophyre dykes of the Falkland Islands (Thomas et al. 1998). The relatively young zircon ages in the Vestfjella quartz metadiorite and equigranular metagranite xenoliths coincide with the Pan-African event in a broader sense, from 800–500 Ma. The meaning of these ages, not dominant within the xenolith suite, raises the question of the source of these zircons. In the case of the Jurassic equigranular metagranite (ALKMB6), discussed in section 11.5, the one ca. 470 Ma Pan-African and one ca. 1090 Ma concordant zircon age probably record zircon inheritance. The quartz metadiorite ca. 860–590 Ma zircon spot ages, although with very low Pb contents in these zircons (Fig. 23A), may record partial lead loss of these zircons, magmatic zircon crystallization, or the assimilation and inheritance of detrital grains from an older sedimentary rock. The metapelitic nature of rutile in this sample complies with the assimilation scenario. Rb-Sr closure of apatite and plagioclase (571 ± 20 Ma) in Proterozoic metagabbro Xe11 (Fig. 20C) may be indicative of slow cooling, 200 Ma after Sm-Nd closure of apatite and whole rock in the same xenolith, of the western Dronning Maud Land Proterozoic middle crust. This contradicts quartz metadiorite zircon crystallization (>900 °C) at 860–590 Ma and may indicate a difference in crustal depth or tectonic mixing of lithological units.

11.5 Gondwana break-up at 180 Ma, cooling and development of continental margin at 140–100 Ma

In Heimefrontfjella, apatite fission-track studies of Mesoproterozoic basement gneisses and plutonic rocks, together with some younger sandstones, record a long-lasting ca. 170–80 Ma period of moderate heating and subsequent cooling (Jacobs 2009). The probable heat source was the Karoo mantle plume responsible for 180 Ma flood basalt and related intrusive magmatism, which records the Gondwana break-up in the study area (cf. Jacobs et al. 1995, Jacobs & Lisker 1999, Luttinen & Furnes 2000). The lower intercept ages of gneissic and mylonitic metagranites (193 ± 33 and 223 ± 60 Ma, respectively) (Fig. 18) may record opening of the zircon U-Pb system due to crustal heating by the Karoo mantle plume. These lower intercept ages may also mark the ca. 160 Ma melting of lithospheric mantle and intrusion of the host lamproites (cf. Luttinen et al. 2002). Sm-Nd closure of apatite and whole rock (126 ± 39 Ma) in metagabbro xenolith Xe11 likely record cooling of the xenolith and the host dyke. Sm-Nd closure of plagioclase and clinopyroxene (184 ± 30 Ma) in metagabbro xenolith Xe16 is coeval with Jurassic Gondwana break-up magmatism at Vestfjella and in adjacent areas (cf. e.g. Luttinen & Furnes 2000, Luttinen et al. 2015) and may record igneous crystallization or metamorphic re-crystallization. The following Rb-Sr closure of clinopyroxene and whole rock (101 ± 19 Ma) of the same sample may record extremely slow cooling or more likely cooling and re-heating, and, finally, Rb-Sr closure coeval with cooling of the host dyke (Fig. 20).

The crystallization of equigranular metagranite at 165 Ma (Table 10) post-dates A-type granite plutonism of the Ellsworth-Whitmore microplate, West Antarctica (178–174 Ma, zircon U-Pb) (cf. Craddock et al. 2017, Leat et al. 2018). The Ellsworth-Whitmore granite magmatism is associated with the Weddell Sea rift system and

may be interpreted as the final stage of Karoo-Ferrar felsic magmatism (Leat et al. 2018). As the age of Kjakebeinet metagranite closely correlates with ultrapotassic lamproite magmatism, further research is needed to resolve whether these intrusions mark a currently undefined anorogenic event in western Dronning Maud Land. The age of Kjakebeinet Jurassic granite is also a proxy indicating the maximum age of Vestfjella lamproite magmatism and melting of the lithospheric mantle in western Dronning Maud Land.

Large-scale crustal thinning developed the distinctive horst graben topography west of Heimefrontfjella from ca. 140 Ma onwards (Jacobs & Lisker 1999). Erosional unroofing and cooling related to the formation of continental margin has been recorded at ca. 100 Ma (apatite fission-track method) in Heimefrontfjella (Jacobs et al. 1995, Jacobs & Lisker 1999). To summarize, the western flank of Dronning Maud Land has experienced several localized periods of lithospheric thinning and heating.

12 CONCLUDING REMARKS

12.1 Original thickness of the continental crust of western Dronning Maud Land

The xenoliths studied are predominantly metamorphic. They are high grade, yet completely recrystallized, as indicated by petrography and microscopic evidence of partial melting and recrystallization. On a macroscopic scale, the xenoliths are unlike classical migmatitic rocks. The peculiar texture and mineralogy of the metagranitoids can be explained by disequilibrium dehydration melting in the presence of H_2O-CO_2 fluid followed by quench crystallization. The observed high temperatures, recorded by mineral Fe-Mg exchange and whole-rock Zr saturation values, in combination with textural and mineralogical evidence, imply partial melting of the metagranitoids and the metapelites, and the high metamorphic grade of the metagabbros and quartz metadiorites. The xenoliths were rapidly transported onto the surface, as they did not totally dissolve in their extremely high temperature (>1000 °C) host magma; this complies with the nearly-vertical ascent of the ultrapotassic magma through the crust.

Thermobarometry indicates a deep crustal origin for garnet-bearing metagabbro Xe16 (approx. 63 km), metapelite P5 (approx. 59 km), metagabbro Xe11 (approx. <36 km) and the quartz metadiorites (approx. >20 km). These depths probably correspond to lower crust and middle crust during the formation of the protoliths of these xenoliths, respectively. The metatonalites and metagranites originated in a shallower setting, probably at upper crustal (<15 km) levels. Regionally, the current crustal thickness across Heimefrontfjella (52–44 km) towards the coast (30 km) on western Dronning Maud Land, and the thick crust of the Namaqua-Natal Belt (46-50 km) and Kaapvaal Craton (34–42 km) of southern Africa, correspond to the estimates presented in this study. However, the high pressure conditions recorded by the metagabbro and metapelite xenoliths may indicate locally thick crust relative to the regional values prior to the Cretaceous-Jurassic thinning of the crust.

The geochemistry and age data provided by the metagabbro, metatonalite and gneissic metagranite xenoliths display rock types accreted together and possibly onto the margin of the Mesoproterozoic subduction zone within an arc environment ca. 1.1 Ga ago (Natal-Maud event). In this type of Andean continental arc type environment, thick crust (>50 km), recorded by the garnet metagabbro xenolith Xe16, could have developed. As the pressure interpretations are based on metamorphic mineral assemblages, the crustal thickness of Vestfjella may have been modified since the formation of those assemblages.

12.2 A xenolith suite with both orogenic and anorogenic origins

Bearing in mind the factors that limit the interpretation of high-grade metamorphic protoliths of the xenoliths examined, the chondrite- and continental crust-normalized incompatible element diagrams of the quartz metadiorites, metatonalites and metagranites show pronounced negative Nb, Ta and Ti anomalies indicative of generation in an arc environment. The concentrations of Y, Nb, Yb and Ta of the metatonalites, metagranites and quartz metadiorites show affinity to volcanic arc and collisional orogeny granitic rocks. In contrast, the concentrations of Zr, Nb and Y of the quartz metadiorites also show affinity to within-plate basaltic rocks and those of the metagabbros to P-type mid-ocean ridge basaltic rocks, indicative of a significant crustal component. The metagabbros have an alkalic, silica-deficient character and they are strongly enriched in REE and incompatible elements relative to the chondrite composition, as well as the P-MORB, oceanic and continental arc basalt compositions.

Comparing these results with proposed continental crust compositions, the incompatible element concentrations of the metagabbros are higher than those of average lower continental crust and the proposed entity of lower, middle and upper continental arc crust. The likely explanation for this unexpected fertility of these alkalic granulite-facies metagabbro xenoliths is metasomatic (re-)enrichment of the protoliths by a crustal fluid. The initial εNd(1450) of +7.1 (Xe11) for the pargasite-rich garnet-free metagabbro and initial εNd(180) of -8.5 (Xe16) for the garnet-bearing metagabbro resemble the isotopic signature of Vestfjella enriched lithospheric mantle and old enriched crust, respectively. The present day Sm-Nd isotopic composition of the xenoliths falls within the array defined by the Karoo igneous province gabbroic rocks (Jurassic) and granulite xenoliths (Proterozoic or undefined) and are similar to the Lesotho lower crustal xenoliths.

On the basis of continental crust compositions, the metatonalite and quartz metadiorite xenoliths probably represent middle crust that originated in a continental arc setting. The quartz metadiorite, however, is likely to be a hybrid rock with arc magmatic and sedimentary source material. The metapelitic and metagreywacke xenoliths show affinity to average upper continental crust and sedimentary rocks of an island-arc environment. Accordingly, their source and depositional environment comply with the metasedimentary Maud Belt rocks. The Mesoproterozoic gneissic and mylonitic metagranite xenoliths represent crustal melts derived from heterogeneous sources with a significant continental arc component. REE enrichment of the mylonitic metagranites may relate to processes active during the ductile deformation of the crust. Equigranular metagranite of Jurassic age may represent A-type granitic magmatism, despite the fact that it is extremely enriched in Ba and Sr relative to typical A-type compositions.

12.3 Thermal evolution of the crustal domain of western Dronning Maud Land

The evolution of the Proterozoic crust of western Dronning Maud Land revealed by the studied Vestfjella xenoliths began in the Mesoproterozoic with conceptual arc magmatism at ca. 1300 Ma. The accretion of arc terrains and development of a continental Namaqua-Natal-Maud belt by the Grenvillian-Kibaran orogeny was followed by breaking up of the Rodinia Supercontinent and, as indicated by the zircon populations of metatonalite, quartz metadiorite and metagranite xenoliths, a long-lasting thermal event at 1150–950 Ma. Crustal anatexis and cooling is recorded by granite crystallization at ca. 1100–1090 Ma and subsequent Neoproterozoic mylonitic deformation at 1050–990 Ma. The zircon populations of metatonalites and quartz metadiorite show that the Vestfella continental crust was also subject to prolonged heating from the Neoproterozoic to the Cambrian, probably due to the heat generated by mantle upwelling during Rodinia rifting and finally related to the silicic magmatism of Gondwana assembly.

Finally, Vestfjella was positioned into its present rifted continental margin setting after the basement had been covered with and transected by Karoo flood basalts and related sheet-like

gabbroic intrusions during the Jurassic. As the age of Kjakebeinet metagranite (165 Ma) also records the maximum age of Vestfjella lamproites and closely correlates with ultrapotassic lamproite magmatism (ca. 160 Ma), further research is needed to resolve whether these intrusions mark a previously unknown anorogenic event in western Dronning Maud Land.

12.4 Tectonic evolution of the crustal domain of western Dronning Maud Land

At northern Vestfjella, a large-scale aeromagnetic anomaly is indicative of an Archean–Proterozoic boundary. Where exposed, these boundary regions are often lithologically heterogeneous and the tectonic mixing of rocks of different ages and origins has occurred. The contradiction between the temperatures recorded by the quartz metadiorite 860–590 Ma zircon population and Rb-Sr cooling "age" of 570 Ma for the metagabbro Xe11 may indicate that the crustal lithological units beneath Vestfjella have been tectonically mixed, or that the quartz metadiorite and metagabbro Xe11 originated at very different depths. Tectonostratigraphy, however, is likely to dominate the structure of the crust in mobile belts and Archean–Proterozoic boundaries. Accordingly, even the adjacent surface outcrops may be of a different metamorphic grade and age, also relative to the unexposed crust. Therefore, neither terrain nor craton boundaries have been defined in this investigation. The continuation of geochronological work together with deep scientific drilling, high-resolution geophysical measurements and satellite imaginary of the surface morphology would be the tools for further research on this topic.

A plethora of geological processes, including arc magmatism, arc accretion, subduction, assimilation, partial fusion and anatexis of pre-existing crust, high-grade thermal modification, intra-crustal recycling and dehydration melting have driven the evolution of the continental crust of western Dronning Maud Land. These were active processes during the periods of plate convergence, divergence and trans-tension, which, over 1100 million years, thermally modified the lithosphere of western Dronning Maud Land and are recorded by the Vestfjella xenoliths studied in this thesis.

ACKNOWLEDGEMENTS

I thank the steering group (M. Kurhila, S. Kultti, A. Luttinen and T. Rämö) for comments over the life span of the manuscript, J. Jacobs for the zircon SHRIMP data, M. Kurhila for co-operation in the zircon investigation and interpretation, T. Hokkanen, L. Järvinen, M. Lehtonen, I. Mänttäri and L. Pakkanen for support and assistance in mineralogical and isotope studies at the Geological Survey of Finland (GTK), A. Luttinen and S. Vuori for sampling and preliminary work, the FINNARP 2007 Crew for logistics and field assistance, K. Linden, L. Iljyinsky and M. Whitehouse for support in the NORDSIMS laboratory, H. Korkka, T. Vaahtojärvi, P. Hölttä, M. Poutiainen and R. Törnroos for technical support in the University of Helsinki (HU) and R. Siddall for correcting the language. I would especially like to thank T. Rämö for guiding me to produce this monograph. R. Jokisaari, P. Kuikka-Niemi, R. Turunen (GTK) and M. Afflick provided valuable help with the final layout of this thesis. Friends and relatives over a decade, especially my spouse T. Kellokoski, have provided invaluable support on the home front.

This investigation was a NordSIMS project 5666. I acknowledge funding from the Academy of Finland project Large Igneous Provinces and their Sources (2007–2011), the Finnish Occupational Fund (2013–2018) and the Doctoral School of Natural Sciences, University of Helsinki (2018). I am grateful to the Department of Geography and Geoscience (HU), GTK, the Swedish Museum of Natural History (NORDSIMS) and the Australian National University (ANU) for the support of these organizations and their personnel provided during this work.

REFERENCES

Agar, R. A. & Le Bel, L. 1985. The Linga Super-unit: high-K diorites of the Arequipa segment. In: Pitcher, W. S., Atherton, M. P., Cobbing, E. J. & Beckinsale, R. D. Magmatism at a Plate Edge – The Peruvian Andes. Glasgow and London: Blackie, 119–127.

Allen, J. C. & Boettcher, A. L. 1983. The stability of amphibole in andesite and basalt at high pressures. American Mineralogist 68, 307–314.

Allsopp, H. L. & Neethling, D. C. 1970. Rb-Sr isotopic ages of Precambrian intrusives from Queen Maud Land, Antarctica. Earth and Planetary Science Letters 8, 66–70.

Arculus, R. J. & Ruff, L. J. 1990. Genesis of continental crust: evidence from island arcs, granulites, and exospheric processes. In: Vielzeuf, D. & Vidal, Ph. Granulites and Crustal Evolution. NATO ASI Series C: Mathematical and Physical Sciences -Vol. 311, 7–23.

Arima, M., Tani, M., Kawate, S. & Johnston, S. T. 2001. Geochemical characteristics and tectonic setting of metamorphosed rocks in the Tugela terrane, Natal Belt, South Africa. Memoir. Tokyo, Japan: National Institute of Polar Research, Special Issue No. 55, 1–39.

Arndt, N. T. 2013. Formation and Evolution of the Continental Crust. Geochemical Perpectives 2. 533 p.

Arndt, N. T., Todt, W., Chauvel, C., Tapfer, M. & Weber, K. 1991. U-Pb zircon age and Nd isotopic composition of granitoids, charnockites and supracrustal rocks from Heimefrontfjella, Antarctica. Geologische Rundschau 80, 759–777.

Bacon, C. R, Bruggmann, P. E., Christiansen, R. L., Clynne, M. A., Donnelly-Nolan, J. M. & Hildreth, W. 1997. Primitive magmas at five Cascade volcanic fields: melts from hot, heterogeneous sub-arc mantle. Canadian Mineralogist 35, 397–423.

Barton, J. M. & Copperthwaite, Y. E. 1983. Sr-isotopic studies of some intrusive rocks in the Ahlmann Ridge and Annandagstoppane, western Queen Maud Land, Antarctica. In: Oliver, R. L., James, P. R. &. Jago, J. B (eds) Antarctic Earth Science. Cambridge: Cambridge University Press, 59–62.

Barton, J. M., Klemd, Jr. R., Allsopp, H. L., Auret, S. H. & Copperthwaite, Y. E. 1987. The geology and geochronology of the Annandagstoppane granite, Western Dronning Maud Land, Antarctica. Contributions to Mineralogy and Petrology 97, 488–496.

Bauer, W. 1995. Structural evolution and petrogenesis of the metamorphic basement complex of the northern Heimefrontfjella (western Dronning Maud Land Antarctica). Ber. Polarforschung 171. PhD thesis, Rheinisch-Westfäischen Technischen Hochschule Aachen (in German).

Bauer, W., Fielitz, W., Jacobs, J., Fanning, C. M. & Spaeth, G. 2003a. Mafic Dykes from Heimefrontfjella and implications for the post-Grenvillian to pre-Pan-African geological evolution of western Dronning Maud Land (Antarctica). Antarctic Science 15, 1–13.

Bauer, W., Jacobs, J., Fanning, C. M. & Schmidt, R. 2003b. Late Mesoproterozoic Arc and Back-arc Volcanism in the Heimefrontfjella (East Antarctica) and Implications for the Palaeogeography at the Southeastern Margin of the Kaapvaal-Grunehogna Craton. Gondwana Research 6, 449–465.

Bauer, W., Jacobs, J., Thomas, B., Spaeth, G. & Weber, K. 2009. Geology of the Vardeklettane Terrane, Heimefrontfjella (East Antarctica). Polarforschung 79, 29–32.

Bauer, W., Siemes, H., Spaeth, G. & Jacobs, J. 2016. Transpression and tectonic exhumation in the Heimefrontfjella, western orogenic front of the East African/Antarctic Orogen, revealed by quartz textures of high strain domains. Polar Research 35, 25420. Available at: http://dx.doi.org/10.3402/polar.v35.25420

Bayer, B., Geissler, W. H., Eckstaller, A. & Jokat, W. 2009. Seismic imaging of the crust beneath Dronning Maud Land, East Antarctica. Geophysical Journal International 178, 860–876.

Berman, R. G. 1991. Thermobarometry using multi-equilibrium calculations: a new technique, with petrological applications. Canadian Mineralogist 29, 833–856.

Bisnath, A., Frimmel, H. E., Armstrong, R. A. & Board, W. S. 2006. Tectono-thermal evolution of the Maud Belt: New SHRIMP U-Pb zircon data from Gjelsvikfjella, Dronning Maud Land, East Antarctica. Precambrian Research 150, 95–121.

Boger, S. D. 2011. Antarctica - Before and after Gondwana. Gondwana Research 19, 335–371.

Cavosie, A. J., Wilde, S. A., Liu, D., Weiblen, P. W. & Valley, J. V. 2004. Internal zoning and U–Th–Pb chemistry of Jack Hills detrital zircons: a mineral record of early Archean to Mesoproterozoic (4348–1576 Ma) magmatism. Precambrian Research 135, 251–279.

Clemens, J. D. & Droop, G. T. R. 1998. Fluid, P–T paths and the fates of anatectic melts in the Earth's crust. Lithos 44, 21–36.

Coleman, R. G., Lee, D. E., Beatty, L. B. & Brannock, W. W. 1965. Eclogites and Eclogites: Their Differences and Similarities. Geological Society of America Bulletin 76, 483–508.

Compston, W., Williams, I. S., Kirschvink, J. L., Zhang, Z. & Ma, G. 1992. Zircon U-Pb ages for the Early Cambrian time-scale. Journal of the Geological Society London 149, 171–184.

Cornell, D. H. & Thomas, R. J. 2006. Age and tectonic significance of the Banana Beach Gneiss, KwaZulu-Natal South Coast, South Africa. South African Journal of Geology 109, 335–340.

Cornell, D. H., Thomas, R. J., Bowring, S. A., Armstrong, R. A. & Grantham, G. H. 1996. Protolith interpretation in metamorphic terranes: a back-arc environment with Besshi-type base metal potential for the Quha Formation, Natal Province, South Africa. Precambrian Research 77, 243–271.

Corner, B. 1994. Geological evolution of western Dronning Maud Land within a Gondwana framework: Geophysics subprogramme. Final project report to SACAR. Department of Geophysics, Whitwaterstrand University, South Africa. 21p.

Cox, K. G., Bell, J. D. & Pankhurst, R. J. 1979. The Interpretation of Igneous Rocks. London: Allen & Unwin.. 450 p.

Craddock, J. P., Schmitz, M. D., Crowley, J. L., Larocque, J., Pankhurst, R. J., Juda, N., Konstantinou, A. & Storey, B. 2017. Precise U-Pb zircon ages and geochemistry of Jurassic granites, Ellsworth-Whitmore terrane, central Antarctica.The Geological Society of America Bulletin 129, 118–136. Available at: https://doi.org/10.1130/B31485.1

Curtis, M. L. & Storey, B. C. 1996. A review of geological constraints on the pre-break-up position of the Ellsworth Mountains within Gondwana: implications for Weddell Sea evolution. In: Storey, B. C., King, E. C. & Livermore, R. A. (eds) Weddell Sea Tectonics and Gondwana Breakup. London: Geological Society, Special Publications 108, 11–30.

Curtis, M. L., Leat, P. T., Riley, T. R., Storey, B. C., Millar, I. L. & Randall, D. E. 1999. Middle Cambrian rift-related volcanism in the Ellsworth Mountains, Antarctica: tectonic implications for the palaeo-Pacific margin of Gondwana. Tectonophysics 304, 275–299.

Dalziel, W. D. & Grunow, A. M. 1992. Late Gondwanide tectonic rotations within Gondwanaland. Tectonics 11, 603–606.

Davidson, J. P. & Arculus, R. J. 2006. The significance of Phanerozoic arc magmatism in generating continental crust. In: Brown, M. & Rushmer. T. (eds) Evolution and Differentiation of the Continental Crust. Cambridge: Cambridge University Press, 134172.

De La Roche, H., Leterrier, J., Grandclaude, P. & Marchal, M. 1980. A classification of volcanic and plutonic rocks using R1R2- diagram and major element analyses - its relationships with current nomenclature. Chemical Geology 29, 183–210.

DePaolo, D. J. 1981. Neodymium isotopes in the Colorado front range and crust-mantle evolution in proterozoic. Nature 291, 684–687.

Eglington, B. M. 2006. Evolution of the Namaqua-Natal Belt, southern Africa – A geochronological and isotope geochemical review. Journal of African Earth Sciences 46, 93–111.

Eglington, B. M. & Armstrong, R. A. 2003. Geochronological and isotopic constraints on the Mesoproterozoic Namaqua–Natal Belt: evidence from deep borehole intersections in South Africa. Precambrian Research 125, 179–189.

Eglington, B. M., Thomas, R. J., Armstrong, R. A. & Walraven, F. 2003. Zircon geochronology of the Oribi Gorge Suite, Kwazulu-Natal, South Africa, constraints on the timing of transcurrent shearing in the Namaqua–Natal Belt. Precambrian Research 123, 29–46.

Ferry, J. M. & Watson, E. B. 2007. New thermodynamic models and revised calibrations for the Ti-in-zircon and Zr-in-rutile thermometers. Contributions to Mineralogy and Petrology 154, 429–437.

Frost, B. R., Barnes, C. G., Collins, W. J., Arculus, R. J., Ellis, D. J. & Frost, C. D. 2001. A Geochemical Classification for Granitic Rocks. Journal of Petrology 42, 2033–2048.

Golynsky, A. V. 2007. Magnetic anomalies in East Antarctica and surrounding regions: a window on major tectonic provinces and their boundaries. In: Cooper, A. K. & Raymond, C. R. (eds) Proceedings of the 10th ISAES, USGS Open-File Report 2007–1047, Short Research Paper 006. 4 p. Doi:10.3133/of2007-1047.srp006

Goodge, J. W., Vervoort, J. D., Fanning, C. M., Brecke, D. M., Farmer, G. L., Williams, I. S., Myrow, P. M. & DePaolo, D. J. 2008. A positive test of East Antarctica-Laurentia juxtaposition within the Rodinia supercontinent. Science 321, 235–240.

Gose, W. A., Dalziel, I. W. D., Helper, M. A., Hutson, F. & Connelly, J. 1997. Paleomagnetic data and U–Pb isotopic age determinations from Coats Land, Antarctica: implications for late Proterozoic reconstructions. Journal of Geophyical Research 102 (B4), 7887–7902.

Grantham, G. G., Storey, B. C., Thomas, R. J. & Jacobs, J. 1997. The pre-break-up position of Haag Nunataks within Gondwana: Possible correlations in Natal and Dronning Maud Land. The Antarctic Region: Geological Evolution and Proccesses, 13–20.

Grantham, G. H., Manhica, A. D. S. T., Armstrong, R. A., Kruger, F. J. & Loubser, M. 2011. New SHRIMP, Rb/Sr and Sm/Nd isotope and whole rock chemical data from central Mozambique and western Dronning Maud Land, Antarctica: Implications for the nature of the eastern margin of the Kalahari Craton and the amalgamation of Gondwana. Journal of African Earth Sciences 59, 74–100.

Green, D. H. & Ringwood, A. E. 1967. An experimental investigation of the gabbro to eclogite transformation and its petrological applications. Geochimica et Cosmochimica Acta 31, 767–833.

Groenewald, P. B., Moyes, A. B., Grantham, G. H. & Krynauw, J. R. 1995. East Antarctic crustal evolution: geological constraints and modelling in western Dronning Maud Land. Precambrian Research 75, 23I–250.

Hanson, R. E., Crowley, J. L., Bowring, S. A, Ramezani, J., Gose, W. A., Dalziel, I. W. D., Pancake, J. A., Seidel, E. K., Blenkinsop, T. G. & Mukwakwami, J. 2004. Coeval Large-Scale Magmatism in the Kalahari and Laurentian Cratons During Rodinia Assembly. Science 304, 1126–1129. Doi: 10.1126/science.1096329

Hanson, R. E., Martin, M. W., Bowring, S. A. & Munyanyiwa, H. 1998. U-Pb zircon age for the Umkondo dolerites, eastern Zimbabwe: 1.1 Ga large igneous province in southern Africa–East Antarctica and possible Rodinia correlations. Geology 26, 1143–1146. Doi: 10.1130/0091-7613(1998)026

Herron, M. M. 1988. Geochemical classification of terrigenous sands and shales from core or log data. Journal of Sedimentary Petrology 58, 820–829.

Hodges, K. V. 2004. Geochronology and Thermochronology in Orogenic Systems. In: Rudnick, R. L. (ed.) Treatise on Geochemistry, Volume 3: The Crust, 263–292.

Holland, T. & Powell, R. 2000. Calculation of Phase Relations Involving Haplogranitic Melts Using an Internally Consistent Thermodynamic Dataset. Journal of Petrology 42, 673–683.

Hoskin, P. W. O. & Schaltegger, U. 2003. Considerations in Zircon Geochronology by SIMS. In: Hanchar, J. M. & Hoskin, P. W. O (eds) The Composition of Zircon and Igneous and Metamorphic Petrogenesis. Reviews in Mineralogy and Geochemistry 53, 27–62. Doi: 10.2113/0530027

Huang, Y.-M, Van Calsteren, P. & Hawkesworth, C. J. 1995. The evolution of the lithosphere in southern Africa: A perspective on the basic granulite xenoliths from kimberlites in South Africa. Geochimica et Cosmochimica Acta 23, 4905–4920.

Ireland, T.R. & Williams, I.S. 2003. Considerations in Zircon Geochronology by SIMS. In: Hanchar, J.M. & Hoskin, P.W.O (Eds.). The Composition of Zircon and Igneous and Metamorphic Petrogenesis. Reviews in Mineralogy and Geochemistry 53, 27–62.

Jacobs, J. 2009. A Review of Two Decades (1986–2008) of Geochronological Work in Heimefrontfjella, and Geotectonic Interpretation of Western Dronning Maud Land, East Antarctica. Polarforschung 79, 47–57.

Jacobs, J. & Lisker, F. 1999. Post Permian tectono-thermal evolution of western Dronning Maud Land, East Antarctica: an apatite fission-track approach. Antarctic Science 11, 451–460.

Jacobs, J. & Thomas, J. T. 2004. Himalayan-type indenter-escape tectonics model for the southern part of the late Neoproterozoic–early Paleozoic East African–Antarctic orogen. Geology 2004, 32, 721–724. Doi: 10.1130/G20516.1

Jacobs, J. & Thomas, R. J. 1994. Oblique collision at about 1.1 Ga along the southern margin of the Kaapvaal continent, south-east Africa. Geologische Rundschau 83, 322–333.

Jacobs, J. & Thomas, R. J. 1996. Pan-African rejuvenation of the c. 1.1 Ga Natal Metamorphic Province(South Africa): K-Ar muscovite and titanite fission track evidence. Journal of the Geological Society 153, 971–978.

Jacobs, J., Ahrendt, H., Kreutzerb, H. & Weber, K. 1995. K-Ar, 40Ar-39Ar and apatite fission-track evidence for Neoproterozoic and Mesozoic basement rejuvenation events in the Heimefrontfjella and Mannefallknausane (East Antarctica). Precambrian Research 75, 251–261.

Jacobs, J., Bauer, W., Spaeth, G., Thomas, R. & Weber, K. 1996. Lithology and structure of the Grenville-aged (~1.1 Ga) basement of Heimefrontfjella (East Antarctica). Geologische Rundschau 85, 800–821.

Jacobs, J., Bauer, W., Weber, K., Spaeth, G. & Thomas, R. J. 2009. Geology of the Sivorg Terrane, Heimefrontfjella, (East Antarctica), and new U-Pb Zircon Provenance Analyses of Metasedimentary Rocks. Polarforschung 79, 11–19.

Jacobs, J., Fanning, C. M. & Bauer, W. 2003. Timing of Grenville-age vs. Pan-African medium- to high grade metamorphism in western Dronning Maud Land (East Antarctica) and significance for correlations in Rodinia and Gondwana. Precambrian Research 125, 1–20.

Jacobs, J., Fanning, C. M., Henjes-Kunst, F., Olesch, M. & Paech, H.-J. 1998. Continuation of the Mozambique Belt into East Antarctica: Grenville-aged metamorphism and polyphase Pan-African high-grade events in Central Dronning Maud Land. Chicago: The Journal of Geology 106, 385–406.

Jacobs, J., Pisarevsky, S., Thomas, R. J. & Becker, T. 2008. The Kalahari Craton during the assembly and dispersal of Rodinia. Precambrian Research 160, 142–158.

Jacobs, J., Thomas, R. J., Armstrong, R. A. & Henjes-Kunst, F. 1999. Age and thermal evolution of the Mesoproterozoic Cape Meredith Complex, West Falkland. Journal of the Geological Society 156, 917–928.

Jacobs, J., Thomas, R. J. & Weber, K. 1993. Accretion and indentation tectonics at the southern edge of the Kaapvaal craton during the Kibaran (Grenville) orogeny. Geology 21, 203–206.

Johannes, W. & Holtz, F. 1987. Formation and composition of H2O-undersaturated granitic melts. In: Asworth, J. R. & Brown, M. (eds) High-temperature Metamorphism and Crustal Anatexis. London: Unwin Hyman, 87–104.

Johnson, D. M., Hooper, P. R. & Conrey, R. M. 1999. XRF analysis of rocks and minerals for major and 1127 trace elements on a single low dilution Li-tetraborate fused bead. Advances in X-ray Analysis 41, 843–867.

Johnston, S. T., Armstrong, R. A., Heaman, L., McCourt, S., Mitchell, A. A., Bisnath, A. & Arima, A. 2001. Preliminary U–Pb geochronology of the Tugela terrane, Natal belt, eastern South Africa. Memoir. Tokyo, Japan: National Institute of Polar Research, Special Issue No.55, 40–58.

Jones, D. L., Bates, M. P., Lia, Z. X., Corner, B. & Hodgkinson, G. 2003. Palaeomagnetic results from the ca. 1130 Ma Borgmassivet intrusions in the Ahlmannryggen region of Dronning Maud Land, Antarctica, and tectonic implications. Tectonophysics 375, 247–260.

Karlstrom, K. E. & Williams, M. L. 2006. Nature and evolution of the middle crust: heterogeneity of structure and process due to pluton-enhanced tectonism. In: Brown, M. & Rushmer, T. (eds) Evolution and Differentiation of the Continental Crust. Cambridge: Cambridge University Press, 267–295.

Kelemen, P. B., Hanghøj, K. & Greene, A. R. 2004. One View of the Geochemistry of Subduction-related Magmatic Arcs, with an Emphasis on Primitive Andesite and Lower Crust. In: Rudnick, R. L. (ed.) Treatise on Geochemistry, Volume 3: The Crust, 593–659.

King, S. D. & Anderson, D. L. 1998. Edge-driven convection. Eart and Planetary Science Letters 160, 289–296.

Kleinschmidt, G., Helferich, S., Henjes-Kunst, F., Jackson, C. & Frimmel, H. E. 1996. The pre-Permo-Carboniferous Rocks and Structures from Southern Kirwanveggen, Dronning Maud Land, Antarctica. Polarforschung 66, 7–18.

Knaack, C., Cornelius, S. B. & Hooper, P. R. 1994. Trace element analyses of rocks and minerals by ICP-MS. GeoAnalytical Lab, Washington State University. Available at: https://environment.wsu.edu/facilities/geoanalytical-lab

Kretz, R. 1983. Symbols for rock-forming minerals. American Mineralogist 68, 277–279.

Kudryavtzek, G., Butzenko, V. & Kadmina, I. 1991. Crustal section across western Dronning Maud Land continental margin from geophysical data. In: Yoshida, Y., Kaminuma, K. & Shiraishi, K. (eds) Proceedings of the Sixth International Symposium on Antarctic Earth Science, Abstracts. Tokyo: National Institute for Polar Reasearch, 330–335.

Le Maitre, R.W., Bateman, P., Dudek, A., Keller, J., Lameyre, J., Le Bas, M. J., Sabine, P. A., Schmid, R., Sorensen, H., Streckeisen, A., Woolley, A. R. & Zanettin, B. 1989. A Classification of Igneous Rocks and Glossary of terms: Recommendations of the International Union of Geological Sciences Subcommission on the Systematics of Igneous Rocks. Oxford, U.K.: Blackwell Scientific Publications.

Leake, B. E., Woolley, A. R., Arps, C. E. S., Birch, W. D., Gilbert, M. C., Grice, J. D., Hawthorne, F. C., Kato, A., Kisch, H. J., Krivovichev, V. G., Linthout, K., Laird, J., Mandarino, J. A., Maresch, W. V., Nickel, E. H., Rock, N. M. S., Schumacher, J. C., Smith, D. C., Stephenson, N. C. N., Ungaretti, L., Whittaker, E. J. W. & Guo, Y. Z. 1997. Nomenclature of amphiboles: Report of the subcommittee on amphiboles of the international mineralogical association, commission on new minerals and mineral names. The Canadian Mineralogist 35, 219–246.

Leat, P. T., Jordan, T. A., Flowerdew, M. J., Riley, T. R., Ferraccioli, F. & Whitehouse, M. J. 2018. Jurassic high heat production granites associated with the Weddell Sea rift system, Antarctica. Tectonophysics 722, 249–264. Doi:10.1016/j.tecto.2017.11.011

Levander, A., Lenardic, A. & Karlstrom, K. 2006. Structure of the Continental Crust. In: Brown, M. & Rushmer, T. (eds) Evolution and Differentiation of the Continental Crust. Cambridge: Cambridge University Press, 21–66.

Li, Z. X., Bogdanova, S. V., Collins, A. S., Davidson, A., De Waele, B., Ernst, R. E., Evans, D. A. D., Fitzsimons, I. C. W., Fuck, R. A., Gladkochub, D. P., Jacobs, J., Karlstrom, K. E., Lu, S., Natapov, L. M., Pease, V., Pisarevsky, S. A., Thrane, K. & Vernikovsky, V. 2008. Assembly, configuration, and break-up history of Rodinia: A synthesis. Precambrian Research 160, 179–210.

Ludwig, K. R. 1999. User's Manual for Isoplot/Ex, Version 2.10, A Geochronological Toolkit for Microsoft Excel. Berkeley, USA: Berkeley Geochronology Center, Special Publication.

Ludwig, K. R. 2000. SQUID 1.00, A User's Manual. Berkeley, USA: Berkeley Geochronology Center, Special Publication.

Ludwig, K. R. 2003. Isoplot/Ex 3. A Geochronological Toolkit for Microsoft Excel. Berkeley Geochronologicy Center, Special Publication No. 4.

Ludwig, K. R. 2012. User's Manual for Isoplot/Ex, Version 3.75, A Geochronological Toolkit for Microsoft Excel. Berkeley, USA: Berkeley Geochronology Center, Special Publication 5. 75p.

Luttinen, A. V. & Furnes, H. 2000. Flood Basalts of Vestfjella: Jurassic Magmatism Across an Archaean-Proterozoic Lithospheric Boundary in Dronning Maud Land, Antarctica. Journal of Petrology 41, 1271–1305. Doi: 10.1093/petrology/41.8.1271

Luttinen, A. V., Heinonen, J. S., Kurhila, M., Jourdan, F., Mänttäri, I., Vuori, S. K. & Huhma, H. 2015. Depleted mantle-sourced CFB magmatism in the Jurassic

Africa-Antarctica rift: petrology and 40Ar/39Ar and U/Pb chronology of the Vestfjella dyke swarm, Dronning Maud Land, Antarctica. Journal of Petrology 56, 919–952.

Luttinen, A. V., Zhang, X. & Foland, K. A. 2002. 159 Ma Kjakebeinet lamproites (Dronning Maud Land, Antarctica) and their implications for Gondwana breakup processes. Geological Magazine 139, 525–539.

Marschall, H., Hawkesworth, C. J. & Leat, P. T. 2013a. Mesoproterozoic subduction under the eastern edge of the Kalahari-Grunehogna Craton preceding Rodinia assembly: The Ritscherflya detrital zircon record, Ahlmannryggen (Dronning Maud Land, Antarctica). Precambrian Research 236, 31–45.

Marschall, H., Hawkesworth, C. J., Leat, P. T., Dhuime, B. & Storey, C. 2013b. Zircon from Mesoproterozoic sediments sheds light on the subduction-collision history at the eastern active continental margin of the Archaean Kalahari-Grunehogna Craton. American Geophysical Union, Fall Meeting 2013, abstract #T13A-2503. Available at: http://adsabs.harvard.edu/abs/2013AGUFM.T13A2503M. Site visited 2.1.2018.

Marschall, H. R., Hawkesworth, C. J., Storey, C. D., Dhuime, B., Leat, P. T., Meyer, H.-P. & Tamm-Buckle, S. 2010. The Annandagstoppane granite, East Antarctica: evidence for Archaean intracrustal recycling in the Kaapvaal-Grunehogna Craton from zircon O and Hf isotopes. Submitted to Journal of Petrology.

Marschall, H. R., Storey, C., Dhuime, B., Leat, P. & Hawkesworth, C. 2009. Archean-Proterozoic evolution in East Antarctica. Geochimica et Cosmochimica Acta 73, A837.

McCourt, S., Armstrong, R. A., Grantham, G. H. & Thomas, R. J. 2006. Geology and evolution of the Natal belt, South Africa. Journal of African Earth Sciences 46, 71–92.

McDonough, W. F. & Sun, S.-S. 1995. Composition of the Earth. Chemical Geology 120, 223–253. Doi: 10.1016/0009-2541(94)00140-4

McLennan, S. M. 1989. Rare earth elements in sedimentary rocks; influence of provenance and sedimentary processes. In: Lipin, B. R. & McKay, G. A. (eds) Geochemistry and mineralogy of rare earth elements. Reviews in Mineralogy 21, 169–200.

McLennan, S. M., Taylor, S. R. & Hemming, S. R. 2006. Composition, differentation, and evolution of continental crust. In: Brown, M. & Rushmer, T. (eds) Evolution and Differentiation of the Continental Crust. Cambridge: Cambridge University Press, 92–134.

McLoughlin, S., Larsson, K. & Lindström, S. 2005. Permian plant macrofossils from Fossilryggen, Vestfjella, Dronning Maud Land. Antarctic Science 17, 73–86.

Meert, J. G. 2003. A synopsis of events related to the assembly of eastern Gondwana. Tectonophysics 362, 1–40.

Mendonidis, P. & Armstrong, R. A. 2009. A new U-Pb zircon age for the Portobello granite from the southern part of the Natal metamorphic belt. South African Journal of Geology 112, 197–208.

Mendonidis, P., Armstrong, R. A., Eglington, B. M., Grantham, G. H. & Thomas, R. J. 2002. Metamorphic history and U-Pb Zircon (SHRIMP) geochronology of the Glenmore Granite: Implications for the tectonic evolution of the Natal Metamorphic Province. South African Journal of Geology 105, 325–336.

Mendonidis, P., Armstrong, R. A. & Grantham, G. H. 2009. U–Pb SHRIMP ages and tectonic setting of the Munster Suite of the Margate Terrane of the Natal Metamorphic Belt. Gondwana Research 15, 28–37.

Mendonidis, P., Thomas, B., Grantham, G. & Armstrong, R. 2015. Geochronology of emplacement and charnockite formation of the Margate Granite Suite, Natal Metamorphic Province, South Africa: Implications for Natal-Maud Belt correlations. Precambrian Research 265, 189–202.

Meschede, M. 1986. A method of discriminating between different types of mid-ocean ridge basalts and continental tholeiites with the Nb-Zr-Y diagram. Chemical Geology 56, 207–218.

Millar, I. L. & Pankhurst, R. J. 1987. Rb-Sr Geochronology of the Region Between the Antarctic Peninsula and the Transantarctic Mountains: Haag Nunataks and Mesozoic Granitoids. In: McKenzie, G. D. (ed.) Gondwana Six: Structure, Tectonics, and Geophysics, 151–160.

Moorbath, S. & Taylor, P. N. 1986. Geochronology and related isotope geochemistry of high-grade metamorphic rocks from the lower continental crust. In: Dawson, J. B., Carswell, D. A., Hall, J. & Wedepohl, K. H. (eds) The Nature of the Lower Continental Crust. Geological Society, Special Publication 24, 211–220.

Morimoto, N., Fabries, J., Ferguson, A. K, Ginzburg, I. V., Ross, M., Seifeit, F. A. & Zussman, J. 1989. Nomenclature of pyroxenes. Canadian Mineralogist 27,143–156.

Moyes, A. B., Krynauw, J. R. & Barton, Jnr., J. M. 1995. The age of the Ritscherflya Supergroup and Borgmassivet Intrusions, Dronning Maud Land, Antarctica. Antarctic Science 7, 87–97.

Nair, S. K., Gao, S. S., Liu, K. H. & Silver, P. G. 2006. Southern African crustal evolution and composition: Constraints from receiver function studies. Journal of Geophysical Research 111, B02304.

Nye, C. J. & Reid, M. R. 1986. Geochemistry of primary and least-fractionated lavas from Okmok Volcano, central Aleutians: implications for arc magma genesis. Journal of Geophysical Research, 91, 10 271–10 287.

Paces, J. B. & Miller, J. D. 1993. Precise U-Pb ages of Duluth Complex and related mafic intrusions, northeastern Minnesota: geochronological insights to physical, petrogenetic, paleomagnetic, and tectonomagmatic processes associated with the 1.1 Ga Midcontinent Rift System. J. Geophys. Res. 98, 13997–14013.

Pan, Y. & Fleet, M. E. 1996. Rare earth element mobility during prograde granulite facies metamorphism: significance of fluorine. Contributions to Mineralogy and Petrology 123, 251–262.

Paulsson, O. & Austrheim, H. 2003. A geochronological and geochemical study of rocks from Gjelsvikfjella, Dronning Maud Land, Antarctica – implications for Mesoproterozoic correlations and assembly of Gondwana. Precambrian Research 125, 113–138.

Pearce, J. A. 1996. A User's Guide to Basalt Discrimination Diagrams. In: Wyman, D. A. (ed.) Trace Element Geochemistry of Volcanic Rocks: Applications for Massive Sulphide Exploration. Geological Association of Canada, Short Course Notes 12, 79–113.

Pearce, J. A., Harris, N. B. W. & Tindle, A. G. 1984. Trace Element Discrimination Diagrams for the Tectonic Interpretation of Granitic Rocks. Journal of Petrology 25, 956-983.

Pettijohn, F. J., Potter, P. E. & Siever, R. 1972. Sand and sandstones. New York: Springer-Verlag. 553 p.

Pitcher, W. S., Atherton, M. P., Cobbing, E. J. & Beckinsale, R. D. 1985. Magmatism at a Plate Edge – The Peruvian Andes. London: Blackie. 328 p.

Popov, S. V. & Leitchenkov, G. L. 1997. Radio-echo sounding investigations of western Dronning Maud Land and north-eastern Coats Land, East Antarctica. Polarforschung 67, 155–161.

Pouchou, J. L. & Pichoir, F. 1986. Basic expression of "PAP" computation for quantitative EPMA. In: Brown, J. D. & Packwood, R. H. (eds) 11 th international Congress on X – ray Optics and Microanalysis (ICXOM), 249–253.

Powell, R. & Holland, T. J. B. 1988. An internally consistent thermodynamic dataset with uncertainties and correlations: 3: application methods, worked examples and a computer program. Journal of Metamorphic Geology 6, 173–204.

Powell, R. & Holland, T. J. B. 2009. Thermocalc 3.33. Windows version.

Preston, J. & Still, J. 2001. Spreadsheet tools for amphibole calculations. Available at: http://www.gabbrosoft.org/index.html. Site visited 16.1.2018.

Rajesh, H. M., Santosh, M. & Yoshikura, S. 2011. The Nagercoil Charnockite: a Magnesian, Calcic to Calc-alkalic Granitoid Dehydrated during a Granulite-facies Metamorphic Event. Journal of Petrology, 52, 375–400.

Rämö, O. T., Luttinen, A. V., Andersen, T. & Kurhila, M. I. 2008. Mesoproterozoic A-type granites in Mannefallknausane, western Dronning Maud Land, Antarctica: U-Pb (LAMS) zircon chronology and Nd (whole-rock ID-TIMS) and Hf (zircon LAMS) isotope geochemistry. In: Ojala, A. E. K. (ed.) Congress of the International Polar Year 2007/08, Program and Abstracts, p. 41.

Randall, D. R. & Niocaill, C. M. 2004. Cambrian paleomagnetic data confirm a Natal embayment location for Ellsworth-Whitmore Mountains, Antarctica, in Gondwana reconstructions. Geophysical Journal International 157, 105–116.

Richard, P., Shimizu, N. & Allègre, C. J. 1976. 143Nd/146Nd, a natural tracer: an application to oceanic basalts. Earth and Planetary Science Letters 31, 269–278.

Riley, T. R., Leat, P. T., Curtis, M. L., Millar, I. L., Duncan, R. A. & Fazel, A. 2005. Early-Middle Jurassic Dolerite Dykes from Western Dronning Maud Land (Antarctica): Identifying Mantle Sources in the Karoo Large Igneous Province. Journal of Petrology 46, 1489–1524.

Robb, L., Armstrong, R. & Waters, D. 1999. The History of Granulite-Facies Metamorphism and Crustal Growth from Single Zircon U-Pb Geochronology: Namaqualand, South Africa. Journal of Petrology, 40, 1747–1770.

Rogers, N. W. & Hawkesworth, C. J. 1982. Proterozoic age and cumulate origin for granulite xenoliths, Lesotho. Nature 299, 409–413.

Rolland, Y., Cox, S., Boullier, A.-M., Pennacchioni, G. & Mancktelow, N. 2003. Rare earth and trace element mobility in mid-crustal shear zones: insights from the Mont Blanc Massif (Western Alps). Earth and Planetary Science Letters, 214, 203–219.

Rollinson, H. 1993. Using geochemical data: evaluation, presentation, interpretation. Harlow Essex: Longman. 352 p.

Romu, I. 2006. Petrography and mineral chemistry of lamproite-hosted xenoliths from Kjakebeinet, western Dronning Maud Land, Antarctica. M.Sc thesis, Department of Geology, University of Helsinki. 104 p. Available at: http://hdl.handle.net/10138/42262

Rosenbaum, G., Regenauer-Lieb, K. & Weinberg, R. F. 2010. Interaction between mantle and crustal detachments: A nonlinear system controlling lithospheric extension. JGR 115, B11412.

Roser, B. P. & Korsch, R. J. 1986. Determination of tectonic setting of sandstone-mudstone suites using SiO2 content and K2O/Na2O ratio. Journal of Geology, 94, 635–650.

Rubie, D. C. & Brearley, A. J. 1987. A model for rates of disequilibrium melting during metamorphism. In: Asworth, J. R. & Brown, M. (eds) High-temperature Metamorphism and Crustal Anatexis. London: Unwin Hyman, 57–86.

Rudnick, R. L. 1992. Xenoliths - Samples of the lower continental crust. In: Fountain, D. M., Arculus, R. & Kay, R. W. (eds) Continental Lower Crust, Amsterdam: Elsevier, 269–313.

Rudnick, R. L. & Fountain, D. M. 1995. Nature and composition of the continental crust: A lower crustal perspective. Reviews of Geophysics, 33, 267–309.

Rudnick, R. L. & Gao, S. 2004. Composition of the continental crust. In: Rudnick, R. L. (ed.) Treatise on Geochemistry, Volume 3: The Crust, 1–65.

Sandhäger, H. & Blindow, N. 1997. Ice-Sheet Geometry in Western Neuschwabenland, Antarctica. Polarforschung 67, 77–86.

Sandiford, M. & McLaren, S. 2006. Thermo-mechanical controls on heat production distributions and the long-term evolution of the continents. In: Brown, M. & Rushmer, T. (eds) Evolution and Differentiation of the Continental Crust. Cambridge: Cambridge University Press, 67–91.

Schmidt, M. W. & Thompson, A. B. 1996. Epidote in calc-alkaline magmas: An experimental study of stability, phase relationships, and the role of epidote in magmatic evolution. American Mineralogist 81, 462–474.

Schmitz, M. D. & Bowring, S. A. 2004. Lower crustal granulite formation during Mesoproterozoic Namaqua-Natal collisional orogenesis, southern Africa. South African Journal of Geology, 107, 19–42.

Selverstone, J., Pun, A. & Condie, K. C. 1999. Xenolithic evidence for Proterozoic crustal evolution beneath the Colorado Plateau. GSA Bulletin, 111, 590–606.

Shand, S. J. 1943. The Eruptive Rocks. New York: John Wiley. 444 p.

Siivola, J., Luttinen, A., Grind, H. & Räisänen, M. 1991. The Granitic Complex of Mannefallknausane in Western Queen Maud Land, Antarctica. FINNARP -89 Symposium, Report n:o 1, 7–11.

Smith, J. V. 1974. Feldspar Minerals. II. Chemical and textural properties. Berlin: Springer-Verlag. 690 p.

Spear, F. S. 1981. An experimental study of hornblende stability and compositional variability in amphibolite. American Journal of Science 281, 697–734.

Spear, F. S. 1993. Metamorphic phase equilibria and pressure-temperature-time paths. Mineralogical Society of America, Monographs 1. 799 p.

Stacey, J. S. & Kramers, J. D. 1975. Approximation of terrestrial lead isotope evolution by a two-stage model. Earth and Planetary Science Letters 26, 207–221.

Storey, B. C. & Dalziel, I. W. 1987. Outline of the structural and tectonic history of the Ellsworth Mountains-Thiel Mountains Ridge, West Antarctica.

Streckeisen, A. 1974. Classification and nomenclature of plutonic rocks recommendations of the IUGS subcommission on the systematics of Igneous Rocks. Geologische Rundschau 63, 773–786.

Sun, S. S. & McDonough, W. F. 1989. Chemical and isotopic systematics of oceanic basalts; implications for mantle composition and processes. In: Saunders, A. D. & Norry, M. J. (eds) Magmatism in the ocean basins. London: Geological Society of London 42, 313–345.

Sweatman, T. R. & Long, J. V. P. 1969. Quantitative electron-probe microanalysis of rock-forming minerals. Journal of Petrology 10, 332–379.

Taylor, S. R. & McLennan, S. M. 1995. The geochemical evolution of the continental crust. Reviews of Geophysics, 33, 241–265.

Tera, F. & Wasserburg, G. 1972. U-Th-Pb systematics in three Apollo 14 basalts and the problem of initial Pb in lunar rocks. Earth Planet. Sci. Lett. 14, 281–304.

Thomas, R. J. & Eglington, B. M. 1990. A Rb-Sr, Sm-Nd and U-Pb zircon isotopic study of the Mzumbe Suite, the oldest intrusive granitoid in southern Natal, South Africa. South African Journal of Geology, 93, 761–765.

Thomas, R. J., Armstrong, R. A. & Eglington, B. M. 2003. Geochronology of the Sikombe Granite, Transkei, Natal Metamorphic Province, South Africa. South African Journal of Geology 106, 403–408.

Thomas, R. J., Cornell, D. H. & Armstrong, R. A. 1999. Provenance age and metamorphic history of the Quha Formation, Natal Metamorphic Province: a U–Th–Pb zircon SHRIMP study. S. Afr. J. Geol. 102, 83–88.

Thomas, R. J., De Beer, C. H. & Bowring, S. A. 1996. A comparative study of the Mesoproterozoic late orogenic porphyritic granitoids of southwest Namaqualand and Natal, South Africa. Journal of African Earth Sciences 23, 485–508.

Thomas, R. J., Henjes-Kunst, F. & Jacobs, J. 1998. Prelamprophyre mafic dykes of the Cape Meredith Complex, West Falkland. Geological Magazine 135, 495–500.

Thomas, R. J., Von Veh, M. W. & McCourt, S. 1993. The tectonic evolution of southern Africa: an overview. Journal of African Earth Sciences, 16, 5–24.

Thompson, A. B. 1990. Heat, fluids, and melting in the granulite facies. In: Vielzeuf, D. & Vidal, Ph. Granulites and Crustal Evolution. NATO ASI Series C: Mathematical and Physical Sciences -Vol. 311, 37–57.

Tomkins, H. S., Powell, R. & Ellis, D. J. 2007. The pressure dependence of the zirconium-in-rutile thermometer. Journal of Metamorphic Geology 25, 703–713.

Treloar, P. J., Carney, J. N., Crow, M. J., Evans, J. A. & Barton, C. N. 1990. Pressure-Temperature-Time paths of granulite metamorphism and uplift, Zambesi belt, N.E. Zimbabwe. In: Vielzeuf, D. & Vidal, Ph. Granulites and Crustal Evolution. NATO ASI Series C: Mathematical and Physical Sciences -Vol. 311. 223–241.

Triebold, S., von Eynatten, H., Luvizotto, G. L. & Zack, T. 2007. Deducing source rock lithology from detrital rutile geochemistry: An example from the Erzgebirge, Germany. Chemical Geology 244, 421–436.

Tsuchiyama, A. 1986. Melting and dissolution kinetics - Application to partial melting and dissolution of xenoliths. Journal of Geophysical Research 91, 9395–9406.

Valley, J. W., Cavosie, A. J., Ushikubo, T., Reinhard, D. A., Lawrence, D. F., Larson, D. J., Clifton, P. H., Kelly, T. F., Wilde, S. A., Moser, D. E. & Spicuzza, M. J. 2014. Hadean age for a post-magma-ocean zircon confirmed by atom-probe tomography. Nature Geoscience 7, 219–223.

Washington State University 2015a. XRF Method. Site visited 11.2.2015. Available at: https://environment.wsu.edu/facilities/geoanalytical-lab/technical-notes/

Washington State University 2015b. ICP-MS Method. Site visited 11.2.2015. Available at: https://environment.wsu.edu/facilities/geoanalytical-lab/technical-notes/

Watson, E. B. & Harrison, T. M. 1983. Zircon saturation revisited: temperature and composition effects in a variety of crustal magma types. Earth and Planetary Science Letters 64, 295–304.

Watson, E. B., Wark, D. A. & Thomas, J. B. 2006. Crystallization thermometers for zircon and rutile. Contributions to Mineralogy and Petrology 151, 413–433.

Watters, B. R., Krynauw, J. R. & Hunter, D. R. 1991. Volcanicrocks of the Proterozoic Jutulstraumen Group in western Dronning Maud Land, Antarctica. In: Thomson, M. R. A., Crame, J. A. & Thomson, J. W. (eds) Geological Evolution of Antarctica. Cambridge: Cambridge University Press, 41–46.

Vavra, G. & Schaltegger, U. 1999. Post-granulite facies monazite growth and rejuvenation during Permian to Lower Jurassic thermal and fluid events in the Ivrea Zone (Southern Alps). Contributions to Mineralogy and Petrology 134, 405–414.

Vennum, W. R. & Storey, B. C. 1987a. Correlation of gabbroic and diabasic rocks from the Ellsworth Mountains, Hart Hills, and Thiel Mountains, West Antarctica. In: McKenzie, G. D. (ed.) Gondwana Six: Structure, Tectonics, and Geophysics, 129–138.

Vennum, W. R. & Storey, B. C 1987b. Petrology, geochemistry, and tectonic setting of granitic rocks from the Ellsworth-Whitmore Mountains crustal block and Thiel Mountains, West Antarctica. In: McKenzie, G. D. (ed.) Gondwana Six: Structure, Tectonics, and Geophysics, 139–150.

Whalen, J. B., Currie, K. L. & Chappell, B. W. 1987. A-Type Granites - Geochemical Characteristics, Discrimination and Petrogenesis. Contributions to Mineralogy and Petrology 95, 407–419.

Whitehouse, M. J. & Kamber, B. S. 2005. Assigning Dates to Thin Gneissic Veins in High-Grade Metamorphic Terranes: A Cautionary Tale from Akilia, Southwest Greenland. J.Pet. 46, 291–318.

Wickham, S. M. 1987. Isotopic modification of the continental crust: implications for the use of isotope tracers in granite petrogenesis. In: Asworth, J. R. & Brown, M. (eds) High-temperature Metamorphism and Crustal Anatexis. London: Unwin Hyman, 124–148.

Wiedenbeck, M., Allé, P., Corfu, F., Griffin, W. L., Meier, M., Oberli, F., Von Quadt, A., Roddick, J. C. & Spiegel, W. 1995. Three natural zircon standards for U-Th-Pb, Lu-Hf, trace element and REE analyses. Geostandards Newsletter 19, 1–23.

Williams, I. S. 1998. U-Th-Pb geochronology by ion microprobe. In: McKibben, M. A., Shanks III, W. C. & Ridley, W. I. (eds) Applications of Microanalytical Techniques to Understanding Mineralizing Processes. Rev. Economic Geol. 7, 1–35.

Wilson, M. 1989. Igneous petrogenesis. Unwin Hyman, London. 466p.

Vuori, S. K. 2004. Petrogenesis of the Jurassic gabbroic intrusions of Vestfjella, Dronning Maud Land, Antarctica. PhD thesis, University of Helsinki. 25 p.

Vuori, S. K. & Luttinen, A. V. 2003. The Jurassic gabbroic intrusions of Utpostane and Muren: insights into Karoo-related plutonism in Dronning Maud Land, Antarctica. Antarctic Science 15, 283–301. Doi: 10.1017/S0954 102003

Xiang, W., Griffin, W. L., Jie, C., Pinyun, H. & Xiang, L. 2011. U and Th Contents and Th/U Ratios of Zircon in Felsic and Mafic Magmatic Rocks: Improved Zircon-Melt Distribution Coefficients. Acta Geologica Sinica, 85, 164–174. Available at: https://doi.org/10.1111/j.1755-6724.2011.00387.x

Xiong, X. L., Adam, J. & Green, T. H. 2005. Rutile stability and rutile/melt HFSE partitioning during partial melting of hydrous basalt: Implications for TTG genesis. Chemical Geology 218, 339–359.

Zack, T., Kronz, A., Foley, S. F. & Rivers, T. 2002. Trace element abundances in rutiles from eclogites and associated garnet mica schists. Chemical Geology 184, 97–122.

Zack, T., Moraes, R. & Kronz. A. 2004a. Temperature dependence of Zr in rutile: empirical calibration of a rutile thermometer. Contributions to Mineralogy and Petrology 148, 471–488. Doi: 10.1107/s00410-004-0617-8

Zack, T., von Eynatten, H. & Kronz, A. 2004b. Rutile geochemistry and its potential use in quantitative provenance studies. Sedimentary Geology 171, 37–58.

APPENDIX 1

Table 1 Apatite analyses.

	1	2	3	4	5	6	7	8	9	10
	P3	P7	P7	P8	P8	P8	Xe1	Xe1	Xe4	Xe4
Sample	(R3_7)	(R2_10)	(R3_4)	(R3_4)	(R4_5)	(R5_9)	(R3_2)	(R3_4)	(R1_3)	(R1_4)
placCaO	56.67	52.90	51.78	56.45	54.58	57.07	56.20	55.82	50.88	56.99
Na_2O	0.41	0.57	0.41	0.49	0.34	0.41	0.00	0.00	0.00	0.00
FeO	0.00	0.00	0.00	0.67	1.43	0.96	0.39	0.64	0.62	0.00
MnO	0.00	0.00	0.00	0.00	0.00	0.00	0.00	0.43	0.00	0.00
MgO	0.00	0.51	0.50	0.00	0.61	0.00	0.00	0.00	0.77	0.00
P_2O_5	42.92	40.64	40.93	42.01	42.41	41.55	43.41	43.11	40.54	43.01
SiO_2	0.00	0.00	0.00	0.00	0.00	0.00	0.00	0.00	0.00	0.00
Cl	0.00	0.00	1.58	0.38	0.62	0.00	0.00	0.00	0.19	0.00
F	0.00	5.39	4.79	0.00	0.00	0.00	0.00	0.00	7.00	0.00
total	100.0	100.0	100.0	100.0	100.0	100.0	100.0	100.0	100.0	100.0

	11	12	13	14	15	16	17	18	19	20
	Xe4	Xe5	Xe9	Xe11	Xe11	Xe15	Xe15	Xe16	Xe16	Xe16
Sample	(R1_10)	(R1_1)	(R3_1)	(R5_9)	(R5_14)	(R1_8)	(R1_13)	(R1_1)	(R1_5)	(R2_5)
CaO	53.05	37.56	51.79	60.04	59.59	58.39	58.28	55.85	55.03	55.04
Na_2O	0.00	0.00	0.34	0.52	0.00	0.00	0.33	0.00	0.38	0.00
FeO	0.00	0.00	0.62	0.00	0.00	0.00	0.00	0.00	0.56	0.97
MnO	0.00	0.00	0.00	0.00	0.00	0.00	0.00	0.00	0.00	0.00
MgO	0.00	0.00	0.00	0.28	0.00	0.00	0.00	0.39	0.39	0.38
P_2O_5	41.02	57.95	40.01	39.16	40.41	40.54	38.61	42.87	42.60	43.16
SiO_2	0.00	0.00	0.00	0.00	0.00	1.07	2.77	0.00	0.00	0.00
Cl	0.00	0.00	0.66	0.00	0.00	0.00	0.00	0.92	1.04	0.45
F	5.93	4.48	6.59	0.00	0.00	0.00	0.00	0.00	0.00	0.00
total	100.0	100.0	100.0	100.0	100.0	100.0	100.0	100.0	100.0	100.0

Table 2 Amphibole analyses.

	1	2	3	4	5	6	7	8	9	10
	P3	P3	P3	P3	P3	P4	P4		P4	P7
Sample	(R1_5)	(R1_7)	(R2_9)	(R2_10)	(R2_1)	(R2_6)	(R3_1)	P4 R3_4)	(R3_5)	(R2_2)
SiO_2	53.06	56.30	52.66	55.01	55.72	44.36	43.47	43.84	43.96	43.67
TiO_2	6.93	7.10	5.97	5.53	6.26	1.88	2.18	1.87	2.13	3.21
Al_2O_3	0.00	0.81	0.00	0.00	0.47	15.29	14.84	15.16	15.26	13.52
Cr_2O_3	0.00	0.00	0.00	0.00	0.00	0.00	0.00	0.00	0.00	0.00
FeO	11.18	13.20	15.11	15.89	14.14	11.47	12.35	11.97	11.59	14.90
MnO	0.00	0.00	1.05	1.16	0.00	0.00	0.00	0.00	0.00	0.00
MgO	11.63	10.86	10.03	10.34	11.38	11.99	12.17	12.08	11.97	11.05
CaO	3.46	3.39	3.44	3.34	3.00	9.65	9.67	9.69	9.69	9.62
Na_2O	3.03	2.72	6.13	3.16	3.45	3.07	3.05	3.02	3.11	2.60
K_2O	10.71	5.62	5.59	5.56	5.58	2.29	2.26	2.38	2.29	1.42
total	100.00	100.00	100.00	100.00	100.00	100.00	100.00	100.00	100.00	99.99
Number of cations on the basis of 23 oxygen atoms										
Si	7.79	8.00	7.76	8.00	7.98	6.32	6.21	6.25	6.27	6.24
Al	0.00	0.00	0.00	0.00	0.02	1.68	1.79	1.75	1.73	1.76
Al	0.00	0.14	0.00	0.00	0.06	0.89	0.70	0.80	0.84	0.52
Fe(iii)	0.00	0.00	0.00	0.00	0.00	0.18	0.41	0.31	0.19	0.62
Ti	0.76	0.76	0.66	0.61	0.67	0.20	0.23	0.20	0.23	0.35
Cr	0.00	0.00	0.00	0.00	0.00	0.00	0.00	0.00	0.00	0.00
Fe(ii)	1.37	1.57	1.86	1.93	1.69	1.18	1.06	1.12	1.20	1.16
Mn	0.00	0.00	0.13	0.14	0.00	0.00	0.00	0.00	0.00	0.00
Mg	2.55	2.30	2.21	2.24	2.43	2.55	2.59	2.57	2.55	2.35
Ca	0.54	0.52	0.54	0.52	0.46	1.47	1.48	1.48	1.48	1.47
Na	0.86	0.75	1.75	0.89	0.96	0.85	0.84	0.83	0.86	0.72
K	2.01	1.02	1.05	1.03	1.02	0.42	0.41	0.43	0.42	0.26
TOTAL	15.88	15.05	15.98	15.36	15.29	15.74	15.73	15.75	15.76	15.45
Mg#	64.97	59.47	52.51	51.92	58.93	65.09	63.72	64.28	64.80	56.94

	11	12	13	14	15	16	17	18	19	20
Sample	P7 (R2_8)	P7 (R3_8)	Xe11 (R2_9)	Xe11 (R4_1)	Xe11 (R4_20)	Xe11 (R4_21)	Xe11 (R5_10)	Xe11 (R5_13)	Xe11 (R5_22)	Xe11 (R5_23)
SiO_2	43.41	43.33	41.31	43.29	41.53	41.32	41.74	43.52	42.24	44.09
TiO_2	3.51	3.42	3.97	1.95	3.58	3.72	3.79	3.68	4.02	3.10
Al_2O_3	13.54	13.63	14.41	14.86	14.77	14.08	14.33	14.94	13.96	15.55
Cr_2O_3	0.00	0.00	0.00	0.00	0.00	0.00	0.00	0.00	0.00	0.00
FeO	15.51	14.71	17.42	17.32	17.64	17.30	17.40	15.59	16.80	16.45
MnO	0.00	0.00	0.58	0.00	0.00	0.00	0.00	0.00	0.00	0.00
MgO	10.94	11.39	7.71	7.34	8.17	7.36	7.48	7.25	7.85	6.80
CaO	9.19	9.45	11.61	11.76	11.28	11.42	12.11	11.71	11.96	9.32
Na_2O	2.38	2.64	1.49	1.90	1.45	1.83	1.66	1.81	1.66	1.41
K_2O	1.51	1.43	1.51	1.57	1.57	2.97	1.50	1.50	1.50	3.29
total	99.99	100.00	100.00	100.00	100.00	100.00	100.00	100.00	100.00	100.00
Number of cations on the basis of 23 oxygen atoms										
Si	6.18	6.17	6.11	6.36	6.10	6.15	6.16	6.33	6.21	6.43
Al	1.82	1.83	1.89	1.64	1.90	1.85	1.84	1.67	1.79	1.57
Al	0.45	0.46	0.62	0.93	0.65	0.62	0.66	0.89	0.63	1.10
Fe(iii)	0.88	0.76	0.00	0.00	0.21	0.00	0.00	0.00	0.00	0.00
Ti	0.38	0.37	0.44	0.22	0.40	0.42	0.42	0.40	0.45	0.34
Cr	0.00	0.00	0.00	0.00	0.00	0.00	0.00		0.00	0.00
Fe(ii)	0.97	0.99	2.16	2.13	1.96	2.15	2.15	1.90	2.07	2.01
Mn	0.00	0.00	0.07	0.00	0.00	0.00	0.00	0.00	0.00	0.00
Mg	2.32	2.42	1.70	1.61	1.79	1.63	1.65	1.57	1.72	1.48
Ca	1.40	1.44	1.84	1.85	1.77	1.82	1.92	1.83	1.88	1.46
Na	0.66	0.73	0.43	0.54	0.41	0.53	0.47	0.51	0.47	0.40
K	0.27	0.26	0.28	0.29	0.29	0.56	0.28	0.28	0.28	0.61
TOTAL	15.33	15.43	15.55	15.56	15.48	15.74	15.55	15.38	15.51	15.40
Mg#	55.70	57.99	43.29	43.05	45.24	43.15	43.40	45.34	45.45	42.44

	21	22	23	24	25	26
Sample	Xe14 (R1_3)	Xe14 (R1_4)	Xe14 (R1_7)	Xe16 (R3_1)	Xe16 (R3_2)	Xe16 (R3_5)
SiO_2	59.02	54.51	54.01	43.83	44.18	43.40
TiO_2	4.38	3.42	3.79	3.30	3.09	3.02
Al_2O_3	0.00	0.00	0.00	13.04	12.84	12.97
Cr_2O_3	0.00	0.00	0.00	0.00	0.00	0.00
FeO	7.85	19.06	18.46	14.86	15.00	15.67
MnO	0.00	0.92	0.93	0.00	0.00	0.00
MgO	15.58	9.26	10.00	11.30	11.51	11.27
CaO	1.03	2.35	2.17	9.46	9.37	9.77
Na_2O	7.45	6.06	6.03	2.58	2.43	2.34
K_2O	4.69	4.42	4.63	1.63	1.59	1.57
total	100.00	100.00	100.00	100.00	100.00	100.00
Number of cations on the basis of 23 oxygen atoms						
Si	8.19	8.04	7.96	6.35	6.40	6.32
Al	0.00	0.00	0.00	1.65	1.60	1.68
Al	0.00	0.00	0.00	0.58	0.59	0.55
Fe(iii)	0.00	0.00	0.00	0.00	0.00	0.00
Ti	0.46	0.38	0.42	0.36	0.34	0.33
Cr	0.00	0.00	0.00	0.00	0.00	0.00
Fe(ii)	0.91	2.35	2.28	1.80	1.82	1.91
Mn	0.00	0.12	0.12	0.00	0.00	0.00
Mg	3.22	2.04	2.20	2.44	2.49	2.45
Ca	0.15	0.37	0.34	1.47	1.45	1.53
Na	2.00	1.73	1.72	0.72	0.68	0.66
K	0.83	0.83	0.87	0.30	0.29	0.29
TOTAL	15.77	15.86	15.91	15.68	15.66	15.71
Mg#	77.96	45.22	47.90	57.55	57.78	56.18

Mg#= magnesium ratio

1-5 Accessory, subhedral. brownish in ppl (=plain polarized light)

6-12 Pale yellow-brownish to yellow pleochroic ppl. abundant tiny inclusions with varying

density. 13-20 Pale yellow-brownish to yellow pleochroic ppl.

21-23 Accessory, subhedral, occurs with accessory alkalic pyroxene. TiO_2. and

barite 24-26 Accessory, brownish-yellow ppl, alteration product?

Table 3 Carbonate analyses.

	1	2	3	4	5	6	7	8	9	10
	P3	P3	P3	P3	P4	P8	P9	Xe1	Xe1	Xe2
Sample	(R1_8)	(R1_9)	(R2_7)	(R2_11)	(R2_7)	(R1_12)	(R1_4)	(R1_2)	(R2_4)	(R1_6)
FeO	25.65	18.10	21.93	20.03	7.00	13.76	1.36	1.91	33.98	1.06
MnO	0.00	0.00	1.18	1.21	3.98	1.49	0.00	0.00	1.24	1.82
MgO	16.30	20.65	18.78	19.72	30.61	26.71	0.00	0.00	15.40	0.00
CaO	58.04	60.86	58.11	59.05	58.41	57.46	98.64	98.09	49.37	97.12
SrO	0.00	0.39	0.00	0.00	0.00	0.00	0.00	0.00	0.00	0.00
total	99.99	100.00	100.00	100.01	100.00	99.42	100.00	100.00	99.99	100.00
The number of cations on the basis of 6 oxygen atoms										
Fe	0.51	0.36	0.44	0.40	0.14	0.28	0.03	0.04	0.68	0.02
Mn	0.00	0.00	0.02	0.02	0.08	0.03	0.00	0.00	0.02	0.04
Mg	0.33	0.41	0.38	0.39	0.61	0.53	0.00	0.00	0.31	0.00
Ca	1.16	1.22	1.16	1.18	1.17	1.15	1.97	1.96	0.99	1.94
Sr	0.00	0.01	0.00	0.00	0.00	0.00	0.00	0.00	0.00	0.00
Total	2.00	2.00	2.00	2.00	2.00	1.99	2.00	2.00	2.00	2.00
Mg/Ca	0.28	0.34	0.32	0.33	0.52	0.46	0.00	0.00	0.31	0.00
Fe/Ca	0.44	0.30	0.38	0.34	0.12	0.24	0.01	0.02	0.69	0.01

	11	12	13	14	15	16	17	18	19	20
	Xe2	Xe3	Xe4	Xe4	Xe4	Xe4	Xe5	Xe5	Xe6	Xe7
Sample	(R2_1)	(R2_3)	(R1_5)	(R1_7)	(R2_5)	(R3_4)	(R1_2)	(R2_2)	(R1_1)	(R1_2)
FeO	0.00	0.00	32.98	32.47	34.97	3.41	26.66	29.26	0.91	0.00
MnO	0.00	2.35	2.20	1.93	0.89	0.83	0.00	0.00	0.00	0.87
MgO	0.00	0.00	13.33	12.74	15.29	0.00	17.98	15.35	0.00	0.00
CaO	100.00	97.48	51.49	52.86	48.85	95.55	55.26	55.38	99.09	99.13
SrO	0.00	0.18	0.00	0.00	0.00	0.20	0.10	0.00	0.00	0.00
total	100.00	100.01	100.00	100.00	100.00	99.99	100.00	99.99	100.00	100.00
The number of cations on the basis of 6 oxygen atoms										
Fe	0.00	0.00	0.66	0.65	0.70	0.07	0.53	0.59	0.02	0.00
Mn	0.00	0.05	0.04	0.04	0.02	0.02	0.00	0.00	0.00	0.02
Mg	0.00	0.00	0.27	0.25	0.31	0.00	0.36	0.31	0.00	0.00
Ca	2.00	1.95	1.03	1.06	0.98	1.91	1.11	1.11	1.98	1.98
Sr	0.00	0.00	0.00	0.00	0.00	0.00	0.00	0.00	0.00	0.00
Total	2.00	2.00	2.00	2.00	2.00	2.00	2.00	2.00	2.00	2.00
Mg/Ca	0.00	0.00	0.26	0.24	0.31	0.00	0.33	0.28	0.00	0.00
Fe/Ca	-	-	0.64	0.61	0.72	0.04	0.48	0.53	0.01	-

	21	22	23	24	25	26	27	28	29	30	31
	Xe7	Xe11	Xe12	Xe13	Xe13	Xe14	Xe15	Xe15	Xe15_2	Xe16	Xe16
Sample	(R2_1)	(R1_4)	(R2_1)	(R1_8)	(R3_2)	(R1_6)	(R2_2)	(R4_6)	(R1_1)	(R1_4)	(R4_4)
FeO	0.73	0.00	0.00	26.95	28.64	11.84	0.00	0.00	0.00	0.00	0.00
MnO	2.73	0.00	0.00	1.48	1.67	1.02	0.00	0.00	0.00	1.45	0.00
MgO	1.02	0.39	0.00	17.17	19.38	27.91	0.00	0.00	0.00	0.00	0.34
CaO	95.51	99.61	99.91	54.39	50.30	59.23	100.00	96.73	99.76	98.42	99.66
SrO	0.00	0.00	0.09	0.00	0.00	0.00	0.00	3.27	0.24	0.13	0.00
total	99.99	100.00	100.00	99.99	99.99	100.00	100.00	100.00	100.00	100.00	100.00
The number of cations on the basis of 6 oxygen atoms											
Fe	0.01	0.00	0.00	0.54	0.57	0.24	0.00	0.00	0.00	0.00	0.00
Mn	0.05	0.00	0.00	0.03	0.03	0.02	0.00	0.00	0.00	0.03	0.00
Mg	0.02	0.01	0.00	0.34	0.39	0.56	0.00	0.00	0.00	0.00	0.01
Ca	1.91	1.99	2.00	1.09	1.01	1.18	2.00	1.93	2.00	1.97	1.99
Sr	0.00	0.00	0.00	0.00	0.00	0.00	0.00	0.07	0.00	0.00	0.00
Total	2.00	2.00	2.00	2.00	2.00	2.00	2.00	2.00	2.00	2.00	2.00
Mg/Ca	0.01	0.00	0.00	0.32	0.39	0.47	0.00	0.00	0.00	0.00	0.00
Fe/Ca	0.01	-	-	0.64	1.48	0.42	-	-	-	-	-

Table 4 Garnet analyses.

	1	2	3	4	5	6	7	8	9	10
	P7	P7	Xe4	Xe9	Xe9	Xe13	Xe13	Xe16	Xe16	Xe16
Sample	(R4_1)	(R4_2)	(R4_1)	(R2_1)	(R2_6)	(R4_1)	(R4_2)	(R2_6)	(R5_3)	(R5_5)
SiO_2	40.76	40.74	39.00	39.12	39.08	39.28	39.34	39.72	39.95	39.90
TiO_2	0.00	0.00	0.00	0.00	0.00	0.00	0.00	0.00	0.00	0.00
Al_2O_3	22.20	21.65	20.63	21.32	21.19	22.21	22.05	22.14	21.65	21.85
FeO	21.34	21.74	25.57	24.55	24.55	29.37	29.68	22.82	23.42	23.10
MnO	0.94	1.10	4.51	4.50	4.95	0.42	0.00	0.81	1.09	1.06
MgO	9.04	9.07	4.68	3.58	3.65	6.92	7.35	8.58	8.25	8.71
CaO	5.72	5.70	5.61	6.93	6.58	1.81	1.58	5.93	5.64	5.38
Total	100.00	100.00	100.00	100.00	100.00	100.00	100.00	100.00	100.00	100.00
Number of cations on the basis of 24 oxygen atoms										
Si	6.15	6.17	6.13	6.14	6.14	6.08	6.09	6.05	6.11	6.08
Ti	0.00	0.00	0.00	0.00	0.00	0.00	0.00	0.00	0.00	0.00
Al	3.95	3.86	3.82	3.94	3.92	4.05	4.02	3.98	3.90	3.93
Fe(2+)	2.69	2.75	3.36	3.22	3.22	3.80	3.84	2.91	2.99	2.95
Mn	0.12	0.14	0.60	0.60	0.66	0.05	0.00	0.10	0.14	0.14
Mg	2.03	2.05	1.10	0.84	0.85	1.60	1.70	1.95	1.88	1.98
Ca	0.92	0.92	0.95	1.16	1.11	0.30	0.26	0.97	0.92	0.88
Total	15.87	15.90	15.96	15.89	15.90	15.89	15.90	15.96	15.94	15.95
End-members per cent										
Pyp	35.24	34.91	18.29	14.38	14.61	28.34	29.25	32.87	31.65	33.31
Alm	46.66	46.93	55.97	55.33	55.17	65.85	66.22	49.04	50.42	49.57
Gro	16.02	15.76	15.75	20.01	18.95	5.82	4.52	16.32	15.55	14.80
Spe	2.08	2.40	10.00	10.28	11.26	0.00	0.00	1.77	2.38	2.31
Total	100.00	100.00	100.00	100.00	100.00	100.00	100.00	100.00	100.00	100.00

	11	12	13	14	15	16	17	18	19	20
	Xe15	Xe15	Xe15	Xe15	Xe15	Xe15	Xe15	Xe15	Xe15	Xe15
Sample	(R1_1)	(R1_2)	(R1_14)	(R1_15)	(R1_16)	(R1_18)	(R2_1)	(R2_4)	(R2_6)	(R3_3)
SiO_2	36.12	27.91	37.10	33.71	31.79	32.41	30.37	27.44	31.09	31.81
TiO_2	4.65	16.79	3.90	3.09	4.21	3.38	12.19	15.78	12.58	9.81
Al_2O_3	2.14	0.48	2.60	2.31	4.02	2.08	6.07	5.88	4.14	4.61
FeO	22.75	18.35	22.44	24.50	23.95	25.44	17.81	17.53	18.18	19.90
MnO	0.00	0.00	0.00	0.00	0.00	0.00	0.00	0.00	0.00	0.00
MgO	0.78	1.24	0.64	0.31	0.50	0.22	0.43	0.36	1.07	0.61
CaO	33.56	31.38	33.31	36.08	35.52	36.47	33.14	33.02	32.94	33.27
ZrO2	0.00	3.85	0.00	0.00	0.00	0.00	0.00	0.00	0.00	0.00
Total	100.00	100.00	100.00	100.00	100.00	100.00	100.01	100.00	100.00	100.00
Number of cations on the basis of 24 oxygen atoms										
Si	6.23	5.05	6.36	5.96	5.62	5.79	5.18	4.72	5.31	5.47
Ti	0.60	2.28	0.50	0.41	0.56	0.45	1.56	2.04	1.62	1.27
Al	0.43	0.10	0.53	0.48	0.84	0.44	1.22	1.19	0.83	0.93
Fe2+	1.94	1.88	1.97	1.70	1.60	1.71	1.60	1.59	1.65	1.71
Fe3+	1.34	0.89	1.25	1.92	1.94	2.10	0.94	0.93	0.95	1.14
Mn	0.00	0.00	0.00	0.00	0.00	0.00	0.00	0.00	0.00	0.00
Mg	0.20	0.33	0.16	0.08	0.13	0.06	0.11	0.09	0.27	0.16
Ca	6.20	6.08	6.11	6.83	6.72	6.98	6.05	6.08	6.03	6.12
Total	16.95	16.62	16.88	17.39	17.41	17.53	16.65	16.65	16.66	16.80
End-members per cent										
Pyp	2.41	4.03	1.99	0.96	1.57	0.67	1.41	1.19	3.44	1.95
Alm	23.22	22.66	23.85	19.77	18.93	19.49	20.58	20.46	20.76	21.44
Gro	13.57	2.31	17.11	13.56	19.96	11.68	25.54	22.41	18.60	21.37
Spe	0.00	0.00	0.00	0.00	0.00	0.00	0.00	0.00	0.00	0.00
And	60.80	71.00	57.05	65.70	59.54	68.15	52.46	55.93	57.21	55.25
Total	100.00	100.00	100.00	100.00	100.00	100.00	100.00	100.00	100.00	100.00

Sample	21 Xe15 (R3_4)	22 Xe15 (R3_5)	23 Xe15 (R6_1)	24 Xe15 (R6_2)	25 Xe15 (R6_3)	26 Xe15 (R6_4)	27 Xe15 (R6_12)	28 Xe15.2 (R1_2)	29 Xe15.2 (R2_2)
SiO_2	30.06	28.14	23.11	23.93	34.88	35.64	32.40	27.94	31.07
TiO_2	12.59	15.23	18.57	17.35	0.81	0.00	4.53	18.47	13.71
Al_2O_3	5.17	5.42	1.18	0.86	3.70	6.37	1.84	0.00	0.00
FeO	18.44	17.78	18.93	20.47	23.14	19.99	25.00	19.05	21.62
MnO	0.00	0.00	0.00	0.00	0.00	0.00	0.00	0.00	0.00
MgO	0.00	0.53	1.06	0.74	0.25	0.00	0.40	0.98	0.00
CaO	33.74	32.90	32.55	32.94	37.22	37.99	35.83	33.55	33.60
ZrO2	0.00	0.00	4.60	3.71	0.00	0.00	0.00	0.00	0.00
Total	100.00	100.00	100.00	100.00	100.00	100.00	100.00	100.00	100.00
Number of cations on the basis of 24 oxygen atoms									
Si	5.16	4.84	4.32	4.45	6.11	6.11	5.77	4.89	5.45
Ti	1.63	1.97	2.61	2.43	0.11	0.00	0.61	2.43	1.81
Al	1.05	1.10	0.26	0.19	0.76	1.29	0.39	0.00	0.00
Fe2+	1.66	1.62	1.62	1.74	1.45	1.13	1.75	1.82	2.11
Fe3+	0.99	0.93	1.34	1.45	1.94	1.73	1.97	0.97	1.06
Mn	0.00	0.00	0.00	0.00	0.00	0.00	0.00	0.00	0.00
Mg	0.00	0.13	0.30	0.21	0.07	0.00	0.11	0.26	0.00
Ca	6.21	6.06	6.51	6.57	6.98	6.98	6.84	6.30	6.31
Total	16.69	16.65	16.95	17.03	17.41	17.24	17.43	16.67	16.74
End-members per cent									
Pyp	0.00	1.72	3.50	2.43	0.78	0.00	1.22	3.06	0.00
Alm	21.06	20.75	19.20	20.43	17.04	13.98	20.18	21.77	25.02
Gro	22.55	21.27	4.80	0.00	22.31	36.69	10.25	0.00	0.00
Spe	0.00	0.00	0.00	3.59	0.00	0.00	0.00	0.00	0.00
And	56.39	56.26	72.50	73.55	59.88	49.33	68.35	75.17	74.98
Total	100.00	100.00	100.00	100.00	100.00	100.00	100.00	100.00	100.00

KEY: Pyp=pyrope Alm=almandine Gro=grossulare Spe=spessartine And=andradite in molecular percentages. Oxide proportions are in weight percents End-members per cent = molecular proportion of the end-member. Analysis point in the core: 12,14,15,21,23.,24. In rim: 11,13,16,20,22. In colourless rim: 25,26,27.

Table 5 Mica analyses.

	1	2	3	4	5	6	7	8	9	10
	P2			P3	P3	P3	P3	P3	P4	P6
Sample	(R2_6) P3	(k2_1) P3	(k2_2)	(R2_4)	(R2_6)	(R2_15)	(R3_5)	(R3_6)	(R2_2)	(R3_3)
SiO_2	39.49	43.35	43.03	42.63	42.52	41.97	42.43	41.28	40.50	37.43
TiO_2	3.74	10.70	11.69	10.67	11.24	11.05	8.98	8.86	3.03	2.01
Al_2O_3	16.12	9.99	10.02	10.03	9.85	10.48	11.67	12.56	15.92	12.98
FeO	16.19	9.34	9.78	10.11	10.22	11.11	7.64	7.45	12.93	30.03
MnO	0.00	0.00	0.00	0.00	0.00	0.00	0.00	0.00	0.00	0.00
MgO	14.73	14.36	13.80	14.18	13.81	13.41	19.22	19.42	17.75	7.03
BaO	0.00	0.00	0.00	0.00	0.00	0.00	0.00	0.00	0.00	0.00
K_2O	9.72	12.27	11.68	12.38	12.36	11.98	10.06	10.43	9.86	10.52
total	100.00	100.01	100.00	100.00	100.00	100.00	100.00	100.00	100.00	100.00
Numbers of cations on the basis of 22 anions.										
Si	5.61	6.06	6.01	5.99	5.98	5.92	5.82	5.68	5.67	5.75
Al (Z)	2.39	1.64	1.65	1.66	1.63	1.74	1.89	2.04	2.33	2.25
Al (Y)	0.31	0.00	0.00	0.00	0.00	0.00	0.00	0.00	0.29	0.10
Ti	0.40	1.12	1.23	1.13	1.19	1.17	0.93	0.92	0.32	0.23
Fe(ii)	1.92	1.09	1.14	1.19	1.20	1.31	0.88	0.86	1.51	3.86
Mn	0.00	0.00	0.00	0.00	0.00	0.00	0.00	0.00	0.00	0.00
Mg	3.12	2.99	2.87	2.97	2.90	2.82	3.93	3.98	3.70	1.61
K	1.76	2.19	2.08	2.22	2.22	2.15	1.76	1.83	1.76	2.06
Ba	0.00	0.00	0.00	0.00	0.00	0.00	0.00	0.00	0.00	0.00
total	15.52	15.09	14.98	15.16	15.12	15.12	15.19	15.30	15.58	15.87
Mg#	61.86	73.27	71.56	71.43	70.67	68.27	81.77	82.29	71.00	29.45

	11	12	13	14	15	16	17	18	19	20
	P6	P8	P8	P8	P8	P8	P8	Xe11	Xe11	Xe11
Sample	(R4_1)	(R1_6)	(R1_7)	(R2_6)	(R4_12)	(R5_10)	(R5_11)	(R1_5)	(R2_1)	(R2_2)
SiO_2	38.97	39.92	37.82	42.80	39.69	38.15	38.16	36.65	38.66	38.98
TiO_2	6.13	6.74	3.83	0.62	4.48	4.14	0.00	5.72	5.77	6.28
Al_2O_3	12.34	10.01	8.05	12.73	8.20	8.56	16.09	7.35	14.69	14.43
FeO	21.57	24.61	33.17	22.81	31.70	34.06	27.02	31.69	18.05	17.17
MnO	0.00	0.42	0.99	0.00	0.00	0.00	0.93	0.82	0.00	0.00
MgO	10.12	9.14	6.57	12.03	6.49	5.31	9.91	6.68	10.97	11.51
BaO	0.00	0.00	9.57	9.02	9.44	9.77	7.90	11.09	11.86	11.62
K_2O	10.86	9.17	0.00	0.00	0.00	0.00	0.00	0.00	0.00	0.00
total	100.00	100.00	100.00	100.00	100.00	100.00	100.00	100.00	100.00	100.00
Numbers of cations on the basis of 22 anions.										
Si	5.75	5.93	5.94	6.20	6.11	5.98	5.67	5.80	5.63	5.65
Al (Z)	2.15	1.75	1.49	1.80	1.49	1.58	2.33	1.37	2.37	2.35
Al (Y)	0.00	0.00	0.00	0.38	0.00	0.00	0.49	0.00	0.16	0.11
Ti	0.68	0.75	0.45	0.07	0.52	0.49	0.00	0.68	0.63	0.68
Fe(ii)	2.66	3.06	4.36	2.76	4.08	4.47	3.36	4.19	2.20	2.08
Mn	0.00	0.05	0.13	0.00	0.00	0.00	0.12	0.11	0.00	0.00
Mg	2.23	2.02	1.54	2.60	1.49	1.24	2.20	1.58	2.38	2.49
K	2.04	1.74	1.92	1.67	1.86	1.95	1.50	2.24	2.20	2.15
BaO	0.00	0.00	0.00	0.00	0.00	0.00	0.00	0.00	0.00	0.00
Total	15.52	15.31	15.82	15.48	15.55	15.72	15.67	15.96	15.57	15.51
Mg#	45.55	39.42	25.53	48.46	26.73	21.76	38.73	26.81	52.01	54.44

	21	22	23	24	25	26
Sample	Xe11 (R2_10)	Xe15 (R3_6)	Xe15 (R3_7)	Xe15 (R4_1)	Xe15 (R4_3)	Xe15 (R6_8)
SiO_2	36.83	38.88	37.92	40.48	39.98	42.19
TiO_2	5.90	0.00	0.00	1.74	1.63	0.00
Al_2O_3	9.91	18.36	18.83	14.86	14.81	14.30
FeO	30.35	7.48	6.71	12.50	13.44	12.91
MnO	0.00	0.00	0.00	0.00	0.00	0.59
MgO	5.78	22.52	22.78	18.91	19.64	17.46
BaO	11.24	9.78	9.72	10.08	9.23	11.59
K_2O	0.00	2.98	4.04	1.43	1.28	0.96
total	100.00	100.00	100.00	100.00	100.01	100.00
Numbers of cations on the basis of 22 anions.						
Si	5.74	5.43	5.33	5.73	5.66	6.00
Al (Z)	1.82	2.57	2.67	2.27	2.34	2.00
Al (Y)	0.00	0.46	0.45	0.21	0.13	0.39
Ti	0.69	0.00	0.00	0.19	0.17	0.00
Fe(ii)	3.95	0.87	0.79	1.48	1.59	1.53
Mn	0.00	0.00	0.00	0.00	0.00	0.07
Mg	1.34	4.69	4.77	3.99	4.14	3.70
K	2.23	1.74	1.74	1.82	1.67	2.10
BaO	0.00	0.16	0.22	0.08	0.07	0.05
Total	15.78	15.93	15.98	15.76	15.70	15.80
Mg#	25.34	84.30	85.82	72.95	72.26	69.74

KEY: Oxides in weight percentages. Al(Z)=aluminium in Z site. Al(Y)=aluminium in Y site. Mg#=magnesium ratio (Mg/(Mg+Fe+Mn

Table 6 Plagioclase analyses.

	1	2	3	4	5	6	7	8	9	10
Sample	P1 (R2_1)	P1 (R2_6)	P2 (R1_1)	P2 (R1_4)	P2 (R2_2)	P2 (R3_2)	P2 (R3_3)	P6 (R1_4)	P6 (R1_5)	P6 (R4_4)
SiO_2	68.60	69.05	64.81	62.26	59.14	59.75	59.71	56.51	68.41	57.83
Al_2O_3	19.36	19.38	27.30	26.02	28.55	25.63	25.56	26.45	25.21	26.29
FeO	0.00	0.00	0.00	0.00	0.00	0.00	0.00	0.40	0.00	0.00
CaO	0.00	0.00	7.27	3.71	2.57	7.08	6.80	13.18	0.00	11.49
Na_2O	12.04	11.57	0.00	7.06	5.58	6.81	7.54	2.69	6.39	2.98
K_2O	0.00	0.00	0.62	0.95	4.16	0.73	0.39	0.78	0.00	1.41
Total	100.00	100.00	100.00	100.00	100.00	100.00	100.00	100.00	100.01	100.00
Number of cations on the basis of 32 oxygen atoms										
Si	11.99	12.04	9.45	10.95	10.54	10.65	10.65	10.20	10.00	10.38
Al	3.99	3.98	7.96	5.39	6.00	5.39	5.37	5.62	7.37	5.56
Fe	0.00	0.00	0.00	0.00	0.00	0.00	0.00	0.06	0.00	0.00
Ca	0.00	0.00	1.06	0.70	0.49	1.35	1.30	2.55	0.00	2.21
Na	4.08	3.91	0.00	2.41	1.93	2.35	2.61	0.94	1.87	1.04
K	0.00	0.00	0.18	0.21	0.95	0.17	0.09	0.18	0.00	0.32
Total	20.06	19.93	18.66	19.66	19.90	19.91	20.01	19.55	19.24	19.52
End-members per cent										
An	0.00	0.00	100.00	21.05	14.58	34.91	32.50	69.49	0.00	61.90
Ab	100.00	100.00	0.00	72.50	57.29	60.78	65.27	25.61	100.00	29.06
Or	0.00	0.00	0.00	6.45	28.13	4.31	2.23	4.89	0.00	9.03

	11	12	13	14	15	16	17	18	19	20
	P6	P6	P6	P7	P7	P7	P8	P8	P8	P8
Sample	(R4_6)	(R4_7)	(R4_8)	(R2_1)	(R2_3)	(R3_9)	(R1_5)	(R2_1)	(R4_9)	(R4_10)
SiO_2	62.52	61.72	61.68	59.66	67.22	62.79	58.83	63.79	64.05	64.10
Al_2O_3	23.79	24.31	24.12	27.74	18.98	23.95	27.51	22.75	24.12	22.65
FeO	0.00	0.00	0.00	1.25	0.41	0.00		0.00	0.00	0.00
CaO	9.20	9.67	9.94	0.62	1.87	2.43	1.15	3.75	0.65	3.13
Na_2O	3.91	3.69	3.70	5.46	11.36	8.10	12.22	9.11	6.29	9.17
K_2O	0.58	0.62	0.56	5.28	0.17	2.74	0.28	0.60	4.90	0.96
Total	100.00	100.00	100.00	100.00	100.00	100.00	100.00	100.00	100.01	100.01
Number of cations on the basis of 32 oxygen atoms										
Si	11.05	10.93	10.93	10.68	11.85	11.16	10.49	11.28	11.35	11.33
Al	4.95	5.07	5.04	5.85	3.94	5.01	5.78	4.74	5.04	4.72
Fe	0.00	0.00	0.00	0.19	0.06	0.00	0.00	0.00	0.00	0.00
Ca	1.74	1.83	1.89	0.12	0.35	0.46	0.22	0.71	0.12	0.59
Na	1.34	1.27	1.27	1.89	3.88	2.79	4.22	3.12	2.16	3.14
K	0.13	0.14	0.13	1.21	0.04	0.62	0.06	0.14	1.11	0.22
Total	19.21	19.24	19.25	19.94	20.13	20.04	20.77	19.98	19.77	19.99
End-members per cent										
An	54.19	56.63	57.47	3.67	8.26	11.94	4.87	17.90	3.64	15.00
Ab	41.71	39.07	38.66	58.83	90.85	72.05	93.70	78.69	63.71	79.52
Or	4.10	4.30	3.87	37.50	0.89	16.01	1.43	3.41	32.65	5.48

	21	22	23	24	25	26	27	28	29	30
	P9	P9	P9	P9	Xe1	Xe1	Xe1	Xe1	Xe1	Xe3
Sample	(R1_1)	(R1_2)	(R1_3)	(R1_5)	(R1_3)	(R1_4)	(R2_5)	(R4_3)	(R4_4)	(R1_4)
SiO_2	64.33	65.73	67.04	65.52	62.13	62.44	66.31	59.13	63.93	63.11
Al_2O_3	22.77	22.94	21.55	22.96	24.17	23.59	24.11	25.15	22.89	22.91
FeO	0.00	0.00	0.00	0.00	0.00	0.00	0.00	0.72	0.00	0.00
CaO	4.59	0.88	1.88	1.12	5.59	5.56	0.00	7.29	3.58	4.16
Na_2O	7.51	8.25	8.97	8.36	7.42	7.65	8.03	7.21	8.93	8.54
K_2O	0.79	2.20	0.56	2.05	0.68	0.76	1.55	0.49	0.67	1.29
Total	99.99	100.00	100.00	100.01	100.00	100.00	100.00	100.00	100.00	100.00
Number of cations on the basis of 32 oxygen atoms										
Si	11.34	11.53	11.71	11.50	11.01	11.07	11.53	10.60	11.29	11.20
Al	4.73	4.74	4.44	4.75	5.05	4.93	4.94	5.32	4.76	4.79
Fe	0.00	0.00	0.00	0.00	0.00	0.00	0.00	0.11	0.00	0.00
Ca	0.87	0.17	0.35	0.21	1.06	1.06	0.00	1.40	0.68	0.79
Na	2.57	2.81	3.04	2.85	2.55	2.63	2.71	2.51	3.06	2.94
K	0.18	0.49	0.12	0.46	0.15	0.17	0.34	0.11	0.15	0.29
Total	19.67	19.74	19.66	19.77	19.82	19.86	19.52	20.05	19.94	20.02
End-members per cent										
An	24.01	4.78	10.01	5.99	28.19	27.36	0.00	34.83	17.41	19.67
Ab	71.08	81.01	86.44	80.95	67.70	68.20	88.75	62.36	78.71	73.08
Or	4.92	14.21	3.55	13.06	4.11	4.44	11.25	2.81	3.88	7.25

	31	32	33	34	35	36	37	38	39	40
Sample	Xe3 (R1_5)	Xe3 (R3_2)	Xe3 (R3_3)	Xe4 (R1_1)	Xe4 (R1_2)	Xe4 (R2_1)	Xe4 (R2_2)	Xe4 (R3_6)	Xe4 (R3_7)	Xe5 (R1_5)
SiO_2	64.27	63.86	63.55	62.55	62.32	67.32	62.17	67.77	65.91	60.79
Al_2O_3	22.81	22.78	22.81	23.75	23.71	21.06	23.77	20.58	22.07	25.06
FeO	0.42	0.00	0.00	0.00	0.00	0.00	0.00	0.00	0.00	0.00
CaO	1.01	3.83	4.26	5.16	4.84	0.45	5.23	0.00	1.34	6.13
Na_2O	7.13	8.82	8.58	7.95	8.54	10.36	7.87	10.85	9.49	7.20
K_2O	4.35	0.71	0.81	0.59	0.59	0.81	0.96	0.80	1.20	0.82
Total	100.00	100.00	100.00	100.00	100.00	100.00	100.00	100.00	100.01	100.00
Number of cations on the basis of 32 oxygen atoms										
Si	11.43	11.28	11.25	11.08	11.05	11.78	11.04	11.85	11.57	10.81
Al	4.78	4.74	4.76	4.96	4.96	4.34	4.97	4.24	4.57	5.25
Fe	0.06	0.00	0.00	0.00	0.00	0.00	0.00	0.00	0.00	0.00
Ca	0.19	0.73	0.81	0.98	0.92	0.08	0.99	0.00	0.25	1.17
Na	2.46	3.02	2.94	2.73	2.94	3.51	2.71	3.68	3.23	2.48
K	0.99	0.16	0.18	0.13	0.13	0.18	0.22	0.18	0.27	0.19
Total	19.91	19.93	19.94	19.88	20.00	19.90	19.94	19.95	19.89	19.90
End-members per cent										
An	5.30	18.58	20.53	25.48	23.05	2.23	25.37	0.00	6.72	30.43
Ab	67.55	77.31	74.82	71.05	73.60	92.98	69.09	95.37	86.12	64.71
Or	27.14	4.11	4.64	3.47	3.35	4.78	5.54	4.63	7.16	4.86

	41	42	43	44	45	46	47	48	49	50
Sample	Xe6 (R1_3)	Xe6 (R1_4)	Xe6 (R1_5)	Xe6 (R2_1)	Xe6 (R2_2)	Xe9 (R1_3)	Xe9 (R1_4)	Xe9 (R2_7)	Xe9 (R3_2)	Xe10 (R1_1)
SiO_2	66.09	64.06	64.50	64.28	68.29	61.80	64.83	65.86	66.64	61.91
Al_2O_3	21.29	22.58	22.32	22.32	20.37	23.71	22.65	22.73	23.02	24.17
FeO	0.00	0.00	0.00	0.00	0.00	0.00	0.00	0.34	0.00	0.00
CaO	1.25	3.12	3.19	3.18	0.42	5.83	1.69	0.00	0.00	5.20
Na_2O	10.86	9.21	9.77	9.89	10.74	8.65	9.84	9.18	9.32	7.88
K_2O	0.51	1.03	0.23	0.33	0.18	0.00	0.99	1.88	1.01	0.84
Total	100.00	100.00	100.00	100.00	100.00	100.00	100.00	100.00	100.00	100.00
Number of cations on the basis of 32 oxygen atoms										
Si	11.62	11.33	11.37	11.35	11.90	10.98	11.42	11.56	11.61	10.99
Al	4.41	4.71	4.64	4.65	4.18	4.96	4.70	4.70	4.73	5.06
Fe	0.00	0.00	0.00	0.00	0.00	0.00	0.00	0.05	0.00	0.00
Ca	0.23	0.59	0.60	0.60	0.08	1.11	0.32	0.00	0.00	0.99
Na	3.70	3.16	3.34	3.39	3.63	2.98	3.36	3.13	3.15	2.71
K	0.11	0.23	0.05	0.07	0.04	0.00	0.22	0.42	0.22	0.19
Total	20.08	20.01	20.00	20.06	19.84	20.03	20.02	19.86	19.71	19.93
End-members per cent										
An	5.80	14.85	15.08	14.80	2.11	27.14	8.18	0.00	0.00	25.43
Ab	91.37	79.32	83.64	83.38	96.84	72.86	86.13	88.13	93.33	69.65
Or	2.83	5.84	1.28	1.82	1.05	0.00	5.69	11.87	6.67	4.91

	51	52	53	54	55	56	57	58	59	60
Sample	Xe10 (R2_7)	Xe10 (R2_9)	Xe10 (R3_2)	Xe10 (R4_1)	Xe10 (R4_2)	Xe10 (R4_6)	Xe10 (R5_5)	Xe11_2(R1_1)	Xe11_2(R1_2)	Xe11_2(R1_3)
SiO_2	61.69	54.66	61.56	61.86	61.60	61.72	63.15	62.50	65.56	67.38
Al_2O_3	24.20	28.71	24.19	24.09	24.16	24.16	23.19	26.18	22.38	22.24
FeO	0.00	0.63	0.00	0.00	0.00	0.00	0.39	0.00	0.00	0.00
CaO	5.42	11.13	5.43	5.66	5.56	5.48	6.60	0.70	4.14	0.99
Na_2O	7.98	4.56	8.05	7.65	7.87	7.82	5.84	10.62	7.01	7.23
K_2O	0.71	0.32	0.76	0.74	0.82	0.82	0.84	0.00	0.92	2.16
Total	100.00	100.00	100.00	100.00	100.00	100.00	100.00	100.00	100.00	100.00
Number of cations on the basis of 32 oxygen atoms										
Si	10.96	9.87	10.94	10.98	10.95	10.97	11.17	10.97	11.50	11.75
Al	5.07	6.11	5.07	5.04	5.06	5.06	4.83	5.41	4.62	4.57
Fe	0.00	0.10	0.00	0.00	0.00	0.00	0.06	0.00	0.00	0.00
Ca	1.03	2.15	1.03	1.08	1.06	1.04	1.25	0.13	0.78	0.18
Na	2.75	1.60	2.77	2.63	2.71	2.69	2.00	3.61	2.38	2.44
K	0.16	0.07	0.17	0.17	0.19	0.19	0.19	0.00	0.21	0.48
Total	19.96	19.90	20.00	19.90	19.97	19.94	19.51	20.13	19.49	19.43
End-members per cent										
An	26.17	56.32	25.98	27.75	26.74	26.61	36.33	3.52	23.09	5.95
Ab	69.73	41.77	69.66	67.92	68.56	68.67	58.17	96.48	70.80	78.63
Or	4.10	1.91	4.35	4.34	4.69	4.72	5.50	0.00	6.11	15.43

	61	62	63	64	65
Sample	Xe16 (R1_2)	Xe16 (R1_6)	Xe16 (R2_7)	Xe16 (R2_8)	Xe16 (R5_6)
SiO_2	62.73	62.87	62.67	62.51	63.61
Al_2O_3	23.37	23.26	23.46	23.37	23.55
FeO	0.00	0.00	0.00	0.00	0.00
CaO	4.12	4.07	4.34	4.28	4.61
Na_2O	8.13	8.19	7.68	8.16	8.23
K_2O	1.65	1.62	1.86	1.67	0.00
Total	100.00	100.00	100.00	100.00	100.00
Number of cations on the basis of 32 oxygen atoms					
Si	11.14	11.17	11.14	11.12	11.20
Al	4.89	4.87	4.91	4.90	4.89
Fe	0.00	0.00	0.00	0.00	0.00
Ca	0.78	0.77	0.83	0.82	0.87
Na	2.80	2.82	2.64	2.81	2.81
K	0.37	0.37	0.42	0.38	0.00
Total	20.00	19.99	19.94	20.03	19.76
End-members per cent					
An	19.80	19.57	21.21	20.34	23.62
Ab	70.73	71.16	67.97	70.20	76.38
Or	9.47	9.27	10.82	9.46	0.00

KEY An=CaAl2Si2O8 Ab=NaAlSi3O8 Or=KAlSi3O8. The oxides are in weight percentages.

Table 7 Potassium feldspar analyses.

	1	2	3	4	5	6	7	8	9	10
	P1	P1	P1	P1	P2	P3	P5	P5	P5	P5
Sample	(R1_1)	(R2_2)	(R3_1)	(R3_3)	(R1_5)	(R1_4)	(R2_3)	(R2_6)	(R2_9)	(R3_4)
SiO_2	65.2	66.0	65.8	65.7	58.7	64.2	65.9	65.6	65.9	65.6
Al_2O_3	18.9	18.2	18.7	18.8	15.6	15.4	16.7	17.1	18.7	19.2
FeO	0.0	0.0	0.0	0.0	0.0	2.1	2.0	1.5	0.0	0.0
CaO	0.0	0.0	0.0	0.0	0.3	0.0	0.0	0.0	0.0	0.0
Na_2O	0.3	0.3	0.0	0.3	0.3	0.0	0.6	0.8	1.1	2.0
K_2O	15.6	15.5	15.6	15.2	25.2	18.2	14.9	15.0	14.3	13.2
Total	100.0	100.0	100.0	100.0	100.0	100.0	100.0	100.0	100.0	100.0
Number of cations on the basis of 32 oxygen atoms										
Si	12.0	12.1	12.1	12.0	11.6	12.2	12.2	12.1	12.1	12.0
Al	4.1	3.9	4.0	4.1	3.6	3.4	3.6	3.7	4.0	4.1
Fe	0.0	0.0	0.0	0.0	0.0	0.3	0.3	0.2	0.0	0.0
Ca	0.0	0.0	0.0	0.0	0.1	0.0	0.0	0.0	0.0	0.0
Na	0.1	0.1	0.0	0.1	0.1	0.0	0.2	0.3	0.4	0.7
K	3.7	3.6	3.6	3.6	6.4	4.4	3.5	3.5	3.3	3.1
Total	19.8	19.8	19.7	19.8	21.8	20.3	19.9	19.9	19.8	19.9
End-members per cent										
An	0.0	0.0	0.0	0.0	0.9	0.0	0.0	0.0	0.0	0.0
Ab	2.5	2.6	0.0	3.1	1.6	0.0	5.7	7.2	10.1	18.9
Or	97.5	97.4	100.0	96.9	97.5	100.0	94.3	92.8	89.9	81.1

	11	12	13	14	15	16	17	18	19	20
	P8	P8	P8	Xe1	Xe2	Xe2	Xe2	Xe2	Xe2	Xe3
Sample	(R3_7)	(R4_1)	(R4_2)	(R1_5)	(R1_1)	(R1_3)	(R1_4)	(R1_7)	(R2_4)	(R2_1)
SiO_2	65.3	65.0	65.5	72.3	66.8	66.5	66.8	66.9	66.8	67.1
Al_2O_3	18.6	20.6	19.5	15.0	18.7	19.1	18.9	18.9	18.8	18.7
FeO	0.0	0.0	0.0	0.0	0.0	0.0	0.0	0.0	0.0	0.0
CaO	0.0	0.0	0.0	0.0	0.0	0.0	0.0	0.0	0.0	0.0
Na_2O	0.4	0.4	0.3	0.5	4.3	3.9	4.2	4.6	4.5	3.7
K_2O	15.8	14.1	14.7	12.2	10.2	10.5	10.0	9.6	9.9	10.6
Total	100.0	100.0	100.0	100.0	100.0	100.0	100.0	100.0	100.0	100.0
Number of cations on the basis of 32 oxygen atoms										
Si	12.0	11.8	12.0	12.9	12.1	12.0	12.0	12.0	12.0	12.1
Al	4.0	4.4	4.2	3.2	4.0	4.1	4.0	4.0	4.0	4.0
Fe	0.0	0.0	0.0	0.0	0.0	0.0	0.0	0.0	0.0	0.0
Ca	0.0	0.0	0.0	0.0	0.0	0.0	0.0	0.0	0.0	0.0
Na	0.1	0.1	0.1	0.2	1.5	1.4	1.5	1.6	1.6	1.3
K	3.7	3.3	3.4	2.8	2.3	2.4	2.3	2.2	2.3	2.4
Total	19.9	19.7	19.7	19.0	19.9	19.9	19.8	19.8	19.9	19.8
End-members per cent										
An	0.0	0.0	0.0	0.0	0.0	0.0	0.0	0.0	0.0	0.0
Ab	3.4	3.7	3.3	5.3	39.2	36.2	39.1	42.0	40.7	34.5
Or	96.6	96.3	96.7	94.7	60.8	63.8	60.9	58.0	59.3	65.5

	21	22	23	24	25	26	27	28	29	30
Sample	Xe3 (R2_2)	Xe4 (R3_5)	Xe4 (R1_6)	Xe5 (R2_1)	Xe6 (R1_2)	Xe6 (R2_3)	Xe7 (R1_3)	Xe7 (R2_3)	Xe7 (R2_5)	Xe7 (R2_7)
SiO_2	65.8	65.9	66.2	66.8	65.9	67.2	65.7	66.5	66.8	69.3
Al_2O_3	18.7	18.5	18.6	18.5	18.4	18.8	18.6	18.9	18.7	16.7
FeO	0.0	0.0	0.0	0.0	0.0	0.0	0.0	0.0	0.0	0.0
CaO	0.0	0.0	0.0	0.0	0.0	0.0	0.0	0.0	0.0	0.0
Na_2O	1.6	0.0	1.2	2.2	0.4	4.7	0.4	2.5	3.6	0.3
K_2O	13.9	15.6	14.0	12.5	15.3	9.3	15.4	12.1	11.0	13.8
Total	100.0	100.0	100.0	100.0	100.0	100.0	100.0	100.0	100.0	100.0
Number of cations on the basis of 32 oxygen atoms										
Si	12.0	12.1	12.1	12.1	12.1	12.1	12.1	12.1	12.1	12.5
Al	4.0	4.0	4.0	4.0	4.0	4.0	4.0	4.0	4.0	3.6
Fe	0.0	0.0	0.0	0.0	0.0	0.0	0.0	0.0	0.0	0.0
Ca	0.0	0.0	0.0	0.0	0.0	0.0	0.0	0.0	0.0	0.0
Na	0.6	0.0	0.4	0.8	0.1	1.6	0.1	0.9	1.2	0.1
K	3.2	3.6	3.3	2.9	3.6	2.1	3.6	2.8	2.5	3.2
Total	19.9	19.7	19.8	19.7	19.8	19.8	19.8	19.8	19.8	19.3
End-members per cent										
An	0.0	0.0	0.0	0.0	0.0	0.0	0.0	0.0	0.0	0.0
Ab	14.6	0.0	11.4	20.7	3.6	43.3	3.7	24.0	33.0	2.8
Or	85.4	100.0	88.6	79.3	96.4	56.7	96.3	76.0	67.0	97.2

	31	32	33	34	35	36	37	38	39	40
Sample	Xe12 (R1_1)	Xe12 (R2_2)	Xe13 (R2_8)	Xe13 (R3_5)	Xe14 (R1_2)	Xe14 (R1_8)	Xe14 (R3_2)	Xe14 (R3_3)	Xe15 (R1_11)	Xe15 (R2_3)
SiO_2	66.3	66.3	66.5	66.5	66.4	66.0	66.3	66.1	65.8	65.5
Al_2O_3	18.5	18.4	18.3	20.0	15.4	18.2	16.7	17.9	18.1	17.8
FeO	0.0	0.0	0.0	0.0	0.0	0.0	0.0	0.0	0.0	0.0
CaO	0.0	0.0	0.0	0.0	2.4	0.0	1.7	0.6	0.0	0.0
Na_2O	1.8	2.1	0.0	2.9	0.3	0.4	0.3	0.2	0.0	0.7
K_2O	13.4	13.1	15.3	10.7	15.5	15.4	15.0	15.1	16.1	16.1
Total	100.0	100.0	100.0	100.0	100.0	100.0	100.0	100.0	100.0	100.0
Number of cations on the basis of 32 oxygen atoms										
Si	12.1	12.1	12.2	12.0	12.3	12.1	12.2	12.1	12.1	12.1
Al	4.0	4.0	3.9	4.2	3.4	3.9	3.6	3.9	3.9	3.9
Fe	0.0	0.0	0.0	0.0	0.0	0.0	0.0	0.0	0.0	0.0
Ca	0.0	0.0	0.0	0.0	0.5	0.0	0.3	0.1	0.0	0.0
Na	0.7	0.7	0.0	1.0	0.1	0.1	0.1	0.1	0.0	0.2
K	3.1	3.1	3.6	2.5	3.6	3.6	3.5	3.5	3.8	3.8
Total	19.8	19.8	19.7	19.7	19.9	19.8	19.8	19.7	19.8	20.0
End-members per cent										
An	0.0	0.0	0.0	0.0	11.1	0.0	8.5	3.4	0.0	0.0
Ab	17.3	19.6	0.0	28.8	2.9	3.3	2.9	1.9	0.0	6.0
Or	82.7	80.4	100.0	71.2	86.0	96.7	88.6	94.7	100.0	94.0

	41	42	43	44
Sample	Xe15 (R2_3)	Xe15 (R3_1)	Xe15 (R3_2)	Xe15_2 (R4_1)
SiO_2	65.5	65.9	65.9	65.4
Al_2O_3	17.8	18.4	18.7	17.3
FeO	0.0	0.0	0.0	0.0
CaO	0.0	0.0	0.0	0.0
Na_2O	0.7	0.0	0.0	0.2
K_2O	16.1	15.7	15.5	17.0
Total	100.0	100.0	100.0	100.0
Number of cations on the basis of 32 oxygen atoms				
Si	12.1	12.1	12.1	12.1
Al	3.9	4.0	4.0	3.8
Fe	0.0	0.0	0.0	0.0
Ca	0.0	0.0	0.0	0.0
Na	0.2	0.0	0.0	0.1
K	3.8	3.7	3.6	4.0
Total	20.0	19.8	19.7	20.0
End-members per cent				
An	0.0	0.0	0.0	0.0
Ab	6.0	0.0	0.0	2.2
Or	94.0	100.0	100.0	97.8

KEY An=CaAl2Si2O8 Ab=NaAlSi3O8 Or=KAlSi3O8. The oxides are in weight percentages

Table 8 Symplectic feldspar analyses.

	1	2	3	4	5	6	7	8	9	10
Sample	P4 (R2_4)	P7 (R2_5)	P7 (R2_7)	P8 (R4_15)	P8 (R5_3)	Xe10 (R2_2)	Xe10 (R4_4)	Xe11 (R1_7)	Xe11_2 (R2_2)	Xe16 (R2_2)
SiO_2	56.05	56.34	64.60	60.62	62.20	55.17	65.10	66.14	58.75	66.33
Al_2O_3	32.92	29.10	20.06	26.21	28.30	28.04	19.28	26.26	26.36	19.09
FeO	0.94	1.52	0.00	0.71	0.00	1.15	0.68	0.00	0.72	0.00
CaO	2.03	0.00	0.87	1.84	1.40	9.99	0.68	0.91	8.93	0.00
Na_2O	6.76	0.29	1.41	10.38	8.20	4.93	3.72	6.69	5.00	3.59
K_2O	1.31	12.76	13.06	0.23	0.00	0.73	10.55	0.00	0.25	10.99
Total	100.00	100.00	100.00	99.99	100.10	100.00	100.00	100.00	100.00	100.00
Number of cations on the basis of 32 oxygens										
Si	9.93	10.37	11.79	10.76	10.82	9.98	11.84	11.37	10.49	12.00
Al	6.87	6.31	4.32	5.48	5.80	5.98	4.13	5.32	5.55	4.07
Fe	0.14	0.23	0.00	0.11	0.00	0.17	0.10	0.00	0.11	0.00
Ca	0.39	0.00	0.17	0.35	0.26	1.94	0.13	0.17	1.71	0.00
Na	2.32	0.10	0.50	3.57	2.77	1.73	1.31	2.23	1.73	1.26
K	0.30	3.00	3.04	0.05	0.00	0.17	2.45	0.00	0.06	2.54
Total	19.94	20.02	19.82	20.31	19.66	19.97	19.97	19.09	19.63	19.86
End-members per cent										
An	12.85	0.00	4.59	8.80	8.62	50.51	3.39	6.96	48.87	0.00
Ab	77.31	3.34	13.49	89.88	91.38	45.11	33.73	93.04	49.52	33.19
Or	9.84	96.66	81.92	1.31	0.00	4.38	62.89	0.00	1.62	66.81

	11	12	13
Sample	P4 (R2_11)	Xe11 (R5_12)	Xe11 (R5_25)
SiO_2	50.25	55.94	53.08
Al_2O_3	34.49	25.89	29.41
FeO	2.85	5.57	3.44
MgO	2.91	1.42	1.29
CaO	1.31	0.00	0.63
Na_2O	3.37	0.39	0.65
K_2O	4.81	10.80	11.49
Total	100.00	100.00	100.00

Oxides in weight percentages.
Analyses represent vermicular intergrowths occuring in/with clinopyroxene. Pyroxene in analysis 6 is exceptionally orthopyroxene which is enclosed by opaque mineral. Analyses 11–13 contain magnesium propably because the analysed area has been too narrow and the beam (1µm) has hit the pyroxene.

Table 9 Pyroxene analyses.

	1	2	3	4	5	6	7	8	9	10
	P2	P2	P2	P2	P2	P3	P3	P3		P3
Sample	(R2_1)	(R2_3)	(R2_4)	(R2_5)	(R3_1)	(R1_1)	(R1_2)	(k3_1) P3	(k3_2)	(R2_2)
SiO_2	55.63	53.06	54.46	52.44	53.14	55.60	54.86	55.00	55.90	54.60
TiO_2	0.00	0.00	0.00	0.00	0.00	0.00	1.17	1.10	0.00	1.70
Al_2O_3	0.00	1.26	2.62	1.55	1.34	0.00	0.00	0.00	0.00	0.00
Cr_2O_3	0.00	0.00	0.00	0.00	0.00	0.00	0.00	0.00	0.00	0.00
FeO	9.37	25.18	9.96	27.15	24.87	7.00	6.37	6.80	6.45	6.80
MnO	0.00	0.77	0.00	0.00	0.77	0.00	0.00	0.00	0.00	0.00
MgO	13.33	19.34	12.73	17.72	19.30	12.40	12.08	12.30	13.23	11.70
CaO	21.66	0.39	20.24	1.15	0.58	25.00	25.52	24.80	24.42	25.20
Na_2O	0.00	0.00	0.00	0.00	0.00	0.00	0.00	0.00	0.00	0.00
K_2O	0.00	0.00	0.00	0.00	0.00	0.00	0.00	0.00	0.00	0.00
Total	100.00	100.00	100.00	100.00	100.00	100.00	100.00	100.00	100.00	100.00
Number of cations on the basis of 6 oxygens										
Si	2.06	2.00	2.01	1.99	2.00	2.06	2.03	2.03	2.06	2.02
Al (T)	0.00	0.00	0.00	0.01	0.00	0.00	0.00	0.00	0.00	0.00
Al (M1)	0.00	0.05	0.11	0.06	0.06	0.00	0.00	0.00	0.00	0.00
Fe(3+)	0.00	0.00	0.00	0.00	0.00	0.00	0.00	0.00	0.00	0.00
Cr	0.00	0.00	0.00	0.00	0.00	0.00	0.00	0.00	0.00	0.00
Ti	0.00	0.00	0.00	0.00	0.00	0.00	0.03	0.03	0.00	0.05
Fe(2+)	0.29	0.80	0.31	0.87	0.79	0.22	0.20	0.21	0.20	0.21
Mn	0.00	0.02	0.00	0.00	0.02	0.00	0.00	0.00	0.00	0.00
Mg	0.74	1.09	0.70	1.00	1.08	0.68	0.67	0.68	0.73	0.65
Ca	0.86	0.02	0.80	0.05	0.02	0.99	1.01	0.98	0.96	1.00
Na	0.00	0.00	0.00	0.00	0.00	0.00	0.00	0.00	0.00	0.00
K	0.00	0.00	0.00	0.00	0.00	0.00	0.00	0.00	0.00	0.00
total	3.95	3.98	3.94	3.98	3.98	3.95	3.94	3.94	3.95	3.93
Mg#	71.72	57.05	69.51	53.78	57.29	75.95	77.17	76.33	78.53	75.42
Per cent end-members										
Wo	45.48	0.81	44.13	2.43	1.23	52.31	53.78	52.42	50.78	53.75
En	38.94	56.43	38.63	52.31	56.42	36.10	35.51	36.18	38.52	34.73
Fs	15.58	42.75	17.24	45.26	42.36	11.59	10.70	11.40	10.71	11.53
Ae	0.00	0.00	0.00	0.00	0.00	0.00	0.00	0.00	0.00	0.00
total	100.00	100.00	100.00	100.00	100.00	100.00	100.00	100.00	100.00	100.00

	11	12	13	14	15	16	17	18	19	20
	P3	P3	P3	P4	P4	P4	P5	P5	P5	P6
Sample	(R2_3)	(R3_1)	(R3_3)	(R2_3)	(R2_10)	(R3_2)	(R4_3)	(R4_5)	(R5_3)	(R1_2)
SiO_2	55.20	55.08	55.61	51.88	52.27	54.09	45.04	45.79	51.47	51.08
TiO_2	1.30	1.27	1.05	0.55	0.54	0.00	0.00	0.00	0.00	0.54
Al_2O_3	0.00	0.66	0.00	4.59	4.33	2.87	11.36	10.18	10.19	3.28
Cr_2O_3	0.00	0.00	0.00	0.00	0.00	0.00	0.00	0.00	0.00	0.00
FeO	6.80	6.45	7.18	8.48	8.60	6.55	32.10	31.80	23.48	12.53
MnO	0.00	0.00	0.00	0.00	0.00	0.00	0.65	0.82	0.00	0.00
MgO	12.20	15.67	15.68	12.95	12.37	13.94	10.86	11.05	14.58	8.50
CaO	24.50	20.31	20.49	20.98	20.88	21.84	0.00	0.35	0.28	24.07
Na_2O	0.00	0.57	0.00	0.57	1.01	0.70	0.00	0.00	0.00	0.00
K_2O	0.00	0.00	0.00	0.00	0.00	0.00	0.00	0.00	0.00	0.00
total	100.00	100.01	100.00	100.00	100.00	100.00	100.00	100.00	100.00	100.00
Number of cations on basis of 6 oxygens										
Si	2.04	2.01	2.03	1.92	1.94	1.98	1.76	1.79	1.90	1.94
Al (T)	0.00	0.00	0.00	0.08	0.06	0.02	0.24	0.21	0.10	0.06
Al (M1)	0.00	0.03	0.00	0.12	0.13	0.11	0.28	0.26	0.34	0.09
Fe(3+)	0.00	0.00	0.00	0.00	0.00	0.00	0.00	0.00	0.00	0.00
Cr	0.00	0.00	0.00	0.00	0.00	0.00	0.00	0.00	0.00	0.00
Ti	0.04	0.03	0.03	0.02	0.02	0.00	0.00	0.00	0.00	0.02
Fe(2+)	0.21	0.20	0.22	0.26	0.27	0.20	1.05	1.04	0.75	0.40
Mn	0.00	0.00	0.00	0.00	0.00	0.00	0.02	0.03	0.00	0.00
Mg	0.67	0.85	0.85	0.71	0.68	0.76	0.63	0.64	0.80	0.48
Ca	0.97	0.79	0.80	0.83	0.83	0.86	0.00	0.01	0.01	0.98
Na	0.00	0.04	0.00	0.04	0.07	0.05	0.00	0.00	0.00	0.00
K	0.00	0.00	0.00	0.00	0.00	0.00	0.00	0.00	0.00	0.00
total	3.93	3.96	3.94	3.99	3.99	3.98	3.99	3.98	3.90	3.97
Mg#	76.18	81.24	79.57	73.15	71.93	79.14	37.15	37.65	52.54	54.74
Per cent end-members										
Wo	52.26	41.98	42.68	44.95	44.77	45.83	0.00	0.85	0.71	52.59
En	36.21	45.18	45.46	38.61	36.89	40.71	37.04	37.21	51.41	25.86
Fs	11.54	10.59	11.86	14.23	14.43	10.79	62.96	61.94	47.88	21.55
Ae	0.00	2.25	0.00	2.21	3.91	2.67	0.00	0.00	0.00	0.00
total	100.00	100.00	100.00	100.00	100.00	100.00	100.00	100.00	100.00	100.00

	21	22	23	24	25	26	27	28	29	30
	P6	P6	P6	P7	P7	P7	P7	P7	P8	P8
Sample	(R1_3)	(R4_2)	(R4_5)	(R2_4)	(R2_6)	(R2_9)	(R3_5)	(R3_7)	(R1_1)	(R1_2)
SiO_2	51.21	51.17	51.66	52.77	53.44	52.49	52.09	51.34	50.25	53.87
TiO_2	0.43	1.02	0.00	0.80	0.56	0.57	0.79	0.94	1.49	0.94
Al_2O_3	2.58	2.05	2.49	3.15	2.70	4.30	6.29	4.97	5.59	0.15
Cr_2O_3	0.00	0.00	0.00	0.00	0.00	0.00	0.00	0.00	0.00	0.00
FeO	11.56	10.98	11.13	10.47	9.13	8.68	10.97	10.79	10.18	18.33
MnO	0.42	0.00	0.00	0.00	0.00	0.00	0.00	0.00	0.00	0.45
MgO	8.71	10.02	9.17	13.65	13.79	14.17	11.27	11.80	10.75	6.53
CaO	25.10	24.76	25.55	19.16	20.38	19.79	16.62	20.16	21.74	14.91
Na_2O	0.00	0.00	0.00	0.00	0.00	0.00	1.97	0.00	0.00	4.82
K_2O	0.00	0.00	0.00	0.00	0.00	0.00	0.00	0.00	0.00	0.00
total	100.00	100.00	100.00	100.00	100.00	100.00	100.00	100.00	100.00	100.00
Number of cations on basis of 6 oxygens										
Si	1.95	1.94	1.96	1.96	1.97	1.93	1.93	1.91	1.88	2.08
Al (T)	0.05	0.06	0.04	0.04	0.03	0.07	0.07	0.09	0.01	0.00
Al (M1)	0.07	0.03	0.07	0.09	0.09	0.12	0.20	0.13	0.23	0.01
Fe(3+)	0.00	0.00	0.00	0.00	0.00	0.00	0.00	0.00	0.00	0.21
Cr	0.00	0.00	0.00	0.00	0.00	0.00	0.00	0.00	0.00	0.00
Ti	0.01	0.03	0.00	0.02	0.02	0.02	0.02	0.03	0.04	0.03
Fe(2+)	0.37	0.35	0.35	0.33	0.29	0.27	0.34	0.34	0.32	0.37
Mn	0.01	0.00	0.00	0.00	0.00	0.00	0.00	0.00	0.00	0.01
Mg	0.49	0.57	0.52	0.75	0.76	0.78	0.62	0.66	0.60	0.38
Ca	1.02	1.01	1.04	0.76	0.81	0.78	0.66	0.80	0.87	0.62
Na	0.00	0.00	0.00	0.00	0.00	0.00	0.14	0.00	0.00	0.36
K	0.00	0.00	0.00	0.00	0.00	0.00	0.00	0.00	0.00	0.00
total	3.98	3.98	3.98	3.96	3.96	3.96	3.99	3.96	3.96	4.06
Mg#	56.44	61.94	59.50	69.92	72.93	74.44	64.69	66.09	65.31	38.25
Per cent end-members										
Wo	53.85	52.35	54.32	41.28	43.56	42.70	37.38	44.70	48.60	31.63
En	25.99	29.47	27.13	40.91	41.03	42.54	35.28	36.40	33.44	19.27
Fs	20.16	18.18	18.55	17.81	15.41	14.76	19.33	18.90	17.96	30.58
Ae	0.00	0.00	0.00	0.00	0.00	0.00	8.01	0.00	0.00	18.52
total	100.00	100.00	100.00	100.00	100.00	100.00	100.00	100.00	100.00	100.00

	31	32	33	34	35	36	37	38	39	40
	P8	P8	P8	P8	P8	P8	P8	P9	Xe2	Xe9
Sample	(R1_3)	(R1_4)	(R1_11)	(R2_2)	(R4_16)	(R4_19)	(R5_2)	(R2_1)	(R1_5)	(R1_5)
SiO_2	53.43	53.45	53.84	51.88	52.98	51.88	51.80	65.68	53.54	56.48
TiO_2	2.89	1.37	2.05	0.77	0.67	0.63	1.00	0.00	3.59	0.86
Al_2O_3	0.91	1.25	0.40	3.21	2.77	3.34	3.60	21.09	0.00	0.00
Cr_2O_3	0.00	0.00	0.00	0.00	0.00	0.00	0.00	0.00	0.00	0.00
FeO	17.64	17.18	20.77	11.26	10.46	12.37	9.80	1.80	26.92	28.31
MnO	0.00	0.00	0.00	0.55	0.00	0.00	0.00	0.00	0.00	0.00
MgO	5.92	7.23	4.59	12.17	12.01	11.63	11.70	0.00	6.66	0.00
CaO	13.24	16.02	10.81	19.58	21.11	19.48	22.10	0.62	0.69	1.58
Na_2O	5.98	3.51	7.54	0.58	0.00	0.67	0.00	7.79	6.78	12.77
K_2O	0.00	0.00	0.00	0.00	0.00	0.00	0.00	3.02	1.82	0.00
total	100.00	100.01	100.00	100.00	100.00	100.00	100.00	100.00	100.00	100.00
Number of cations on basis of 6 oxygens										
Si	2.05	2.04	2.09	1.94	1.97	1.95	1.93	2.19	2.09	2.23
Al (T)	0.00	0.00	0.00	0.06	0.03	0.00	0.07	0.00	0.00	0.00
Al (M1)	0.04	0.06	0.02	0.09	0.09	0.15	0.09	0.83	0.00	0.00
Fe(3+)	0.20	0.05	0.36	0.00	0.00	0.00	0.00	0.00	0.30	0.66
Cr	0.00	0.00	0.00	0.00	0.00	0.00	0.00	0.00	0.00	0.00
Ti	0.08	0.04	0.06	0.02	0.02	0.02	0.03	0.00	0.11	0.03
Fe(2+)	0.35	0.49	0.29	0.35	0.33	0.39	0.31	0.05	0.56	0.22
Mn	0.00	0.00	0.00	0.02	0.00	0.00	0.00	0.00	0.00	0.00
Mg	0.34	0.41	0.27	0.68	0.67	0.65	0.65	0.00	0.39	0.00
Ca	0.54	0.66	0.45	0.79	0.84	0.78	0.88	0.02	0.03	0.07
Na	0.44	0.26	0.57	0.04	0.00	0.05	0.00	0.50	0.51	0.98
K	0.00	0.00	0.00	0.00	0.00	0.00	0.00	0.13	0.09	0.00
total	4.06	4.02	4.10	3.99	3.95	3.99	3.96	3.72	4.08	4.18
Mg#	37.46	42.87	28.28	64.74	67.18	62.63	68.04	0.00	30.62	0.00
Per cent end-members										
Wo	28.88	34.99	23.23	41.72	45.77	42.04	47.93	3.83	1.61	3.48
En	17.98	21.98	13.72	36.13	36.22	35.10	35.31	0.00	21.71	0.00
Fs	29.53	29.16	33.76	19.84	18.01	20.10	16.76	9.31	47.97	45.82
Ae	23.61	13.87	29.29	2.31	0.00	2.77	0.00	86.86	28.71	50.70
total	100.00	100.00	100.00	100.00	100.00	100.00	100.00	100.00	100.00	100.00

Sample	41 Xe9 (R3_3)	42 Xe9 (R3_5)	43 Xe10 (R2_1)	44 Xe10 (R2_3)	45 Xe10 (R2_6)	46 Xe10 (R3_1)	47 Xe10 (R4_3)	48 Xe10 (R4_5)	49 Xe11 (R4_19)	50 Xe11 (R5_11)
SiO_2	55.97	55.69	50.36	50.56	52.05	52.20	53.56	52.68	48.00	50.55
TiO_2	1.84	0.58	0.58	0.00	0.86	0.55	0.72	0.60	2.00	1.11
Al_2O_3	0.00	0.00	8.73	7.96	5.77	5.84	3.48	5.63	5.90	3.35
Cr_2O_3	0.00	0.00	0.00	0.00	0.00	0.00	0.00	0.00	0.00	0.00
FeO	28.24	29.48	15.71	16.44	11.21	11.17	11.43	10.77	10.80	9.59
MnO	0.00	0.00	0.00	0.48	0.00	0.00	0.00	0.00	0.00	0.00
MgO	0.00	0.00	23.60	23.55	12.19	12.25	12.50	12.28	8.00	9.56
CaO	0.00	0.44	1.02	1.01	16.68	16.72	17.00	16.95	24.90	25.83
Na_2O	13.95	13.80	0.00	0.00	1.24	1.27	1.31	1.10	0.40	0.00
K_2O	0.00	0.00	0.00	0.00	0.00	0.00	0.00	0.00	0.00	0.00
total	100.00	100.00	100.00	100.00	100.00	100.00	100.00	100.00	100.00	99.99
Number of cations on basis of 6 oxygens										
Si	2.21	2.22	1.82	1.83	1.93	1.93	1.98	1.94	1.83	1.91
Al (T)	0.00	0.00	0.18	0.17	0.07	0.07	0.02	0.06	0.17	0.09
Al (M1)	0.00	0.00	0.19	0.17	0.18	0.18	0.14	0.19	0.09	0.06
Fe(3+)	0.75	0.83	0.00	0.00	0.00	0.00	0.00	0.00	0.00	0.00
Cr	0.00	0.00	0.00	0.00	0.00	0.00	0.00	0.00	0.00	0.00
Ti	0.05	0.02	0.02	0.00	0.02	0.02	0.02	0.02	0.06	0.03
Fe(2+)	0.12	0.08	0.48	0.50	0.35	0.35	0.36	0.34	0.34	0.30
Mn	0.00	0.00	0.00	0.01	0.00	0.00	0.00	0.00	0.00	0.00
Mg	0.00	0.00	1.27	1.27	0.67	0.68	0.69	0.67	0.45	0.54
Ca	0.00	0.02	0.04	0.04	0.66	0.66	0.67	0.67	1.02	1.05
Na	1.07	1.06	0.00	0.00	0.09	0.09	0.09	0.08	0.03	0.00
K	0.00	0.00	0.00	0.00	0.00	0.00	0.00	0.00	0.00	0.00
total	4.21	4.23	3.99	4.00	3.97	3.98	3.97	3.96	4.00	3.98
Mg#	0.00	0.00	72.81	71.28	65.96	66.17	66.10	67.03	56.91	63.99
Per cent end-members										
Wo	0.00	0.94	2.22	2.15	37.32	37.29	37.15	38.07	55.10	55.37
En	0.00	0.00	71.12	69.73	37.94	38.03	38.02	38.39	24.63	28.52
Fs	45.01	45.73	26.67	28.12	19.73	19.58	19.66	19.08	18.67	16.12
Ae	54.99	53.33	0.00	0.00	5.02	5.11	5.17	4.45	1.60	0.00
total	100.00	100.00	100.00	100.00	100.00	100.00	100.00	100.00	100.00	100.00

Sample	51 Xe11 (R5_24)	52 Xe11 (R1_6)	53 Xe11 (R2_3)	54 Xe11 (R4_2)	55 Xe11 (R4_3)	56 Xe11 (R4_5)	57 Xe11_2 (R2_1)	58 Xe11_2 (R2_3)	59 Xe15_2 (R1_1)	60 Xe15_2 (R1_3)
SiO_2	49.62	50.80	49.10	51.00	50.40	49.80	48.73	49.15	54.27	53.09
TiO_2	1.20	1.38	1.50	1.00	1.10	1.10	1.69	1.23	0.00	0.00
Al_2O_3	3.67	3.84	3.90	3.20	2.80	3.50	7.21	6.29	0.00	0.00
Cr_2O_3	0.00	0.00	0.00	0.00	0.00	0.00	0.00	0.00	0.00	0.00
FeO	11.25	6.87	11.40	9.80	11.50	11.40	9.01	10.28	10.82	12.48
MnO	0.51	0.00	0.50	0.00	0.00	0.00	0.00	0.00	0.00	0.00
MgO	8.39	10.45	8.20	9.50	8.90	8.70	10.10	9.70	10.11	9.12
CaO	25.36	26.66	25.40	25.50	25.30	25.50	23.26	23.35	24.81	25.32
Na_2O	0.00	0.00	0.00	0.00	0.00	0.00	0.00	0.00	0.00	0.00
K_2O	0.00	0.00	0.00	0.00	0.00	0.00	0.00	0.00	0.00	0.00
total	100.00	100.00	100.00	100.00	100.00	100.00	100.00	100.00	100.00	100.00
Number of cations on basis of 6 oxygens										
Si	1.90	1.90	1.88	1.93	1.92	1.90	1.82	1.85	2.04	2.02
Al (T)	0.10	0.10	0.12	0.07	0.08	0.10	0.18	0.15	0.00	0.00
Al (M1)	0.06	0.07	0.06	0.07	0.05	0.06	0.14	0.13	0.00	0.00
Fe(3+)	0.00	0.00	0.00	0.00	0.00	0.00	0.00	0.00	0.00	0.00
Cr	0.00	0.00	0.00	0.00	0.00	0.00	0.00	0.00	0.00	0.00
Ti	0.03	0.04	0.04	0.03	0.03	0.03	0.05	0.03	0.00	0.00
Fe(2+)	0.36	0.22	0.37	0.31	0.37	0.36	0.28	0.33	0.34	0.40
Mn	0.02	0.00	0.02	0.00	0.00	0.00	0.00	0.00	0.00	0.00
Mg	0.48	0.58	0.47	0.53	0.51	0.49	0.56	0.54	0.57	0.52
Ca	1.04	1.07	1.04	1.03	1.03	1.04	0.93	0.94	1.00	1.03
Na	0.00	0.00	0.00	0.00	0.00	0.00	0.00	0.00	0.00	0.00
K	0.00	0.00	0.00	0.00	0.00	0.00	0.00	0.00	0.00	0.00
total	3.99	3.98	3.99	3.98	3.99	3.99	3.97	3.98	3.96	3.98
Mg#	55.97	73.06	55.11	63.35	57.98	57.64	66.67	62.71	62.49	56.57
Per cent end-members										
Wo	54.82	57.14	55.06	54.93	54.18	54.81	52.38	51.98	52.34	52.96
En	25.23	31.27	24.74	28.48	26.52	26.02	31.66	30.04	29.66	26.54
Fs	19.94	11.59	20.20	16.59	19.30	19.17	15.95	17.98	18.01	20.50
Ae	0.00	0.00	0.00	0.00	0.00	0.00	0.00	0.00	0.00	0.00
total	100.00	100.00	100.00	100.00	100.00	100.00	100.00	100.00	100.00	100.00

	61	62	63	64	65	66	67	68	69	70
Sample	Xe15_2 (R2_1)	Xe15_2 (R2_4)	Xe15_2 (R2_5)	Xe15_2 (R3_2)	Xe15_2 (R3_3)	Xe15_2 (R3_4)	Xe16 (R1_4)	Xe16 (R2_1)	Xe16 (R2_4)	Xe16 (R5_2)
SiO_2	53.31	52.82	52.28	53.09	53.88	53.36	52.48	53.49	53.49	52.21
TiO_2	0.98	0.85	1.03	0.73	0.91	1.38	0.64	0.00	0.34	0.48
Al_2O_3	0.00	0.00	0.00	0.00	0.00	0.91	5.03	2.17	3.11	5.23
Cr_2O_3	0.00	0.00	0.00	0.00	0.00	0.00	0.00	0.00	0.00	0.00
FeO	12.20	11.39	18.08	11.78	14.50	10.19	11.47	10.66	9.75	11.78
MnO	0.00	0.41	0.82	1.05	0.84	0.75	0.00	0.00	0.00	0.00
MgO	9.92	10.00	6.14	9.26	7.66	9.82	11.70	13.68	13.38	11.51
CaO	22.45	23.21	19.09	23.10	20.49	22.29	17.32	20.00	19.93	17.24
Na_2O	1.14	1.32	2.56	0.99	1.71	1.31	1.36	0.00	0.00	1.56
K_2O	0.00	0.00	0.00	0.00	0.00	0.00	0.00	0.00	0.00	0.00
total	100.00	100.00	100.00	100.00	100.00	100.00	100.00	100.00	100.00	100.00
Number of cations on basis of 6 oxygens										
Si	2.02	2.01	2.04	2.02	2.06	2.01	1.95	1.99	1.98	1.94
Al (T)	0.00	0.00	0.00	0.00	0.00	0.00	0.05	0.01	0.02	0.06
Al (M1)	0.00	0.00	0.00	0.00	0.00	0.04	0.17	0.08	0.11	0.17
Fe(3+)	0.00	0.05	0.09	0.00	0.00	0.00	0.00	0.00	0.00	0.00
Cr	0.00	0.00	0.00	0.00	0.00	0.00	0.00	0.00	0.00	0.00
Ti	0.03	0.02	0.03	0.02	0.03	0.04	0.02	0.00	0.01	0.01
Fe(2+)	0.39	0.31	0.50	0.38	0.47	0.32	0.36	0.33	0.31	0.37
Mn	0.00	0.01	0.03	0.03	0.03	0.02	0.00	0.00	0.00	0.00
Mg	0.56	0.57	0.36	0.53	0.44	0.55	0.65	0.76	0.74	0.64
Ca	0.91	0.95	0.80	0.94	0.84	0.90	0.69	0.80	0.79	0.69
Na	0.08	0.10	0.19	0.07	0.13	0.10	0.10	0.00	0.00	0.11
K	0.00	0.00	0.00	0.00	0.00	0.00	0.00	0.00	0.00	0.00
total	3.99	4.02	4.03	3.99	3.98	3.98	3.98	3.97	3.95	3.99
Mg#	59.18	60.17	36.68	56.26	47.08	61.53	64.52	69.58	70.97	63.53
Per cent end-members										
Wo	46.91	47.66	40.68	48.30	44.26	47.51	38.42	42.17	43.08	38.06
En	28.85	28.58	18.22	26.96	23.02	29.13	36.12	40.13	40.24	35.35
Fs	19.94	18.85	31.24	20.99	26.02	18.30	19.99	17.70	16.68	20.36
Ae	4.30	4.91	9.86	3.75	6.70	5.06	5.48	0.00	0.00	6.23
total	100	100	100	100	100	100	100	100	100	100

	71	72	73	74	75
Sample	Xe16 (R5_7)	Xe16 (R2_3)	Xe16 (R4_1)	Xe16 (R4_2)	Xe16 (R4_3)
SiO_2	52.06	51.80	54.29	53.77	55.84
TiO_2	0.63	0.71	2.68	3.25	2.86
Al_2O_3	4.92	5.18	0.81	0.41	0.44
Cr_2O_3	0.00	0.00	0.00	0.00	0.00
FeO	12.38	12.47	20.11	18.86	18.44
MnO	0.00	0.00	0.00	0.00	0.43
MgO	11.37	11.27	4.60	5.37	3.54
CaO	17.24	17.28	9.52	11.28	11.05
Na_2O	1.40	1.30	7.99	7.06	7.40
K_2O	0.00	0.00	0.00	0.00	0.00
total	100.00	100.00	100.00	100.00	100.00
Number of cations on basis of 6 oxygens					
Si	1.94	1.93	2.09	2.07	2.14
Al (T)	0.06	0.07	0.00	0.00	0.00
Al (M1)	0.16	0.16	0.04	0.02	0.02
Fe(3+)	0.00	0.00	0.32	0.26	0.14
Cr	0.00	0.00	0.00	0.00	0.00
Ti	0.02	0.02	0.08	0.09	0.08
Fe(2+)	0.39	0.39	0.31	0.33	0.45
Mn	0.00	0.00	0.00	0.00	0.01
Mg	0.63	0.63	0.26	0.31	0.20
Ca	0.69	0.69	0.39	0.47	0.45
Na	0.10	0.09	0.60	0.53	0.55
K	0.00	0.00	0.00	0.00	0.00
total	3.98	3.98	4.09	4.08	4.04
Mg#	62.09	61.70	28.95	33.67	25.07
Per cent end-members					
Wo	38.06	38.32	20.86	24.56	25.14
En	34.94	34.77	14.01	16.27	11.22
Fs	21.42	21.69	33.47	31.35	33.15
Ae	5.58	5.21	31.66	27.82	30.49
total	100.00	100.00	100.00	100.00	100.00

Following analyses contain ferric iron. FeO and Fe2O3 content in weight percentages:

Analysis	30	31	32	33
Fe2O3	7.36	7.11	1.91	12.79
FeO	11.71	11.24	15.46	9.25
Analysis	42.00	62.00	63.00	73.00
Fe2O3	29.92	1.74	3.02	11.35
FeO	2.56	9.82	15.37	9.90

Analysis	39	40	41
Fe2O3	10.42	23.58	27.03
FeO	17.54	7.09	3.92
Analysis	74	75	
Fe2O3	9.31	4.79	
FeO	10.48	14.12	

KEY: Wt-%=weight percentage. FeO is total iron. Number of cations on the basis of 6 oxygens: Al(T)=Aluminium on T site, Al(M1)=aluminium on M1 site, Fe3+, Cr and Ti on M1 site. Ca. Na and Mn on M2 site. Fe2+ and Mg the distribution between M1 and M2 not defined. Mg#=magnesium ratio Mg/(Mg+Fetot+Mn). Per cent end-members: $Wo=Ca_2Si_2O_6$ $En=Mg_2Si_2O_6$ $Fs=Fe_2Si_2O_6$

$Ae=NaFe^{3+}Si_2O_6$, modified from spread sheets by Preston (1999) using Morimoto et al. 1989. Iron oxide weight percentages are calculated according to equation $FeO(tot)=FeO+0.8998*Fe_2O_3$.

Table 10 Rutile analyses.

	1	2	3	4	5	6	7	8	9	10
	P3	P3	P8	Xe1	Xe10	Xe10	Xe13	Xe13	Xe13	Xe14
Sample	(R1_6)	(R2_8)	(R5_4)	(R1_1)	(R3_3)	(R3_4)	(R1_6)	(R2_1)	(R2_10)	(R1_1)
SiO_2	0.00	0.00	0.00	0.00	0.00	0.00	0.43	0.00	0.00	0.00
TiO_2	96.85	97.27	98.81	99.72	98.27	98.86	96.70	98.55	99.02	98.88
Al_2O_3	0.00	0.00	0.00	0.00	0.00	0.00	0.00	0.00	0.00	0.00
Cr_2O_3	0.00	0.00	0.00	0.00	0.00	0.00	0.00	0.00	0.00	0.00
FeO	0.00	0.00	1.04	0.00	1.09	0.00	0.00	0.00	0.00	0.00
MgO	0.00	0.00	0.00	0.00	0.00	0.00	0.00	0.00	0.00	0.00
CaO	0.00	0.00	0.00	0.28	0.00	0.24	0.00	0.00	0.00	0.00
V_2O_5	0.71	0.83	0.14	0.00	0.00	0.00	2.87	1.45	0.98	0.00
ZnO	0.00	0.00	0.00	0.00	0.00	0.00	0.00	0.00	0.00	1.12
Nb_2O_5	2.44	1.90	0.00	0.00	0.64	0.91	0.00	0.00	0.00	0.00
BaO	0.00	0.00	0.00	0.00	0.00	0.00	0.00	0.00	0.00	0.00
Total	100.00	100.00	100.00	100.00	100.00	100.00	100.00	100.00	100.00	100.00
The number of cations on the basis of 2 oxygen atoms										
Si	0.00	0.00	0.00	0.00	0.00	0.00	0.01	0.00	0.00	0.00
Ti	0.97	0.98	0.99	1.00	0.99	0.99	0.96	0.98	0.99	0.99
Al	0.00	0.00	0.00	0.00	0.00	0.00	0.00	0.00	0.00	0.00
Cr	0.00	0.00	0.00	0.00	0.00	0.00	0.00	0.00	0.00	0.00
Fe(tot)	0.00	0.00	0.01	0.00	0.01	0.00	0.00	0.00	0.00	0.00
Mg	0.00	0.00	0.00	0.00	0.00	0.00	0.00	0.00	0.00	0.00
Ca	0.00	0.00	0.00	0.00	0.00	0.00	0.00	0.00	0.00	0.00
V	0.01	0.01	0.00	0.00	0.00	0.00	0.03	0.01	0.01	0.00
Zn	0.00	0.00	0.00	0.00	0.00	0.00	0.00	0.00	0.00	0.01
Nb	0.02	0.01	0.00	0.00	0.00	0.01	0.00	0.00	0.00	0.00
Ba	0.00	0.00	0.00	0.00	0.00	0.00	0.00	0.00	0.00	0.00
Total	1.00	1.00	1.01	1.00	1.01	1.00	0.99	1.00	1.00	1.01

	11	12
	Xe15	Xe16
Sample	(R4_5)	(R3_5)
SiO_2	0.44	0.00
TiO_2	94.56	98.59
Al_2O_3	0.00	0.00
Cr_2O_3	0.00	0.00
FeO	0.00	1.41
MgO	0.00	0.00
CaO	1.35	0.00
V_2O_5	1.25	0.00
ZnO	0.00	0.00
Nb_2O_5	0.00	0.00
BaO	2.40	0.00
Total	100.00	100.00
The number of cations on the basis of 2 oxygen atoms		
Si	0.01	0.00
Ti	0.96	0.99
Al	0.00	0.00
Cr	0.00	0.00
Fe(tot)	0.00	0.02
Mg	0.00	0.00
Ca	0.02	0.00
V	0.01	0.00
Zn	0.00	0.00
Nb	0.00	0.00
Ba	0.01	0.00
Total	1.01	1.01

Table 11 Spinel group mineral analyses.

	1	2	3	4	5	6	7	8	9	10
	P4	P4	P4	P5	P5	P5	P5	P6	P6	P7
Sample	(R2_5)	(R2_8)	(R3_3)	(R3_5)	(R4_3)	(R4_4)	(R5_1)	(R2_4)	(R3_4)	(R4_6)
SiO_2	1.54	1.52	0.77	2.44	0.00	0.00	1.44	0.00	3.12	2.36
TiO_2	11.40	6.12	8.98	26.69	0.00	0.00	0.00	24.01	0.00	27.48
Al_2O_3	0.63	0.92	4.36	3.26	59.95	58.97	66.55	5.89	0.00	1.84
Cr_2O_3	1.56	0.62	0.00	0.00	0.00	0.00	0.00	1.52	0.00	0.00
V_2O_5	0.00	0.00	0.00	0.00	0.00	0.00	0.00	3.33	0.00	0.00
FeO	84.28	90.41	85.30	67.61	35.26	36.74	25.09	65.25	96.32	67.39
MnO	0.00	0.00	0.00	0.00	0.00	0.00	0.00	0.00	0.00	0.92
MgO	0.00	0.00	0.00	0.00	4.79	4.29	6.92	0.00	0.56	0.00
CaO	0.59	0.41	0.59	0.00	0.00	0.00	0.00	0.00	0.00	0.00
ZnO	0.00	0.00	0.00	0.00	0.00	0.00	0.00	0.00	0.00	0.00
Total	100.00	100.00	100.00	100.00	100.00	100.00	100.00	100.00	100.00	100.00
The number of cations on the basis of 32 oxygen atoms										
Si	0.44	0.44	0.22	0.71	0.00	0.00	0.31	0.00	0.89	0.69
Ti	2.47	1.32	1.92	5.81	0.00	0.00	0.00	5.19	0.00	6.03
Al	0.21	0.31	1.46	1.11	15.81	15.65	16.93	2.00	0.00	0.63
Cr	0.36	0.14	0.00	0.00	0.00	0.00	0.00	0.35	0.00	0.00
V	0.00	0.00	0.00	0.00	0.00	0.00	0.00	0.77	0.00	0.00
Fe3+	9.59	12.04	10.28	1.85	0.19	0.35	0.00	2.50	14.23	1.94
Fe2+	10.74	9.63	9.95	14.52	6.40	6.56	4.53	13.19	8.65	14.49
Mn	0.00	0.00	0.00	0.00	0.00	0.00	0.00	0.00	0.00	0.23
Mg	0.00	0.00	0.00	0.00	1.60	1.44	2.23	0.00	0.24	0.00
Ca	0.18	0.13	0.18	0.00	0.00	0.00	0.00	0.00	0.00	0.00
Zn	0.00	0.00	0.00	0.00	0.00	0.00	0.00	0.00	0.00	0.00
Total	24.00	24.00	24.00	24.00	24.00	24.00	24.00	24.00	24.00	24.00

	11	12	13	14	15	16	17	18	19	20
	P8	P8	P8	P8	P8	P8	P8	P9	Xe1	Xe1
Sample	(R2_8)	(R3_1)	(R3_2)	(R3_3)	(R4_6)	(R5_1)	(R5_5)	(R2_3)	(R2_1)	(R2_2)
SiO_2	3.83	0.51	1.12	0.38	0.00	1.14	0.00	0.47	0.00	4.11
TiO_2	0.00	15.68	77.24	31.43	30.45	9.97	21.80	16.65	4.18	0.00
Al_2O_3	0.00	6.95	0.00	1.83	4.26	3.47	3.94	1.28	3.61	0.00
Cr_2O_3	0.00	0.00	0.00	0.00	0.00	0.00	0.00	0.00	0.00	0.00
V_2O_5	0.00	0.00	0.00	0.00	0.00	0.00	0.96	0.00	0.00	0.00
FeO	94.98	76.09	20.62	65.98	64.88	84.05	73.30	81.60	90.81	88.63
MnO	0.00	0.78	0.71	0.00	0.00	0.00	0.00	0.00	0.00	0.00
MgO	1.18	0.00	0.32	0.39	0.41	0.00	0.00	0.00	1.40	7.26
CaO	0.00	0.00	0.00	0.00	0.00	0.00	0.00	0.00	0.00	0.00
ZnO	0.00	0.00	0.00	0.00	0.00	1.38	0.00	0.00	0.00	0.00
Total	100.00	100.00	100.00	100.00	100.00	100.00	100.00	100.00	100.00	100.00
The number of cations on the basis of 32 oxygen atoms										
Si	1.08	0.14	0.35	0.11	0.00	0.32	0.00	0.14	0.00	1.11
Ti	0.00	3.34	17.98	6.93	6.64	2.14	4.74	3.63	0.88	0.00
Al	0.00	2.32	0.00	0.63	1.46	1.17	1.34	0.44	1.20	0.00
Cr	0.00	0.00	0.00	0.00	0.00	0.00	0.00	0.00	0.00	0.00
V	0.00	0.00	0.00	0.00	0.00	0.00	0.22	0.00	0.00	0.00
Fe3+	13.84	6.72	0.00	1.30	1.27	9.90	4.97	8.02	13.04	13.78
Fe2+	8.58	11.30	5.34	14.87	14.46	10.18	12.74	11.77	8.30	6.19
Mn	0.00	0.19	0.18	0.00	0.00	0.00	0.00	0.00	0.00	0.00
Mg	0.50	0.00	0.15	0.17	0.18	0.00	0.00	0.00	0.58	2.92
Ca	0.00	0.00	0.00	0.00	0.00	0.00	0.00	0.00	0.00	0.00
Zn	0.00	0.00	0.00	0.00	0.00	0.29	0.00	0.00	0.00	0.00
Total	24.00	24.00	24.00	24.00	24.00	24.00	24.00	24.00	24.00	24.00

Sample	21 Xe1 (R3_1)	22 Xe1 (R4_1)	23 Xe1 (R4_2)	24 Xe1 (R4_6)	25 Xe3 (R1_6)	26 Xe3 (R3_1)	27 Xe4 (R2_3)	28 Xe4 (R3_1)	29 Xe4 (R3_2)	30 Xe9 (R1_1)
SiO_2	0.00	0.00	1.04	0.43	0.41	0.36	4.64	0.00	3.42	0.62
TiO_2	4.68	7.24	0.00	37.45	0.00	0.00	0.00	0.00	0.00	15.84
Al_2O_3	2.72	3.91	0.00	1.39	0.41	0.00	0.00	0.00	0.00	2.51
Cr_2O_3	0.00	0.00	0.00	0.00	0.00	0.00	0.00	0.00	0.00	0.00
V_2O_5	0.00	0.00	0.00	0.00	0.00	0.00	0.00	0.00	0.00	0.00
FeO	91.84	88.19	73.23	58.04	98.44	99.15	88.62	85.71	89.53	81.02
MnO	0.00	0.00	0.00	0.00	0.00	0.00	1.11	1.70	0.00	0.00
MgO	0.77	0.65	25.04	2.69	0.74	0.49	5.26	9.03	6.22	0.00
CaO	0.00	0.00	0.69	0.00	0.00	0.00	0.37	3.56	0.82	0.00
ZnO	0.00	0.00	0.00	0.00	0.00	0.00	0.00	0.00	0.00	0.00
Total	100.00	100.00	100.00	100.00	100.00	100.00	100.00	100.00	100.00	100.00
The number of cations on the basis of 32 oxygen atoms										
Si	0.00	0.00	0.25	0.13	0.12	0.10	1.27	0.00	0.93	0.18
Ti	1.00	1.54	0.00	8.17	0.00	0.00	0.00	0.00	0.00	3.44
Al	0.91	1.31	0.00	0.47	0.14	0.00	0.00	0.00	0.00	0.85
Cr	0.00	0.00	0.00	0.00	0.00	0.00	0.00	0.00	0.00	0.00
V	0.00	0.00	0.00	0.00	0.00	0.00	0.00	0.00	0.00	0.00
Fe3+	13.10	11.61	15.50	0.00	15.63	15.79	13.47	16.00	14.14	7.92
Fe2+	8.67	9.27	-0.86	14.07	7.80	7.90	6.76	3.03	6.17	11.62
Mn	0.00	0.00	0.00	0.00	0.00	0.00	0.26	0.38	0.00	0.00
Mg	0.32	0.28	8.93	1.16	0.31	0.21	2.14	3.57	2.52	0.00
Ca	0.00	0.00	0.18	0.00	0.00	0.00	0.11	1.01	0.24	0.00
Zn	0.00	0.00	0.00	0.00	0.00	0.00	0.00	0.00	0.00	0.00
Total	24.00	24.00	24.00	24.00	24.00	24.00	24.00	24.00	24.00	24.00

Sample	31 Xe9 (R2_3)	32 Xe9 (R2_5)	33 Xe9 (R3_6)	34 Xe10 (R3_6)	35 Xe11 (R4_15)	36 Xe11 (R4_16)	37 Xe11 (R5_27)	38 Xe13 (R1_9)	39 Xe15_2 (R1_5)	40 Xe16 (R1_1)
SiO_2	0.55	0.00	0.00	0.44	1.50	0.00	0.00	4.41	0.00	0.00
TiO_2	1.09	6.46	6.97	36.71	8.00	11.72	13.79	0.44	18.12	14.64
Al_2O_3	6.57	6.38	7.66	0.00	3.78	2.89	7.41	16.91	0.00	0.00
Cr_2O_3	0.00	0.00	0.00	0.00	0.00	0.00	0.55	0.00	0.00	0.00
V_2O_5	0.00	0.00	0.00	0.00	0.00	0.00	0.00	0.00	0.00	0.00
FeO	90.17	84.90	82.42	62.85	86.72	83.95	77.74	75.13	81.60	84.60
MnO	1.00	1.38	0.56	0.00	0.00	1.45	0.00	0.00	0.00	0.77
MgO	0.38	0.87	2.39	0.00	0.00	0.00	0.00	2.27	0.00	0.00
CaO	0.25	0.00	0.00	0.00	0.00	0.00	0.52	0.84	0.28	0.00
ZnO	0.00	0.00	0.00	0.00	0.00	0.00	0.00	0.00	0.00	0.00
Total	100.00	100.00	100.00	100.00	100.00	100.00	100.00	100.00	100.00	100.00
The number of cations on the basis of 32 oxygen atoms										
Si	0.15	0.00	0.00	0.13	0.43	0.00	0.00	1.15	0.00	0.00
Ti	0.23	1.36	1.44	8.22	1.71	2.53	2.93	0.09	3.98	3.21
Al	2.15	2.10	2.48	0.00	1.27	0.98	2.46	5.21	0.00	0.00
Cr	0.00	0.00	0.00	0.00	0.00	0.00	0.12	0.00	0.00	0.00
V	0.00	0.00	0.00	0.00	0.00	0.00	0.00	0.00	0.00	0.00
Fe3+	13.09	11.18	10.63	0.00	10.46	9.97	7.56	8.31	8.04	9.59
Fe2+	7.91	8.67	8.33	15.65	10.14	10.18	10.77	8.12	11.89	11.02
Mn	0.23	0.33	0.13	0.00	0.00	0.35	0.00	0.00	0.00	0.19
Mg	0.16	0.36	0.98	0.00	0.00	0.00	0.00	0.88	0.00	0.00
Ca	0.08	0.00	0.00	0.00	0.00	0.00	0.16	0.23	0.09	0.00
Zn	0.00	0.00	0.00	0.00	0.00	0.00	0.00	0.00	0.00	0.00
Total	24.00	24.00	24.00	24.00	24.00	24.00	24.00	24.00	24.00	24.00

	41	42	43
	Xe16	Xe16	Xe16
Sample	(R1_2)	(R3_4)	(R5_1)
SiO_2	0.51	0.78	0.00
TiO_2	84.84	26.36	32.97
Al_2O_3	0.00	2.91	1.87
Cr_2O_3	0.00	0.00	0.00
V_2O_5	0.00	0.00	0.00
FeO	14.65	69.94	59.37
MnO	0.00	0.00	4.31
MgO	0.00	0.00	1.48
CaO	0.00	0.00	0.00
ZnO	0.00	0.00	0.00
Total	100.00	100.00	100.00
The number of cations on the basis of 32 oxygens Si	0.16	0.23	0.00
Ti	20.00	5.77	7.21
Al	0.00	1.00	0.64
Cr	0.00	0.00	0.00
V	0.00	0.00	0.00
Fe3+	0.00	3.01	0.93
Fe2+	3.84	13.99	13.51
Mn	0.00	0.00	1.06
Mg	0.00	0.00	0.64
Ca	0.00	0.00	0.00
Zn	0.00	0.00	0.00
Total	24.00	24.00	24.00

Table 12 Ilmenite analyses.

Ilmenite	1	2	3
	P5	Xe9	Xe16
Sample	(R5_5)	(R1_2)	(R1_2)
SiO_2	0.00	0.32	0.51
TiO_2	56.59	47.24	84.84
Al_2O_3	0.00	0.00	0.00
Cr_2O_3	0.00	0.00	0.00
V_2O_5	0.00	0.00	0.00
FeO	40.92	50.71	14.65
MnO	1.72	1.73	0.00
MgO	0.77	0.00	0.00
CaO	0.00	0.00	0.00
ZnO	0.00	0.00	0.00
Total	100.00	100.00	100.00
The number of cations on the basis of 6 oxygens Si	0.00	0.02	0.02
Ti	2.09	1.85	2.74
Al	0.00	0.00	0.00
Cr	0.00	0.00	0.00
V	0.00	0.00	0.00
Fe(2+)	1.69	1.75	0.53
Fe(3+)	0.00	0.47	0.00
Mn	0.07	0.08	0.00
Mg	0.06	0.00	0.00
Ca	0.00	0.00	0.00
Zn	0.00	0.00	0.00
Total	3.91	4.16	3.28

APPENDIX 2

Geologian Tutkimuskeskus Geological Survey of Finland, Espoo
Mikroanalyysilaboratorio
Ilona Romu / silicate, phosphate, and oxide analyses / original file IR1May09.xls /

SiO2	TiO2	Al2O3	Cr2O3	V2O3	FeO	MnO	MgO	CaO	Na2O	K2O	BaO	SrO	NiO	P2O5	SO2	F	F = O	Cl	Cl = O	Total	Näyte / analyysipiste / kommentti
51.57	0.77	2.71	0.07	Bdl.	12.77	0.40	9.84	19.34	2.12	Bdl.	Nd.	Bdl.	Nd.	Bdl.	Nd.	0.06	-0.03	0.01	-0.00	99.77	ALKBM6-98 / r1 / 1 = cpx (augiitti)
51.63	0.92	2.59	Bdl.	Bdl.	12.97	0.41	9.81	19.34	2.08	Nd.	Nd.	Bdl.	Nd.	Nd.	Bdl.	0.08	-0.03	0.00	0.00	99.91	ALKBM6-98 / r1 / 1 = cpx (augiitti)
51.94	0.79	2.73	Bdl.	Bdl.	12.77	0.30	9.79	19.39	2.11	Bdl.	Nd.	Bdl.	Nd.	Nd.	Nd.	0.06	-0.02	0.00	0.00	100.09	ALKBM6-98 / r1 / 1 = cpx (augiitti)
51.87	0.81	2.67	Bdl.	Bdl.	12.83	0.31	9.76	19.36	2.14	Nd.	Nd.	Bdl.	Nd.	Bdl.	Bdl.	0.02	-0.01	0.00	-0.00	100.04	ALKBM6-98 / r1 / 1 = cpx (augiitti)
0.27	Bdl.	Nd.	Nd.	Nd.	0.61	0.12	**0.16**	**52.19**	**0.48**	Bdl.	Nd.	0.73	Nd.	**42.33**	Bdl.	**2.01**	-0.85	**1.61**	-0.36	**99.35**	ALKBM6-98 / r1 / 2 = apat (F, Cl)
0.22	Bdl.	Bdl.	Bdl.	Nd.	0.60	0.09	**0.20**	**52.06**	**0.47**	Nd.	Nd.	0.73	Nd.	**42.46**	Bdl.	**1.74**	-0.73	**1.70**	-0.38	99.21	ALKBM6-98 / r1 / 2 = apat (F, Cl)
65.06	Bdl.	**19.31**	Nd.	Bdl.	Bdl.	Nd.	Nd.	1.20	**8.02**	**4.01**	**0.38**	0.38	Nd.	Bdl.	Nd.	0.06	-0.02	0.00	-0.00	98.54	ALKBM6-98 / r1 / 3 = anortoklaasi
65.05	Bdl.	**19.21**	Nd.	Nd.	0.15	Bdl.	Nd.	1.28	**7.99**	**3.99**	**0.49**	0.40	Nd.	Nd.	Nd.	0.02	-0.01	0.00	0.00	98.63	ALKBM6-98 / r1 / 3 = anortoklaasi
64.93	Bdl.	**19.35**	Nd.	Nd.	0.15	Bdl.	Nd.	1.32	**7.97**	**3.94**	**0.45**	0.40	Nd.	Bdl.	Bdl.	0.04	-0.01	0.00	-0.00	98.63	ALKBM6-98 / r1 / 3 = anortoklaasi
51.58	0.84	2.71	Bdl.	Bdl.	12.39	0.31	9.99	19.39	2.13	Nd.	Nd.	Nd.	Bdl.	Nd.	Nd.	0.00	0.00	0.01	-0.00	99.49	ALKBM6-98 / r2 / 1 = cpx (augiitti)
52.11	0.75	2.51	Bdl.	Bdl.	12.70	0.33	9.92	19.52	2.09	Nd.	Nd.	Bdl.	Bdl.	Bdl.	Bdl.	0.04	-0.02	0.00	0.00	100.15	ALKBM6-98 / r2 / 1 = cpx (augiitti)
52.22	0.78	2.60	Bdl.	Bdl.	12.54	0.41	10.11	19.29	2.08	Nd.	Nd.	Bdl.	Bdl.	Bdl.	Bdl.	0.05	-0.02	0.01	-0.00	100.33	ALKBM6-98 / r2 / 1 = cpx (augiitti)
64.14	Bdl.	**17.42**	Nd.	Nd.	Bdl.	Nd.	Nd.	0.02	0.40	**16.15**	Nd.	Nd.	Bdl.	Nd.	Bdl.	0.07	-0.03	0.00	-0.00	98.27	ALKBM6-98 / r2 / 2a = kms
65.97	Bdl.	18.86	Bdl.	Nd.	0.18	Nd.	**Bdl.**	0.86	7.89	**4.49**	**0.45**	0.23	Nd.	**Bdl.**	Nd.	0.07	-0.03	0.01	-0.00	99.09	ALKBM6-98 / r2 / 2b = anortoklaasi
66.22	Bdl.	18.69	Nd.	Nd.	0.16	Nd.	Nd.	0.85	7.89	**4.55**	**0.39**	0.30	Nd.	Nd.	Nd.	0.00	0.00	0.01	-0.00	99.10	ALKBM6-98 / r2 / 2b = anortoklaasi
66.18	Bdl.	18.74	Nd.	Nd.	0.22	Nd.	Nd.	0.90	7.94	**4.47**	**0.41**	0.22	Bdl.	Bdl.	Bdl.	0.03	-0.01	0.00	0.00	99.19	ALKBM6-98 / r2 / 2b = anortoklaasi
65.58	Bdl.	19.09	Nd.	Bdl.	0.13	Nd.	Bdl.	1.10	**7.99**	**4.17**	0.48	0.34	Bdl.	Bdl.	Nd.	0.00	-0.00	0.00	0.00	98.98	ALKBM6-98 / r2 / 3 = anortoklaasi
Nd.	**50.04**	Nd.	Bdl.	0.30	**45.37**	1.03	0.81	Bdl.	0.00	Nd.	Nd.	Bdl.	Bdl.	Nd.	Bdl.	0.07	-0.03	0.01	-0.00	97.71	ALKBM6-98 / r2 / 4 = opaakki (ilmeniitti)
Bdl.	**50.45**	Nd.	Nd.	0.33	**45.35**	1.03	0.95	Bdl.	0.00	Nd.	Nd.	Nd.	Nd.	Bdl.	Nd.	0.09	-0.04	0.01	-0.00	98.24	ALKBM6-98 / r2 / 4 = opaakki (ilmeniitti)
Nd.	**49.58**	Nd.	Bdl.	0.37	**46.43**	1.31	Bdl.	Nd.	0.00	Nd.	Nd.	Bdl.	Bdl.	Bdl.	Nd.	0.07	-0.03	0.02	-0.00	97.93	ALKBM6-98 / r2 / 4 = opaakki (ilmeniitti)
62.54	Bdl.	22.67	Bdl.	Bdl.	0.13	Nd.	Nd.	**4.28**	**9.01**	0.75	Nd.	0.20	Nd.	Bdl.	Nd.	0.00	0.00	0.01	-0.00	99.65	xell-pl (rikki) / r1 / 1 = plagioklaasi
62.24	Bdl.	22.75	Nd.	Nd.	0.14	Bdl.	Bdl.	**4.30**	**8.94**	0.75	Nd.	0.32	Bdl.	Nd.	Nd.	0.06	-0.02	0.00	-0.00	99.57	xell-pl (rikki) / r1 / 1 = plagioklaasi
48.33	1.05	5.94	Bdl.	Bdl.	10.18	0.22	11.15	21.84	1.11	Bdl.	Nd.	Bdl.	Nd.	Nd.	Nd.	0.05	-0.02	0.00	-0.00	100.02	xell-pl (rikki) / r1 / 3a = cpx
49.87	0.71	4.26	Bdl.	Bdl.	9.34	0.29	12.41	22.49	0.84	Bdl.	Nd.	Nd.	Nd.	Bdl.	Nd.	0.11	-0.04	0.00	0.00	100.44	xell-pl (rikki) / r1 / 3a = cpx
49.66	0.82	4.46	Bdl.	Bdl.	10.11	0.28	11.73	22.26	0.93	Nd.	Nd.	Bdl.	Nd.	Bdl.	Nd.	0.07	-0.03	0.00	0.00	100.43	xell-pl (rikki) / r1 / 3a = cpx
56.32	Bdl.	26.28	Bdl.	Bdl.	**0.79**	Bdl.	**0.23**	8.69	6.47	0.46	Nd.	0.19	Nd.	Bdl.	Nd.	0.04	-0.02	0.00	-0.00	99.63	xell-pl (rikki) / r1 / 3b = suotauma "ms" (FeO- ja tai MgO-pitoinen andesiini)
56.29	Bdl.	26.19	Nd.	Nd.	**0.60**	Bdl.	Bdl.	9.35	6.44	0.21	Bdl.	0.26	Bdl.	Nd.	Nd.	0.00	0.00	0.00	0.00	99.46	xell-pl (rikki) / r1 / 3b = suotauma "ms" (FeO- ja tai MgO-pitoinen andesiini)

Appendix 2. Cont.

SiO2	TiO2	Al2O3	Cr2O3	V2O3	FeO	MnO	MgO	CaO	Na2O	K2O	BaO	SrO	NiO	P2O5	SO2	F	F = O	Cl	Cl = O	Total	Näyte / analyysipiste / kommentti
57.22	Bdl.	25.53	Bdl.	Nd.	**0.55**	Bdl.	0.09	8.40	6.99	0.26	Bdl.	0.22	Nd.	Bdl.	Bdl.	0.02	-0.01	0.00	-0.00	99.45	xell-pl (rikki) / r1 / 3b = suotauma "ms" (FeO- ja tai MgO-pitoinen andesiini)
56.79	Bdl.	**23.10**	Nd.	Bdl.	Nd.	Bdl.	Nd.	0.13	**13.41**	0.13	Nd.	Bdl.	Nd.	Bdl.	Nd.	0.02	-0.01	0.00	0.00	93.69	Xell-p1 (rikki) / r1 / 4 = Na-Al-silikaatti = todennäköisesti analsiimi
55.93	Bdl.	**22.34**	Bdl.	Nd.	Nd.	Nd.	Nd.	0.09	**13.88**	0.13	Nd.	Nd.	Bdl.	Nd.	Bdl.	0.00	0.00	0.01	-0.00	92.44	Xell-p1 (rikki) / r1 / 4 = Na-Al-silikaatti = todennäköisesti analsiimi
41.87	**2.08**	**9.24**	Bdl.	Bdl.	**15.17**	0.12	**16.27**	0.09	0.07	**9.96**	Nd.	Nd.	Nd.	Bdl.	Nd.	**1.20**	-0.50	0.00	0.00	95.65	xell-pl (rikki) / r1 / 5 = kiille plagioklaasin ja cpx:n välissä
41.62	**2.29**	**9.03**	0.00	0.17	**15.13**	0.24	**15.87**	Bdl.	0.07	**10.06**	Nd.	Nd.	Nd.	Bdl.	Bdl.	**1.19**	-0.50	0.00	0.00	95.26	xell-pl (rikki) / r1 / 5 = kiille plagioklaasin ja cpx:n välissä
42.55	**2.20**	**9.06**	Bdl.	0.15	**14.56**	0.15	**16.03**	Bdl.	0.07	**10.09**	Nd.	Nd.	Bdl.	Bdl.	Nd.	**0.96**	-0.40	0.00	-0.00	95.56	xell-pl (rikki) / r1 / 5 = kiille plagioklaasin ja cpx:n välissä
1.76	4.33	2.43	Bdl.	0.19	80.00	0.16	0.14	0.32	0.19	0.06	Nd.	Nd.	Bdl.	Bdl.	Bdl.	0.21	-0.09	0.08	-0.02	89.87	xell-pl (rikki) / r1 / 6 = Fe-Ti-Ox / rae1
0.14	10.50	3.38	Bdl.	0.36	75.34	0.80	Bdl.	0.18	0.00	0.04	Nd.	Bdl.	Nd.	Bdl.	Nd.	0.17	-0.07	0.00	0.00	91.01	xell-pl (rikki) / r1 / 6 = Fe-Ti-Ox / rae2
1.31	2.56	2.37	Bdl.	0.18	82.22	0.29	Bdl.	0.34	0.14	0.24	Nd.	Bdl.	Nd.	Bdl.	Nd.	0.15	-0.06	0.05	-0.01	89.96	xell-pl (rikki) / r1 / 6 = Fe-Ti-Ox / rae3
0.39	6.35	5.75	Nd.	Bdl.	75.92	0.66	0.12	0.24	0.00	0.07	Nd.	Bdl.	Bdl.	Nd.	Nd.	0.15	-0.06	0.03	-0.01	89.88	xell-pl (rikki) / r1 / 6 = Fe-Ti-Ox / rae4
0.16	Bdl.	0.00	Nd.	Bdl.	0.36	0.14	0.36	**53.02**	**1.07**	Nd.	Bdl.	0.42	Nd.	**41.30**	0.08	**1.34**	-0.57	**0.35**	-0.08	98.00	Xell-pl (rikki) / r2 / 1 = apatiitti (F, Cl, Na)
0.18	Bdl.	Bdl.	Bdl.	Nd.	0.37	0.13	0.37	**52.96**	**1.04**	Nd.	Nd.	0.40	Nd.	**41.38**	0.06	**1.16**	-0.49	**0.36**	-0.08	97.90	Xell-pl (rikki) / r2 / 1 = apatiitti (F, Cl, Na)
0.20	Bdl.	0.00	Bdl.	Bdl.	0.39	0.12	0.38	**53.16**	**1.16**	Nd.	Nd.	0.46	Nd.	**41.48**	0.06	**1.24**	-0.52	**0.34**	-0.08	98.44	Xell-pl (rikki) / r2 / 1 = apatiitti (F, Cl, Na)
0.17	Bdl.	0.00	Bdl.	Bdl.	0.33	0.10	0.40	**53.16**	**1.06**	Nd.	Nd.	0.41	Bdl.	**41.07**	0.06	**1.17**	-0.49	**0.35**	-0.08	97.77	Xell-pl (rikki) / r2 / 1 = apatiitti (F, Cl, Na)
62.89	Bdl.	21.63	Nd.	Bdl.	0.12	Bdl.	Nd.	3.79	9.18	0.83	Bdl.	0.33	Nd.	Bdl.	Nd.	0.01	-0.00	0.01	-0.00	98.96	Xell-pl (rikki) / r2 / 2 = plagioklaasi
63.20	Bdl.	21.88	Nd.	Nd.	0.12	Nd.	Nd.	3.80	9.06	0.80	Bdl.	0.28	Nd.	Bdl.	Bdl.	0.08	-0.03	0.00	0.00	99.26	Xell-pl (rikki) / r2 / 2 = plagioklaasi
62.98	Bdl.	21.83	Nd.	Bdl.	0.13	Bdl.	0.01	3.87	9.09	0.83	Nd.	0.36	Bdl.	Bdl.	Bdl.	0.01	-0.01	0.00	0.00	99.29	Xell-pl (rikki) / r2 / 2 = plagioklaasi
39.31	3.17	9.07	Bdl.	0.29	17.62	0.32	14.08	0.11	Bdl.	**9.97**	Nd.	Nd.	Bdl.	Nd.	Nd.	**0.88**	-0.37	0.00	0.00	94.53	Xell-pl (rikki) / r2 / 3 = kiille-ylikasvu täysin muuttuneessa amfibolissa
39.13	3.56	9.30	Bdl.	0.23	18.58	0.35	13.48	0.20	0.00	**9.91**	Nd.	Nd.	Bdl.	Nd.	Bdl.	**0.67**	-0.28	0.02	-0.01	95.22	Xell-pl (rikki) / r2 / 3 = kiille-ylikasvu täysin muuttuneessa amfibolissa
38.46	3.57	9.40	Nd.	0.24	19.75	0.40	12.53	0.09	0.00	**9.84**	Nd.	Nd.	Nd.	Bdl.	Bdl.	**0.52**	-0.22	0.00	0.00	94.67	Xell-pl (rikki) / r2 / 3 = kiille-ylikasvu täysin muuttuneessa amfibolissa
38.03	2.87	10.30	Bdl.	0.14	20.64	0.34	12.53	0.07	0.00	**9.80**	Nd.	Nd.	Bdl.	Nd.	Bdl.	**0.61**	-0.26	0.02	-0.00	95.16	Xell-pl (rikki) / r2 / 3 = kiille-ylikasvu täysin muuttuneessa amfibolissa
39.60	2.63	15.58	Nd.	0.12	14.32	0.26	9.84	9.72	3.11	1.44	Nd.	Nd.	Nd.	Bdl.	Bdl.	0.20	-0.09	0.04	-0.01	96.80	Xell-pl (rikki) / r2 / 4 = muuttunut amfiboli (koostumus: tschermak., Mg-hast., pargas...)

Appendix 2. Cont.

SiO2	TiO2	Al2O3	Cr2O3	V2O3	FeO	MnO	MgO	CaO	Na2O	K2O	BaO	SrO	NiO	P2O5	SO2	F	F = O	Cl	Cl = O	Total	Näyte / analyysipiste / kommentti
39.58	2.65	15.99	Bdl.	Bdl.	14.33	0.24	9.92	9.65	3.00	1.51	Nd.	Bdl.	Nd.	Bdl.	Bdl.	0.19	-0.08	0.04	-0.01	97.18	Xell-pl (rikki) / r2 / 4 = muuttunut amfiboli (koostumus: tschermak., Mg-hast., pargas...)
39.09	2.74	15.38	Nd.	Bdl.	14.51	0.24	10.28	9.99	3.24	1.27	Nd.	Bdl.	Bdl.	Nd.	Bdl.	0.27	-0.11	0.03	-0.01	97.04	Xell-pl (rikki) / r2 / 4 = muuttunut amfiboli (koostumus: tschermak., Mg-hast., pargas...)
40.11	2.53	16.12	Bdl.	Bdl.	13.92	0.27	9.88	9.52	3.09	1.40	Nd.	Nd.	Bdl.	Bdl.	0.08	0.28	-0.12	0.04	-0.01	97.27	Xell-pl (rikki) / r2 / 4 = muuttunut amfiboli (koostumus: tschermak., Mg-hast., pargas...)
40.17	2.61	15.98	Bdl.	Nd.	14.14	0.26	9.69	9.62	3.63	1.24	Nd.	Bdl.	Nd.	Bdl.	0.06	0.17	-0.07	0.04	-0.01	97.62	Xell-pl (rikki) / r2 / 4 = muuttunut amfiboli (koostumus: tschermak., Mg-hast., pargas...)
0.23	**11.76**	**11.89**	0.11	0.40	**64.86**	0.12	0.13	0.18	0.00	Bdl.	Nd.	Bdl.	0.06	Bdl.	Nd.	0.17	-0.07	0.01	-0.00	89.89	Xe11 / r1 / 1a = omamuot FeOx (Fe-Ti-Ox) / rae1
0.24	**11.89**	**11.84**	0.14	0.33	**64.41**	0.04	0.20	0.21	0.00	Bdl.	Nd.	Bdl.	Bdl.	Bdl.	Nd.	0.15	-0.06	0.01	-0.00	89.52	Xe11 / r1 / 1a = omamuot FeOx (Fe-Ti-Ox) / rae1
0.52	**11.23**	**9.51**	0.21	0.25	**67.69**	0.14	0.31	0.26	0.00	0.05	Nd.	Nd.	0.07	Nd.	Nd.	0.19	-0.08	0.02	-0.00	90.35	Xe11 / r1 / 1a = omamuot FeOx (Fe-Ti-Ox) / rae1
0.21	**10.84**	**11.16**	0.24	0.30	**65.96**	0.14	0.16	0.24	0.00	0.07	Nd.	Bdl.	Bdl.	Nd.	Bdl.	0.19	-0.08	0.00	-0.00	89.49	Xe11 / r1 / 1a = omamuot FeOx (Fe-Ti-Ox) / rae2
0.19	**10.33**	**11.05**	0.25	0.22	**67.06**	0.14	0.09	0.22	0.00	0.05	Nd.	Nd.	Bdl.	Nd.	Bdl.	0.12	-0.05	0.01	-0.00	89.71	Xe11 / r1 / 1a = omamuot FeOx (Fe-Ti-Ox) / rae2
0.81	**10.12**	**7.67**	0.27	0.26	**69.35**	0.27	0.85	0.22	0.00	0.06	Nd.	Bdl.	Bdl.	Nd.	Nd.	0.07	-0.03	0.01	-0.00	90.01	Xe11 / r1 / 1a = omamuot FeOx (Fe-Ti-Ox) / rae3
47.80	1.45	6.13	0.08	Bdl.	8.97	0.22	11.39	22.00	0.93	Bdl.	Nd.	Bdl.	Nd.	Bdl.	Nd.	0.07	-0.03	0.00	0.00	99.21	Xe11 / r1 / 1b = cpx
47.83	1.37	6.09	0.14	Bdl.	9.24	0.24	11.52	21.90	0.94	Nd.	Nd.	Bdl.	Bdl.	Bdl.	Nd.	0.11	-0.04	0.00	0.00	99.52	Xe11 / r1 / 1b = cpx
47.17	1.57	6.05	0.14	Bdl.	9.34	0.28	11.67	21.83	1.02	Bdl.	Nd.	Bdl.	Bdl.	Bdl.	Nd.	0.02	-0.01	0.00	-0.00	99.27	Xe11 / r1 / 1b = cpx
48.27	1.33	5.49	0.12	Bdl.	8.51	0.21	11.98	22.28	0.91	Bdl.	Nd.	Bdl.	Bdl.	Nd.	Bdl.	0.02	-0.01	0.00	0.00	99.25	Xe11 / r1 / 1b = cpx
48.40	0.16	28.55	Nd.	Nd.	**3.26**	Nd.	2.07	**0.41**	**0.76**	**8.91**	Nd.	Bdl.	Bdl.	Bdl.	Nd.	0.06	-0.02	0.01	-0.00	92.61	Xe11 / r1 / 1c = "ms"-suotauma (on mahdollisesti illiittiä / mont-morilloniittia) edellisessä cpx: ssä.
47.98	0.12	28.17	Nd.	Nd.	**3.49**	Bdl.	2.31	**0.27**	**0.30**	**9.27**	Nd.	Bdl.	Nd.	Nd.	Nd.	0.07	-0.03	0.00	0.00	91.99	Xe11 / r1 / 1c = "ms"-suotauma (on mahdollisesti illiittiä / mont-morilloniittia) edellisessä cpx: ssä.
48.66	Bdl.	29.07	Bdl.	Nd.	**2.66**	Bdl.	1.77	**0.50**	**1.54**	**8.62**	Nd.	Nd.	Nd.	Nd.	Nd.	0.06	-0.03	0.01	-0.00	93.02	Xe11 / r1 / 1c = "ms"-suotauma (on mahdollisesti illiittiä / mont-morilloniittia) edellisessä cpx: ssä.
48.38	Bdl.	28.92	Bdl.	Nd.	**3.18**	Bdl.	2.63	**0.19**	**0.32**	**9.76**	Bdl.	Nd.	Bdl.	Bdl.	Bdl.	0.00	0.00	0.01	-0.00	93.56	Xe11 / r1 / 1c = "ms"-suotauma (on mahdollisesti illiittiä / mont-morilloniittia) edellisessä cpx: ssä.

Appendix 2. Cont.

SiO2	TiO2	Al2O3	Cr2O3	V2O3	FeO	MnO	MgO	CaO	Na2O	K2O	BaO	SrO	NiO	P2O5	SO2	F	F = O	Cl	Cl = O	Total	Näyte / analyysipiste / kommentti
48.48	0.11	28.82	Bdl.	Bdl.	**3.18**	Bdl.	2.72	**0.17**	**0.12**	**9.66**	Bdl.	Nd.	Nd.	Nd.	Nd.	0.07	-0.03	0.00	0.00	93.38	Xe11 / r1 / 1c = "ms"-suotauma (on mahdollisesti illiittiä / mont-morilloniittia) edellisessä cpx: ssä.
40.03	3.05	14.96	0.09	Bdl.	13.72	0.29	10.18	9.57	3.93	1.26	Nd.	Bdl.	Bdl.	Bdl.	0.07	0.25	-0.10	0.03	-0.01	97.47	Xe11 / r1 / 2 = amfiboli
40.03	3.01	15.05	Bdl.	Bdl.	13.84	0.22	9.92	9.39	4.01	1.21	Nd.	Nd.	0.06	Bdl.	Bdl.	0.21	-0.09	0.04	-0.01	97.04	Xe11 / r1 / 2 = amfiboli
40.06	3.00	15.30	0.10	Bdl.	13.63	0.25	9.92	9.49	3.99	1.23	Nd.	Bdl.	Nd.	Bdl.	Bdl.	0.20	-0.08	0.05	-0.01	97.30	Xe11 / r1 / 2 = amfiboli
40.07	3.11	15.06	0.09	Bdl.	13.58	0.31	9.97	9.59	3.97	1.18	Nd.	Nd.	Bdl.	Bdl.	Bdl.	0.24	-0.10	0.04	-0.01	97.27	Xe11 / r1 / 2 = amfiboli
39.89	2.93	15.01	0.07	Bdl.	13.75	0.18	9.95	9.53	4.04	1.21	Nd.	Bdl.	Bdl.	Bdl.	0.07	0.21	-0.09	0.04	-0.01	96.89	Xe11 / r1 / 2 = amfiboli
40.23	**4.60**	**12.78**	0.09	Bdl.	**9.42**	0.16	**13.87**	11.92	**3.33**	**0.23**	Nd.	Bdl.	Nd.	Bdl.	Bdl.	0.40	-0.17	0.01	-0.00	97.06	Xe11 / r1 / 3 = oksidisuotaumia sisältävää "kiillemäistä" ylikasvua amfibolissa (ilmeisesti amfiboli tämäkin)
40.27	4.51	12.71	0.10	Bdl.	**9.50**	0.18	**14.05**	11.83	**3.33**	**0.33**	Nd.	Bdl.	Bdl.	Bdl.	Nd.	0.47	-0.20	0.01	-0.00	97.37	Xe11 / r1 / 3 = oksidisuotaumia sisältävää "kiillemäistä" ylikasvua amfibolissa (ilmeisesti amfiboli tämäkin)
40.42	**4.27**	**12.93**	0.13	Bdl.	**9.55**	0.17	**14.03**	12.02	**3.35**	**0.22**	Nd.	Bdl.	Bdl.	Bdl.	Bdl.	0.44	-0.18	0.01	-0.00	97.57	Xe11 / r1 / 3 = oksidisuotaumia sisältävää "kiillemäistä" ylikasvua amfibolissa (ilmeisesti amfiboli tämäkin)
40.07	**4.64**	**12.72**	0.11	0.12	**9.38**	0.14	**13.63**	12.01	**3.38**	**0.20**	Nd.	Bdl.	Bdl.	Nd.	Bdl.	0.38	-0.16	0.01	-0.00	96.71	Xe11 / r1 / 3 = oksidisuotaumia sisältävää "kiillemäistä" ylikasvua amfibolissa (ilmeisesti amfiboli tämäkin)
40.14	**4.30**	**12.97**	0.12	Bdl.	**10.04**	0.20	**13.45**	11.82	**3.38**	**0.15**	Nd.	Bdl.	Nd.	Bdl.	Nd.	0.42	-0.18	0.00	0.00	96.94	Xe11 / r1 / 3 = oksidisuotaumia sisältävää "kiillemäistä" ylikasvua amfibolissa (ilmeisesti amfiboli tämäkin)
39.86	**4.09**	**12.94**	0.10	Bdl.	**10.58**	0.22	**13.13**	11.92	**3.37**	**0.18**	Nd.	0.17	Nd.	Bdl.	Nd.	0.38	-0.16	0.00	0.00	96.93	Xe11 / r1 / 3 = oksidisuotaumia sisältävää "kiillemäistä" ylikasvua amfibolissa (ilmeisesti amfiboli tämäkin)
39.92	4.61	13.15	0.07	Bdl.	**10.01**	0.19	**13.49**	11.90	**3.38**	**0.14**	Nd.	Bdl.	Bdl.	Bdl.	Bdl.	0.41	-0.17	0.01	-0.00	97.44	Xe11 / r1 / 3 = oksidisuotaumia sisältävää "kiillemäistä" ylikasvua amfibolissa (ilmeisesti amfiboli tämäkin)
0.14	Bdl.	Nd.	0.00	Bdl.	0.28	Bdl.	0.26	**53.81**	**0.71**	Bdl.	Nd.	**0.42**	Nd.	**41.45**	Bdl.	**1.60**	-0.67	**0.34**	-0.08	**98.41**	Xe11 / r2 / 1 = apatiitti (F, Cl, Na)
0.14	Bdl.	Nd.	Nd.	Nd.	0.20	Bdl.	0.30	**53.92**	**0.76**	Bdl.	Nd.	**0.36**	Bdl.	**41.61**	Bdl.	**1.32**	-0.56	**0.37**	-0.08	**98.47**	Xe11 / r2 / 1 = apatiitti (F, Cl, Na)
0.20	Bdl.	Bdl.	0.01	Nd.	0.23	0.11	0.30	**53.59**	**0.77**	Nd.	Nd.	**0.39**	Bdl.	**41.47**	Bdl.	**1.29**	-0.54	**0.38**	-0.08	**98.19**	Xe11 / r2 / 1 = apatiitti (F, Cl, Na)
0.22	Bdl.	Nd.	Nd.	Nd.	0.23	Bdl.	0.26	**53.80**	**0.70**	Nd.	Nd.	**0.39**	Nd.	**41.88**	Bdl.	**1.45**	-0.61	**0.40**	-0.09	**98.70**	Xe11 / r2 / 1 = apatiitti (F, Cl, Na)

Appendix 2. Cont.

SiO2	TiO2	Al2O3	Cr2O3	V2O3	FeO	MnO	MgO	CaO	Na2O	K2O	BaO	SrO	NiO	P2O5	SO2	F	F = O	Cl	Cl = O	Total	Näyte / analyysipiste / kommentti
0.14	Bdl.	0.05	Nd.	Bdl.	0.24	Bdl.	0.29	**53.64**	**0.69**	Nd.	Nd.	**0.33**	Bdl.	**41.50**	Bdl.	**1.70**	-0.72	**0.36**	-0.08	**98.28**	Xe11 / r2 / 1 = apatiitti (F, Cl, Na)
0.17	**Bdl.**	Nd.	Nd.	0.00	0.29	Bdl.	0.30	**54.17**	**0.74**	Nd.	Nd.	**0.39**	Bdl.	**42.00**	Bdl.	**1.63**	-0.69	**0.34**	-0.08	**99.41**	Xe11 / r2 / 1 = apatiitti (F, Cl, Na)
47.19	1.46	7.28	0.12	Bdl.	8.60	0.27	11.49	21.21	1.26	Bdl.	Nd.	Bdl.	Bdl.	Bdl.	Nd.	0.09	-0.04	0.00	0.00	99.14	Xe11 / r2 / 3a = cpx
48.03	1.42	6.00	0.10	Bdl.	8.56	0.30	11.99	22.20	0.87	Bdl.	Nd.	Bdl.	Nd.	Nd.	Bdl.	0.03	-0.01	0.00	0.00	99.68	Xe11 / r2 / 3a = cpx
48.59	1.26	5.22	0.12	Bdl.	8.22	0.26	12.43	22.31	0.76	Bdl.	Nd.	Nd.	Bdl.	Nd.	Nd.	0.03	-0.01	0.00	0.00	99.32	Xe11 / r2 / 3a = cpx
48.95	1.15	4.92	0.11	Bdl.	8.30	0.23	12.66	22.30	0.76	Nd.	Nd.	Bdl.	Nd.	Bdl.	Bdl.	0.04	-0.02	0.01	-0.00	99.57	Xe11 / r2 / 3a = cpx
48.85	0.12	**29.52**	Nd.	Nd.	**2.49**	Bdl.	**1.90**	**0.36**	**0.87**	**9.01**	Bdl.	Bdl.	Bdl.	Bdl.	Bdl.	0.04	**-0.02**	**0.02**	-0.00	93.34	Xe11 / r2 / 3b = cpx:n "maasälpä-suotauma" (todennäköisesti mont-morilloniittia / illiittiä tämäkin)
50.43	0.13	**30.52**	0.04	Nd.	**2.60**	Bdl.	**2.03**	**0.34**	**0.20**	**6.91**	Nd.	Nd.	Nd.	Bdl.	Bdl.	0.11	-0.05	0.00	0.00	93.42	Xe11 / r2 / 3b = cpx:n "maasälpä-suotauma" (todennäköisesti mont-morilloniittia / illiittiä tämäkin)
49.15	Bdl.	**29.60**	Nd.	Nd.	**2.52**	Bdl.	**1.91**	**0.38**	**0.39**	**8.34**	Nd.	Nd.	Nd.	Nd.	Nd.	0.07	-0.03	0.02	-0.00	92.43	Xe11 / r2 / 3b = cpx:n "maasälpä-suotauma" (todennäköisesti mont-morilloniittia / illiittiä tämäkin)
49.28	Bdl.	**29.33**	0.04	Bdl.	**1.93**	Nd.	**1.43**	**0.81**	**2.71**	**7.27**	Nd.	Bdl.	Nd.	Bdl.	Nd.	0.01	**-0.00**	**0.00**	**0.00**	**93.01**	Xe11 / r2 / 3b = cpx:n "maasälpä-suotauma" (todennäköisesti mont-morilloniittia / illiittiä tämäkin)
0.20	**11.47**	**7.98**	0.22	0.26	**68.68**	0.09	Bdl.	0.14	0.00	Bdl.	Nd.	Bdl.	Bdl.	Nd.	Bdl.	0.14	**-0.06**	**0.01**	**-0.00**	**89.24**	Xe11 / r2 / 3c = omamuot oksidi / rae1
0.16	**11.48**	**7.86**	0.30	0.39	**69.27**	0.13	Bdl.	0.14	0.00	0.07	Nd.	Bdl.	Bdl.	0.03	Nd.	0.23	**-0.10**	**0.01**	-0.00	90.09	Xe11 / r2 / 3c = omamuot oksidi / rae2
0.13	**11.79**	**10.35**	0.24	0.38	**66.35**	0.08	0.04	0.14	0.00	0.05	Nd.	Nd.	Bdl.	Nd.	Bdl.	0.12	-0.05	0.01	-0.00	89.67	Xe11 / r2 / 3c = omamuot oksidi / rae2
0.13	**12.28**	**8.34**	0.19	0.24	**68.37**	0.08	0.57	0.14	Bdl.	0.08	Nd.	Bdl.	0.07	Nd.	Bdl.	0.10	-0.04	0.00	-0.00	90.62	Xe11 / r2 / 3c = omamuot oksidi / rae2
0.16	**11.75**	**8.65**	0.22	0.34	**68.14**	0.11	Bdl.	0.19	0.00	0.05	Nd.	Nd.	Bdl.	Bdl.	Bdl.	0.10	-0.04	0.00	-0.00	89.83	Xe11 / r2 / 3c = omamuot oksidi / rae2
0.17	**11.68**	**11.69**	0.14	0.24	**65.21**	Bdl.	0.17	0.15	0.00	Bdl.	Nd.	Nd.	Bdl.	Nd.	Nd.	0.18	**-0.07**	**0.00**	**-0.00**	**89.69**	Xe11 / r2 / 3c = omamuot oksidi / rae3
0.13	**11.84**	**11.71**	0.14	0.30	**65.38**	0.14	0.18	0.15	0.00	Bdl.	Nd.	Bdl.	Bdl.	Nd.	Bdl.	0.12	**-0.05**	**0.01**	-0.00	90.16	Xe11 / r2 / 3c = omamuot oksidi / rae3
0.18	**11.28**	**8.22**	0.24	0.29	**68.93**	0.10	Bdl.	0.15	0.00	Bdl.	Nd.	Bdl.	0.06	Bdl.	Nd.	0.21	-0.09	0.02	-0.00	89.74	Xe11 / r2 / 3c = omamuot oksidi / rae4
50.61	0.76	5.55	Nd.	Bdl.	11.09	0.11	12.26	17.60	**1.57**	Bdl.	Nd.	Bdl.	Bdl.	Bdl.	Nd.	0.07	-0.03	0.01	-0.00	99.79	ALKBM1-98 / 1 = cpx
50.67	0.74	5.58	Bdl.	Bdl.	11.24	0.13	12.23	17.75	**1.55**	Nd.	Nd.	Nd.	Bdl.	Nd.	Bdl.	0.04	**-0.02**	**0.01**	**-0.00**	**100.06**	ALKBM1-98 / 1 = cpx
50.41	0.80	5.57	Bdl.	Bdl.	11.25	0.16	12.45	17.82	**1.55**	Nd.	Nd.	Nd.	Bdl.	Bdl.	Nd.	0.09	**-0.04**	**0.01**	**-0.00**	**100.20**	ALKBM1-98 / 1 = cpx
50.56	0.77	5.61	Bdl.	Bdl.	11.21	Bdl.	12.31	17.76	**1.57**	Bdl.	Nd.	Bdl.	Bdl.	Bdl.	Nd.	0.07	**-0.03**	**0.00**	-0.00	100.11	ALKBM1-98 / 1 = cpx

Appendix 2. Cont.

SiO2	TiO2	Al2O3	Cr2O3	V2O3	FeO	MnO	MgO	CaO	Na2O	K2O	BaO	SrO	NiO	P2O5	SO2	F	F = O	Cl	Cl = O	Total	Näyte / analyysipiste / kommentti
Bdl.	**97.55**	Nd.	Bdl.	0.85	**0.94**	Bdl.	Nd.	Bdl.	0.00	Bdl.	Nd.	Nd.	Bdl.	Nd.	Nd.	0.05	-0.02	0.00	0.00	99.50	ALKBM1-98 / 2 = rutiili
Bdl.	**97.81**	Nd.	Bdl.	0.77	**1.00**	Nd.	Nd.	Bdl.	0.00	Nd.	Nd.	Bdl.	Nd.	Nd.	Bdl.	0.08	-0.03	0.00	0.00	99.73	ALKBM1-98 / 2 = rutiili
Bdl.	**97.59**	Nd.	Bdl.	0.82	**1.01**	Bdl.	Nd.	0.10	0.00	Nd.	Nd.	Bdl.	Nd.	Bdl.	Nd.	0.01	-0.00	0.00	-0.00	99.66	ALKBM1-98 / 2 = rutiili
60.79	Bdl.	23.17	Bdl.	Bdl.	0.17	Nd.	Bdl.	**6.04**	**7.72**	0.76	Bdl.	Bdl.	Bdl.	Nd.	Bdl.	0.00	0.00	0.00	0.00	98.92	ALKBM1-98 / 3 = plagioklaasi
61.40	Bdl.	23.08	Nd.	Nd.	0.21	Nd.	Nd.	**6.00**	**7.76**	0.78	Bdl.	Bdl.	Nd.	Nd.	Nd.	0.03	-0.01	0.00	0.00	99.33	ALKBM1-98 / 3 = plagioklaasi
61.12	Bdl.	23.21	Nd.	Bdl.	0.21	Bdl.	Bdl.	**6.01**	**7.71**	0.78	Nd.	Bdl.	Nd.	Bdl.	Bdl.	0.03	-0.01	0.00	-0.00	99.29	ALKBM1-98 / 3 = plagioklaasi
60.84	Bdl.	22.90	Nd.	Bdl.	0.20	Bdl.	Nd.	**6.68**	**7.11**	0.68	Bdl.	Bdl.	Nd.	Bdl.	Bdl.	0.00	0.00	0.00	0.00	98.73	ALKBM1-98 / r2 / 1 = plagioklaasi
61.05	Bdl.	22.96	Bdl.	Bdl.	0.18	Bdl.	Nd.	**6.55**	**7.11**	0.70	Bdl.	Bdl.	Bdl.	Bdl.	Nd.	0.01	-0.00	0.00	0.00	98.83	ALKBM1-98 / r2 / 1 = plagioklaasi
61.05	Bdl.	23.03	Bdl.	Nd.	0.18	Nd.	Bdl.	**6.71**	**7.16**	0.71	Nd.	0.19	Nd.	Nd.	Nd.	0.01	-0.00	0.00	0.00	99.07	ALKBM1-98 / r2 / 1 = plagioklaasi
50.39	0.73	5.50	Nd.	Bdl.	11.26	0.12	**12.09**	17.55	1.52	Nd.	Nd.	Nd.	Bdl.	Bdl.	Nd.	0.12	-0.05	0.00	-0.00	99.35	ALKBM1-98 / r2 / 2 = cpx
50.72	0.84	5.63	Bdl.	Bdl.	11.20	0.13	**12.12**	17.49	1.54	Nd.	Nd.	Bdl.	Bdl.	Bdl.	Bdl.	0.02	-0.01	0.01	-0.00	99.83	ALKBM1-98 / r2 / 2 = cpx
50.32	0.73	5.52	0.00	Bdl.	11.25	Bdl.	**12.13**	17.56	1.52	Nd.	Nd.	Nd.	Nd.	Nd.	Bdl.	0.04	-0.02	0.00	0.00	99.15	ALKBM1-98 / r2 / 2 = cpx
40.62	0.15	**20.70**	Nd.	Nd.	**19.78**	0.38	**11.00**	**5.00**	**1.07**	Bdl.	Nd.	Bdl.	Bdl.	Bdl.	Bdl.	0.12	-0.05	0.01	-0.00	98.87	ALKBM1-98 / r2 / 3a = tumma aines (amfiboli?)
39.53	0.17	**20.79**	Nd.	Nd.	**20.92**	0.36	**11.35**	**4.82**	**0.88**	Bdl.	Nd.	Bdl.	Nd.	Bdl.	Nd.	0.07	-0.03	0.00	0.00	98.93	ALKBM1-98 / r2 / 3a = tumma aines (amfiboli?)
38.84	0.16	**20.48**	Nd.	Bdl.	**22.34**	0.50	**11.45**	**4.42**	**0.60**	Nd.	Nd.	Bdl.	Nd.	Nd.	Bdl.	0.08	-0.03	0.00	-0.00	98.92	ALKBM1-98 / r2 / 3a = tumma aines (amfiboli?)
39.49	0.21	**19.69**	Nd.	Bdl.	**23.07**	0.54	**12.12**	**4.16**	**0.45**	Bdl.	Nd.	Bdl.	Bdl.	Nd.	Bdl.	0.05	-0.02	0.01	-0.00	99.86	ALKBM1-98 / r2 / 3a = tumma aines (amfiboli?)
56.10	Bdl.	25.78	Bdl.	Nd.	0.84	Bdl.	Bdl.	10.12	5.72	0.17	Nd.	Nd.	Bdl.	Bdl.	Nd.	0.00	0.00	0.00	0.00	98.83	ALKBM1-98 / r2 / 3b = sulkeuma1 = plg
56.83	Bdl.	25.48	Bdl.	Bdl.	0.95	Nd.	Bdl.	9.26	6.22	0.15	Bdl.	Bdl.	Nd.	Nd.	Bdl.	0.00	0.00	0.00	-0.00	99.09	ALKBM1-98 / r2 / 3c = sulkeuma2 = plg
56.51	Bdl.	25.32	Bdl.	Bdl.	0.93	Bdl.	Bdl.	9.11	6.30	0.17	Nd.	Bdl.	Nd.	Bdl.	Bdl.	0.03	-0.01	0.00	0.00	98.57	ALKBM1-98 / r2 / 3c = sulkeuma2 = plg
Bdl.	**47.72**	Nd.	Bdl.	**0.45**	**46.74**	**1.87**	0.14	0.05	0.00	Bdl.	Nd.	Bdl.	Bdl.	Nd.	Bdl.	0.09	-0.04	0.00	0.00	97.19	ALKBM1-98 / r2 / 4 = opaakki = ilmeniitti
Bdl.	**48.19**	Nd.	Bdl.	**0.40**	**46.24**	**1.93**	0.11	0.06	0.00	Bdl.	Nd.	Bdl.	Nd.	Bdl.	Nd.	0.13	-0.05	0.02	-0.00	97.21	ALKBM1-98 / r2 / 4 = opaakki = ilmeniitti
Bdl.	**48.09**	Nd.	Bdl.	**0.42**	**47.62**	**1.85**	Bdl.	0.04	0.00	Bdl.	Nd.	Bdl.	Nd.	Nd.	Nd.	0.07	-0.03	0.00	0.00	98.18	ALKBM1-98 / r2 / 4 = opaakki = ilmeniitti
50.21	0.78	5.57	Nd.	Bdl.	11.09	0.14	12.21	17.70	1.56	Bdl.	Nd.	Nd.	Bdl.	Bdl.	Nd.	0.10	-0.04	0.00	-0.00	99.54	ALKBM1-98 / r3 / 1 = cpx
50.30	0.70	5.49	Bdl.	Bdl.	11.35	0.13	12.11	17.53	1.52	Nd.	Nd.	Bdl.	Bdl.	Bdl.	Nd.	0.12	-0.05	0.01	-0.00	99.40	ALKBM1-98 / r3 / 1 = cpx
50.27	0.86	5.47	Bdl.	0.14	11.32	0.12	12.26	17.67	1.55	Bdl.	Nd.	Bdl.	Bdl.	Bdl.	Nd.	0.11	-0.05	0.00	0.00	99.78	ALKBM1-98 / r3 / 1 = cpx
60.72	Bdl.	23.35	Nd.	Bdl.	0.21	Bdl.	0.03	**6.36**	**7.44**	**0.79**	Nd.	Bdl.	Nd.	Bdl.	Bdl.	0.11	-0.05	0.00	0.00	99.24	ALKBM1-98 / r3 / 2 = plg
10.30	0.00	**0.90**	Nd.	Bdl.	**63.54**	1.87	**2.28**	1.30	0.00	0.08	Bdl.	Bdl.	Bdl.	Nd.	Bdl.	0.39	-0.17	0.07	-0.02	80.76	ALKBM1-98 / r3 / 3 = magnetiitti (götiitti) / rae1

Appendix 2. Cont.

SiO2	TiO2	Al2O3	Cr2O3	V2O3	FeO	MnO	MgO	CaO	Na2O	K2O	BaO	SrO	NiO	P2O5	SO2	F	F = O	Cl	Cl = O	Total	Näyte / analyysipiste / kommentti
11.20	Bdl.	**0.82**	Bdl.	Nd.	**63.56**	1.27	**1.30**	1.67	0.00	0.10	Bdl.	Bdl.	Bdl.	Bdl.	0.10	0.21	-0.09	0.05	-0.01	80.45	ALKBM1-98 / r3 / 3 = magnetiitti (götiitti) / rae1
12.08	Bdl.	**1.02**	Bdl.	Bdl.	**61.58**	2.63	**1.58**	1.86	0.00	0.10	Bdl.	0.20	Bdl.	Nd.	0.07	0.28	-0.12	0.13	-0.03	81.63	ALKBM1-98 / r3 / 3 = magnetiitti (götiitti) / rae2
12.50	Bdl.	**1.16**	Nd.	Bdl.	**64.35**	1.21	**1.34**	1.53	0.00	0.06	Bdl.	0.15	Bdl.	Bdl.	Bdl.	0.27	-0.11	0.11	-0.02	82.72	ALKBM1-98 / r3 / 3 = magnetiitti (götiitti) / rae2
12.98	Bdl.	**1.09**	Nd.	Nd.	**63.55**	2.78	**1.51**	1.68	0.00	0.08	Bdl.	Bdl.	Nd.	Bdl.	0.09	0.21	-0.09	0.14	-0.03	84.27	ALKBM1-98 / r3 / 3 = magnetiitti (götiitti) / rae2
61.22	0.00	23.36	Nd.	Bdl.	0.36	Bdl.	Bdl.	**6.70**	**7.17**	**0.48**	Nd.	Bdl.	Nd.	Bdl.	Nd.	0.00	-0.00	0.00	0.00	99.47	ALKBM1-98 / r3 / 4a = sulkeuma = plagioklaasi
60.96	Bdl.	23.05	Bdl.	Nd.	0.30	0.00	Bdl.	**6.73**	**7.12**	**0.38**	Bdl.	Bdl.	Nd.	Bdl.	Nd.	0.08	-0.03	0.00	-0.00	98.82	ALKBM1-98 / r3 / 4a = sulkeuma = plagioklaasi
60.90	Bdl.	23.17	Nd.	Nd.	0.41	Bdl.	Bdl.	**6.95**	**7.10**	**0.36**	Nd.	0.21	Nd.	Nd.	Nd.	0.03	-0.01	0.01	-0.00	99.24	ALKBM1-98 / r3 / 4a = sulkeuma = plagioklaasi
56.49	Bdl.	25.43	Nd.	Bdl.	1.00	Bdl.	Bdl.	**8.91**	**6.23**	**0.45**	Nd.	Nd.	Nd.	Nd.	Bdl.	0.04	-0.02	0.01	-0.00	98.68	ALKBM1-98 / r3 / 4b = sulkeuma = plagioklaasi
56.64	0.00	25.30	Bdl.	Nd.	0.99	Nd.	Bdl.	**8.88**	**6.08**	**0.34**	Nd.	Nd.	Bdl.	Nd.	Bdl.	0.08	-0.04	0.00	-0.00	98.39	ALKBM1-98 / r3 / 4b = sulkeuma = plagioklaasi
56.53	Bdl.	25.46	Bdl.	0.03	0.80	Nd.	Bdl.	**9.29**	**6.11**	**0.26**	Nd.	Nd.	Nd.	Nd.	Bdl.	0.05	-0.02	0.01	-0.00	98.64	ALKBM1-98 / r3 / 4b = sulkeuma = plagioklaasi
56.33	Bdl.	25.90	0.00	Bdl.	0.85	Bdl.	Bdl.	**9.64**	**6.05**	**0.22**	Nd.	Bdl.	Bdl.	Nd.	Nd.	0.09	-0.04	0.02	-0.00	99.27	ALKBM1-98 / r3 / 4b = sulkeuma = plagioklaasi
56.65	Bdl.	25.41	Bdl.	Bdl.	0.94	Bdl.	Bdl.	**8.78**	**6.00**	**0.49**	Nd.	Bdl.	Nd.	Bdl.	Bdl.	0.09	-0.04	0.00	0.00	98.52	ALKBM1-98 / r3 / 4b = sulkeuma = plagioklaasi
56.50	Bdl.	25.42	Bdl.	Nd.	0.77	Nd.	Bdl.	**9.18**	**5.90**	**0.37**	Nd.	Bdl.	Nd.	Nd.	Nd.	0.08	-0.03	0.01	-0.00	98.38	ALKBM1-98 / r3 / 4b = sulkeuma = plagioklaasi
41.09	1.95	13.85	0.20	Bdl.	12.07	0.26	11.78	9.94	3.21	2.11	Nd.	Bdl.	Bdl.	Bdl.	Bdl.	0.27	-0.11	0.02	-0.00	96.86	P4 / r1 / 1 = amfiboli
40.92	1.83	13.75	0.20	Bdl.	12.24	0.26	12.03	9.99	3.28	2.10	Nd.	Bdl.	Bdl.	Bdl.	Bdl.	0.32	-0.14	0.03	-0.01	97.04	P4 / r1 / 1 = amfiboli
41.04	1.99	14.03	0.22	0.12	12.26	0.20	11.88	9.89	3.28	2.12	Nd.	Bdl.	Bdl.	Bdl.	Bdl.	0.23	-0.10	0.03	-0.01	97.36	P4 / r1 / 1 = amfiboli
40.81	1.94	13.48	0.20	Bdl.	12.08	0.17	11.96	9.85	3.23	2.14	Nd.	Bdl.	Bdl.	Bdl.	Bdl.	0.34	-0.14	0.04	-0.01	96.24	P4 / r1 / 1 = amfiboli
0.29	7.97	6.43	1.13	0.21	72.94	Bdl.	0.13	0.13	0.00	0.06	Nd.	0.16	0.08	Bdl.	Nd.	0.14	-0.06	0.00	0.00	89.68	P4 / r1 / 2a = omamuotinen mgt = Fe-Ti-Al-ox / rae1
0.25	8.34	6.30	1.15	0.25	72.90	Bdl.	0.09	0.13	0.00	0.08	Nd.	Bdl.	Bdl.	Bdl.	Nd.	0.19	-0.08	0.00	0.00	89.79	P4 / r1 / 2a = omamuotinen mgt = Fe-Ti-Al-ox / rae1
0.23	7.84	6.60	1.10	0.21	73.47	Bdl.	0.12	0.11	0.00	0.09	Nd.	Bdl.	Bdl.	Bdl.	Nd.	0.13	-0.05	0.01	-0.00	90.11	P4 / r1 / 2a = omamuotinen mgt = Fe-Ti-Al-ox / rae1
0.16	8.31	6.11	0.98	0.28	73.59	Bdl.	Bdl.	0.13	0.13	0.08	Nd.	Nd.	Bdl.	Nd.	Bdl.	0.14	-0.06	0.01	-0.00	90.06	P4 / r1 / 2a = omamuotinen mgt = Fe-Ti-Al-ox / rae1
0.15	7.66	5.99	1.08	0.27	74.70	Bdl.	0.10	0.13	0.00	Bdl.	Nd.	Bdl.	0.07	Bdl.	Nd.	0.10	-0.04	0.00	0.00	90.35	P4 / r1 / 2a = omamuotinen mgt = Fe-Ti-Al-ox / rae2

Appendix 2. Cont.

SiO2	TiO2	Al2O3	Cr2O3	V2O3	FeO	MnO	MgO	CaO	Na2O	K2O	BaO	SrO	NiO	P2O5	SO2	F	F = O	Cl	Cl = O	Total	Näyte / analyysipiste / kommentti
0.18	7.69	6.53	1.08	0.33	73.73	0.10	0.13	0.11	0.00	Bdl.	Nd.	Bdl.	Bdl.	Bdl.	Nd.	0.14	-0.06	0.01	-0.00	90.13	P4 / r1 / 2a = omamuotinen mgt = Fe-Ti-Al-ox / rae2
0.85	5.31	4.73	0.87	0.20	77.62	Bdl.	0.26	0.10	0.10	0.09	Nd.	Nd.	0.06	Bdl.	Nd.	0.17	-0.07	0.00	0.00	90.34	P4 / r1 / 2a = omamuotinen mgt = Fe-Ti-Al-ox / rae3
0.62	5.94	5.69	0.92	0.14	75.78	Bdl.	0.13	0.11	Bdl.	0.10	Nd.	Bdl.	Bdl.	Nd.	Bdl.	0.13	-0.05	0.02	-0.00	89.75	P4 / r1 / 2a = omamuotinen mgt = Fe-Ti-Al-ox / rae3
0.55	6.33	6.10	0.98	0.23	75.29	0.09	0.17	0.11	0.05	0.12	Nd.	Bdl.	Bdl.	Bdl.	Bdl.	0.13	-0.06	0.01	-0.00	90.26	P4 / r1 / 2a = omamuotinen mgt = Fe-Ti-Al-ox / rae3
0.36	6.95	7.40	1.08	0.17	72.63	0.09	0.13	0.17	0.00	0.07	Nd.	0.15	0.07	Bdl.	Bdl.	0.13	-0.05	0.02	-0.00	89.40	P4 / r1 / 2a = omamuotinen mgt = Fe-Ti-Al-ox / rae4
0.25	7.25	7.86	1.11	0.25	72.28	Nd.	0.14	0.15	0.00	0.08	Nd.	Bdl.	Bdl.	Bdl.	Nd.	0.18	-0.07	0.00	0.00	89.65	P4 / r1 / 2a = omamuotinen mgt = Fe-Ti-Al-ox / rae4
0.25	7.23	7.91	1.08	0.20	72.01	Bdl.	0.16	0.13	0.00	0.06	Nd.	Bdl.	Bdl.	Bdl.	Nd.	0.15	-0.06	0.01	-0.00	89.25	P4 / r1 / 2a = omamuotinen mgt = Fe-Ti-Al-ox / rae4
0.15	7.76	7.14	0.94	0.20	72.24	Nd.	Bdl.	0.18	0.00	0.05	Nd.	Bdl.	Bdl.	Nd.	Bdl.	0.13	-0.05	0.00	-0.00	88.91	P4 / r1 / 2a = omamuotinen mgt = Fe-Ti-Al-ox / rae4
36.38	**2.65**	**13.30**	0.11	Bdl.	**17.33**	0.29	**13.79**	0.08	0.39	**9.50**	Nd.	Nd.	Bdl.	Bdl.	Bdl.	**1.08**	-0.46	0.00	0.00	94.55	P4 / r1 / 2b = omamuotoinen kiille
36.76	2.71	12.88	0.14	Bdl.	**17.95**	0.22	**13.92**	Bdl.	0.38	**9.44**	Nd.	Nd.	Bdl.	Bdl.	Bdl.	**1.10**	-0.46	0.01	-0.00	95.18	P4 / r1 / 2b = omamuotoinen kiille
36.13	**2.60**	**14.65**	0.03	Bdl.	**15.21**	0.24	**15.36**	Bdl.	0.42	**9.41**	Nd.	Nd.	Bdl.	Nd.	Bdl.	**1.21**	-0.51	0.00	0.00	94.99	P4 / r1 / 2b = omamuotoinen kiille
36.39	**2.58**	**13.26**	0.12	Bdl.	**17.59**	0.24	**13.76**	0.07	0.36	**9.42**	Nd.	Nd.	Bdl.	Nd.	Bdl.	**1.05**	-0.44	0.01	-0.00	94.53	P4 / r1 / 2b = omamuotoinen kiille
52.12	0.26	2.23	0.21	Bdl.	7.77	0.20	13.67	21.76	1.01	Nd.	Nd.	Bdl.	Nd.	Bdl.	Nd.	0.01	-0.00	0.00	0.00	99.33	P4 / r1 / 3a = cpx
51.94	0.29	2.17	0.17	Bdl.	7.99	0.25	13.80	22.04	1.00	Bdl.	Nd.	Bdl.	Bdl.	Bdl.	Nd.	0.00	0.00	0.00	0.00	99.85	P4 / r1 / 3a = cpx
52.44	0.25	1.61	0.18	Bdl.	7.94	0.31	14.10	22.19	0.78	Nd.	Nd.	Bdl.	Bdl.	Nd.	Nd.	0.01	-0.00	0.01	-0.00	100.01	P4 / r1 / 3a = cpx
50.05	0.00	27.17	Bdl.	Nd.	**2.84**	Nd.	**2.19**	**0.53**	0.57	**8.77**	Nd.	Nd.	Bdl.	Nd.	Bdl.	0.01	-0.00	0.02	-0.00	92.17	P4 / r1 / 3b = "ms"-suotauma edellisessä cpx: ssä (montmorilloniitti / illiitti, paikoin myös Na-rikas)
51.14	Bdl.	27.63	Bdl.	Nd.	**2.71**	Bdl.	**2.12**	**0.61**	0.74	**7.11**	Bdl.	Bdl.	Bdl.	Nd.	Nd.	0.05	-0.02	0.01	-0.00	92.33	P4 / r1 / 3b = "ms"-suotauma edellisessä cpx: ssä (montmorilloniitti / illiitti, paikoin myös Na-rikas)
56.13	0.00	22.28	Nd.	Nd.	**0.27**	Bdl.	**0.04**	**1.15**	**12.51**	**0.34**	Bdl.	Bdl.	Nd.	Bdl.	0.18	0.00	0.00	0.01	-0.00	93.34	P4 / r1 / 3b = "ms"-suotauma edellisessä cpx: ssä (montmorilloniitti / illiitti, paikoin myös Na-rikas)
52.85	0.00	28.81	Bdl.	Nd.	**2.33**	Bdl.	**2.46**	**1.65**	0.72	**4.03**	Nd.	Bdl.	Bdl.	Nd.	Nd.	0.02	-0.01	0.03	-0.01	93.06	P4 / r1 / 3b = "ms"-suotauma edellisessä cpx: ssä (montmorilloniitti / illiitti, paikoin myös Na-rikas)
53.55	Bdl.	28.52	Bdl.	Nd.	**3.05**	Bdl.	**2.67**	**0.40**	0.15	**6.12**	Nd.	Nd.	Nd.	Nd.	Nd.	0.10	-0.04	0.00	0.00	94.67	P4 / r1 / 3b = "ms"-suotauma edellisessä cpx: ssä (montmorilloniitti / illiitti, paikoin myös Na-rikas)

Appendix 2. Cont.

SiO2	TiO2	Al2O3	Cr2O3	V2O3	FeO	MnO	MgO	CaO	Na2O	K2O	BaO	SrO	NiO	P2O5	SO2	F	F = O	Cl	Cl = O	Total	Näyte / analyysipiste / kommentti
52.39	0.00	28.02	Nd.	Bdl.	**2.94**	Bdl.	**2.44**	**0.47**	0.38	**5.10**	Nd.	Bdl.	Nd.	Bdl.	Nd.	0.01	-0.01	0.00	0.00	91.83	P4 / r1 / 3b = "ms"-suotauma edellisessä cpx: ssä (montmorilloniitti / illiitti, paikoin myös Na-rikas)
58.97	0.00	23.19	Nd.	Nd.	0.39	Nd.	0.28	0.81	9.97	0.27	Nd.	Nd.	Nd.	Nd.	Nd.	0.00	0.00	0.00	0.00	93.88	P4 / r1 / 3b = "ms"-suotauma edellisessä cpx: ssä (montmorilloniitti / illiitti, paikoin myös Na-rikas)
57.06	0.00	24.52	Nd.	Nd.	0.21	0.10	0.09	0.57	7.17	0.12	Nd.	Bdl.	Bdl.	Bdl.	Bdl.	0.00	0.00	0.00	0.00	89.98	P4 / r1 / 3b = "ms"-suotauma edellisessä cpx: ssä (montmorilloniitti / illiitti, paikoin myös Na-rikas)
41.06	1.98	13.86	0.19	Bdl.	12.18	0.16	11.86	9.80	3.27	2.10	Nd.	Bdl.	Nd.	Bdl.	Bdl.	0.35	-0.15	0.03	-0.01	96.84	P4 / r2 / 1 = amfiboli
40.95	2.01	13.87	0.20	Bdl.	12.22	0.20	11.76	9.86	3.28	2.17	Nd.	Bdl.	Bdl.	Bdl.	Bdl.	0.35	-0.15	0.03	-0.01	96.86	P4 / r2 / 1 = amfiboli
40.93	2.03	13.91	0.23	Bdl.	12.31	0.18	11.90	9.93	3.24	2.15	Nd.	Bdl.	Bdl.	Bdl.	Bdl.	0.27	-0.11	0.02	-0.00	97.20	P4 / r2 / 1 = amfiboli
40.80	1.95	13.83	0.20	Bdl.	12.31	0.24	11.74	9.87	3.26	2.15	Nd.	Bdl.	Bdl.	Bdl.	Bdl.	0.31	-0.13	0.04	-0.01	96.81	P4 / r2 / 1 = amfiboli
37.00	2.56	13.26	0.24	Bdl.	15.68	0.22	15.04	Nd.	0.32	**9.50**	Nd.	Nd.	Bdl.	Nd.	Bdl.	0.86	-0.36	0.01	-0.00	94.49	P4 / r2 / 2 = omamuotoinen kiille
37.09	2.77	13.65	0.27	Bdl.	15.91	0.25	15.52	Bdl.	0.32	**9.57**	Nd.	Nd.	Bdl.	Nd.	Bdl.	0.78	-0.33	0.01	-0.00	95.95	P4 / r2 / 2 = omamuotoinen kiille
36.95	2.79	13.60	0.24	Bdl.	16.04	0.17	15.19	Bdl.	0.33	**9.50**	Nd.	Nd.	Bdl.	Bdl.	Bdl.	0.75	-0.31	0.01	-0.00	95.39	P4 / r2 / 2 = omamuotoinen kiille
37.04	2.77	13.63	0.25	0.11	16.44	0.23	14.92	Bdl.	0.31	**9.56**	Nd.	Nd.	Bdl.	Nd.	Bdl.	0.76	-0.32	0.00	-0.00	95.74	P4 / r2 / 2 = omamuotoinen kiille
40.92	1.93	13.76	0.23	Nd.	12.20	0.21	11.78	9.85	3.25	2.14	Nd.	Bdl.	Bdl.	Bdl.	Nd.	0.31	-0.13	0.02	-0.01	96.56	P4 / r2 / 3a = cpx
40.84	1.96	13.88	0.18	Bdl.	12.25	0.17	11.62	9.87	3.28	2.16	Nd.	Bdl.	Nd.	Bdl.	Bdl.	0.32	-0.13	0.03	-0.01	96.66	P4 / r2 / 3a = cpx
41.01	1.96	13.93	0.20	Bdl.	12.24	0.18	11.70	10.00	3.28	2.06	Nd.	Bdl.	Bdl.	Bdl.	Bdl.	0.34	-0.14	0.03	-0.01	96.91	P4 / r2 / 3a = cpx
41.14	1.92	14.05	0.20	Bdl.	12.19	0.25	11.91	9.83	3.19	2.14	Nd.	Bdl.	Nd.	Nd.	Bdl.	0.36	-0.15	0.02	-0.00	97.20	P4 / r2 / 3a = cpx
0.29	**10.42**	**7.89**	0.90	0.34	**68.53**	Nd.	0.10	0.30	0.00	Bdl.	Nd.	Bdl.	0.08	Nd.	Nd.	0.22	-0.09	0.00	0.00	89.10	P4 / r2 / 3b = magnetiitti / rae1
0.43	**10.27**	**8.02**	0.99	0.27	**68.47**	Bdl.	0.11	0.29	0.00	Bdl.	Nd.	Bdl.	0.09	Bdl.	Bdl.	0.12	-0.05	0.00	0.00	89.15	P4 / r2 / 3b = magnetiitti / rae1
1.09	**10.16**	**7.24**	0.93	0.32	**68.18**	Bdl.	0.45	0.28	0.00	0.07	Nd.	Bdl.	0.09	Nd.	Bdl.	0.16	-0.07	0.00	0.00	89.03	P4 / r2 / 3b = magnetiitti / rae1
0.16	**10.62**	**7.27**	0.73	0.28	**69.30**	Bdl.	Bdl.	0.36	0.00	0.05	Nd.	Bdl.	Bdl.	Nd.	Nd.	0.13	-0.05	0.01	-0.00	89.04	P4 / r2 / 3b = magnetiitti / rae2
0.15	**10.69**	**7.30**	0.74	0.28	**69.08**	Bdl.	Bdl.	0.37	0.00	Bdl.	Nd.	Bdl.	0.09	Nd.	Bdl.	0.15	-0.06	0.00	0.00	88.98	P4 / r2 / 3b = magnetiitti / rae2
0.12	**10.23**	**7.45**	0.79	0.27	**69.16**	Bdl.	Bdl.	0.38	0.00	Bdl.	Nd.	Bdl.	Bdl.	Nd.	Bdl.	0.16	-0.07	0.00	0.00	88.80	P4 / r2 / 3b = magnetiitti / rae2
0.35	**10.62**	**6.77**	0.86	0.20	**69.17**	Bdl.	Bdl.	0.39	0.00	0.08	Nd.	Bdl.	0.10	Nd.	Nd.	0.16	-0.07	0.00	0.00	88.74	P4 / r2 / 3b = magnetiitti / rae2
0.28	**10.06**	**7.95**	0.66	0.23	**68.80**	0.10	0.09	0.37	0.00	Bdl.	Nd.	Bdl.	0.06	Nd.	Bdl.	0.15	-0.06	0.00	-0.00	88.80	P4 / r2 / 3b = magnetiitti / rae2
0.10	**9.90**	**9.29**	0.95	0.28	**68.78**	Bdl.	0.10	0.29	0.00	Bdl.	Nd.	Bdl.	0.09	Nd.	Nd.	0.17	-0.07	0.00	0.00	90.02	P4 / r2 / 3b = magnetiitti / rae3
0.13	**9.67**	**9.14**	1.03	0.28	**69.21**	Nd.	Bdl.	0.26	0.00	Bdl.	Nd.	Bdl.	0.11	Bdl.	Bdl.	0.11	-0.05	0.00	0.00	**90.10**	P4 / r2 / 3b = magnetiitti / rae3
50.28	0.68	3.95	0.22	Bdl.	7.17	0.23	13.51	22.69	0.75	Bdl.	Nd.	Bdl.	Bdl.	Bdl.	Bdl.	0.08	-0.03	0.00	0.00	99.71	P4 / r2 / 4a = cpx
49.82	0.72	4.52	0.26	Nd.	7.59	0.19	13.41	22.18	0.81	Bdl.	Nd.	Bdl.	Nd.	Bdl.	Nd.	0.04	-0.02	0.00	0.00	99.69	P4 / r2 / 4a = cpx
48.93	0.85	5.32	0.21	Bdl.	7.70	0.27	13.05	21.53	1.01	Bdl.	Nd.	Bdl.	Bdl.	Bdl.	Nd.	0.08	-0.03	0.00	-0.00	99.04	P4 / r2 / 4a = cpx
51.45	0.42	2.87	0.32	Bdl.	7.32	0.26	13.88	22.63	0.77	Nd.	Nd.	Bdl.	Bdl.	Nd.	Nd.	0.03	-0.01	0.00	-0.00	100.09	P4 / r2 / 4a = cpx
50.86	0.46	3.25	0.29	Bdl.	7.28	0.15	13.82	22.40	0.80	Bdl.	Nd.	Bdl.	Bdl.	Bdl.	Nd.	0.00	-0.00	0.00	0.00	99.58	P4 / r2 / 4a = cpx

Appendix 2. Cont.

SiO2	TiO2	Al2O3	Cr2O3	V2O3	FeO	MnO	MgO	CaO	Na2O	K2O	BaO	SrO	NiO	P2O5	SO2	F	F = O	Cl	Cl = O	Total	Näyte / analyysipiste / kommentti
46.61	Bdl.	**32.92**	Bdl.	Bdl.	1.26	Bdl.	**0.70**	1.63	3.67	3.22	Nd.	Bdl.	Nd.	Bdl.	Nd.	0.00	-0.00	0.02	-0.00	90.20	P4 / r2 / 4b = "ms"-suotauma edellisessä cpx: ssä (todennäköisesti illiitti)
47.80	0.00	**31.69**	Bdl.	Bdl.	1.31	Bdl.	**0.68**	1.85	6.07	3.19	Nd.	0.17	Nd.	Nd.	Bdl.	0.00	0.00	0.00	-0.00	92.82	P4 / r2 / 4b = "ms"-suotauma edellisessä cpx: ssä (todennäköisesti illiitti)
48.33	Bdl.	**32.81**	Bdl.	Bdl.	1.41	Bdl.	**0.88**	1.72	2.56	3.41	Nd.	0.19	Nd.	Bdl.	Bdl.	0.00	0.00	0.00	-0.00	91.48	P4 / r2 / 4b = "ms"-suotauma edellisessä cpx: ssä (todennäköisesti illiitti)
47.20	Bdl.	**31.57**	Bdl.	Nd.	1.55	Bdl.	**1.10**	1.95	5.43	3.88	Nd.	Bdl.	Bdl.	Bdl.	Bdl.	0.02	-0.01	0.01	-0.00	92.88	P4 / r2 / 4b = "ms"-suotauma edellisessä cpx: ssä (todennäköisesti illiitti)
44.61	Bdl.	**29.23**	Bdl.	Bdl.	3.08	Nd.	**4.41**	1.31	1.82	4.94	Nd.	Bdl.	Bdl.	Nd.	Nd.	0.03	-0.01	0.00	0.00	89.82	P4 / r2 / 4b = "ms"-suotauma edellisessä cpx: ssä (todennäköisesti illiitti)
45.35	Bdl.	**29.44**	Bdl.	Bdl.	2.85	Bdl.	**3.92**	1.35	1.76	4.86	Nd.	0.17	Bdl.	Bdl.	Bdl.	0.01	-0.01	0.01	-0.00	89.89	P4 / r2 / 4b = "ms"-suotauma edellisessä cpx: ssä (todennäköisesti illiitti)
45.79	Bdl.	**30.31**	0.00	Nd.	**3.01**	Bdl.	**4.13**	**1.35**	**1.29**	**4.58**	Bdl.	Bdl.	Bdl.	Nd.	Nd.	0.11	-0.05	0.02	-0.00	90.63	P4 / r2 / 4b = "ms"-suotauma edellisessä cpx: ssä (todennäköisesti illiitti)
46.51	Bdl.	**30.35**	0.02	Nd.	**3.12**	Bdl.	**4.56**	**1.34**	**0.67**	**4.41**	Nd.	Bdl.	Nd.	Nd.	Nd.	0.05	-0.02	0.02	-0.00	91.25	P4 / r2 / 4b = "ms"-suotauma edellisessä cpx: ssä (todennäköisesti illiitti)
47.23	Bdl.	**31.50**	Bdl.	Nd.	**2.18**	Nd.	**2.28**	**1.43**	**2.21**	**4.64**	Nd.	Bdl.	0.06	Nd.	Nd.	0.04	-0.02	0.01	-0.00	91.78	P4 / r2 / 4b = "ms"-suotauma edellisessä cpx: ssä (todennäköisesti illiitti)
46.06	Bdl.	**30.60**	Bdl.	Nd.	**2.18**	Bdl.	**2.37**	**1.40**	**1.08**	**4.34**	Nd.	Nd.	Nd.	Bdl.	Bdl.	0.11	-0.05	0.00	0.00	88.22	P4 / r2 / 4b = "ms"-suotauma edellisessä cpx: ssä (todennäköisesti illiitti)
36.88	3.31	15.65	Bdl.	Bdl.	8.91	0.09	19.30	Bdl.	0.46	**9.42**	Bdl.	Nd.	Nd.	Bdl.	Bdl.	1.14	-0.48	0.01	-0.00	94.90	P4 / r3 / 2 = kiille
36.80	3.33	15.49	0.10	Bdl.	8.99	0.13	19.27	Bdl.	0.44	**9.44**	Bdl.	Nd.	Bdl.	Nd.	Bdl.	1.01	-0.42	0.00	-0.00	94.83	P4 / r3 / 2 = kiille
36.46	3.15	15.31	0.17	Bdl.	9.02	0.14	18.97	Bdl.	0.33	**9.65**	Nd.	Nd.	Bdl.	Nd.	Nd.	0.92	-0.39	0.01	-0.00	93.85	P4 / r3 / 2 = kiille
36.51	3.37	14.96	0.15	Bdl.	9.08	0.18	18.76	Bdl.	0.38	**9.49**	Bdl.	Nd.	Bdl.	Bdl.	Nd.	0.98	-0.41	0.00	0.00	93.54	P4 / r3 / 2 = kiille
36.63	3.44	15.55	Bdl.	Bdl.	8.85	0.09	19.32	0.07	0.46	**9.53**	Nd.	Nd.	Bdl.	Bdl.	Nd.	1.11	-0.47	0.01	-0.00	94.75	P4 / r3 / 2 = kiille
1.74	**1.93**	**1.33**	0.44	Bdl.	**80.60**	Bdl.	0.10	0.21	0.13	0.16	Nd.	Nd.	0.06	Bdl.	Nd.	0.18	-0.08	0.06	-0.01	87.01	P4 / r3 / 3 = magnetiitti kiilteen sisältä (hyvin pieni raekoko = > Si ja Al saattavat tulla ympäröivästä kiilteestä)

Appendix 2. Cont.

SiO2	TiO2	Al2O3	Cr2O3	V2O3	FeO	MnO	MgO	CaO	Na2O	K2O	BaO	SrO	NiO	P2O5	SO2	F	F = O	Cl	Cl = O	Total	Näyte / analyysipiste / kommentti
1.90	**1.97**	**1.39**	0.50	Bdl.	**80.58**	Bdl.	0.33	0.21	0.10	0.15	Nd.	Nd.	Bdl.	Bdl.	Nd.	0.19	-0.08	0.02	-0.01	87.44	P4 / r3 / 3 = magnetiitti kiilteen sisältä (hyvin pieni raekoko = > Si ja Al saattavat tulla ympäröivästä kiilteestä)
1.64	**2.16**	**1.13**	0.38	Bdl.	**81.45**	0.13	0.10	0.22	0.07	0.13	Nd.	Nd.	0.06	Bdl.	Bdl.	0.14	-0.06	0.04	-0.01	87.67	P4 / r3 / 3 = magnetiitti kiilteen sisältä (hyvin pieni raekoko = > Si ja Al saattavat tulla ympäröivästä kiilteestä)
1.63	**1.93**	**0.99**	0.36	0.12	**80.57**	0.12	0.05	0.22	0.11	0.12	Nd.	Nd.	Bdl.	Bdl.	Bdl.	0.12	-0.05	0.01	-0.00	86.47	P4 / r3 / 3 = magnetiitti kiilteen sisältä (hyvin pieni raekoko = > Si ja Al saattavat tulla ympäröivästä kiilteestä)
41.80	2.08	12.99	0.21	Bdl.	12.15	0.23	12.24	9.80	3.26	2.12	Nd.	Bdl.	Bdl.	Bdl.	Bdl.	0.28	-0.12	0.02	-0.01	97.23	P4 / r3 / 4 = amfiboli
41.56	1.97	13.26	0.21	Bdl.	12.13	0.18	12.27	9.77	3.16	2.09	Nd.	Bdl.	Bdl.	Bdl.	Bdl.	0.34	-0.14	0.03	-0.01	96.93	P4 / r3 / 4 = amfiboli
41.49	1.99	13.22	0.22	Bdl.	12.20	0.23	12.26	9.88	3.26	2.08	Nd.	Bdl.	Bdl.	Bdl.	Bdl.	0.31	-0.13	0.01	-0.00	97.14	P4 / r3 / 4 = amfiboli
41.50	1.94	13.12	0.20	Bdl.	12.04	0.17	12.12	9.84	3.24	2.06	Nd.	Bdl.	Bdl.	Bdl.	Bdl.	0.35	-0.15	0.02	-0.01	96.59	P4 / r3 / 4 = amfiboli
51.69	0.57	0.65	0.00	Bdl.	10.75	0.51	11.43	22.46	1.42	Nd.	Nd.	0.21	Bdl.	Bdl.	Bdl.	0.06	-0.03	0.00	0.00	99.81	Xe15 / r1 / 1 = cpx core
51.53	0.62	0.60	Bdl.	Bdl.	10.76	0.51	11.29	22.41	1.41	Bdl.	Nd.	0.15	Nd.	Bdl.	Nd.	0.11	-0.05	0.00	0.00	99.45	Xe15 / r1 / 1 = cpx core
51.00	0.49	0.70	Bdl.	0.12	16.68	0.80	7.43	18.88	3.08	Nd.	Nd.	Bdl.	0.07	Bdl.	Nd.	0.05	-0.02	0.00	0.00	99.42	Xe15 / r1 / 2 = cpx-rim
51.22	0.52	0.73	Bdl.	0.13	16.15	0.71	7.66	19.08	3.09	Nd.	Nd.	Bdl.	Nd.	Bdl.	Bdl.	0.02	-0.01	0.00	0.00	99.48	Xe15 / r1 / 2 = cpx-rim
51.25	0.52	0.63	Bdl.	Bdl.	15.17	0.85	8.07	19.59	2.93	Bdl.	Nd.	Bdl.	Bdl.	Bdl.	Nd.	0.10	-0.04	0.00	0.00	99.39	Xe15 / r1 / 3a = rim
51.59	0.44	0.70	0.00	Bdl.	15.23	0.84	7.94	19.32	2.88	Bdl.	Nd.	Bdl.	Nd.	Nd.	Nd.	0.00	0.00	0.00	-0.00	99.12	Xe15 / r1 / 3a = rim
51.85	0.92	0.53	Bdl.	Bdl.	10.62	0.47	11.41	21.94	1.70	Bdl.	Nd.	0.21	Bdl.	Nd.	Nd.	0.11	-0.04	0.00	0.00	99.77	Xe15 / r1 / 3b = core
51.68	0.79	0.55	Nd.	Bdl.	10.56	0.45	11.34	21.65	1.78	Nd.	Nd.	0.21	Nd.	Bdl.	Nd.	0.08	-0.03	0.00	-0.00	99.15	Xe15 / r1 / 3b = core
29.12	**13.25**	0.78	Bdl.	0.22	19.25	0.24	1.15	**32.20**	0.12	Nd.	Nd.	Bdl.	Bdl.	Bdl.	Nd.	0.11	-0.05	0.00	0.00	96.57	Xe15 / r1 / 4 = Ti-Ca-granaatti
29.50	**13.79**	1.10	Bdl.	0.18	18.55	0.23	1.24	**32.30**	0.11	Bdl.	Nd.	Bdl.	Bdl.	Bdl.	Nd.	0.08	-0.03	0.00	0.00	97.21	Xe15 / r1 / 4 = Ti-Ca-granaatti
29.73	**13.77**	1.20	Bdl.	0.16	18.76	0.25	1.31	**32.62**	0.09	Nd.	Nd.	Bdl.	Nd.	Bdl.	Nd.	0.11	-0.05	0.00	0.00	98.13	Xe15 / r1 / 4 = Ti-Ca-granaatti
26.98	**16.24**	5.78	0.11	0.20	14.51	0.14	0.85	**32.43**	0.00	Nd.	Nd.	Bdl.	Nd.	Bdl.	Bdl.	0.09	-0.04	0.00	0.00	97.45	Xe15 / r1 / 5a = Ti-Ca-granaatti-core (tiheysero ytimen ja reunan välillä)
26.65	**15.73**	5.97	0.09	Bdl.	14.31	0.24	0.79	**32.49**	0.01	Nd.	Nd.	Bdl.	Bdl.	Bdl.	Nd.	0.03	-0.01	0.02	-0.01	96.49	Xe15 / r1 / 5a = Ti-Ca-granaatti-core
29.01	**14.93**	0.21	Bdl.	0.17	18.76	0.55	0.74	**30.86**	0.62	Bdl.	Nd.	Bdl.	Nd.	Bdl.	Nd.	0.06	-0.02	0.00	0.00	96.04	Xe15 / r1 / 5b = Ti-Ca-granaatti-rim
29.25	**14.89**	0.15	Nd.	0.18	19.15	0.54	0.71	**30.94**	0.56	Bdl.	Nd.	Bdl.	Nd.	Bdl.	Nd.	0.10	-0.04	0.00	0.00	96.63	Xe15 / r1 / 5b = Ti-Ca-granaatti-rim
0.82	Nd.	Nd.	Nd.	Bdl.	0.13	Bdl.	Nd.	54.24	0.10	Nd.	Nd.	2.35	Bdl.	**41.13**	Bdl.	**1.73**	-0.73	0.01	-0.00	99.90	Xe15 / r1 / 8 = apatiitti
0.79	Bdl.	Bdl.	Nd.	Bdl.	Bdl.	Bdl.	Bdl.	53.70	0.11	Nd.	Nd.	2.31	Bdl.	**41.51**	Nd.	**1.75**	-0.74	0.03	-0.01	99.61	Xe15 / r1 / 8 = apatiitti
0.86	Bdl.	Bdl.	Nd.	Bdl.	Bdl.	Bdl.	Nd.	53.03	0.07	Bdl.	Nd.	2.99	Bdl.	**41.64**	Bdl.	**1.74**	-0.73	0.01	-0.00	99.91	Xe15 / r1 / 8 = apatiitti
1.38	Bdl.	Nd.	Bdl.	Bdl.	Bdl.	Nd.	Bdl.	54.09	0.16	Bdl.	Bdl.	1.91	Nd.	**39.65**	Bdl.	**1.93**	-0.81	0.00	0.00	98.55	Xe15 / r1 / 9 = apatiitti
1.16	Bdl.	Bdl.	Bdl.	Bdl.	Bdl.	Bdl.	Bdl.	55.29	0.11	Bdl.	Nd.	1.98	Nd.	**40.28**	Bdl.	**1.66**	-0.70	0.02	-0.00	100.00	Xe15 / r1 / 9 = apatiitti

Appendix 2. Cont.

SiO2	TiO2	Al2O3	Cr2O3	V2O3	FeO	MnO	MgO	CaO	Na2O	K2O	BaO	SrO	NiO	P2O5	SO2	F	F = O	Cl	Cl = O	Total	Näyte / analyysipiste / kommentti
0.83	Bdl.	Nd.	Bdl.	Bdl.	0.14	Bdl.	Bdl.	52.87	0.05	Bdl.	Bdl.	2.87	Bdl.	**41.31**	Bdl.	**1.61**	-0.68	0.00	0.00	99.32	Xe15 / r1 / 9 = apatiitti
0.78	Bdl.	0.02	Bdl.	Nd.	0.13	Bdl.	Nd.	54.31	0.06	Bdl.	Nd.	3.00	Nd.	**40.84**	Nd.	**1.12**	-0.47	0.00	0.00	99.90	Xe15 / r1 / 9 = apatiitti_rim
51.14	1.18	0.80	Bdl.	0.13	13.53	0.73	8.86	19.60	**2.80**	Bdl.	Nd.	Bdl.	Nd.	Bdl.	Bdl.	0.03	-0.01	0.00	0.00	98.99	Xe-15 / r2 / 3 = cpx
51.31	0.60	0.69	Bdl.	0.08	15.26	0.89	8.14	18.63	**3.24**	Bdl.	Nd.	Bdl.	Bdl.	Bdl.	Nd.	0.04	-0.02	0.00	0.00	98.94	Xe-15 / r2 / 3 = cpx
51.30	0.59	0.73	Nd.	0.14	15.40	0.85	8.03	18.83	**3.25**	Nd.	Nd.	0.17	Bdl.	Bdl.	Nd.	0.06	-0.02	0.00	0.00	99.38	Xe-15 / r2 / 3 = cpx
51.37	0.69	0.61	Nd.	0.14	14.75	0.96	8.46	20.34	**2.28**	Bdl.	Nd.	Bdl.	Bdl.	Bdl.	Bdl.	0.09	-0.04	0.00	0.00	99.75	Xe-15 / r2 / 3 = cpx
50.84	1.89	0.92	Nd.	0.18	13.04	0.78	9.13	19.23	**2.92**	Nd.	Nd.	Bdl.	Nd.	Bdl.	Nd.	0.10	-0.04	0.00	0.00	99.18	Xe-15 / r2 / 4 = cpx
50.81	2.02	0.92	Nd.	0.17	12.79	0.71	9.14	19.16	**2.95**	Bdl.	Nd.	Bdl.	Nd.	Nd.	Bdl.	0.04	-0.02	0.00	0.00	98.84	Xe-15 / r2 / 4 = cpx
51.44	1.59	0.74	Nd.	0.16	12.04	0.74	9.65	19.81	**2.66**	Nd.	Nd.	Bdl.	Bdl.	Nd.	Bdl.	0.01	-0.00	0.00	0.00	98.92	Xe-15 / r2 / 4 = cpx
51.18	1.78	0.88	Nd.	0.11	12.52	0.70	9.57	19.28	**2.92**	Bdl.	Nd.	Bdl.	Nd.	Bdl.	Nd.	0.05	-0.02	0.00	-0.00	99.05	Xe-15 / r2 / 4 = cpx
39.27	0.38	10.45	Nd.	Bdl.	12.91	0.47	19.69	0.16	0.05	**9.40**	0.25	Nd.	Bdl.	Nd.	Nd.	0.34	-0.14	0.00	0.00	93.27	Xe-15 / r3 / 1 = flogopiitti
38.59	0.36	11.09	Nd.	Bdl.	13.94	0.53	19.25	0.14	0.08	**9.77**	0.28	Nd.	Bdl.	Bdl.	Bdl.	0.20	-0.09	0.01	-0.00	94.24	Xe-15 / r3 / 1 = flogopiitti
37.79	0.45	11.09	Bdl.	Bdl.	13.77	0.49	19.26	0.07	Bdl.	**9.99**	0.32	Nd.	Nd.	Nd.	Nd.	0.29	-0.12	0.00	0.00	93.46	Xe-15 / r3 / 1 = flogopiitti
38.31	0.40	11.29	Bdl.	Nd.	12.84	0.44	19.59	0.17	Bdl.	**9.68**	0.26	Nd.	Bdl.	Bdl.	Bdl.	0.31	-0.13	0.00	0.00	93.29	Xe-15 / r3 / 1 = flogopiitti
38.18	0.47	11.64	Nd.	Nd.	13.42	0.48	19.37	0.15	Bdl.	**9.76**	0.37	Nd.	Bdl.	Bdl.	Nd.	0.26	-0.11	0.00	-0.00	94.05	Xe-15 / r3 / 1 = flogopiitti
38.92	0.44	11.12	Nd.	Bdl.	13.00	0.50	19.73	0.12	0.05	**9.62**	0.18	Nd.	Nd.	Nd.	Nd.	0.59	-0.25	0.00	0.00	94.04	Xe-15 / r3 / 2 = flogopiitti
39.14	0.50	11.01	Nd.	Bdl.	13.17	0.40	19.71	0.19	0.06	**9.32**	0.25	Nd.	Bdl.	Nd.	Bdl.	0.39	-0.17	0.01	-0.00	94.08	Xe-15 / r3 / 2 = flogopiitti
38.73	0.47	11.15	Bdl.	Bdl.	12.95	0.46	19.69	0.08	Bdl.	**9.81**	0.26	Nd.	Nd.	Nd.	Nd.	0.43	-0.18	0.01	-0.00	93.96	Xe-15 / r3 / 2 = flogopiitti
38.55	0.31	11.77	Nd.	Nd.	12.53	0.40	19.66	0.31	0.08	**9.50**	0.30	Nd.	Bdl.	Nd.	Nd.	0.53	-0.22	0.01	-0.00	93.74	Xe-15 / r3 / 3 = flogopiitti
38.66	0.24	11.64	Nd.	Bdl.	12.39	0.36	20.00	0.16	0.05	**9.60**	0.27	Nd.	Nd.	Bdl.	Bdl.	0.34	-0.14	0.01	-0.00	93.66	Xe-15 / r3 / 3 = flogopiitti
38.44	0.23	11.14	Nd.	Bdl.	13.92	0.52	19.31	0.16	Bdl.	**9.75**	0.27	Nd.	Bdl.	Bdl.	Bdl.	0.56	-0.23	0.00	0.00	94.14	Xe-15 / r3 / 3 = flogopiitti
52.23	0.51	0.74	Nd.	Bdl.	9.60	0.80	11.70	23.01	1.02	Nd.	Nd.	Bdl.	Bdl.	Bdl.	Nd.	0.07	-0.03	0.01	-0.00	99.82	Xe-15 / r3 / 4 = cpx
52.04	0.47	0.78	Nd.	Bdl.	9.49	0.83	11.72	22.84	1.05	Nd.	Nd.	Bdl.	Nd.	Bdl.	Bdl.	0.09	-0.04	0.00	0.00	99.53	Xe-15 / r3 / 4 = cpx
52.03	0.60	0.75	Nd.	Bdl.	9.76	0.78	11.70	23.08	1.04	Nd.	Nd.	Bdl.	Bdl.	Bdl.	Nd.	0.03	-0.01	0.02	-0.00	99.95	Xe-15 / r3 / 4 = cpx
51.73	1.02	0.81	Nd.	0.17	11.41	0.82	10.31	21.54	1.85	Nd.	Nd.	Bdl.	Nd.	Bdl.	Bdl.	0.05	-0.02	0.01	-0.00	99.88	Xe-15 / r3 / 4 = cpx
51.75	0.62	0.73	Nd.	0.08	9.80	0.78	11.42	22.76	1.19	Nd.	Nd.	Bdl.	Nd.	Bdl.	Bdl.	0.01	-0.01	0.00	0.00	99.23	Xe-15 / r3 / 4 = cpx
0.55	**28.32**	0.00	Bdl.	0.34	**59.92**	0.85	Nd.	0.15	Nd.	Bdl.	Nd.	Bdl.	Nd.	Bdl.	Nd.	0.12	-0.05	0.00	-0.00	90.35	Xe-15 / r3 / 6 = opaakki = Fe-Ti-Ox (muuttunut ilmeniitti?)
0.55	**23.34**	Nd.	Bdl.	0.28	**64.28**	0.37	Bdl.	0.23	Nd.	Bdl.	Nd.	Bdl.	Nd.	Nd.	Nd.	0.13	-0.05	0.00	0.00	89.24	Xe-15 / r3 / 6 = opaakki = Fe-Ti-Ox (muuttunut ilmeniitti?)
0.49	**27.22**	Nd.	Bdl.	0.34	**61.10**	0.62	Bdl.	0.21	Nd.	Bdl.	Nd.	Nd.	Nd.	Nd.	Nd.	0.09	-0.04	0.00	0.00	90.17	Xe-15 / r3 / 6 = opaakki = Fe-Ti-Ox (muuttunut ilmeniitti?)
0.42	**24.11**	Nd.	0.11	0.19	**64.01**	0.61	Bdl.	0.24	Bdl.	Bdl.	Nd.	Nd.	Bdl.	Nd.	Nd.	0.10	-0.04	0.00	0.00	89.83	Xe-15 / r3 / 6 = opaakki = Fe-Ti-Ox (muuttunut ilmeniitti?)
0.43	**26.86**	Nd.	Bdl.	0.25	**61.81**	0.77	Bdl.	0.16	0.00	Bdl.	Nd.	Bdl.	Bdl.	Nd.	Bdl.	0.13	-0.05	0.02	-0.00	90.51	Xe-15 / r3 / 6 = opaakki = Fe-Ti-Ox (muuttunut ilmeniitti?)
1.58	0.00	Nd.	Bdl.	Bdl.	Bdl.	Bdl.	Bdl.	**55.18**	0.09	0.05	Nd.	**0.81**	Bdl.	**39.76**	0.16	**1.80**	-0.76	0.02	-0.00	98.93	Xe-15 / r3 / 7 = apatiitti / rae1

Appendix 2. Cont.

SiO2	TiO2	Al2O3	Cr2O3	V2O3	FeO	MnO	MgO	CaO	Na2O	K2O	BaO	SrO	NiO	P2O5	SO2	F	F = O	Cl	Cl = O	Total	Näyte / analyysipiste / kommentti
1.20	Bdl.	Nd.	Nd.	Nd.	Bdl.	Bdl.	Bdl.	**54.61**	0.07	0.05	Nd.	**1.33**	Nd.	**40.30**	0.06	**1.65**	-0.70	0.02	-0.00	98.72	Xe-15 / r3 / 7 = apatiitti / rae1
1.05	0.00	Nd.	Nd.	Bdl.	Bdl.	Nd.	Nd.	**54.08**	0.07	0.06	Nd.	**1.64**	Nd.	**40.25**	Bdl.	**1.73**	-0.73	0.00	0.00	98.31	Xe-15 / r3 / 7 = apatiitti / rae2
1.11	Bdl.	Nd.	Nd.	Bdl.	Bdl.	Nd.	Nd.	**54.27**	0.08	0.07	Nd.	**1.59**	Nd.	**39.70**	Bdl.	**1.87**	-0.79	0.01	-0.00	98.07	Xe-15 / r3 / 7 = apatiitti / rae2
1.38	Bdl.	Nd.	Nd.	0.12	Bdl.	Bdl.	Nd.	**54.60**	0.07	0.09	Nd.	**1.28**	Nd.	**39.37**	Bdl.	**1.81**	-0.76	0.02	-0.00	98.12	Xe-15 / r3 / 7 = apatiitti / rae2
1.61	Nd.	Nd.	Bdl.	Nd.	Nd.	Bdl.	Nd.	**54.84**	0.09	0.11	Nd.	**0.98**	Nd.	**39.22**	Bdl.	**1.92**	-0.81	0.02	-0.00	98.05	Xe-15 / r3 / 7 = apatiitti / rae2
1.12	Nd.	Nd.	Nd.	Bdl.	Bdl.	Bdl.	Nd.	**54.51**	0.09	0.06	Nd.	**1.78**	Nd.	**40.75**	0.06	**1.91**	-0.80	0.00	-0.00	99.58	Xe-15 / r3 / 7 = apatiitti / rae2
1.65	Nd.	Nd.	Bdl.	Bdl.	Bdl.	Nd.	Nd.	**55.10**	0.11	0.14	Nd.	**0.85**	Nd.	**38.94**	0.08	**1.83**	-0.77	0.02	-0.00	98.04	Xe-15 / r3 / 7 = apatiitti / rae2
39.11	**8.73**	**10.53**	0.13	Bdl.	**6.15**	Bdl.	**18.69**	Bdl.	0.06	**9.83**	Nd.	Nd.	0.10	Nd.	Bdl.	**0.74**	-0.31	0.00	0.00	93.94	P3 / r1 / 1 = flogo rim
39.10	**8.46**	**10.78**	0.17	Bdl.	**5.95**	Bdl.	**18.42**	Bdl.	0.05	**9.93**	Nd.	Nd.	0.09	Bdl.	Bdl.	**0.62**	-0.26	0.03	-0.01	93.56	P3 / r1 / 1 = flogo rim
39.25	**8.70**	**10.56**	0.18	Bdl.	**6.09**	Bdl.	**18.79**	Bdl.	0.06	**9.74**	Nd.	Nd.	0.11	Nd.	0.07	**0.61**	-0.26	0.01	-0.00	94.01	P3 / r1 / 1 = flogo rim
38.61	**8.56**	**10.25**	0.07	Bdl.	**8.91**	Bdl.	**17.42**	Bdl.	0.10	**9.75**	Nd.	Nd.	0.07	Nd.	Nd.	**0.71**	-0.30	0.02	-0.00	94.32	P3 / r1 / 1 = flogo core
38.49	**8.25**	**10.00**	Bdl.	Bdl.	**8.99**	0.10	**17.45**	Nd.	0.11	**9.67**	Nd.	Bdl.	Bdl.	Nd.	Nd.	**0.67**	-0.28	0.00	0.00	93.64	P3 / r1 / 1 = flogo core
38.64	**8.59**	**10.09**	0.09	Bdl.	**8.94**	0.11	**17.92**	Nd.	0.16	**9.75**	Nd.	Nd.	0.09	Nd.	Bdl.	**0.64**	-0.27	0.01	-0.00	94.84	P3 / r1 / 1 = flogo core
39.76	**8.37**	**10.15**	0.10	Bdl.	**6.90**	0.09	**18.00**	Bdl.	0.11	**9.81**	Nd.	Bdl.	0.09	Nd.	Bdl.	**0.76**	-0.32	0.03	-0.01	94.01	P3 / r1 / 2 = flogo rim
39.65	**8.75**	**10.08**	Bdl.	0.11	**7.09**	Bdl.	**17.81**	Bdl.	0.08	**9.78**	Nd.	Nd.	0.11	Bdl.	Bdl.	**0.64**	-0.27	0.00	0.00	94.03	P3 / r1 / 2 = flogo rim
39.35	**8.51**	**10.07**	Bdl.	0.12	**6.95**	Bdl.	**17.97**	Bdl.	0.14	**9.89**	Nd.	Bdl.	0.07	Bdl.	Bdl.	**0.76**	-0.32	0.00	0.00	93.71	P3 / r1 / 2 = flogo rim
39.77	**8.25**	**10.19**	0.17	Bdl.	**6.58**	Bdl.	**18.44**	Bdl.	0.10	**9.67**	Nd.	Nd.	0.09	Bdl.	0.00	**0.69**	-0.29	0.00	0.00	93.81	P3 / r1 / 2 = flogo core
39.74	**8.65**	**10.24**	0.18	Bdl.	**6.71**	Bdl.	**18.35**	0.09	0.11	**9.82**	Nd.	Nd.	0.11	Nd.	Bdl.	**0.67**	-0.28	0.00	-0.00	94.49	P3 / r1 / 2 = flogo core
39.17	**8.87**	**10.42**	0.12	Bdl.	**6.82**	Bdl.	**18.35**	0.11	0.13	**9.94**	Nd.	Nd.	0.12	Bdl.	0.06	**0.73**	-0.31	0.00	0.00	94.65	P3 / r1 / 2 = flogo core
39.01	**8.66**	**10.17**	0.14	Bdl.	**7.27**	Bdl.	**17.97**	0.09	0.11	**9.70**	Nd.	Nd.	0.07	Nd.	Bdl.	**0.56**	-0.23	0.01	-0.00	93.69	P3 / r1 / 3 = flogo rim
39.18	**8.86**	**10.52**	0.07	Bdl.	**7.49**	Bdl.	**17.71**	Bdl.	0.14	**9.92**	Nd.	Nd.	0.07	Nd.	Nd.	**0.63**	-0.26	0.00	0.00	94.46	P3 / r1 / 3 = flogo rim
39.68	**8.62**	**9.83**	Bdl.	Bdl.	**7.32**	0.09	**17.94**	Bdl.	0.12	**9.76**	Nd.	Nd.	0.09	Nd.	Bdl.	**0.66**	-0.28	0.01	-0.00	93.96	P3 / r1 / 3 = flogo rim
39.42	**8.77**	**10.43**	Bdl.	Bdl.	**7.63**	0.08	**17.78**	Bdl.	0.09	**9.91**	Nd.	Nd.	0.10	Bdl.	Bdl.	**0.62**	-0.26	0.00	0.00	94.71	P3 / r1 / 3 = flogo core
39.31	**8.52**	**10.23**	Bdl.	Bdl.	**7.57**	0.11	**17.82**	Nd.	0.10	**9.90**	Nd.	Nd.	0.08	Nd.	Bdl.	**0.62**	-0.26	0.00	0.00	94.15	P3 / r1 / 3 = flogo core
39.48	**8.67**	**10.19**	Bdl.	0.11	**7.47**	Bdl.	**17.95**	Nd.	0.10	**9.77**	Nd.	Nd.	0.08	Nd.	Bdl.	**0.63**	-0.27	0.03	-0.01	94.37	P3 / r1 / 3 = flogo core
50.94	5.10	0.79	0.09	0.13	8.65	0.17	15.27	2.91	6.01	4.23	Nd.	Bdl.	Nd.	Nd.	Nd.	0.70	-0.30	0.00	-0.00	94.81	P3 / r1 / 4 = amf
51.51	5.34	0.73	Nd.	Bdl.	8.29	0.26	15.92	3.30	5.85	4.48	Nd.	Bdl.	Bdl.	Nd.	Nd.	0.90	-0.38	0.00	0.00	96.45	P3 / r1 / 4 = amf
51.57	5.06	0.65	Bdl.	Bdl.	8.28	0.20	15.95	2.94	6.01	4.46	Nd.	Bdl.	Bdl.	Nd.	Bdl.	0.79	-0.33	0.01	-0.00	95.81	P3 / r1 / 4 = amf
51.62	5.36	0.70	Bdl.	0.12	8.05	0.28	16.01	3.08	5.92	4.53	Nd.	Bdl.	Bdl.	Bdl.	Nd.	0.79	-0.33	0.00	0.00	96.36	P3 / r1 / 4 = amf
52.09	5.15	0.76	Bdl.	0.13	8.10	0.26	15.75	2.91	6.04	4.34	Nd.	Nd.	0.06	Bdl.	Nd.	0.77	-0.32	0.00	0.00	96.14	P3 / r1 / 5 = amf
52.28	5.17	0.73	Bdl.	Bdl.	7.79	0.12	15.53	2.97	5.89	4.47	Nd.	Bdl.	Nd.	Nd.	Nd.	0.83	-0.35	0.01	-0.00	95.70	P3 / r1 / 5 = amf
51.84	5.33	0.57	Bdl.	0.15	8.89	0.18	14.91	2.91	5.96	4.44	Nd.	Bdl.	Bdl.	Nd.	Nd.	0.77	-0.32	0.00	0.00	95.78	P3 / r1 / 5 = amf
52.40	5.01	0.69	Nd.	0.17	7.90	0.17	15.86	2.98	6.05	4.33	Nd.	Bdl.	Bdl.	Bdl.	Bdl.	0.67	-0.28	0.00	-0.00	96.10	P3 / r1 / 5 = amf
52.75	0.72	0.29	0.10	Bdl.	5.11	0.13	16.40	21.17	0.73	Bdl.	Nd.	Bdl.	Bdl.	Bdl.	Nd.	0.03	-0.01	0.00	0.00	97.68	P3 / r1 / 6a = cpx rim
52.84	0.68	0.31	Bdl.	Nd.	5.05	0.13	16.26	21.05	0.76	Bdl.	Nd.	Bdl.	Bdl.	Bdl.	Nd.	0.01	-0.00	0.00	0.00	97.30	P3 / r1 / 6a = cpx rim

Appendix 2. Cont.

SiO2	TiO2	Al2O3	Cr2O3	V2O3	FeO	MnO	MgO	CaO	Na2O	K2O	BaO	SrO	NiO	P2O5	SO2	F	F = O	Cl	Cl = O	Total	Näyte / analyysipiste / kommentti
52.69	0.63	0.34	Bdl.	Nd.	5.67	0.27	15.38	22.05	0.59	Bdl.	Nd.	Bdl.	Nd.	Bdl.	Nd.	0.06	-0.02	0.00	-0.00	97.81	P3 / r1 / 6a = cpx rim
52.93	0.49	0.28	Nd.	Bdl.	4.97	0.16	16.94	20.76	0.50	Bdl.	Nd.	0.15	Bdl.	0.13	Nd.	0.03	-0.01	0.02	-0.00	97.43	P3 / r1 / 6b = cpx core
53.63	0.51	0.21	Bdl.	Bdl.	5.04	0.15	17.12	21.00	0.53	Bdl.	Nd.	0.15	Bdl.	Bdl.	Bdl.	0.07	-0.03	0.00	-0.00	98.59	P3 / r1 / 6b = cpx core
53.03	0.60	0.24	Nd.	Bdl.	4.98	0.15	16.85	20.52	0.48	Bdl.	Nd.	Bdl.	Nd.	Bdl.	Nd.	0.03	-0.01	0.01	-0.00	97.06	P3 / r1 / 6b = cpx core
53.01	0.57	0.22	Bdl.	Nd.	5.20	0.11	16.99	20.67	0.52	Bdl.	Bdl.	Bdl.	Bdl.	Bdl.	Nd.	0.02	-0.01	0.00	0.00	97.60	P3 / r1 / 6b = cpx core
62.42	Bdl.	**16.32**	Nd.	Bdl.	**1.10**	Nd.	Nd.	Bdl.	**0.36**	**15.97**	Bdl.	Nd.	Nd.	Bdl.	Bdl.	0.01	-0.01	0.00	-0.00	96.40	P3 / r1 / 7 = kms
63.01	0.00	**16.26**	Nd.	Nd.	**1.02**	Nd.	Nd.	Bdl.	**0.30**	**15.72**	Bdl.	Nd.	Nd.	Bdl.	Bdl.	0.09	-0.04	0.00	0.00	96.46	P3 / r1 / 7 = kms
62.48	Bdl.	**16.31**	Nd.	Bdl.	**1.17**	Nd.	0.02	Bdl.	**0.33**	**15.85**	Bdl.	Nd.	Nd.	Bdl.	Nd.	0.00	-0.00	0.01	-0.00	96.48	P3 / r1 / 7 = kms
62.70	Bdl.	**16.10**	Bdl.	Bdl.	**1.14**	Bdl.	0.00	Bdl.	**0.30**	**15.59**	Bdl.	Nd.	Bdl.	Bdl.	0.02	0.01	-0.00	0.01	-0.00	96.23	P3 / r1 / 7 = kms
0.28	**95.00**	Nd.	Bdl.	**0.64**	0.32	Nd.	Nd.	0.10	Nd.	0.07	0.00	Bdl.	Nd.	Nd.	Nd.	0.00	0.00	0.01	-0.00	96.50	P3 / r1 / 8 = Ti-oksidi = rutiili
0.10	**95.75**	Nd.	Nd.	**0.58**	0.00	Bdl.	Nd.	0.14	Nd.	Nd.	Nd.	Nd.	Nd.	Bdl.	Bdl.	0.07	-0.03	0.01	-0.00	96.72	P3 / r1 / 8 = Ti-oksidi = rutiili
0.15	**95.92**	Nd.	Bdl.	**0.59**	Bdl.	Nd.	Nd.	0.12	Nd.	Bdl.	Nd.	Nd.	Nd.	Nd.	Bdl.	0.05	-0.02	0.00	0.00	96.94	P3 / r1 / 8 = Ti-oksidi = rutiili
0.20	**96.17**	0.00	Bdl.	**0.60**	0.11	Nd.	Nd.	0.32	Nd.	Bdl.	Nd.	Nd.	Bdl.	Bdl.	Nd.	0.04	-0.01	0.02	-0.00	97.53	P3 / r1 / 8 = Ti-oksidi = rutiili
39.61	8.78	10.75	Bdl.	Bdl.	6.49	Bdl.	18.84	0.07	0.10	**9.68**	Nd.	Nd.	0.13	Nd.	Bdl.	0.66	-0.28	0.03	-0.01	95.06	P3 / r2 / 1a = flogo rim
39.80	8.79	10.52	0.07	Bdl.	6.52	Bdl.	18.56	Bdl.	0.10	**10.00**	Nd.	Nd.	0.09	Nd.	Bdl.	0.71	-0.30	0.01	-0.00	95.07	P3 / r2 / 1a = flogo rim
39.21	8.66	10.67	0.08	Bdl.	6.38	Bdl.	18.65	Bdl.	0.13	**10.02**	Nd.	Nd.	0.09	Nd.	0.07	0.73	-0.31	0.00	-0.00	94.47	P3 / r2 / 1a = flogo rim
39.75	8.19	10.22	0.17	Bdl.	6.21	Nd.	18.63	Bdl.	0.13	**10.07**	Nd.	Nd.	0.12	Nd.	0.06	0.76	-0.32	0.00	-0.00	94.06	P3 / r2 / 1b = flogo core
39.80	8.16	10.35	0.11	Bdl.	6.12	Bdl.	18.91	Bdl.	0.10	**10.23**	Nd.	Nd.	0.11	Bdl.	Bdl.	0.83	-0.35	0.01	-0.00	94.56	P3 / r2 / 1b = flogo core
40.12	8.02	10.15	0.16	0.12	6.48	Nd.	19.05	Bdl.	0.14	**10.15**	Nd.	Nd.	0.09	Bdl.	Bdl.	0.84	-0.35	0.02	-0.00	95.10	P3 / r2 / 1b = flogo core
38.51	8.61	10.64	0.07	Bdl.	7.34	Bdl.	17.47	Bdl.	0.14	**9.88**	Nd.	Nd.	0.09	Bdl.	Bdl.	0.60	-0.25	0.02	-0.00	93.31	P3 / r2 / 2 = flogo
38.03	8.75	10.51	0.10	Bdl.	7.53	Nd.	17.52	Bdl.	0.15	**9.75**	Nd.	Nd.	0.08	Bdl.	Bdl.	0.58	-0.24	0.00	-0.00	92.89	P3 / r2 / 2 = flogo
38.45	8.58	10.83	0.08	Bdl.	7.81	Nd.	17.75	Nd.	0.15	**9.78**	Nd.	Nd.	0.08	Nd.	Bdl.	0.71	-0.30	0.01	-0.00	94.04	P3 / r2 / 2 = flogo
38.95	8.32	10.51	Bdl.	Bdl.	7.38	Bdl.	17.92	Bdl.	0.14	**9.81**	Nd.	Nd.	0.10	Bdl.	Bdl.	0.75	-0.32	0.01	-0.00	93.75	P3 / r2 / 2 = flogo
53.71	0.72	0.50	Bdl.	Bdl.	5.03	0.11	17.38	20.20	0.62	Bdl.	Nd.	Nd.	Nd.	Nd.	Nd.	0.03	-0.01	0.00	0.00	98.39	P3 / r2 / 3 = cpx
53.20	0.79	0.50	Bdl.	Bdl.	4.97	0.14	17.41	20.47	0.59	Bdl.	Nd.	0.20	Nd.	Bdl.	Nd.	0.02	-0.01	0.00	0.00	98.42	P3 / r2 / 3 = cpx
53.20	0.63	0.46	Nd.	Nd.	4.95	0.11	17.36	20.38	0.58	Bdl.	Nd.	0.16	Bdl.	Bdl.	Bdl.	0.00	0.00	0.01	-0.00	98.02	P3 / r2 / 3 = cpx
53.23	**1.04**	Bdl.	Bdl.	Bdl.	**25.68**	0.15	**2.00**	**0.46**	**13.19**	**0.36**	Nd.	Nd.	Nd.	Bdl.	Nd.	0.13	-0.06	0.00	-0.00	96.36	13X-07 / r1 / 2 = "Al2O3" = Fe-Na-silikaatti-sälö (onko egiriini?)
52.85	**0.98**	Bdl.	Bdl.	Bdl.	**25.92**	0.07	**1.74**	**0.48**	**13.37**	**0.37**	Nd.	Nd.	Bdl.	Bdl.	Bdl.	0.16	-0.07	0.01	-0.00	96.04	13X-07 / r1 / 2 = "Al2O3" = Fe-Na-silikaatti-sälö (onko egiriini?)
53.30	**0.95**	Bdl.	Bdl.	Bdl.	**25.36**	0.11	**2.30**	**0.54**	**12.80**	**0.40**	Nd.	Bdl.	Nd.	Bdl.	Nd.	0.08	-0.03	0.00	-0.00	95.98	13X-07 / r1 / 2 = "Al2O3" = Fe-Na-silikaatti-sälö (onko egiriini?)
52.96	**1.08**	Bdl.	Nd.	Bdl.	**26.20**	Bdl.	1.72	**0.43**	**13.29**	**0.34**	Nd.	Bdl.	Nd.	Bdl.	Bdl.	0.13	-0.06	0.00	0.00	96.34	13X-07 / r1 / 2 = "Al2O3" = Fe-Na-silikaatti-sälö (onko egiriini?)
Nd.	**98.26**	Nd.	Nd.	**0.76**	0.37	Bdl.	Nd.	Bdl.	Nd.	Nd.	Nd.	Nd.	Nd.	Nd.	Nd.	0.14	-0.06	0.00	0.00	99.53	13X-07 / r1 / 3 = rutiili
Bdl.	**97.37**	Nd.	Nd.	**0.81**	0.36	Bdl.	Nd.	Bdl.	Nd.	Nd.	Nd.	Nd.	Bdl.	Nd.	Bdl.	0.02	-0.01	0.00	0.00	98.71	13X-07 / r1 / 3 = rutiili

Appendix 2. Cont.

SiO2	TiO2	Al2O3	Cr2O3	V2O3	FeO	MnO	MgO	CaO	Na2O	K2O	BaO	SrO	NiO	P2O5	SO2	F	F = O	Cl	Cl = O	Total	Näyte / analyysipiste / kommentti
Bdl.	**97.27**	0.01	0.07	**0.81**	0.29	Bdl.	Bdl.	Bdl.	Nd.	Bdl.	Nd.	Bdl.	Bdl.	Bdl.	Nd.	0.11	-0.05	0.00	0.00	98.63	13X-07 / r1 / 3 = rutiili
Nd.	**97.64**	Nd.	Bdl.	**0.73**	0.33	Nd.	Nd.	Nd.	Nd.	Bdl.	Nd.	Nd.	Bdl.	Nd.	Nd.	0.08	-0.03	0.00	0.00	98.81	13X-07 / r1 / 3 = rutiili
Nd.	**97.65**	Nd.	Bdl.	**0.85**	0.25	Nd.	Nd.	Bdl.	Nd.	Nd.	Nd.	Nd.	Bdl.	Nd.	Nd.	0.12	-0.05	0.00	0.00	98.92	13X-07 / r1 / 4 = rutiili
Nd.	**98.59**	Nd.	Bdl.	**0.89**	0.29	Nd.	Bdl.	Bdl.	Nd.	Nd.	Nd.	Bdl.	Nd.	Nd.	Nd.	0.08	-0.03	0.01	-0.00	99.91	13X-07 / r1 / 4 = rutiili
Nd.	**97.42**	Nd.	Nd.	**0.73**	0.33	Bdl.	Bdl.	Bdl.	Nd.	Nd.	Nd.	Nd.	Nd.	Nd.	Bdl.	0.09	-0.04	0.00	0.00	98.63	13X-07 / r1 / 4 = rutiili
0.01	**97.83**	Nd.	0.07	**0.77**	0.28	Bdl.	Bdl.	Bdl.	Nd.	0.00	Nd.	Bdl.	Nd.	Nd.	Bdl.	0.15	-0.06	0.00	0.00	99.18	13X-07 / r1 / 4 = rutiili
39.34	0.18	**21.19**	0.00	0.08	**21.46**	**2.75**	**9.15**	**6.02**	0.00	0.01	0.00	0.00	0.00	0.00	0.00	0.06	-0.03	0.01	-0.00	100.23	~~13X-07 / r1 / 5 = granaatti~~
39.16	0.27	**21.39**	Bdl.	Bdl.	**21.59**	**2.61**	**9.07**	**5.97**	0.00	Nd.	Nd.	Nd.	Bdl.	Nd.	Nd.	0.11	-0.05	0.00	0.00	100.17	13X-07 / r1 / 5 = granaatti
38.92	0.20	**21.18**	Nd.	Bdl.	**21.50**	**2.72**	**9.27**	**5.92**	0.00	Bdl.	Nd.	Nd.	Bdl.	Bdl.	Nd.	0.07	-0.03	0.00	0.00	99.83	13X-07 / r1 / 5 = granaatti
~~38.63~~	~~0.08~~	~~**20.92**~~	~~0.00~~	~~0.00~~	~~**21.26**~~	~~**2.61**~~	~~**8.86**~~	~~**5.99**~~	~~0.00~~	~~0.02~~	Nd.	~~0.06~~	~~0.00~~	~~0.03~~	0.03	0.13	-0.05	0.00	0.00	98.57	~~13X-07 / r1 / 5 = granaatti~~
39.09	0.19	**21.00**	Bdl.	Nd.	**21.61**	**2.65**	**9.20**	**5.96**	0.00	0.00	Nd.	Bdl.	Nd.	Bdl.	Nd.	0.09	-0.04	0.00	0.00	99.88	13X-07 / r1 / 6 = granaatti
38.46	0.16	**21.34**	Bdl.	0.01	**21.47**	**2.66**	**9.03**	**5.97**	0.00	Bdl.	Nd.	Nd.	Bdl.	Bdl.	Nd.	0.00	0.00	0.00	0.00	99.20	13X-07 / r1 / 6 = granaatti
38.69	0.21	**21.25**	Nd.	Nd.	**21.64**	**2.53**	**9.04**	**6.04**	0.00	Bdl.	Nd.	Nd.	Nd.	Bdl.	Bdl.	0.07	-0.03	0.00	0.00	99.53	13X-07 / r1 / 6 = granaatti
39.07	Bdl.	**21.28**	Nd.	Nd.	**21.61**	**2.61**	**8.99**	**6.06**	0.00	Nd.	Nd.	Nd.	Nd.	Bdl.	Nd.	0.04	-0.02	0.00	0.00	99.76	13X-07 / r1 / 6 = granaatti
64.95	Bdl.	16.42	Nd.	Nd.	0.58	Bdl.	0.11	Bdl.	0.19	15.86	Bdl.	Nd.	Nd.	Nd.	Bdl.	0.04	-0.02	0.04	-0.01	98.33	13X-07 / r1 / 7 = kms
60.08	Bdl.	20.70	Bdl.	Nd.	0.26	Bdl.	Bdl.	2.35	1.16	12.53	0.34	0.18	Nd.	Nd.	Nd.	0.00	0.00	0.03	-0.01	97.85	13X-07 / r1 / 7 = kms
60.18	Nd.	20.87	Nd.	Nd.	0.33	0.00	Bdl.	2.10	1.33	12.21	0.38	Bdl.	Nd.	Bdl.	Bdl.	0.00	0.00	0.00	0.00	97.65	13X-07 / r1 / 7 = kms
62.09	Nd.	22.22	Bdl.	0.02	0.20	Bdl.	Nd.	**4.55**	**7.19**	**2.55**	Bdl.	Bdl.	Bdl.	Bdl.	Nd.	0.00	0.00	0.00	-0.00	99.12	13X-07 / r1 / 8 = "albiitti" = plagioklaasi
61.80	Bdl.	22.02	Nd.	Nd.	0.17	Nd.	Nd.	**4.86**	**7.49**	**2.35**	Bdl.	0.26	Nd.	Bdl.	Bdl.	0.02	-0.01	0.00	-0.00	99.19	13X-07 / r1 / 8 = "albiitti" = plagioklaasi
61.74	Bdl.	22.16	Bdl.	0.02	0.17	Nd.	Bdl.	**4.87**	**7.45**	**2.34**	Bdl.	Bdl.	Nd.	Bdl.	Nd.	0.07	-0.03	0.00	0.00	99.03	13X-07 / r1 / 8 = "albiitti" = plagioklaasi
61.75	Bdl.	22.06	Nd.	Nd.	0.15	Nd.	Bdl.	**5.03**	**7.50**	**2.32**	0.20	Bdl.	Nd.	Bdl.	Nd.	0.00	-0.00	0.01	-0.00	99.22	13X-07 / r1 / 8 = "albiitti" = plagioklaasi
27.35	**15.39**	0.49	Nd.	0.18	**18.39**	0.59	1.11	30.87	0.33	Nd.	Nd.	Nd.	Nd.	Bdl.	Bdl.	0.14	-0.06	0.00	0.00	94.86	Xe15B / r1 / 3a = granaatti core
27.49	**15.54**	0.59	Bdl.	Bdl.	**18.35**	0.61	1.12	30.55	0.37	Bdl.	Nd.	Nd.	Nd.	Nd.	Bdl.	0.02	-0.01	0.02	-0.00	94.80	Xe15B / r1 / 3a = granaatti core
27.19	**15.19**	0.57	Nd.	0.21	**18.12**	0.56	1.24	**30.82**	0.37	Nd.	Nd.	Nd.	Nd.	Bdl.	Nd.	0.10	-0.04	0.00	0.00	94.38	Xe15B / r1 / 3a = granaatti core
27.07	**15.21**	0.57	Bdl.	0.23	**18.33**	0.50	1.15	**30.72**	0.38	Nd.	Nd.	Nd.	Nd.	Bdl.	Nd.	0.07	-0.03	0.00	0.00	94.26	Xe15B / r1 / 3a = granaatti core
27.04	**15.55**	0.53	Bdl.	0.25	**18.06**	0.61	1.12	**30.88**	0.33	Nd.	Nd.	Bdl.	Nd.	Bdl.	Bdl.	0.15	-0.06	0.00	0.00	94.58	Xe15B / r1 / 3a = granaatti core
26.80	**15.44**	0.52	Nd.	0.18	**17.96**	0.54	1.09	**30.51**	0.30	Nd.	Nd.	Nd.	Nd.	Nd.	Nd.	0.06	-0.03	0.01	-0.00	93.39	Xe15B / r1 / 3a = granaatti core
34.74	2.98	**2.74**	Nd.	0.15	**21.97**	0.18	0.63	**33.63**	0.00	Bdl.	Nd.	Nd.	Nd.	Bdl.	Nd.	0.12	-0.05	0.00	0.00	97.15	Xe15B / r1 / 3b = granaatti rim
34.56	3.06	**2.57**	Bdl.	0.19	**21.76**	0.14	0.65	**33.79**	0.00	Nd.	Nd.	Nd.	Nd.	Bdl.	Nd.	0.07	-0.03	0.01	-0.00	96.89	Xe15B / r1 / 3b = granaatti rim
34.41	3.31	**2.38**	Nd.	0.17	**22.43**	0.15	0.58	**33.50**	Nd.	Nd.	Nd.	Bdl.	Nd.	Bdl.	Nd.	0.06	-0.03	0.00	0.00	97.06	Xe15B / r1 / 3b = granaatti rim
34.47	3.11	**2.60**	Bdl.	0.22	**22.13**	0.21	0.58	**33.56**	Nd.	Nd.	Nd.	Bdl.	Bdl.	Bdl.	Bdl.	0.14	-0.06	0.00	0.00	97.06	Xe15B / r1 / 3b = granaatti rim

Appendix 2. Cont.

SiO2	TiO2	Al2O3	Cr2O3	V2O3	FeO	MnO	MgO	CaO	Na2O	K2O	BaO	SrO	NiO	P2O5	SO2	F	F = O	Cl	Cl = O	Total	Näyte / analyysipiste / kommentti
1.39	Bdl.	Nd.	Nd.	Nd.	0.19	Nd.	Bdl.	53.89	0.10	Bdl.	Nd.	1.73	Nd.	**39.87**	0.14	**1.98**	-0.83	0.07	-0.02	**98.65**	Xe15B / r1 / 3 = granaatin sulkeuma = apatiitti (Si, F, Sr)
1.41	Bdl.	Bdl.	Nd.	Bdl.	0.21	Nd.	Bdl.	53.75	0.09	Bdl.	Bdl.	1.70	Nd.	**40.28**	0.09	**2.16**	-0.91	0.05	-0.01	**98.95**	Xe15B / r1 / 3 = granaatin sulkeuma = apatiitti (Si, F, Sr)
1.49	Nd.	0.01	Nd.	Bdl.	0.19	Bdl.	0.09	53.66	0.15	Bdl.	Nd.	1.50	Nd.	**39.90**	0.16	**1.81**	-0.76	0.08	-0.02	**98.36**	Xe15B / r1 / 3 = granaatin sulkeuma = apatiitti (Si, F, Sr)
1.39	Bdl.	Nd.	Bdl.	Bdl.	0.15	Bdl.	0.11	53.85	0.12	Bdl.	Nd.	1.59	Nd.	**39.92**	0.11	**1.87**	-0.79	0.06	-0.01	**98.59**	Xe15B / r1 / 3 = granaatin sulkeuma = apatiitti (Si, F, Sr)
27.49	**13.54**	**6.38**	Bdl.	Bdl.	**14.95**	Bdl.	0.76	**32.66**	0.00	Bdl.	Nd.	Nd.	Bdl.	Bdl.	Bdl.	0.11	-0.04	0.00	-0.00	96.16	Xe15B / r2 / 1 = ‘granaatti core
27.15	**13.55**	**6.19**	Bdl.	0.14	**14.88**	0.12	0.74	**32.29**	Bdl.	Bdl.	Nd.	Nd.	Bdl.	Bdl.	Bdl.	0.12	-0.05	0.00	0.00	95.29	Xe15B / r2 / 1 = ‘granaatti core
27.57	13.18	6.52	Bdl.	0.25	**15.13**	0.14	0.69	**32.37**	Bdl.	Bdl.	Nd.	Bdl.	Nd.	Bdl.	Bdl.	0.16	-0.07	0.02	-0.00	96.05	Xe15B / r2 / 1 = ‘granaatti core
27.70	**13.34**	**6.22**	Bdl.	Bdl.	**15.01**	0.11	0.64	**32.37**	Bdl.	Nd.	Nd.	Bdl.	Nd.	Bdl.	Nd.	0.19	-0.08	0.00	0.00	95.73	Xe15B / r2 / 1 = ‘granaatti core
26.77	13.53	5.49	Nd.	0.18	17.19	0.15	0.59	32.07	Nd.	Nd.	Nd.	Nd.	Nd.	Bdl.	Nd.	0.00	0.00	0.00	0.00	96.06	Xe15B / r2 / 1 = ‘granaatti core
26.74	13.60	5.38	Nd.	0.20	17.02	0.15	0.59	32.34	Nd.	Nd.	Nd.	Bdl.	Bdl.	Bdl.	Bdl.	0.10	-0.04	0.01	-0.00	96.21	Xe15B / r2 / 1 = ‘granaatti core
27.66	13.32	6.48	Nd.	0.17	14.71	0.19	0.71	32.31	Nd.	Nd.	Nd.	Nd.	Bdl.	Bdl.	Nd.	0.15	-0.07	0.00	0.00	95.71	Xe15B / r2 / 1 = ‘granaatti core
27.69	13.59	6.27	Bdl.	0.13	15.02	0.14	0.67	31.97	Nd.	Bdl.	Nd.	Bdl.	0.06	Bdl.	Nd.	0.12	-0.05	0.00	0.00	95.74	Xe15B / r2 / 1 = ‘granaatti core
37.09	0.53	8.02	Nd.	Nd.	17.18	Bdl.	0.20	34.75	Nd.	Nd.	Bdl.	Bdl.	Nd.	Bdl.	Nd.	0.04	-0.02	0.00	0.00	97.89	Xe15B / r2 / 2 = granaatti rim (hydrougrandiitti mahdollisesti)
36.79	0.50	7.52	Nd.	Bdl.	17.30	Bdl.	0.32	34.64	Nd.	Nd.	Nd.	Nd.	Bdl.	Bdl.	Bdl.	0.14	-0.06	0.00	0.00	97.40	Xe15B / r2 / 2 = granaatti rim (hydrougrandiitti mahdollisesti)
36.57	0.64	7.26	Nd.	Bdl.	17.80	0.10	0.35	34.81	Nd.	Nd.	Nd.	Nd.	Bdl.	Bdl.	Bdl.	0.12	-0.05	0.00	0.00	97.78	Xe15B / r2 / 2 = granaatti rim (hydrougrandiitti mahdollisesti)
36.32	0.64	7.59	Bdl.	Nd.	17.35	Bdl.	0.31	**34.69**	Nd.	Bdl.	Nd.	Nd.	Bdl.	Bdl.	Bdl.	0.15	-0.06	0.00	0.00	97.19	Xe15B / r2 / 2 = granaatti rim (hydrougrandiitti mahdollisesti)
36.92	0.41	8.28	Nd.	Nd.	16.54	0.11	0.24	**34.84**	Nd.	Nd.	Nd.	Bdl.	Bdl.	Nd.	Nd.	0.08	-0.03	0.00	0.00	97.43	Xe15B / r2 / 2 = granaatti rim (hydrougrandiitti mahdollisesti)
36.77	0.35	7.72	Nd.	Bdl.	17.38	Bdl.	0.26	**34.67**	Nd.	Bdl.	Nd.	Bdl.	Nd.	Bdl.	Bdl.	0.13	-0.05	0.01	-0.00	97.46	Xe15B / r2 / 2 = granaatti rim (hydrougrandiitti mahdollisesti)
36.52	0.26	7.56	Nd.	Bdl.	17.15	0.09	0.26	**34.74**	Nd.	Bdl.	Nd.	Bdl.	Nd.	Bdl.	Nd.	0.14	-0.06	0.00	0.00	96.86	Xe15B / r2 / 2 = granaatti rim (hydrougrandiitti mahdollisesti)
36.52	Bdl.	16.83	Bdl.	Bdl.	5.16	0.35	22.83	0.09	Bdl.	**9.36**	2.83	Nd.	Bdl.	Nd.	Bdl.	0.34	-0.14	0.00	0.00	94.29	Xe15B / r2 / 3a = kiille
36.44	Bdl.	16.54	Nd.	Nd.	5.42	0.40	22.55	0.08	Nd.	**9.42**	2.70	Nd.	Bdl.	Nd.	Nd.	0.36	-0.15	0.00	-0.00	93.80	Xe15B / r2 / 3a = kiille
36.95	Bdl.	16.55	Nd.	Nd.	5.13	0.52	22.81	0.08	Nd.	**9.10**	2.74	Nd.	Bdl.	Nd.	Nd.	0.37	-0.16	0.00	0.00	94.14	Xe15B / r2 / 3a = kiille
37.54	1.11	13.52	Nd.	Bdl.	10.89	0.25	19.80	0.08	Bdl.	**9.68**	0.61	Nd.	Bdl.	Nd.	Bdl.	0.39	-0.17	0.01	-0.00	93.83	Xe15B / r2 / 3b = kiille
37.37	0.93	13.56	Nd.	Bdl.	10.87	0.19	19.72	0.12	Bdl.	**9.80**	0.56	Nd.	Bdl.	Nd.	Nd.	0.41	-0.17	0.01	-0.00	93.48	Xe15B / r2 / 3b = kiille
37.83	0.95	13.55	Nd.	Bdl.	10.95	0.26	19.97	0.12	0.00	**9.85**	0.60	Nd.	Bdl.	Nd.	Nd.	0.41	-0.17	0.00	-0.00	94.37	Xe15B / r2 / 3b = kiille
37.50	1.16	13.48	Nd.	Nd.	11.33	0.23	19.72	0.09	Bdl.	**9.47**	0.64	Nd.	Bdl.	Bdl.	Bdl.	0.40	-0.17	0.00	-0.00	93.94	Xe15B / r2 / 3b = kiille
50.86	0.52	4.67	Bdl.	Bdl.	11.68	0.23	11.67	18.27	1.62	Nd.	Nd.	Bdl.	Nd.	Bdl.	Bdl.	0.09	-0.04	0.00	0.00	99.79	Xe16 / r1 / 1 = cpx

Appendix 2. Cont.

SiO2	TiO2	Al2O3	Cr2O3	V2O3	FeO	MnO	MgO	CaO	Na2O	K2O	BaO	SrO	NiO	P2O5	SO2	F	F = O	Cl	Cl = O	Total	Näyte / analyysipiste / kommentti
50.79	0.49	4.61	Bdl.	Bdl.	11.90	0.21	11.76	18.01	1.62	Nd.	Nd.	Bdl.	Bdl.	Bdl.	Nd.	0.12	-0.05	0.00	0.00	99.64	Xe16 / r1 / 1 = cpx
50.37	0.56	4.71	Bdl.	Bdl.	12.02	0.20	11.78	18.14	1.62	Bdl.	Nd.	Bdl.	Bdl.	Nd.	Bdl.	0.02	-0.01	0.00	-0.00	99.77	Xe16 / r1 / 2 = cpx
0.12	Nd.	Bdl.	Nd.	Bdl.	0.50	Bdl.	0.32	54.09	0.29	Nd.	**Nd.**	0.22	**Nd.**	**42.19**	**0.34**	**2.42**	-1.02	0.80	-0.18	**100.18**	Xe16 / r1 / 3 = apatiitti
0.12	Nd.	Nd.	Bdl.	Nd.	0.50	0.09	0.32	54.01	0.36	**Nd.**	**Nd.**	0.27	**Nd.**	**42.26**	**0.35**	**2.44**	-1.03	0.77	-0.17	**100.30**	Xe16 / r1 / 3 = apatiitti
0.13	Nd.	Nd.	**Nd.**	**Bdl.**	0.58	**Bdl.**	0.24	53.53	0.36	**Bdl.**	**Nd.**	0.24	**Nd.**	**41.90**	**0.39**	**2.25**	-0.95	0.63	-0.14	**99.24**	Xe16 / r1 / 3 = apatiitti
40.79	3.24	11.58	Bdl.	Bdl.	15.31	0.13	10.88	9.79	2.54	1.51	Nd.	Bdl.	Bdl.	Bdl.	0.07	0.49	-0.21	0.22	-0.05	96.57	Xe16 / r1 / 4 = amfiboli
41.22	3.03	11.78	Nd.	Bdl.	15.41	0.20	11.03	9.90	2.55	1.60	Nd.	Bdl.	Nd.	Nd.	0.08	0.52	-0.22	0.21	-0.05	97.41	Xe16 / r1 / 4 = amfiboli
41.04	3.26	11.82	Bdl.	Bdl.	15.63	Bdl.	10.98	9.90	2.50	1.51	Nd.	Bdl.	Bdl.	Nd.	Bdl.	0.45	-0.19	0.22	-0.05	97.27	Xe16 / r1 / 4 = amfiboli
Bdl.	25.69	1.63	0.08	0.52	64.20	0.11	0.36	Bdl.	Nd.	Nd.	Nd.	Nd.	Bdl.	Nd.	Bdl.	0.14	-0.06	0.00	-0.00	92.75	Xe16 / r1 / 5a = "mgt" = Fe-Ti-Ox
Bdl.	26.76	2.24	0.11	0.40	63.17	0.13	Nd.	Bdl.	Nd.	Nd.	Nd.	Bdl.	Bdl.	Nd.	Nd.	0.14	-0.06	0.00	0.00	93.08	Xe16 / r1 / 5a = "mgt" = Fe-Ti-Ox
0.25	26.31	2.48	Bdl.	0.35	63.15	0.16	0.11	Bdl.	Bdl.	0.06	Nd.	Bdl.	Nd.	Nd.	Nd.	0.20	-0.09	0.00	0.00	93.08	Xe16 / r1 / 5a = "mgt" = Fe-Ti-Ox
Bdl.	24.67	2.68	Bdl.	0.40	64.16	0.16	Nd.	Bdl.	Nd.	Bdl.	Nd.	Nd.	Nd.	Nd.	Nd.	0.13	-0.05	0.00	0.00	92.28	Xe16 / r1 / 5a = "mgt" = Fe-Ti-Ox
0.13	51.04	Nd.	Nd.	0.38	41.91	**3.29**	**Bdl.**	Nd.	Nd.	**Bdl.**	Nd.	Nd.	Nd.	Nd.	Bdl.	0.10	-0.04	0.00	0.00	96.90	Xe16 / r1 / 5b = Ti-Fe-Ox-lam edellisessä
0.20	51.36	Nd.	Bdl.	0.26	42.07	**3.25**	Bdl.	Bdl.	Nd.	Bdl.	Nd.	Nd.	Bdl.	Nd.	Nd.	0.09	-0.04	0.00	0.00	97.30	Xe16 / r1 / 5b = Ti-Fe-Ox-lam edellisessä
Nd.	52.38	Nd.	Nd.	0.36	42.46	**3.31**	**Bdl.**	Nd.	Nd.	Nd.	Nd.	Bdl.	Nd.	Nd.	Bdl.	0.12	-0.05	0.00	-0.00	98.66	Xe16 / r1 / 5b = Ti-Fe-Ox-lam edellisessä
61.92	Nd.	21.95	Bdl.	0.04	**0.20**	Bdl.	Bdl.	**4.49**	**8.14**	**1.53**	0.28	0.34	Bdl.	Bdl.	Nd.	0.09	-0.04	0.01	-0.00	99.01	Xe16 / r1 / 6 = plagioklaasi (K2O-pitoinen)
62.30	Nd.	22.07	Bdl.	Nd.	**0.21**	Nd.	Bdl.	**4.52**	**8.06**	**1.56**	0.26	0.29	Nd.	Bdl.	Nd.	0.03	-0.01	0.02	-0.00	99.38	Xe16 / r1 / 6 = plagioklaasi (K2O-pitoinen)
62.18	Nd.	22.08	Nd.	Bdl.	**0.22**	Nd.	Nd.	**4.58**	**8.08**	**1.50**	0.24	0.25	0.01	Nd.	Nd.	0.02	-0.01	0.01	-0.00	99.19	Xe16 / r1 / 6 = plagioklaasi (K2O-pitoinen)
62.43	Nd.	22.31	Nd.	Bdl.	**0.22**	Bdl.	Nd.	**4.43**	**7.74**	**1.60**	0.26	0.25	Nd.	Bdl.	Nd.	0.03	-0.01	0.00	-0.00	99.34	Xe16 / r1 / 6 = plagioklaasi (K2O-pitoinen)
39.07	Bdl.	21.22	Nd.	Bdl.	23.59	0.82	9.04	6.23	Nd.	Bdl.	Nd.	Bdl.	Nd.	Nd.	Nd.	0.02	-0.01	0.00	0.00	100.19	Xe16 / r2 / 1 = granaatti
39.25	**0.13**	21.11	Nd.	**Bdl.**	23.36	0.81	9.12	6.19	Nd.	**Nd.**	**Nd.**	**Bdl.**	Nd.	**Bdl.**	Nd.	0.07	-0.03	0.01	-0.00	100.13	Xe16 / r2 / 1 = granaatti
39.28	**0.14**	21.27	Bdl.	Nd.	23.57	0.95	8.77	6.35	Nd.	**Nd.**	**Nd.**	**Bdl.**	**Bdl.**	**Bdl.**	Nd.	0.04	-0.02	0.00	-0.00	100.45	Xe16 / r2 / 2 = granaatti
39.31	**0.06**	20.86	Bdl.	Nd.	23.43	0.90	8.98	6.18	Nd.	**Nd.**	Nd.	Nd.	Nd.	Bdl.	Nd.	0.09	-0.04	0.00	0.00	99.84	Xe16 / r2 / 2 = granaatti
39.06	**0.12**	21.41	Nd.	Nd.	23.58	0.89	9.18	6.19	Nd.	Bdl.	Nd.	Bdl.	Nd.	Bdl.	Bdl.	0.10	-0.04	0.01	-0.00	100.66	Xe16 / r2 / 2 = granaatti
38.99	**0.12**	21.18	Bdl.	Bdl.	23.52	0.89	9.08	6.21	Nd.	Nd.	Bdl.	Bdl.	Nd.	Bdl.	Nd.	0.09	-0.04	0.00	0.00	100.18	Xe16 / r2 / 3 = granaatti
39.52	**0.12**	21.12	Nd.	**Bdl.**	23.66	0.90	9.00	6.23	Nd.	**Nd.**	**Nd.**	**Nd.**	**Bdl.**	**Bdl.**	**Bdl.**	0.05	-0.02	0.00	0.00	100.63	Xe16 / r2 / 3 = granaatti
39.27	Bdl.	21.14	Bdl.	Bdl.	23.22	0.88	8.87	6.26	Nd.	Nd.	Nd.	Nd.	0.01	Bdl.	Nd.	0.00	0.00	0.00	0.00	99.87	Xe16 / r2 / 3 = granaatti
0.13	Nd.	Nd.	Nd.	Bdl.	0.69	Bdl.	0.36	54.28	0.29	Bdl.	**Nd.**	0.24	**Nd.**	**42.38**	0.30	**2.64**	-1.11	0.80	-0.18	**100.86**	Xe16 / r2 / 4 = apatiitti
Bdl.	Bdl.	Bdl.	Nd.	Bdl.	0.51	0.12	0.35	54.41	0.30	**Nd.**	**Nd.**	0.20	**Bdl.**	**42.38**	0.25	**2.59**	-1.09	0.85	-0.19	**100.92**	Xe16 / r2 / 4 = apatiitti

Appendix 2. Cont.

SiO2	TiO2	Al2O3	Cr2O3	V2O3	FeO	MnO	MgO	CaO	Na2O	K2O	BaO	SrO	NiO	P2O5	SO2	F	F = O	Cl	Cl = O	Total	Näyte / analyysipiste / kommentti
62.45	Bdl.	**22.11**	Nd.	Nd.	0.19	Nd.	Bdl.	**4.53**	**8.08**	**1.67**	**0.27**	0.28	Nd.	Nd.	Nd.	0.01	-0.00	0.00	0.00	99.65	Xe16 / r2 / 5 = plagioklaasi (K2O-pitoinen)
61.76	Nd.	**22.60**	Bdl.	0.04	0.15	Bdl.	Nd.	**4.44**	**8.15**	**1.66**	**0.32**	0.33	Nd.	Bdl.	Nd.	0.04	-0.02	0.00	0.00	99.61	Xe16 / r2 / 5 = plagioklaasi (K2O-pitoinen)
62.17	Bdl.	**22.15**	Nd.	Bdl.	0.19	Bdl.	Bdl.	**4.54**	**8.10**	**1.61**	**0.26**	0.21	Nd.	Bdl.	Nd.	0.02	-0.01	0.00	0.00	99.36	Xe16 / r2 / 5 = plagioklaasi (K2O-pitoinen)
Nd.	28.04	1.89	0.07	0.45	60.35	0.25	1.45	Nd.	Nd.	Nd.	Nd.	Nd.	Nd.	Nd.	Bdl.	0.19	-0.08	0.00	-0.00	92.62	Xe16 / r2 / 6a = "mgt" = Fe-Ti-Ox
Bdl.	27.84	1.82	Bdl.	0.45	60.56	0.30	1.48	Bdl.	Nd.	Bdl.	Nd.	Bdl.	Bdl.	Bdl.	Nd.	0.12	-0.05	0.00	0.00	92.72	Xe16 / r2 / 6a = "mgt" = Fe-Ti-Ox
Nd.	28.78	1.72	0.09	0.55	59.64	0.20	1.56	Nd.	Nd.	Bdl.	Nd.	Bdl.	Nd.	Bdl.	Nd.	0.08	-0.04	0.00	0.00	92.66	Xe16 / r2 / 6a = "mgt" = Fe-Ti-Ox
Nd.	**51.04**	Nd.	Bdl.	0.33	**42.58**	**3.93**	0.16	Nd.	Nd.	Bdl.	Nd.	Nd.	Nd.	Nd.	Bdl.	0.04	-0.02	0.01	-0.00	98.11	Xe16 / r2 / 6b = Ti-Fe-Ox-lam. edellisessä
Bdl.	**50.83**	Nd.	Nd.	0.41	**42.44**	**4.01**	0.13	Bdl.	Nd.	Bdl.	Nd.	Nd.	Bdl.	Nd.	Nd.	0.19	-0.08	0.00	0.00	98.00	Xe16 / r2 / 6b = Ti-Fe-Ox-lam. edellisessä
Nd.	**50.78**	Nd.	Bdl.	0.36	**42.28**	**3.93**	0.15	Bdl.	Nd.	Bdl.	Nd.	Nd.	Nd.	Bdl.	Bdl.	0.05	-0.02	0.00	0.00	97.66	Xe16 / r2 / 6b = Ti-Fe-Ox-lam. edellisessä
51.12	0.48	4.76	Nd.	Bdl.	12.04	0.13	11.68	18.02	1.66	Bdl.	Nd.	Bdl.	Nd.	Bdl.	Bdl.	0.04	-0.02	0.00	-0.00	100.12	Xe16 / r3 / 1 = cpx
50.62	0.62	4.79	Bdl.	Bdl.	12.04	0.26	11.62	18.27	1.68	Bdl.	Nd.	Bdl.	Bdl.	Bdl.	Bdl.	0.05	-0.02	0.00	0.00	100.18	Xe16 / r3 / 1 = cpx
34.98	**6.65**	13.92	Bdl.	0.18	17.49	Bdl.	11.06	Bdl.	0.53	**7.81**	**2.91**	Nd.	Bdl.	Bdl.	0.16	0.76	-0.32	0.32	-0.07	96.50	Xe16 / r3 / 2a = kiille
34.93	**6.86**	14.02	Bdl.	0.11	17.57	Bdl.	10.91	Bdl.	0.55	**7.91**	**3.09**	Nd.	Bdl.	Nd.	0.16	0.69	-0.29	0.33	-0.07	96.85	Xe16 / r3 / 2a = kiille
34.95	**6.66**	13.95	Bdl.	0.15	17.54	Bdl.	11.22	Bdl.	0.54	**7.89**	**3.08**	Nd.	Bdl.	Nd.	0.17	0.77	-0.32	0.30	-0.07	96.94	Xe16 / r3 / 2a = kiille
35.23	**6.73**	13.74	Bdl.	0.14	16.69	Bdl.	12.02	0.08	0.60	**7.95**	**2.76**	Nd.	Nd.	Nd.	0.17	0.80	-0.34	0.32	-0.07	96.87	Xe16 / r3 / 2b = kiille
34.83	**6.75**	13.60	Bdl.	0.12	16.42	0.09	11.95	0.09	0.58	**7.72**	**2.82**	Nd.	Bdl.	Bdl.	0.13	0.75	-0.31	0.31	-0.07	95.85	Xe16 / r3 / 2b = kiille
34.94	**6.94**	13.57	Bdl.	0.12	17.15	0.11	11.33	0.07	0.58	**7.73**	**2.79**	Nd.	Bdl.	Bdl.	0.20	0.78	-0.33	0.30	-0.07	96.28	Xe16 / r3 / 2b = kiille
39.28	0.15	21.25	Bdl.	Nd.	23.57	0.99	8.90	5.76	Nd.	Nd.	Nd.	Bdl.	Nd.	Bdl.	Nd.	0.09	-0.04	0.00	-0.00	100.06	Xe16 / r4 / 1 = granaatti
39.04	0.12	20.94	Nd.	Bdl.	23.43	0.90	8.87	5.88	Nd.	Bdl.	Nd.	Nd.	Bdl.	Bdl.	Bdl.	0.09	-0.04	0.00	0.00	99.37	Xe16 / r4 / 2 = granaatti
39.07	Bdl.	21.46	Nd.	Bdl.	23.53	0.91	8.93	6.04	Nd.	Nd.	Nd.	Bdl.	Nd.	Bdl.	Bdl.	0.13	-0.05	0.00	0.00	100.19	Xe16 / r4 / 2 = granaatti
39.28	Bdl.	21.41	Nd.	Bdl.	23.61	0.95	8.99	5.99	Nd.	Nd.	Nd.	Nd.	Bdl.	Nd.	Nd.	0.06	-0.03	0.00	-0.00	100.39	Xe16 / r4 / 2 = granaatti
39.14	Bdl.	21.01	Bdl.	Bdl.	23.64	0.93	9.00	5.82	Nd.	Bdl.	Nd.	Nd.	Bdl.	Nd.	Nd.	0.08	-0.03	0.00	0.00	99.79	Xe16 / r4 / 2 = granaatti
51.52	1.94	0.59	Bdl.	0.22	20.71	0.52	4.62	11.57	**7.32**	Nd.	Nd.	Bdl.	Nd.	Bdl.	Nd.	0.03	-0.01	0.00	0.00	99.18	Xe16 / r4 / 3a = Na-amfiboli
51.80	1.96	0.45	Bdl.	0.25	21.25	0.54	4.18	10.53	**7.93**	Bdl.	Nd.	Bdl.	Bdl.	Bdl.	Nd.	0.08	-0.04	0.00	0.00	99.13	Xe16 / r4 / 3a = Na-amfiboli
51.79	2.26	0.49	Bdl.	0.28	21.34	0.58	3.85	9.70	**8.20**	Nd.	Nd.	Bdl.	Nd.	Bdl.	Bdl.	0.04	-0.02	0.00	0.00	98.65	Xe16 / r4 / 3a = Na-amfiboli
51.84	2.12	0.56	Nd.	0.38	22.02	0.51	3.65	9.28	8.74	Nd.	Nd.	Bdl.	Nd.	Bdl.	Bdl.	0.10	-0.04	0.00	0.00	99.35	Xe16 / r4 / 4 = amfiboli (vrt. 3a)
51.65	1.98	0.66	Bdl.	0.33	22.66	0.47	3.38	8.39	9.05	Bdl.	Nd.	0.15	Nd.	Nd.	Nd.	0.07	-0.03	0.00	0.00	98.83	Xe16 / r4 / 4 = amfiboli (vrt. 3a)
51.81	2.14	0.71	Bdl.	0.25	22.96	0.46	3.12	7.94	9.36	Nd.	Nd.	Bdl.	Nd.	Bdl.	Bdl.	0.07	-0.03	0.00	-0.00	98.87	Xe16 / r4 / 4 = amfiboli (vrt. 3a)
61.83	Bdl.	22.20	Nd.	Nd.	0.18	Nd.	Nd.	**4.73**	**8.08**	**1.59**	**0.32**	0.23	Nd.	Bdl.	Nd.	0.00	0.00	0.00	0.00	99.23	Xe16 / r4 / 5 = plagioklaasi (K2O-pitoinen)

Appendix 2. Cont.

SiO2	TiO2	Al2O3	Cr2O3	V2O3	FeO	MnO	MgO	CaO	Na2O	K2O	BaO	SrO	NiO	P2O5	SO2	F	F = O	Cl	Cl = O	Total	Näyte / analyysipiste / kommentti
61.84	Nd.	22.45	Bdl.	Bdl.	0.23	Nd.	Nd.	**4.70**	**8.11**	**1.60**	**0.27**	0.24	Bdl.	Bdl.	Bdl.	0.03	-0.01	0.00	0.00	99.53	Xe16 / r4 / 5 = plagioklaasi (K2O-pitoinen)
61.68	Nd.	22.21	Nd.	Nd.	0.29	Nd.	Nd.	**4.60**	**8.01**	**1.57**	**0.18**	0.20	Nd.	Bdl.	Bdl.	0.00	0.00	0.00	0.00	98.75	Xe16 / r4 / 5 = plagioklaasi (K2O-pitoinen)
Bdl.	Nd.	Nd.	Bdl.	Nd.	0.26	0.12	0.21	54.82	0.27	Nd.	Bdl.	0.28	Nd.	**41.76**	**0.20**	**2.45**	-1.03	0.47	-0.11	**99.85**	Xe16 / r4 / 6 = apatiitti
Bdl.	Bdl.	Nd.	Bdl.	Nd.	0.30	0.11	0.19	54.71	0.28	Bdl.	Nd.	0.35	Nd.	**42.50**	**0.24**	**2.47**	-1.04	0.53	-0.12	**100.65**	Xe16 / r4 / 6 = apatiitti
0.13	Nd.	Bdl.	Nd.	Nd.	0.29	0.15	0.13	54.47	0.29	Nd.	Nd.	0.31	Nd.	**41.97**	**0.29**	**2.32**	-0.98	0.50	-0.11	**99.77**	Xe16 / r4 / 6 = apatiitti

Acceleration voltage = 15kV, electron beam current and radius 20nA and 5microns, respectively.
F-correction factor = - 0,421070494 ; Cl-correction factor = - 0,225421348.

Detection limits (on average) for the silicate, oxide, and phosphate analyses (above)

	Si	Ti	Al	Cr	V	Fe	Mn	Mg	Ca	Na	K	Ba	Sr	Ni	P	S	F	Cl
ppm	489	585	510	454	775	842	729	563	478	384	351	1674	1210	485	525	318	1191	318
wt-%	0.10	0.10	0.10	0.07	0.11	0.11	0.09	0.09	0.07	0.05	0.04	0.19	0.15	0.06	0.12	0.06	0.17	0.04

Appendix 2. Cont.

SiO2	Al2O3	Cr2O3	FeO	MnO	MgO	CaO	Na2O	SrO	BaO	NiO	ZnO	CoO	SO2	F	Cl	CO2	Total	Total	Näyte / analyysipiste / kommentti
Nd.	Nd.	Nd.	Bdl.	Bdl.	Bdl.	56.32	Nd.	0.21	Nd.	Nd.	Nd.	Nd.	Nd.	Nd.	Nd.	43.34	99.87	100	**xell-pl (rikki) / r1 / 2 = kalsiitti**
Nd.	Bdl.	Nd.	Nd.	Bdl.	Nd.	56.03	Nd.	0.21	Nd.	Nd.	Nd.	Bdl.	Nd.	Nd.	Nd.	43.62	99.86	100	xell-pl (rikki) / r1 / 2 = kalsiitti
Bdl.	Bdl.	Nd.	Bdl.	0.16	Bdl.	55.59	Nd.	0.24	Bdl.	Nd.	Nd.	Bdl.	Bdl.	Nd.	Bdl.	43.72	99.71	100	xell-pl (rikki) / r1 / 2 = kalsiitti
Nd.	Nd.	Nd.	Bdl.	Bdl.	Bdl.	56.33	Nd.	Bdl.	Nd.	Nd.	Nd.	Bdl.	Nd.	Bdl.	Nd.	43.42	99.75	100	xell-pl (rikki) / r1 / 2 = kalsiitti
Bdl.	Nd.	Nd.	Bdl.	Bdl.	Nd.	55.92	Nd.	Bdl.	Nd.	Bdl.	Bdl.	Nd.	Bdl.	Nd.	Nd.	43.64	99.55	100	xell-pl (rikki) / r1 / 2 = kalsiitti
Bdl.	Bdl.	Bdl.	0.30	0.46	Bdl.	54.58	Nd.	Bdl.	Nd.	Bdl.	Bdl.	Nd.	Bdl.	Nd.	Nd.	44.07	99.42	100	**Xe11 / r2 / 2 = kalsiitti**
Nd.	Bdl.	Nd.	Bdl.	Bdl.	Bdl.	55.42	Nd.	0.61	Nd.	Nd.	Nd.	Nd.	Nd.	Nd.	Nd.	43.85	99.87	100	**P4 / r3 / 1 = kalsiitti**
Nd.	Nd.	Nd.	Bdl.	Bdl.	Bdl.	55.27	Nd.	0.54	Nd.	Bdl.	Nd.	Nd.	Nd.	Nd.	Nd.	43.87	99.68	100	P4 / r3 / 1 = kalsiitti
Bdl.	0.01	Bdl.	Nd.	Bdl.	Bdl.	55.45	Nd.	0.53	Nd.	Bdl.	Nd.	Nd.	Nd.	Nd.	Bdl.	43.78	99.77	100	P4 / r3 / 1 = kalsiitti
Bdl.	Nd.	Nd.	Bdl.	Bdl.	Bdl.	54.47	Nd.	**1.72**	**0.27**	Nd.	Bdl.	Nd.	Nd.	Nd.	Nd.	43.32	99.79	100	**Xe15 / r1 / 6 = kalsiitti**
Bdl.	Nd.	Nd.	Bdl.	Bdl.	Nd.	54.21	Nd.	**1.71**	**0.23**	Bdl.	Bdl.	Nd.	Nd.	Nd.	Nd.	43.40	99.56	100	Xe15 / r1 / 6 = kalsiitti
Nd.	Nd.	Nd.	Bdl.	Bdl.	Nd.	54.90	Nd.	**1.54**	Bdl.	Nd.	Nd.	Bdl.	Nd.	Nd.	Nd.	43.10	99.53	100	Xe15 / r1 / 7 = kalsiitti
Nd.	Bdl.	Nd.	Bdl.	Bdl.	Nd.	55.64	Nd.	**1.77**	**0.20**	Bdl.	Bdl.	Bdl.	Bdl.	Nd.	Nd.	42.14	99.75	100	Xe15 / r1 / 7 = kalsiitti
Nd.	Nd.	0.02	Bdl.	Bdl.	Nd.	54.11	Nd.	**1.69**	**0.44**	Nd.	Nd.	Nd.	Nd.	Nd.	Nd.	43.54	99.80	100	**Xe-15 / r2 / 1 = kalsiitti**
Nd.	Nd.	Nd.	Nd.	Nd.	Bdl.	54.35	Nd.	**1.70**	**0.44**	Nd.	Nd.	Bdl.	Bdl.	Nd.	Nd.	43.39	99.87	100	Xe-15 / r2 / 1 = kalsiitti
Nd.	Bdl.	Nd.	Nd.	Nd.	Bdl.	54.24	Nd.	**1.54**	**0.51**	Bdl.	Nd.	Nd.	Nd.	Nd.	Nd.	43.57	99.86	100	Xe-15 / r2 / 1 = kalsiitti
Nd.	Bdl.	Nd.	Bdl.	Nd.	Bdl.	54.52	Nd.	**1.42**	**0.39**	Nd.	Nd.	Bdl.	Nd.	Bdl.	Nd.	43.39	99.71	100	Xe-15 / r2 / 1 = kalsiitti
Nd.	Nd.	Nd.	Bdl.	Bdl.	Bdl.	52.91	Nd.	**1.39**	**0.27**	Nd.	Bdl.	Nd.	Nd.	Nd.	Bdl.	45.24	99.81	100	Xe-15 / r2 / 2 = kalsiitti
Nd.	Nd.	Nd.	Bdl.	Bdl.	Bdl.	52.88	Nd.	**1.47**	**0.28**	Nd.	Nd.	Nd.	Nd.	Nd.	Nd.	45.23	99.87	100	Xe-15 / r2 / 2 = kalsiitti
Nd.	Bdl.	Nd.	Nd.	Bdl.	Bdl.	52.59	Nd.	**1.78**	**0.38**	Nd.	Bdl.	Bdl.	Bdl.	Nd.	Nd.	45.09	99.83	100	Xe-15 / r2 / 2 = kalsiitti
Nd.	Nd.	Nd.	Bdl.	Nd.	Bdl.	52.59	Nd.	**1.85**	**0.39**	Bdl.	Bdl.	Nd.	Nd.	Nd.	Nd.	44.94	99.78	100	Xe-15 / r2 / 2 = kalsiitti
Nd.	Nd.	Nd.	Bdl.	Nd.	Nd.	53.26	Nd.	**1.34**	**0.41**	Nd.	Nd.	Bdl.	Nd.	Nd.	Nd.	44.76	99.77	100	Xe-15 / r3 / 5 = kalsiitti
Nd.	Bdl.	Nd.	Bdl.	Bdl.	Bdl.	53.05	Nd.	**1.28**	**0.49**	Bdl.	Bdl.	Nd.	Nd.	Nd.	Nd.	44.86	99.67	100	Xe-15 / r3 / 5 = kalsiitti
Bdl.	Bdl.	Bdl.	**7.25**	**0.14**	**16.41**	**27.11**	Nd.	1.72	Bdl.	Nd.	Nd.	Nd.	Nd.	Nd.	Nd.	47.24	99.87	100	**P3 / r1 / 9 = Ca-Mg-Fe-karbonaatti**
Bdl.	Nd.	Bdl.	**11.41**	**0.32**	**13.19**	**27.49**	Nd.	0.44	Bdl.	Bdl.	Nd.	Nd.	Nd.	Nd.	Nd.	46.98	99.82	100	P3 / r1 / 9 = Ca-Mg-Fe-karbonaatti
Bdl.	Nd.	Bdl.	**11.09**	**0.46**	**13.41**	**28.17**	Nd.	0.31	Bdl.	Nd.	Bdl.	Nd.	Nd.	Nd.	Nd.	46.10	99.53	100	P3 / r1 / 9 = Ca-Mg-Fe-karbonaatti
Bdl.	Bdl.	Bdl.	**8.10**	**0.27**	**15.22**	**27.12**	Nd.	1.57	Bdl.	Nd.	Bdl.	Bdl.	Nd.	Nd.	Nd.	47.51	99.79	100	P3 / r1 / 9 = Ca-Mg-Fe-karbonaatti
Bdl.	Bdl.	Bdl.	**7.55**	**0.22**	**15.51**	**27.22**	Nd.	1.42	Bdl.	Nd.	Nd.	Bdl.	Nd.	Nd.	Nd.	47.80	99.73	100	P3 / r1 / 9 = Ca-Mg-Fe-karbonaatti
Nd.	Nd.	0.12	**12.12**	**0.54**	**12.80**	**27.36**	Nd.	0.30	Nd.	Nd.	Nd.	Nd.	Bdl.	Nd.	Nd.	46.66	99.90	100	P3 / r1 / 10 = Ca-Mg-Fe-karbonaatti
Bdl.	Nd.	Bdl.	**11.68**	**0.56**	**13.15**	**27.56**	Nd.	0.32	Nd.	Bdl.	Bdl.	Nd.	Bdl.	Nd.	Nd.	46.50	99.78	100	P3 / r1 / 10 = Ca-Mg-Fe-karbonaatti

Appendix 2. Cont.

SiO2	Al2O3	Cr2O3	FeO	MnO	MgO	CaO	Na2O	SrO	BaO	NiO	ZnO	CoO	SO2	F	Cl	CO2	Total	Total	Näyte / analyysipiste / kommentti
Bdl.	Nd.	Bdl.	**11.40**	**0.44**	**13.47**	**27.46**	Nd.	0.39	Nd.	Bdl.	Nd.	Nd.	Bdl.	Nd.	Bdl.	46.57	99.74	100	P3 / r1 / 10 = Ca-Mg-Fe-karbonaatti
Bdl.	Nd.	Bdl.	**11.17**	**0.49**	**13.41**	**27.83**	Nd.	0.57	Nd.	Nd.	Nd.	Nd.	Bdl.	Nd.	Nd.	46.42	99.89	100	P3 / r1 / 10 = Ca-Mg-Fe-karbonaatti
Bdl.	Nd.	Bdl.	**9.62**	**3.00**	**11.35**	**29.89**	Nd.	0.67	Nd.	Bdl.	Nd.	Nd.	Nd.	Nd.	Nd.	45.34	99.87	100	**13X-07 / r1 / 1 = Ca-Mg-Fe-karbonaatti**
Nd.	Nd.	Nd.	**9.66**	**2.83**	**11.30**	**29.29**	Nd.	0.80	Nd.	Nd.	Bdl.	Nd.	Nd.	Nd.	Nd.	46.05	99.95	100	13X-07 / r1 / 1 = Ca-Mg-Fe-karbonaatti
Nd.	Bdl.	Bdl.	**10.02**	**2.76**	**11.97**	**29.25**	Nd.	0.80	Nd.	Nd.	Bdl.	Nd.	Nd.	Nd.	Nd.	45.12	99.90	100	13X-07 / r1 / 1 = Ca-Mg-Fe-karbonaatti
Nd.	Bdl.	Bdl.	**9.14**	**3.23**	**11.24**	**30.19**	Nd.	0.68	Nd.	Bdl.	Nd.	Nd.	Bdl.	Nd.	Nd.	45.33	99.81	100	13X-07 / r1 / 1 = Ca-Mg-Fe-karbonaatti
Bdl.	Nd.	Nd.	Bdl.	Bdl.	Bdl.	53.14	Nd.	**1.96**	**0.23**	Nd.	Nd.	Nd.	Bdl.	Nd.	Bdl.	44.52	99.85	100	**Xe15B / r1 / 1 = kalsiitti**
Nd.	Nd.	Nd.	Nd.	Nd.	Bdl.	52.76	Nd.	**2.03**	Bdl.	Bdl.	Nd.	Nd.	Nd.	Nd.	Nd.	45.00	99.79	100	Xe15B / r1 / 1 = kalsiitti
Nd.	Nd.	Nd.	Nd.	Bdl.	Bdl.	53.25	Nd.	**2.08**	**0.20**	Nd.	Nd.	Nd.	Nd.	Bdl.	Nd.	44.42	99.94	100	Xe15B / r1 / 1 = kalsiitti
Nd.	Bdl.	Bdl.	Bdl.	Bdl.	Bdl.	53.26	Nd.	**1.81**	**0.20**	Nd.	Nd.	Bdl.	Bdl.	Nd.	Nd.	44.43	99.70	100	Xe15B / r2 / 4 = kalsiitti
Bdl.	Bdl.	Nd.	Nd.	Nd.	Nd.	53.99	Nd.	**1.40**	Nd.	Nd.	Nd.	Bdl.	Nd.	Nd.	Nd.	44.23	99.62	100	Xe15B / r2 / 4 = kalsiitti
Nd.	Nd.	Nd.	Nd.	Nd.	Bdl.	54.02	Nd.	**1.61**	Bdl.	Nd.	Bdl.	Nd.	Nd.	Nd.	Nd.	43.98	99.61	100	Xe15B / r2 / 4 = kalsiitti
Bdl.	Nd.	Nd.	Bdl.	Bdl.	Bdl.	55.64	Nd.	**1.53**	**0.24**	Nd.	Nd.	Nd.	Nd.	Nd.	Bdl.	42.42	99.83	100	Xe15B / r2 / 4 = kalsiitti
Bdl.	Nd.	Bdl.	Bdl.	Nd.	Nd.	54.76	Nd.	**0.97**	Nd.	Bdl.	Nd.	Nd.	Bdl.	Nd.	Bdl.	44.00	99.73	100	**Xe15B / r2 / 4 = kalsiitti**
Bdl.	Bdl.	Nd.	Nd.	Nd.	Bdl.	56.16	Nd.	**0.87**	Nd.	Nd.	Nd.	Bdl.	Bdl.	Nd.	Bdl.	42.81	99.84	100	Xe15B / r2 / 4 = kalsiitti
Nd.	Nd.	Nd.	**0.21**	**0.25**	**0.37**	54.40	Nd.	**0.75**	Nd.	Bdl.	Nd.	Nd.	Nd.	Nd.	Bdl.	43.81	99.79	100	**Xe16 / r4 / 3b = kalsiitti**
Nd.	Bdl.	Nd.	**0.26**	**0.33**	**0.26**	54.65	Nd.	**0.73**	Nd.	Nd.	Nd.	Nd.	Nd.	Nd.	Nd.	43.61	99.84	100	Xe16 / r4 / 3b = kalsiitti
Bdl.	Bdl.	Nd.	**0.25**	**0.76**	**0.27**	54.65	Nd.	**0.46**	Nd.	Nd.	Nd.	Nd.	Nd.	Nd.	Nd.	43.57	99.96	100	Xe16 / r4 / 3b = kalsiitti
Bdl.	Nd.	Nd.	**0.27**	**0.78**	**0.08**	54.49	Nd.	**0.55**	Nd.	Nd.	Nd.	Bdl.	Nd.	Nd.	Nd.	43.76	99.92	100	Xe16 / r4 / 3b = kalsiitti

Acceleration voltage = 15kV, electron beam current and radius 10nA and 5-10 microns, respectively.
CO2 = 100 wt-% - analysed total

Detection limits (on average) for the carbonate analyses (above)

	Si	Al	Cr	Fe	Mn	Mg	Ca	Na	Sr	Ba	Ni	Zn	Co	S	F	Cl
ppm	461	467	738	1063	904	610	1344	507	1303	1642	907	2054	1036	390	2095	416
wt-%	0.099	0.088	0.108	0.137	0.117	0.101	0.188	0.060	0.162	0.183	0.115	0.250	0.130	0.078	0.300	0.056

Mikroanalysaattori / operaattori = Cameca SX100 / LKP	Microanalysator / operator = Cameca SX100 / Lasse Pakkanen, GTK.

All GTK's publications online at hakku.gtk.fi

This PhD thesis is a monograph and reveals the Mesoproterozoic–Jurassic origins of xenolith samples from Vestfjella, western Dronning Maud Land, Antarctica. The xenoliths provide direct evidence of this concealed continental crustal domain. Thermal events, which occurred at 590–1150 Ma, are recorded by zircon crystallization in arc-affinity metatonalite, quartz metadiorite and metagranite xenoliths. The evolution of the Vestfjella crust began in the Mesoproterozoic with arc magmatism at ca. 1300–1450 Ma. The arc formation evidences the internal evolution of the Rodinia Supercontinent. The zircon in quartz metadiorite xenolith records heating, possibly due to Gondwana assembly in the Neoproterozoic. The youngest xenolith zircon age, 165 Ma, records crustal heating and granite magmatism post-dating the Gondwana break-up magmatism. The Proterozoic zircon ages recorded by the lamproite-hosted xenoliths are similar to the crustal domains in the Natal Belt of southern Africa, the Maud Belt of central and western Dronning Maud Land and remote Mesoproterozoic basement exposed in the West Falkland Islands and Haag nunataks, West Antarctica.

gtk.fi

ISBN 978-952-217-401-7 (pdf)
ISBN 978-952-217-402-4 (paperback)
ISSN 2489-639X (online)
ISSN 0367-522X (print)